

Design and Analysis of Kinematic Couplings for Modular Machine and Instrumentation Structures

by

Anastasios John Hart
B.S.E. Mechanical Engineering (2000)
University of Michigan

Submitted to the Department of Mechanical Engineering
in partial fulfillment of the requirements for the degree of

Master of Science (S.M.)

at the

MASSACHUSETTS INSTITUTE OF TECHNOLOGY

FEBRUARY 2002

© Massachusetts Institute of Technology, 2002. All Rights Reserved.

Author
Department of Mechanical Engineering
December 10, 2001

Certified by
Alexander H. Slocum
Professor of Mechanical Engineering
Thesis Supervisor

Accepted by
Ain A. Sonin
Chairman, Mechanical Engineering Graduate Committee

Design and Analysis of Kinematic Couplings for Modular Machine and Instrumentation Structures

by

Anastasios John Hart
Precision Engineering Research Group
Massachusetts Institute of Technology

Submitted to the Department of Mechanical Engineering on
December 10, 2001 in partial fulfillment of the requirements for the
degree of Master of Science

Abstract

For decades, kinematic couplings have been developed and used because of their astounding repeatability, but few efforts have been made to unify the design theory into a general strategy for widespread application of deterministic interfaces in flexible automation, where both repeatability and interchangeability are important. Accordingly, this thesis seeks to present a methodology for using kinematic couplings as deterministic interfaces for modular machine and instrumentation structures, with focus applications to design of an industrial robot factory interface and design of a next-generation microscope structure.

Theory is presented for design of traditional ball/groove, canoe ball, traditional quasi-kinematic, three-pin quasi-kinematic, and cylinder/groove quasi-kinematic couplings. Furthermore, the ability to parametrize kinematic coupling performance is extended from reliance on experimental repeatability analysis to an estimate of Total Mechanical Accuracy, based on a closed-form computer model for determining the interchangeability of canoe ball and three-pin interfaces. With calibration of the interface by measurement of the perturbed locations of its contact points, introduction of an interface transformation to a machine's structural loop can reduce the deterministic interchangeability error to essentially that inherent in the routine of the measurement system used for calibration. Perhaps more powerfully, a parametric model of interchangeability allows engineers to predict the accuracy of an interface, based on tolerance distribution parameters assigned to the coupling manufacturing process, plate manufacturing process, interface assembly process, and interface calibration process. This predictive ability enables choice of manufacturing process precision and calibration detail to give the desired interface accuracy at minimum cost. Modularity of structures based on kinematic couplings can also be exploited to provide flexibility through being able to interchange style-specific manufacturing tools without the need for re-calibration of machines, and as demonstrated by the microscope case study, significantly improved thermal performance for ultra high-precision applications.

Looking forward, the ability to characterize performance of kinematic couplings in a closed form makes them well-suited for development of a standard representation for

kinematic couplings. Most powerfully, kinematic couplings can be envisioned as an ideal handshake between precision mechanics and information technology. At the most basic level, encoding of interface calibration data on a wireless tag can initiate communication between the interface and a calibration computer when the interface is in proximity to the machine. A conceptual framework for further thinking in convergence of quick-change interfaces and thin-client information interfaces to build low-cost, intelligent, flexible, automation processes, is given.

Thesis Supervisor: Alexander H. Slocum

Title: Professor, Department of Mechanical Engineering

Table of Contents

1. Introduction	13
1.1 Motivation	13
1.2 Deterministic Systems	15
1.3 Thesis Outline	16
2. Kinematic Coupling Design	19
2.1 Traditional Kinematic Couplings and Fundamental Design Theory	19
2.2 Canoe Ball Couplings	26
2.3 Quasi-Kinematic Couplings	27
2.4 Three-Pin In-Plane Coupling	30
2.5 Fatigue Life Considerations	35
2.6 Interface Packaging and Tightening Torque Specification	36
3. Interchangeability of Deterministic Kinematic Interfaces	39
3.1 Repeatability vs. Interchangeability	39
3.2 Global Error Model of a Kinematic Coupling Interface	40
3.3 Kinematic Coupling Measurement and Calibration	47
3.4 Applied Modeling of Error Components	57
3.5 Parametric Relationship of Calibration Detail vs. Mating Accuracy	64
3.6 Bench-Level Interchangeability Model	72
3.7 Interchangeability Model of Three-Pin Interface	78
3.8 A New, Interface-Driven Machine Module Calibration Process	81
3.9 Conclusions and Future Work Plans	83
4. Machine Case Study: Mechanical Performance of a Quick-Change Industrial Robot Factory Interface	87
4.1 Background and Problem Definition	87
4.2 Current Interface Design and Robot Installation Procedure	91
4.3 Customer Attitudes Towards Interface-Based Modularity	94
4.4 Quick-Change Interface: Applied Kinematic Coupling Design Process	96
4.5 Prototype Repeatability Tests	113
4.6 Factory Interface Interchangeability Simulations	128
4.7 Conceptual Extension to Four-Point Mounting	136
4.8 Improvements to Robot Accuracy	137
4.9 Caveats and Needs for Future Work	140
5. Instrumentation Case Study: Thermal Performance of a Modular Structure for a High-Precision Microscope	143
5.1 Overview of the High Precision Microscope Project	143
5.2 Design and Theoretical Basis of the Modular Structure	145
5.3 Thermal Stability Evaluation	153
5.4 Future Work and Conclusions	184

6. Toward Standard, Low-Cost, Intelligent, Modular Systems	187
6.1 The Interface Design Process	187
6.2 Fundamental Hardware and Software	193
6.3 Intelligent Manufacturing Systems Using Kinematic Couplings	203
7. Conclusion	213
8. Appendices	215
A. References	215
B. Kinematic Coupling Design Code	217
B.1 Design of Traditional and Canoe Ball Couplings	217
B.2 Contact Force Calculation for Three-Pin Interface	229
B.3 In-Plane Preload Calculation (Friction Limit) for Three-Pin Interface	230
B.4 Bolt Tightening Torque Calculation	235
C. Kinematic Exchangeability Analysis Code	237
C.1 Canoe Ball Interface Exchangeability	237
C.2 Three-Pin Interface Exchangeability	252
C.3 Common Routines, Used By Both Simulations	255
D. Appended Thermal Stability Results	257
E. Robot Calibration Pose Set Sequence Optimization	263

List of Figures

Chapter 1

1.1 Summary of kinematic and quasi-kinematic interface designs.	14
1.2 Schematic of an intelligent kinematic interface.	16

Chapter 2

2.1 Model of three-ball/three-groove kinematic coupling (with magnetic preload).	20
2.2 Planar triangular kinematic coupling layout showing coupling centroid [4].	21
2.3 Canoe ball mount with 250 mm contact surface radii.	26
2.4 Typical quasi-kinematic coupling interface.	28
2.5 Quasi-kinematic contactor.	29
2.6 Quasi-kinematic target with $\theta_{CT}= 90$ deg.	29
2.7 Arrangement of three-pin interface.	31
2.8 In-plane preload and contact reaction forces against three-pin interface.	32
2.9 Solid model of three-pin interface showing pins floated (top interface plate blanked) and direction of application for F_p .	

Chapter 3

3.1 Modular machine interface with kinematic couplings, designating reference interface, tool, and measurement system coordinate frames.	41
3.2 Block diagram representation of the error stackup for a kinematic coupling interface.	45
3.3 Canoe ball coupling assembly with tooling ball measurement feature.	48
3.4 Quasi-kinematic coupling assembly with tooling ball measurement feature	48
3.5 Canoe ball mount with integrally machined measurement hemisphere.	49
3.6 In-plane depiction error motion due to perturbations in ball and groove positions and orientations.	54
3.7 Ball error components in local x-direction.	60
3.8 Ball error components in local y-direction.	61
3.9 Ball error components in local z-direction.	62
3.10 Structure of MATLAB model for parametric error analysis of canoe ball interface.	68
3.11 Tool point error versus interface calibration detail - calibration using offset measurement sphere.	71
3.12 Tool point error versus interface calibration detail - calibration using direct measurement of ball and groove contact surfaces.	71
3.13 Tool point error under angular misalignment of a single canoe ball/groove pair.	72
3.14 Prototype groove base for measurement of canoe ball interface interchangeability (three adjacent grooves removed).	73
3.15 Prototype pallet for interchangeability measurements - canoe ball side.	73
3.16 Prototype pallet for interchangeability measurements - measurement sphere side.	73
3.17 Interchangeability setup on Brown & Sharpe MicroVal PFx CMM	75
3.18 Pallet in 60 degree clockwise measurement position.	75
3.19 In-plane angular error of prototype pallets before and after transformation correction.	77
3.20 Simple ball interface calibration to workcell using ball bar.	82

Chapter 4

4.1 Six-axis industrial robot manipulator commonly used in automotive assembly (ABB IRB6400R).	88
4.2 Nomenclature of ABB IRB6400R's six revolute axes [1].	88
4.3 Three-point manipulator foot (ABB IRB6400).	92
4.4 Schematic of four-point manipulator foot (ABB IRB6400R) [1].	92
4.5 Four point, eight-bolt 6400R manipulator foot mounted on test pallet.	92
4.6 Scale prototype canoe coupling interface, with 3/4-scale placement relative to the full-size design.	97
4.7 Tooling ball reference sphere.	98
4.8 Leica laser tracker with retro-reflector in calibration seat.	98
4.9 Prototype steel interface plate to manipulator foot - top side.	100
4.10 Prototype steel interface plate to manipulator foot - bottom side.	100
4.11 Prototype steel interface plate to manipulator foot - top side.	100
4.12 Solid model of interface assembly for static stress analysis.	101
4.13 Deformation of prototype interface assembly under fully-reversed operation loading.	102
4.14 Canoe groove fitted to top interface plate, showing secondary alignment pin.	104
4.15 Canoe ball with integrated tooling ball fitted to bottom interface plate.	104
4.16 Interface plates fitted with canoe ball couplings.	105
4.17 Mounted canoe ball joint with tooling ball.	105
4.18 Prototype shouldered coupling pin - side view.	107
4.19 Prototype shouldered coupling pin - perspective view.	107
4.20 Application of preload through threaded hole in floor interface plate.	107
4.21 Preload screw in prototype floor interface plate.	107
4.22 Shoulder pin fitted to top interface plate.	108
4.23 Interface plates fitted with three-pin couplings.	108
4.24 Mounted three-pin joint.	108
4.25 Flanged mild steel groove.	110
4.26 Aluminum cylinder mounted statically between pair of grooves.	110
4.27 Solid model of quasi-kinematic coupling assembly with measurement ball.	112
4.28 Solid model of prototype quasi-kinematic contactor	112
4.29 Solid model of prototype quasi-kinematic target.	112
4.30 Cell setup for repeatability measurements, showing mounted manipulator in crouched home position and laser tracker.	114
4.31 Leica cat's eye retroreflector mounted on robot tool flange.	114
4.32 Manipulator harnessed to crane, hanging unbolted over floor interface.	116
4.33 Retroreflector seated in measurement hole in top interface plate.	116
4.34 Programmed measurement path - point 1.	117
4.35 Programmed measurement path - point 2.	117
4.36 Programmed measurement path - point 5.	118
4.37 Programmed measurement path - point 3.	118
4.38 Programmed measurement path - point 4.	118
4.39 Progressive average measurement distances from previous trials for interfaces.	121
4.40 Comparison of average relative repeatabilities to performance of current two-pin base.	122
4.41 Cartesian TCP deviations from first trial - three-pin interface, refined mounting.	124
4.42 Cartesian TCP deviations from first trial - canoe ball interface, refined mounting.	125
4.43 Cartesian TCP deviations from first trial - groove-cylinder interface, refined mounting.	126
4.44 Canoe ball surface after eleven base mountings.	127
4.45 Aluminum cylinder after fifteen static base mountings.	127

4.46 Parametric calibration complexity vs. interchangeability relationship for canoe-ball manipulator base interface: offset measurement, low measurement system error, varying form error.	131
4.47 Parametric calibration complexity vs. interchangeability relationship for canoe-ball manipulator base interface: direct measurement, low measurement system error, varying form error.	132
4.48 Calibration complexity vs. interchangeability relationship for three-pin interface.	135
4.49 Split groove canoe ball to accommodate kinematic mounting using all four corners of a bolt rectangle.	137
4.50 Four-point coupling locations on four-corner mounting base.	137

Chapter 5

5.1 Cross-section of High-Precision Microscope (HPM) concept model.	144
5.2 Exploded model of segmented structure including two canoe ball sets.	147
5.3 Close view of canoe ball interfaces between segments.	147
5.4 Theorized constant temperature profiles on tall and short cylindrical tubes.	149
5.5 Temperature sensor placements and nomenclature.	154
5.6 Optical beam path and laser metrology setup.	156
5.7 DPMI assembly on 5" diameter central reference column.	156
5.8 Final test assembly - segmented structure.	157
5.9 Final test assembly - one-piece control structure.	157
5.10 Thermal isolation chamber.	158
5.11 Solid model of segmented structure for finite element simulation.	160
5.12 Solid model of one-piece control structure for finite element simulation.	160
5.13 Steady-state temperature contours on segmented model.	161
5.14 Steady-state temperature contours on one-piece model.	162
5.15 Axial displacement contours on segmented tube model.	163
5.16 Axial displacement contours on one-piece tube model.	163
5.17 Deflection of segmented structure versus time (measurement duration extended to 13 hours to show thermal relaxation).	165
5.18 Comparison of deflections of segmented and one-piece structures over 450-minute test.	166
5.19 Normalized temperatures (10-minute averages) around tube 1 (non-heated) of segmented structure.	167
5.20 End-to-end normalized temperature difference on tube 1 of segmented structure.	168
5.21 Normalized temperatures (10-minute average) around tube 3 of segmented structure.	169
5.22 End-to-end normalized temperature difference on tube 3 of segmented structure.	170
5.23 Circumferential normalized temperature profiles for tube 3 of segmented structure.	171
5.24 Normalized temperatures (10-minute average) around level 3 of one-piece structure.	172
5.25 End-to-end normalized temperature difference at level 3 of one-piece structure.	173
5.26 Comparison of measured and predicted angular deflections of segmented structure.	177
5.27 Axial displacement contours on copper (left) segmented structure.	179
5.28 Axial displacement contours on stainless steel (right) segmented structure.	179
5.29 Angular deflection of segmented and one-piece copper structures with varied thickness.	181
5.30 Angular deflection of structure with varying number of segments.	181
5.31 Angular deflection versus dimensionless segment length to thickness ratio.	182
5.32 Simulation model with insulation bonded to outside surfaces of tube segments.	183
5.33 Steady-state axial displacement contours on 1.5" insulation / 2.5" copper model.	183

Chapter 6

6.1	Parameter heirarchy for a canoe ball interface.	189
6.2	Isometric model view of extruded locator with central hole for clamping bolt.	196
6.3	End view of extruded locator in double mating vee grooves.	196
6.4	Section design parameters of extruded locator.	197
6.5	Non-deformed and deformed waterjet aluminum locators.	197
6.6	Aluminum locator clamped between vee grooves with side datum blocks on test fixture.	198
6.7	Communications architecture of a smart interface with locally-written parameters.	200
6.8	Communications architecture of a smart interface or module with server storage.	201
6.9	Integrated mechanical and information infrastructure for modular factory robotics.	205
6.10	Model of wireless measurement tool kinematically coupled to groove plate on body subassembly welding fixture.	209
6.11	Ball-groove interface holding tool in non-contact evaluation of flange position.	210
6.12	Example wireless communication architecture between measurement unit, part, tool, and offline computer.	211

List of Tables

Chapter 2

2.1 Fatigue strengths of selected steel alloys [12].	36
--	----

Chapter 3

3.1 Representative 3-sigma values for interface error components.	64
3.2 Calibration options for canoe ball interface, using offset measurement feature.	66
3.3 Calibration options for canoe ball interface, directly measuring contact surfaces.	67
3.4 Error component values for parametric study with varied calibration complexity.	69
3.5 Canoe ball interface geometry for parametric study with varied calibration complexity.	69
3.6 Calibration options for three-pin interface.	80

Chapter 4

4.1 Manipulator exchange times under varying levels of on-line calibration.	95
4.2 ABB IRB6400R dynamic loads at center of foot (max, min).	96
4.3 Initial design parameters for canoe ball couplings	103
4.4 Final Specifications of prototype canoe ball coupling	104
4.5 Required preloads to pin interface in cases of partial contact.	106
4.6 Specifications of designed prototype quasi-kinematic couplings.	111
4.7 Average tool point path repeatabilities [mm] of current ABB and new kinematic coupling base designs, relative to previous trials.	120
4.8 Average tool point path repeatabilities [mm] of current and new designs, relative to nominal average of all trials.	123
4.9 Error component values for canoe ball interchangeability simulation.	129
4.10 Error component values for three-pin interchangeability simulation.	133
4.11 Total Mechanical Accuracy (TMA) of manipulator base solutions.	138

Chapter 5

5.1 Steady-state and transient performance index values for various metals.	151
5.2 Simulated and measured end-to-end circumferential temperature differences [C].	174
5.3 Tube material optimization study results (DT = heated minus non-heated).	178

Chapter 6

6.1 Suggested performance parameters for a standard kinematic interface.	188
--	-----

Chapter 1

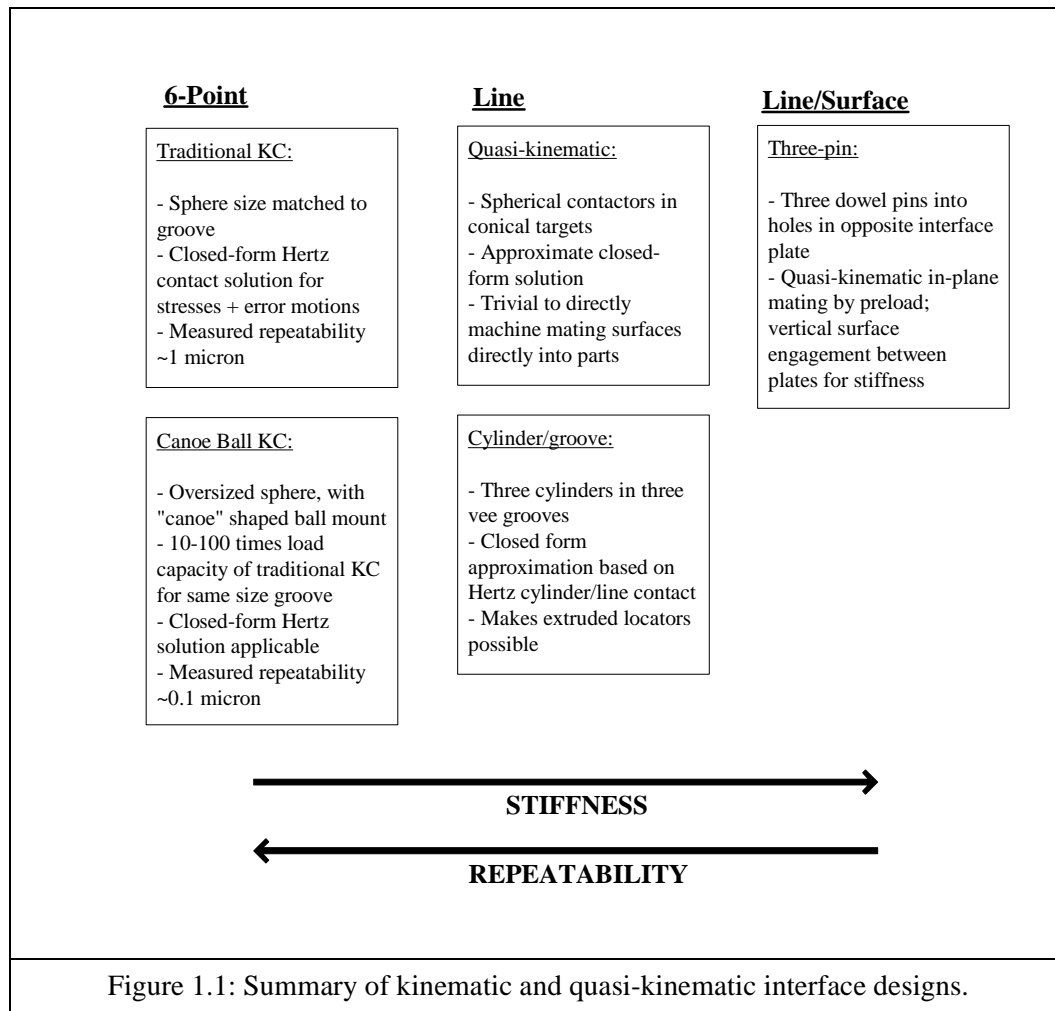
Introduction

1.1 Motivation

As budgetary and manufacturing quality requirements simultaneously become more stringent, manufacturing strategies are focusing on modular machine systems as a means for achieving flexibility to produce multiple products at flexible volumes, minimizing downtime in the case of catastrophic equipment failures, and maximizing reusability of machine modules between product generations. In modularizing machines to build these flexible systems, decisions regarding the degree to which machines should be segmented are often a trade-off against machine accuracy. For example, making a single, non-modular machine, such as an industrial robot, would require full calibration upon initial installation. When the machine fails, one must decide whether to repair the machine online, or replace it with an entirely new spare part. Replacement in this case almost always necessitates a re-calibration before production can be resumed.

One of the main contributors to the error of machine interchanges is the accuracy of the mounting interface, whereby the manufacturing errors in the interface locators, and the potentially non-deterministic nature of the interface contact itself, prevent installation with sufficient accuracy to eliminate the need for re-calibration of the machine. Kinematic couplings, researched and used for decades in large part because of their astounding repeatability, offer a potential solution to the problem of requiring re-calibration when new machine modules are installed. The near-exact constraint of the kinematic coupling relationship means that the error of interchange can be predicted if the positions of the coupling locators are known ahead of time. Hence, a correction for the interface mounting error is a virtual calibration routine in software, rather than a physical measurement routine when the new machine module is mounted into the manufacturing system. Furthermore, once modularity of machines can be achieved with minimum error of interchangeability, other mechanical benefits can be achieved, including ability to interchange style-specific tooling components rapidly, give easier access for critical repairs, and thermally isolation of critical structural areas.

Over the past twenty years, research in kinematic couplings has extended the basic concepts of a traditional coupling between three balls and three grooves, or between three cylinders and three grooves, to numerous variants of exact and near-exact constraint mountings. Figure 1.1 summarizes several common types of kinematic couplings, categorized in terms of their type of contact. Note that an increased level of determinism, e.g. 6-point contact versus line and/or surface contact, results in increasing stiffness and increasing repeatability.



In seeking to extend the applicability of kinematic couplings and low-cost near-deterministic interfaces in general, to widespread industrial situations, a number of research questions must be answered:

1. How do performance parameters of kinematic couplings, such as stiffness and repeatability, change in applications involving extremely high loads?

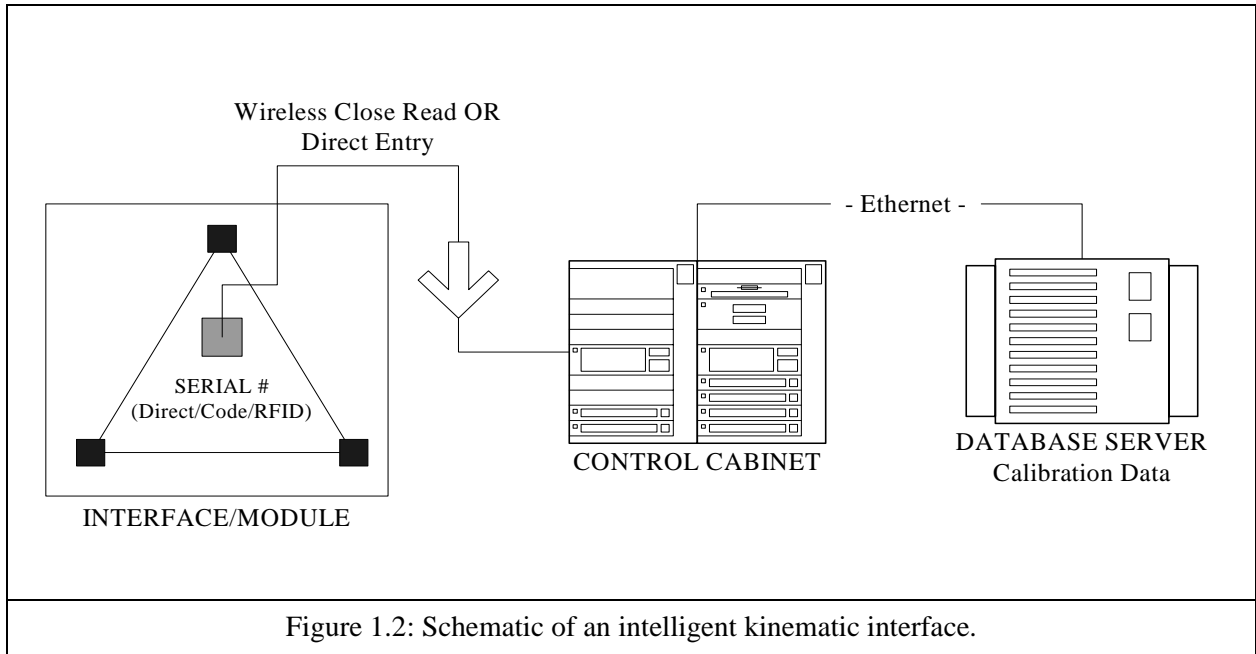
2. How can the deterministic nature of kinematic couplings be exploited to not only provide astounding repeatability, but also very low error of interchangeability; and how can kinematic couplings be calibrated to minimize their interchangeability error?
3. Based on the answers to (1) and (2), can new types of kinematic couplings be designed to provide sufficient accuracy and repeatability for high-load industrial applications, at a significantly lower cost than existing designs?
4. Finally, how can kinematic couplings design, and use of modular machines in general, be made a closed-loop design process? Engineers should be able to predict the accuracy of their designs before mass-production; interfaces should automatically be recognized and calibrated upon installation to a machine; and performance parameters from a machine should automatically be archived and fed back to the designer so remote process control can be conducted.

This thesis provides preliminary answers to the above queries.

1.2 Deterministic Systems

Motivated by the concept of using kinematic couplings to remove the dependence of machine interchangeability error on of mounting the module interfaces, deterministic interfaces are well-suited to a standard mechanical design and information representation. Information is inherently deterministic, and object-oriented representations such as Java and XML improve extensibility of information, and make it easier to network components and define behaviors using standard protocols. Accordingly, kinematic couplings can be treated as deterministic mechanical and information objects, with their design parameters (e.g. interface type, material, etc.) and calibration parameters as member variables. As conceptualized in Figure 1.4, a memory tag on a kinematic coupling can note its calibration parameters, for recognition by a reader-equipped control cabinet upon installation to a machine.

The grand goal would be to develop an accepted standard for mechanical interchangeability among components, so the identification number on a kinematic interface not only gives the calibration parameters to the interface locators, but also gives a unique identifier to the module equipment itself. The identifier can be traced to a centralized database, where specific information about the module equipment is contained, such as geometrical data, manufacturing history, repair history, and additional calibration parameters.



The most apparent application of standardization is to robotics, for which the standards could enable a robotic subassembly, such as a wrist, to be easily changed, without requiring recalibration of the robot. The wrist would mate to a standard plate. A similar master plate would be located at the robot manufacturer, and each subassembly would be calibrated with respect to the mounting plate master. Thus when a replacement subassembly is delivered to the factory, it comes with a set of calibration coefficients with respect to the mounting plate master, and it can be “plugged into place and start working”. Thus should a subassembly fail during use, it could be “unplugged” and a new subassembly could be “plugged in” and used without having to recalibrate it to the line.

1.3 Thesis Outline

This thesis focuses on application of kinematic couplings to enable high-precision modularity of factory automation, with two focus applications: the factory interface of a heavy-duty-industrial robot used for automotive body assembly, and the structure of a next-generation microscope to be used for single-molecule biological investigations. This document is organized as follows:

Chapter 2 is an overview of the basic principles of kinematic coupling design and Hertzian contact mechanics. These principles are applied to present design methodologies for traditional ball/groove, canoe ball/groove, three-pin, groove/cylinder, and quasi-kinematic couplings.

Chapter 3 presents and validates a deterministic model for assessing the interchangeability error of kinematic interfaces caused by assembly variation and form error in the coupling units and interface mounting plates. The model is presented in detail as an exact solution for canoe ball couplings, and is extended with deterministic mating assumptions to the three-pin interface.

Chapter 4 presents an application case study of canoe ball, three-pin, and groove-cylinder couplings to the factory interface of the ABB IRB6400R industrial robot manipulator. Results of static and dynamic repeatability measurements are presented, and the interchangeability of the canoe ball and three-pin designs is simulated using the model described in Chapter 3.

Chapter 5 presents the structural design of a modular high-precision microscope as a series of tube segments connected by canoe ball kinematic couplings. Experimental study and design optimization using finite element simulation show that the segmented design offers a significant thermal stability advantage over a one-piece tubular structure, and the known high repeatability of the kinematic couplings enables the structural modules to be interchanged without recalibration of the optics.

Chapter 6 presents a framework for large-scale implementation of kinematic couplings in a modular manufacturing system. Three developments would be critical: standardization of the kinematic coupling design process through a set of input and output parameters specific to each interface; design of low-cost locators with smart methods to hold interchangeability calibration parameter data; and integration of the interfaces into a networked system to enable ‘plug-and-play’ authentication of interfaced parts or carriers and feedback of process performance data.

Chapter 2

Kinematic Coupling Design

A fundamental technology of high-precision mechanical interfaces for modular machine and instrumentation structures is the kinematic coupling. This chapter provides a fundamental description of kinematic coupling design, with special considerations given to interfaces used in equipment that is subject to large disturbance forces. While traditional ball-groove kinematic couplings are a century-old design offering micron-level repeatability, developments of recent research have produced variants suited to special high-load, high-cycle, and high-volume installation applications, including the canoe ball coupling [1], the quasi-kinematic coupling [2], the three-tooth coupling [3], and most recently the three-pin coupling. For all such types, closed form relations or well-grounded approximations directly guide interface geometry design and material selection when the load case is known. This chapter presents contact mechanics theory applied to kinematic couplings, and briefly discusses design processes for traditional, canoe ball, quasi-kinematic, and three-pin interfaces.

2.1 Traditional Kinematic Couplings and Fundamental Design Theory

Kinematic couplings have been used for over a century as a method of precisely locating components of a mechanical assembly. The oldest, most common form is the three-ball/three-groove kinematic coupling shown schematically in Figure 2.1. The ball/groove coupling matches a planar, triangular arrangement of three hemispheres on one component to three “vee-grooves” on another component. This match deterministically constrains all six degrees of freedom (DOF) -- three directions of translation and three directions of rotation -- between the components.

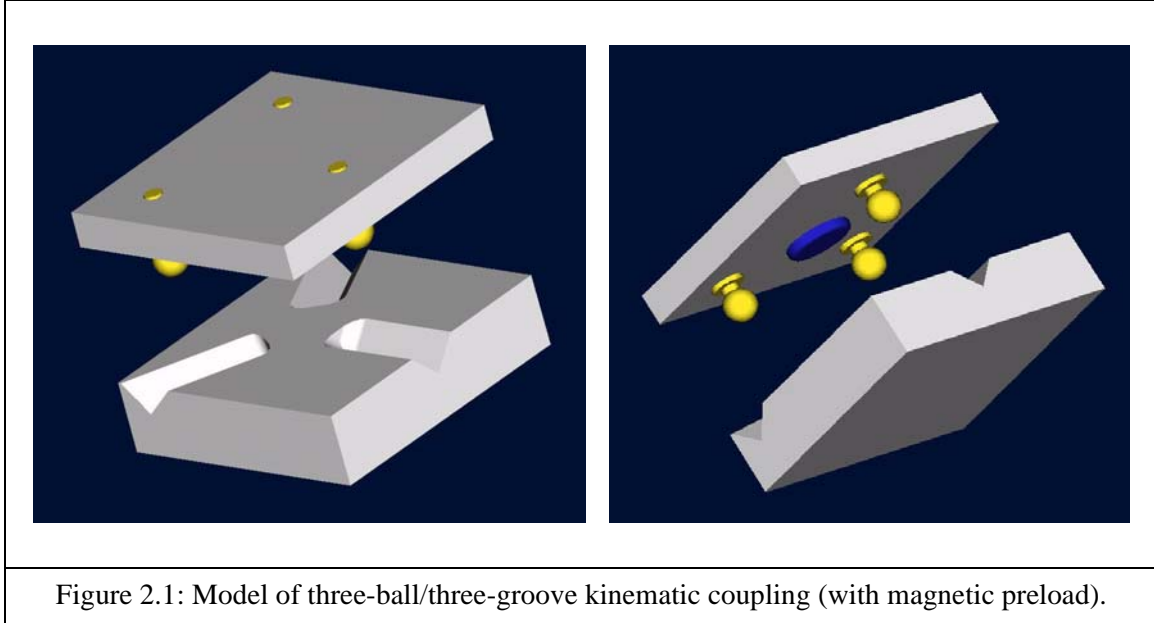
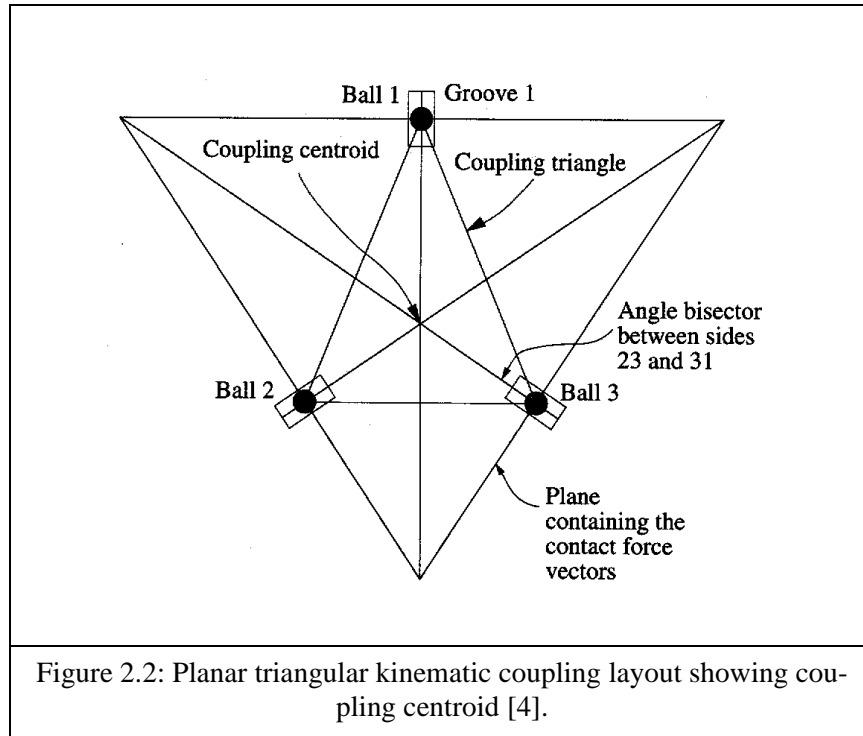


Figure 2.1: Model of three-ball/three-groove kinematic coupling (with magnetic preload).

The stability of a kinematic coupling interface is maximized when the coupling ball and groove centerlines, the normals to the planes containing pairs of contact force vectors, intersect at the centroid of the coupling triangle as shown in Figure 2.2. In other words, the centerlines bisect the angles of the coupling triangle, and intersect at a point called the coupling centroid. For static stability, the planes containing the pairs of contact force vectors must form a triangle [4]. Beyond this, in a specific case of external dynamic loading of the interface, stability is ensured by checking that none of the contact forces reverse from a compressive state, and applying a necessary preload to meet this condition.

Stiffness of a kinematic coupling is also related to the coupling layout. Stiffness is equal in all directions when all the contact force vectors intersect the coupling plane at 45-degree angles. Coupling stiffness can be adjusted by changing the interior angles of the coupling triangle; elongating the triangle in one direction will increase the stiffness about an axis normal to the coupling plane and normal to the direction of elongation, and decrease the stiffness about an axis in the coupling plane and normal to the direction of elongation [4].



Traditionally, kinematic coupling performance is characterized in terms of repeatability versus applied load and the number of interface engagement cycles. Repeatability depends upon several factors including the coupling material and geometry, the preload and the working load, the number of coupling cycles, and the coupling surface finish and its exposure to debris. Hence, repeatability is almost exclusively an experimentally-defined parameter. At high numbers of cycles, fretting corrosion between plain steel surfaces can degrade repeatability; hence, non-corroding materials are best for use in high-cycle applications [4].

Most recently, Hale has presented computational models for predicting repeatability of a coupling interface, parametrized by groove angle and coefficient of friction between the balls and grooves [5]. Maxwell's criterion is applied to determine the sensitive sliding direction for a coupling layout, and the frictional non-repeatability is predicted for when an interface is assembled imperfectly and is stopped short of its nominal seating position by interfacial resistance between the balls and grooves. Maxwell's criterion specifies that each half-groove constraint should be aligned to the direction of motion allowed by the other five constraints, such that in vector notation perfect alignment gives a unit vector inner product of one between the prescribed and constrained sliding directions [6].

For a case study of a simple symmetric ball/groove interface, Hale finds the optimal groove angle to be 58° , with repeatability error at this angle approximately half of that at 30° and 80° [5]. Nonrepeatability (ρ) due to friction decreases linearly with decreasing coefficient of friction between the balls and grooves, following the general relation between the friction coefficient (μ) ball radius (R), the applied load (P), and the elastic modulus (E):

$$\rho = \mu \left(\frac{2}{3R} \right)^{\frac{1}{3}} \left(\frac{P}{E} \right)^{\frac{2}{3}}. \quad (2.1)$$

For example, repeatability could be improved by coating polished steel couplings with a low-friction material such as titanium nitride (TiN, $\mu = 0.05$), or using a two-layer coating of TiN over tungsten disulfide (WS_2) to increase durability of the coated surface.

For industrial applications, simple ball/groove kinematic couplings can achieve excellent repeatability. For example, repeatability below 2 microns is likely attainable with a hardened steel tooling ball and a non-milled mild steel vee groove. This is more than adequate for most robotic applications. In applications of modular interfaces where parts are interchanged between mounting locations, interface interchangeability is also a critical parameter. Here, the repeatability becomes a random non-deterministic error about the deterministic kinematic error caused by manufacturing variation. Neglecting the mechanical deflections between the balls and grooves, a kinematic transformation model of deterministic coupling interchangeability can easily be built knowing the relative positions of the balls and grooves of the mating interface.

2.1.1 Design Considering Hertzian Contact Stresses

For a deterministically-constrained coupling joint, contact forces, contact stresses, and coupling deflections can be calculated directly from the coupling geometry using known mechanical relations based on Hertzian theory of contact between solid bodies. When considering contact between two curved bodies, a straightforward shortcut is to convert the problem into an equivalent case of contact between a sphere and a flat [7]. From the equivalent major and minor radii of the individual bodies, the equivalent radius of the single sphere is:

$$R_e = \frac{1}{\frac{1}{R_{1,major}} + \frac{1}{R_{1,minor}} + \frac{1}{R_{2,major}} + \frac{1}{R_{2,minor}}} \quad (2.2)$$

Similarly, an equivalent Young's modulus of elasticity between the bodies is defined from the individual moduli (E_1, E_2) and Poisson's ratios (ν_1, ν_2):

$$E_e = \frac{1}{\frac{(1-\nu_1^2)}{E_1} + \frac{(1-\nu_2^2)}{E_2}} \quad (2.3)$$

Then, between a sphere and a flat with R_e and E_e , the radius of an equivalent circular contact area upon application of normal force F is:

$$a = \left(\frac{3FR_e}{2E_e} \right)^{\frac{1}{3}} \quad (2.4)$$

The resultant Hertz contact stress, maximum at the center of the interface, is:

$$q = \frac{1}{\pi} \left(\frac{1}{R_e} \right)^{\frac{2}{3}} \left(\frac{3E_e^2 F}{2} \right)^{\frac{1}{3}} = \frac{aE_e}{\pi R_e} \quad (2.5)$$

Hence, between a sphere and a flat, contact pressure increases with the cube root of applied load. In the separate case of contact of cylinders, the width of the contact region (between a semi-infinite cylinder and a plane, ignoring end effects present with a finite cylinder) and contact pressure increase with the square root of applied load. Here, the half-width of the contact area is:

$$b = \left(\frac{2Fd}{\pi LE_e} \right)^{\frac{1}{2}}, \quad (2.6)$$

where F is the total applied force, L is the length of contact, and d is the cylinder diameter. Then, the maximum contact pressure is:

$$q = \left(\frac{2FE_e}{\pi dL} \right)^{\frac{1}{2}} = \frac{2F}{\pi bL} \quad (2.7)$$

The Hertzian relations assume that significant dimensions of the contact area are small compared with the dimensions of each body and with the relative radii of curvature of the surfaces, and that the surfaces are frictionless so that only a normal pressure is transmitted between them. For kinematic couplings, a rule of thumb in the first case is that the vee-groove flat should allow one diameter of the contact area in non-

contacting space all the way around the deformed region. If the assumptions of Hertzian contact are violated, the contact solution becomes much more complex, involving multidimensional integrals with non-uniform boundary conditions. Coverage of these cases is out of scope of this study; Johnson provides an excellent and comprehensive treatment [7].

Based on the principles of contact mechanics, the static mechanics solution for a traditional kinematic coupling interface is a four step process. Assuming negligible friction at the contacts, calculation of the contact forces is decoupled from calculation of the contact deflections and the gross error motion of the interface. The solution procedure is as follows:

1. Input the interface geometry and the disturbance pattern -- the locations of the contact points in the plane, the groove surface angles, and the magnitudes and locations of the external forces and the preloads -- and solve the six-by-six static equilibrium system to determine the contact forces:

$$AF = B, \quad (2.8)$$

where A is a six-by-six matrix composed of the direction cosines of the groove flats, F is a column vector of the six contact forces, and B is a column vector of the applied disturbance forces and moments.

2. Input the ball and groove major and minor radii, and the ball and groove materials, and then calculate the stresses, deflections, and contact zone sizes of the balls and grooves.
3. Knowing the sizes of the contact zones, verify the applicability of Hertz theory to the contact stress solutions.
4. Assuming small movements, calculate the resulting error motion (HTM) of the interface due to the static deflections at the contact points.

These solutions for ball/groove coupling design were first presented in the convenient format of a spreadsheet in 1986 by Slocum, and in 1992 were revised to include calculations of the static error motions of the interface due to mechanical deflections at the contact points [8,9]. For work of this thesis, the spreadsheet was converted to a MATLAB script. Contrasting the visual format of the spreadsheet, the MATLAB code allows one to specify ranges of parameters and execute iterative design studies (through nested loops) through consecutive runs of the model. The script *kcgen.m* is in Appendix B, and has takes the command line argument *kcgen*. This program can be executed for equal- and non-equal-angle interfaces. All design input parameters are specified within the top section of the code.

2.1.2 Design For Interfaces Under High Dynamic Disturbances

Compared to a design for seating with little or no dynamic disturbance, design of kinematic interfaces for high disturbance loads, with high-cycle applications, requires consideration of interface strength and stability in three areas:

1. **Static performance:** resistance of the coupling to compressive yield in the Hertzian contact zones.
2. **Dynamic performance:** stiffness of the coupling interface and deflections at the point of error measurement upon application of large dynamic forces and torques
3. **Long-term durability:** integrity of the contact surfaces over several million load cycles.

When disturbance forces are applied, the interface design must remain stable at all points within the disturbance space. Considering the disturbance to be a set of three orthogonal forces and three orthogonal moments applied at a central point, stability throughout the disturbance space is guaranteed if stability exists at all limits of the disturbance space. Hence, when the six-tuple is defined in a dynamic application as a set of six upper-bound and lower-bound cycle limits, the linear nature of the force-equilibrium system guarantees that the extreme point will be at one of the sixty-four combinations of the individual force and moment limits.

Considering these principles, in the case of a nominally deterministic interface such as one of traditional or canoe ball couplings, an iterative design procedure is defined:

1. Given the disturbance forces (disturbance space) and interface geometry (coupling positions and groove angles), determine the preload necessary to maintain stability of the interface.
2. Given a nominal material choice, determine the contact surface radius (or radii if desired to be different) necessary to support the superposition of this preload onto the disturbance force space, without causing simple compressive failure in the contact zone.
3. Verify the high-cycle performance of the interface based upon surface and mechanical integrity fatigue-life relations, choosing a different material if necessary. Recalculate the necessary surface radius if desired and re-check for durability.
4. Choose an appropriate fastener to support the tensile preload and tensile disturbance loads, considering static and high-cycle dynamic performance. If the preload is applied through the center of the coupling, appropriately package the fastener through a clearance hole, increasing the size of the contact elements if necessary.

With more design freedom, it is straightforward to extend this process into an iterative optimization; e.g. determining the coupling positions and angles that maximize interface stability and/or minimize the contact stress ratios given the magnitude and breadth of the disturbance load space.

2.2 Canoe Ball Couplings

The main caveat to traditional ball/groove couplings, where the sphere diameters are approximately the widths of the vee grooves to which they mount, is that their near-kinematic nature means that their load capacity is limited to that of the six small near-point contacts. To build greater load capacity yet maintain performance, in 1986 Slocum developed the “canoe ball” shape, which emulates the contact region of a ball as large as 1 m in diameter in an element as small as 25 mm across. A canoe ball mount, shown in Figure 2.3, mates to a standard vee groove, with significantly larger safe contact area than a ball of equivalent diameter that would contact the groove at the same points. The canoe ball shape is achieved by means of precision CNC machining, where the block protrusion with cylindrical shank is first made, then the shank is held in a collet and the spherical surfaces are cylindrically ground by programming the grinding head to move about the virtual central axes of the surfaces. Mullenheld’s initial work showed radial repeatability of 0.1 microns for an equilateral triangle configuration of 250 mm radius stainless steel canoe balls mounted to a 0.2 m diameter solid aluminum test fixture [10].



Figure 2.3: Canoe ball mount with 250 mm contact surface radii.

It follows from Hertz theory that if canoe balls with large equivalent radii replace smaller spherical balls, the normal stiffness of the interface will gain by the cube root of the ratio of the contact surface dimensions:

$$G = \left(\frac{R_c}{R_l} \right)^{\frac{1}{3}} \quad (2.9)$$

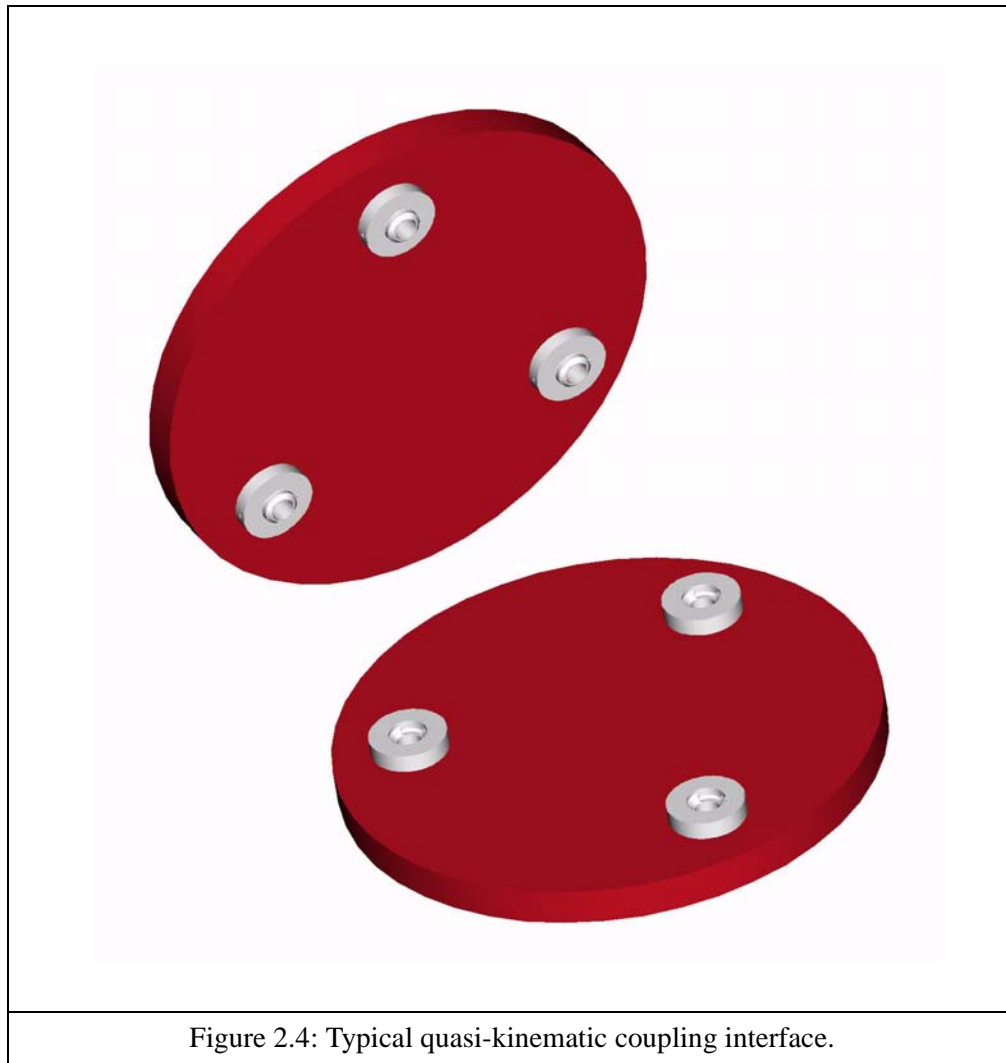
Canoe ball couplings are designed by the same process as traditional ball/groove couplings, only that the input ball radius becomes the large radius of the canoe surfaces, and the contact point locations are defined by specifying the diameter of a sphere that would contact the grooves at the same points as the canoe ball unit.

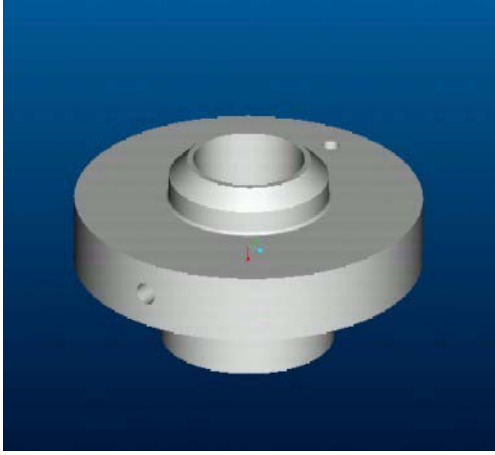
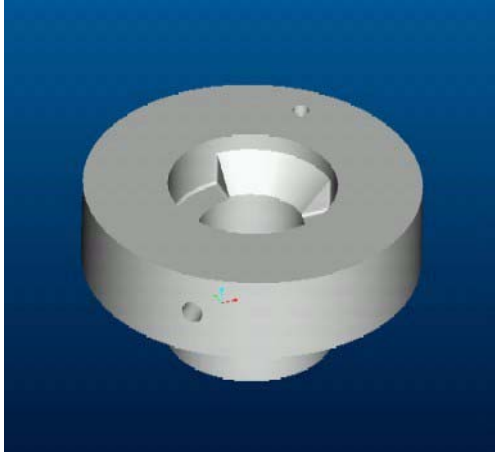
2.3 Quasi-Kinematic Couplings

Compared to the near-exact constraint provided by ball/groove couplings, quasi-kinematic couplings, developed by Culpepper in 2000, create slightly overconstrained attachment using simple, rotationally-symmetric mating units. These cause slight plastic deformation of conical groove surfaces with side reliefs. While quasi-kinematic couplings sacrifice accuracy from ball/groove interfaces, the simple geometry reduces cost and enables direct machining of the coupling halves into mating components. Exploiting this cost vs. accuracy trade-off makes quasi-kinematic coupling well-suited to high-volume precision manufacturing applications.

Figure 2.4 shows a typical quasi-kinematic coupling, with the male halves called *contactors*, and the female halves called *targets*. Based on the contact angle θ_{CT} , each contactor engages in line contact of length $2\pi D_C \theta_{CT}$ with the corresponding target, where D_C is the diameter of the contact circle. Quasi-kinematic interfaces are typically designed such that a static gap exists between the normal contact surfaces of the interface halves when the contactors and targets first touch, and then a preload is applied to seat the interface and close the gap. The preload serves to seek the nominal interface seating position by overcoming contact friction and by brinelling away surface inconsistencies at the contact areas. The deformation of the contactors and targets when the preload is applied may be fully elastic, or it may be partially elastic and partially plastic. In the latter case, only part of the static gap is recovered when the interface is unloaded, and the contactors and/or the targets are permanently deformed (based on choice of same or different

strength materials) and create a sort of “surface memory” for re-seating the interface. Hence, when the gap is closed the large mating horizontal surfaces, not the quasi-kinematic line contacts, dictate the normal stiffness. This high normal stiffness is desirable for high-load bearing machine applications. This design precludes kinematic interchangeability, but for many applications -- such as Culpepper’s case study of repeatably mounting the same engine block to its bedplate during subsequent manufacturing operations -- this design is acceptable.



	
<p>Figure 2.5: Quasi-kinematic contactor.</p>	<p>Figure 2.6: Quasi-kinematic target with $\theta_{CT}=90$ deg.</p>

Because of the arc-shaped line contact of quasi-kinematic couplings, the exact force-equilibrium solution is non-deterministic. To give a good approximation of the exact solution, first displacements are imposed to determine the normal contact stiffnesses, then the forces are calculated. In the case of elastic-plastic contact, nonlinear behavior due to plastic flow dictates the use of finite element analysis (FEA) to estimate a power-law force-deflection relationship for usage in the analytical stiffness relations. For FEA simulation of contact problems, Culpepper showed that the mesh size of contacting elements should be no larger than 5% the width of the contact region.

Presentation of the exact force-deflection relationship for the spherical target and conical contactor are beyond the scope of this thesis; however, based on an initial design geometry, straightforward calculations show the boundary between elastic and plastic deformation of the contacts. The force per unit length (f_{nYIELD}) at which plastic flow begins is:

$$f_{nYIELD} = \frac{2.8\pi R_e \sigma_y}{E_e}, \quad (2.10)$$

where R_e and E_e are the equivalent radius and modulus of the contact, calculated in the traditional Hertzian fashion. Now the contact displacement that induces plastic flow is known from:

$$\delta_n = \left(\frac{f_n}{\pi}\right) \left\{ \frac{(1-v_1^2)}{E_1} \left(2 \ln \left(2R_1 \left(\left(\frac{\pi E_e}{R_e f_n} \right)^{\frac{1}{2}} \right) - 1 \right) \right) + \frac{(1-v_2^2)}{E_2} \left(2 \ln \left(2R_2 \left(\left(\frac{\pi E_e}{R_e f_n} \right)^{\frac{1}{2}} \right) - 1 \right) \right) \right\}. \quad (2.11)$$

By simple trigonometry, the corresponding displacement in the z-direction is:

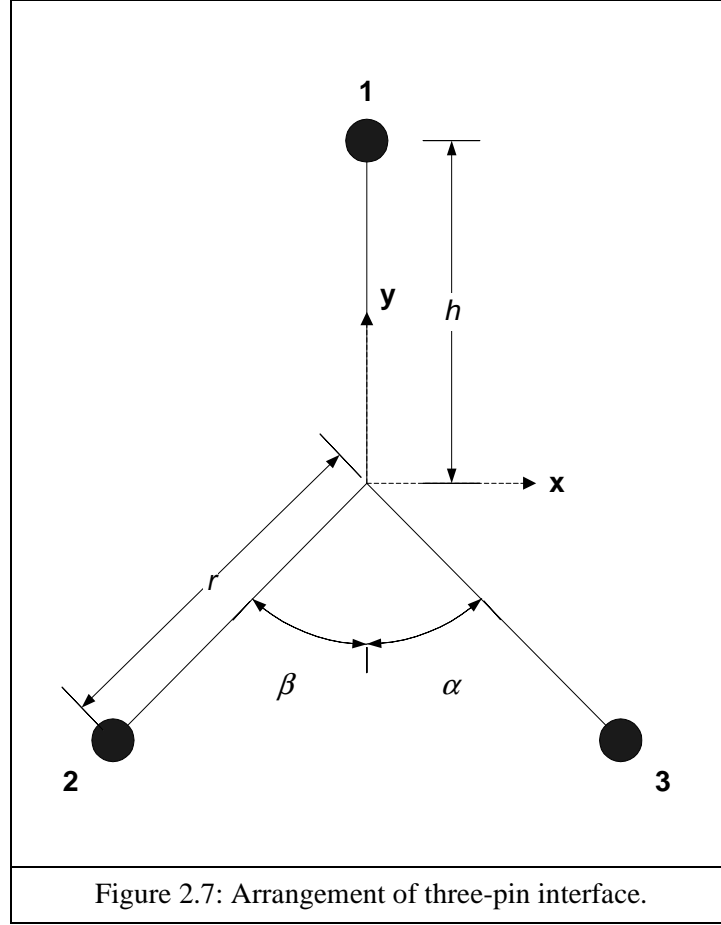
$$\delta_z = \frac{\delta_n}{\sin(\theta_c)}. \quad (2.12)$$

These relations can be used after determining the initial input geometry to qualitatively estimate the magnitude of elastic and plastic contact, and given suitable dimensional tolerances for the gap size, to estimate how manufacturing variation affects the type of deformation at the contacts. With a full force-deflection model, one can calculate the necessary preload to close the gap, and the appropriate gap size and preload necessary to maintain stability under the dynamic loads can be calculated. The contactor radii and target contact angle can be chosen to give the appropriate gap dimension, in-plane stiffness (magnitude and direction coupled), and normal stiffness for closure.

Culpepper [11] gives a thorough explanation of modeling, analysis, design, and manufacture of quasi-kinematic couplings.

2.4 Three-Pin In-Plane Coupling

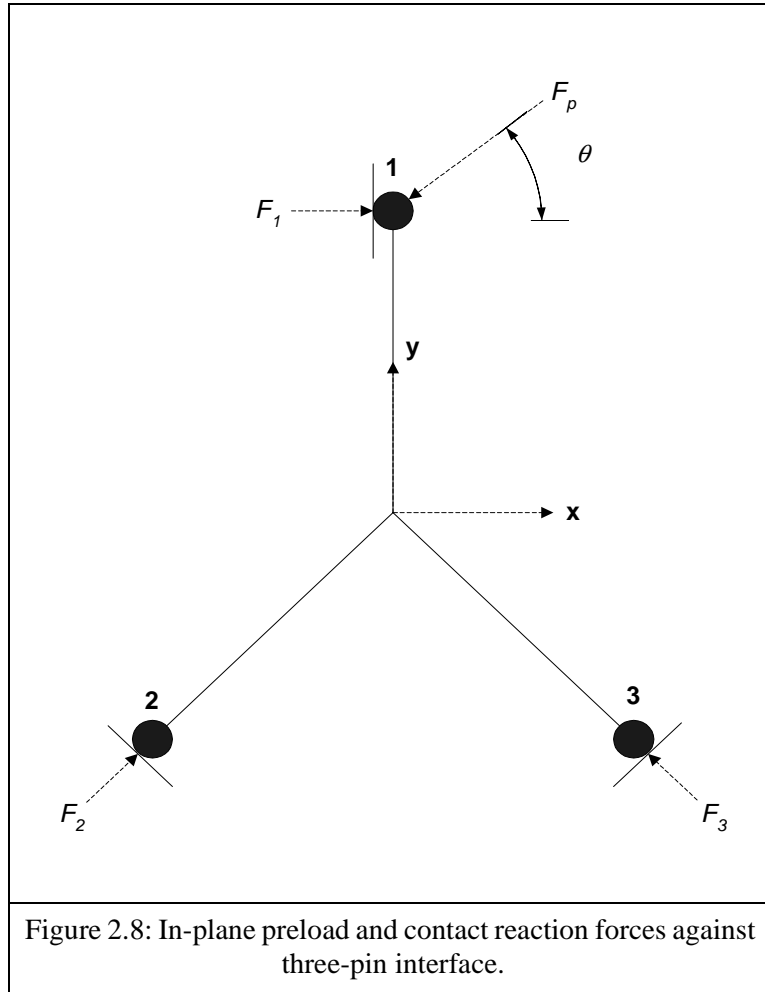
The three-pin coupling is a second type of quasi-kinematic coupling. The three-pin coupling establishes near-exact constraint in the horizontal plane using three pins resting on curved control surfaces perpendicular to the horizontal plane of constraint, and maintains remaining control from normal preload forces against large horizontal contact forces in the plane. The three-pin interface is shown schematically in Figure 2.7, where the first pin lies along the local y-axis at offset h from the frame origin, and the second and third pins are offset by distance r from the origin and angles α and β from the y-axis.

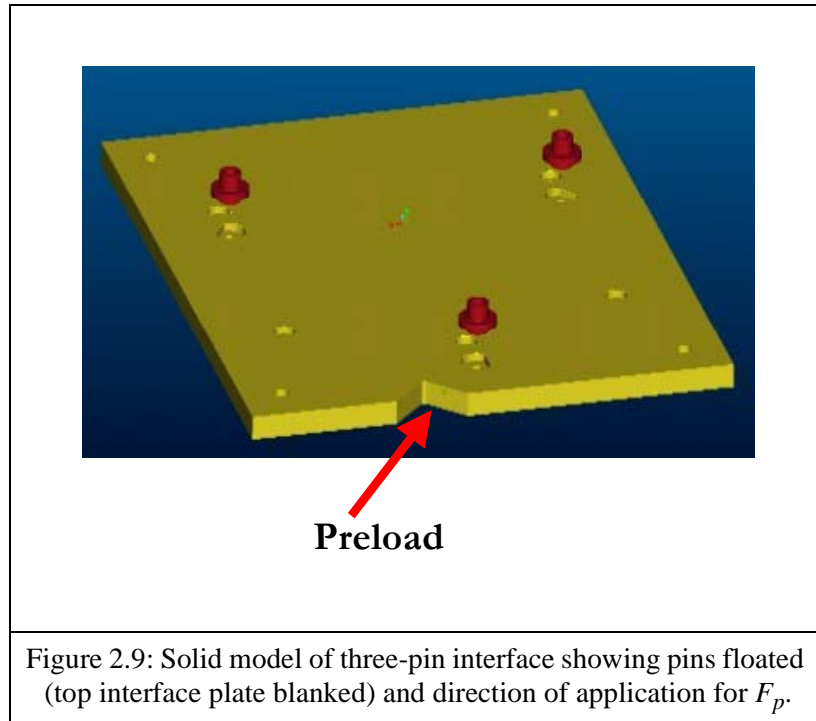


The three-pin interface is realized by fashioning an upper interface plate with a triangular arrangement of shouldered or dowel pins, and manufacturing a bottom interface with a triangular arrangement of oversized cutouts with flat or curved contact surfaces with which the pins make contact. When the top interface plate is engaged with the bottom interface plate, the pins are seated against the contact surfaces by introducing an in-plane preload force (F_p) at the first pin, offset by the angle θ from the local x-axis. A disturbance load $D_o = [D_{x,o}, D_{y,o}, D_{z,o}, DM_{x,o}, DM_{y,o}, DM_{z,o}]$ is resolved into an effective six-tuple $D = [D_x, D_y, D_z, DM_x, DM_y, DM_z]$ applied at the local origin, and normal preload forces F_{z1} , F_{z2} , and F_{z3} are applied using bolts through the centers of pins 1, 2, and 3, respectively. Assuming normal reaction forces at each of the engagement locations between the pins and bottom plate, the in-plane reaction forces and the required normal preloads to maintain dynamic stability are the solution of the static system:

$$\begin{bmatrix} F_1 \\ F_2 \\ F_3 \\ F_{z1} \\ F_{z2} \\ F_{z3} \end{bmatrix} = \begin{bmatrix} 1 & \sin(\alpha) & -\sin(\beta) & 0 & 0 & 0 \\ 0 & \cos(\alpha) & \cos(\beta) & 0 & 0 & 0 \\ 0 & 0 & 0 & 1 & 1 & 1 \\ 0 & 0 & 0 & -r\cos(\alpha) & -r\cos(\beta) & h \\ 0 & 0 & 0 & -r\sin(\alpha) & -r\sin(\beta) & 0 \\ h & 0 & 0 & 0 & 0 & 0 \end{bmatrix}^{-1} \begin{bmatrix} D_x - F_p \cos(\theta) \\ D_y - F_p \cos(\theta) \\ D_z \\ DM_x \\ DM_y \\ DM_z + F_p h \cos(\theta) \end{bmatrix} \quad (2.13)$$

When the pins are engaged to the bottom interface plate and F_p is applied to seat the pins against the contact surfaces, the static reaction forces are those obtained from (2.13) with $D = 0$, hence requiring no vertical preload to maintain stability.





The process of seating the pins against the contact surfaces by applying the in-plane preload involves relative sliding of the horizontal contact surfaces (e.g. pin shoulders) between the top interface assembly and the bottom plate. Before all three pins are in their rest positions, relative sliding of the horizontal contact surfaces, plus relative sliding of one or two pins that may already be in contact, generates frictional resistance against the preload. Hence, the maximum preload needed to seat all three pins properly is the maximum frictional resistance generated among the multiple cases of:

1. No pins in contact.
2. Pin 1 only in contact.
3. Pin 2 only in contact.
4. Pin 3 only in contact.
5. Pins 1 and 2 in contact.
6. Pins 1 and 3 in contact.
7. Pins 2 and 3 in contact.

Cases 3 and 4 result in motion combining rotation of the top interface assembly about the axis of pin in

contact, and translation of the assembly along the line dictated by the contact surface. Here, sub-cases of pure rotation about the pin and pure translation along the contact surface line give the worst-case resistance. Cases 5, 6, and 7, can be considered as rotations of the top assembly about the instant centers determined by the pair of sliding directions of the pins in contact. Denoting the static vertical load on the interface (e.g. weight of the machine module) as F_z , and the static coefficient friction between the horizontal surfaces as μ , the minimum preload needed to overcome case 1 is simply:

$$F_{p1} = \mu F_z. \quad (2.14)$$

For case 2, the minimum preload when the interface slides about pin 1 is given by:

$$F_{p2} = \frac{\mu F_z}{\sin((\theta) - \mu \cos(\theta))}, \quad (2.15)$$

where θ is the in-plane application of F_p , measured relative to the line through the preloaded pin and the coupling centroid. This methodology can be straightforwardly extended, balancing the frictional resistances against the preload and contact forces, in the remaining cases and subcases (3a, 3b, 4a, and 4b for pure rotation and pure translation respectively for each case). Then, the required in-plane preload is formally:

$$F_p = \max[F_{p1}, F_{p2}, F_{p3a}, F_{p3b}, F_{p4a}, F_{p4b}, F_{p5}, F_{p6}, F_{p7}] \quad (2.16)$$

When a bolt is used to apply the load, only a small torque (e.g. 20 N-m) is needed to seat an interface with that bears a relatively large normal load (e.g. 25 kN). To ensure repeatable seating under variation in the preload and surface conditions, a safety factor of 1.5 or 2 is suggested beyond the minimum required preload.

The force balance of (2.13) assumes an ideal case of three-point contact, one in which the contact forces between the pins and the bottom interface load must provide all the necessary in-plane resistance to counteract the disturbance forces. However, since the contacts are lines rather than points, and frictional resistance exists between the horizontal and vertical mates, the necessary resistance after the preload is applied is taken primarily by friction between the contact surfaces. Hence, the vertical preloads calculated from (2.13) are necessary to ensure stability, yet an in-plane preload force not much larger than that required to deterministically seat the pins is needed. To satisfy this assumption, a second model must be

built to show that the frictional resistance between the horizontal contacts, subject to the vertical preloads, is sufficient to prevent slippage when only the required preload for interface seating is applied in the plane. Then the pins can be sized appropriately by limiting the Hertzian line contact stresses experienced from contact with the bottom plate, using the cylinder-line contact relations presented in Section 2.1.1.

The calculations of (2.3) and of all cases of frictional resistance against interface seating are handled by the MATLAB scripts *threepins.m* and *threepins_friction.m*, given in Appendix B. Interface geometry and disturbance force parameters are specified directly in the files.

In summary, the major design process steps for the three-pin interface are:

1. Define the nominal interface geometry, placing the pins and contact surfaces relative to a central reference.
2. Determine the in-plane preload needed to seat the interface in the horizontal plane, based on the static normal load.
3. Determine the vertical preload needed at each pin to maintain dynamic stability of the interface.
4. Apply a factor of safety over the in-plane contact forces dictated by (2), and size the pins appropriately to avoid yield along the line contacts.

2.5 Fatigue Life Considerations

When kinematic couplings are designed for high-cycle applications involving oscillating contact stresses, attention to the long-term durability of the contacting materials is necessary. Quantitatively, the contact stresses can be related to the applied loads through Buckingham's load stress factor (K) to predict the onset of mechanical breakdown of the surfaces. This factor is similar to the factor K_g used in endurance evaluation of gear teeth through extensive periods of cycling Hertzian contact. S_{fe} , the surface endurance strength, gives the maximum sustainable contact stress to keep onset of fatigue from happening before a specified number of cycles. For contact between a cylinder and a flat, the relation is:

$$K = \frac{2Fd}{L} = \frac{\pi S_{fe}^2}{E_e}. \quad (2.17)$$

For contact between a generalized sphere and a flat, the relation is:

$$K = \left(\frac{3F}{2}\right)^{\frac{1}{2}} \left(\frac{1}{R_e}\right) = \frac{(\pi S_{fe})^{\frac{3}{2}}}{E_e}. \quad (2.18)$$

Relations between S_{fe} and the number of load cycles are well-known for many materials; for example, at 10^7 cycles, the allowable contact stress, in kpsi, for steel alloys is related to the Brinell hardness (H_B) by:

$$\sigma = 0.364H_B + 27 \text{ kpsi} \quad (2.19)$$

For between 10^7 and 10^{10} cycles, the allowable contact stress is related to H_B and the number of cycles (N) by:

$$\sigma = 2.46N^{-0.056}(0.364H_B + 27) \text{ kpsi} \quad (2.20)$$

Table 2.1 gives representative fatigue strengths and ratios to nominal yield strength (σ_y) for two selected steel alloys at varying numbers of cycles. For example, AISI 1018 steel can withstand full contact loading to its yield strength for 10^7 and 10^9 cycles, yet the endurance limit drops far below the yield limit 10^{10} cycles. For AISI 420 stainless, the reduction occurs just before 10^9 cycles.

Material	H_B (Rockwell)	N	σ [kpsi]	σ/σ_y
AISI 1018 (as rolled)	126 (B71)	10^7	72.7	1.34
AISI 1018 (as rolled)	126 (B71)	10^9	56.2	1.04
AISI 1018 (as rolled)	126 (B71)	10^{10}	49.4	0.91
AISI 420 Stainless	594 (C67)	10^7	242.6	1.23
AISI 420 Stainless	594 (C67)	10^9	187.5	0.95
AISI 420 Stainless	594 (C67)	10^{10}	164.7	0.83

Table 2.1: Fatigue strengths of selected steel alloys [12].

2.6 Interface Packaging and Tightening Torque Specification

Finally, along with designing the couplings to meet the life-cycle stress demands of an application, consideration must be made to packaging of the couplings on a machine interface, and if necessary to appropriate selection of bolts to apply the preload. In general, couplings should be placed near the outer-

most constraints of the interface, and the holding plate should be designed to limit undesirable mechanical deflections or modal behavior under application of the dynamic loads. Bolts can be placed directly through the coupling centers or directly outboard of the contacts. In either case, applying a higher bolt preload than needed for stability will only enhance stiffness and stability, so the maximum preload within the stress limit of the desired fastener and the Hertz stress allowance for the contacts can be used. Here, one can initially solve the six-by-six equilibrium force system to determine the necessary preloads to maintain stability, then iterate to higher preloads until the Hertz stress limit, considering an appropriate factory of safety, is met.

In terms of the applied torque (Γ), the bolt lead (l , $1/l$ threads per unit length), the efficiency (e), the bolt diameter (D_B), and the coefficient of friction (μ) under the bolt head, the axial force in the bolt is [13]:

$$F = \frac{4\pi\Gamma}{\frac{2l}{e} + 3\pi D_B \mu} . \quad (2.21)$$

When the required axial force is selected in coupling design, this relation gives the required tightening torque.

Shigley [13] and Slocum [4] provide thorough references on bolted joint design.

Chapter 3

Interchangeability of Deterministic Kinematic Interfaces

While traditional studies of kinematic couplings have focused on demonstrations of high repeatability for removal and replacement of interfaces in the same location, application to machine and instrumentation modularity requires low error interchangeability for quick mounting in different locations. While the geometric averaging behavior of the kinematic triangle itself reduces error of the interface to a fraction of the error of the coupling placements, interchangeability can be achieved by exploiting the deterministic nature of the kinematic coupling to predict a homogeneous error transformation based on the measured positions and orientations of the balls and grooves of each interface. This chapter describes a general error model of the kinematic coupling interface, and presents and validates a mathematical structure for calculating the error transformation for the canoe ball and three-pin interfaces.

3.1 Repeatability vs. Interchangeability

Two most important parameters describing the accuracy of a modular kinematic interface are its mechanical repeatability and mechanical interchangeability. For a machine application, these are defined as:

Repeatability - The tendency of the centroidal frame of the top half of the interface to return to the same position and orientation relative to the centroidal frame of the fixed bottom half when repeatedly detached and re-attached.

Past work in designing and testing traditional, canoe ball, and quasi-kinematic couplings has shown repeatability at micron and sub-micron levels, easily sufficient for normal manufacturing applications [1].

Interchangeability - The tendency of the centroidal frame of the top half of the interface to return to the same position and orientation relative to the centroidal frames of different fixed bottom halves when switched between them. This is generalized in terms of the ability to establish consistent positional and angular alignment between the centroidal frames of sets of coupling grooves and sets of coupling balls when pairs of sets are randomly matched from a large population.

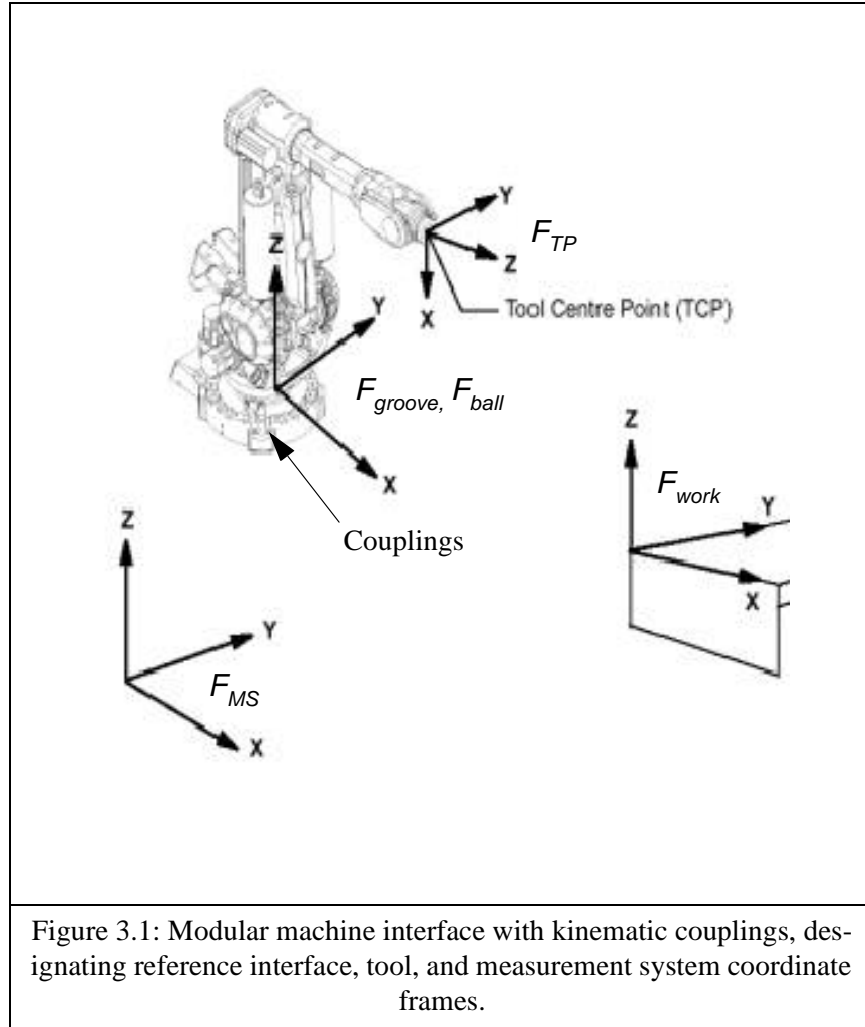
While at the small scale, repeatability of kinematic couplings has been proven to be more than sufficient for most industrial applications, interchangeability has not yet been studied in detail. The fundamental contribution of this analysis is a statistical model of mechanical interchangeability of the canoe ball and three-pin coupling interfaces. Parametric relationships result in terms of the manufacturing tolerances on the couplings and interface plates, the error of the coupling mounting and measurement processes, and the detail of pre-calibration of the contact point locations. Simplification of this model to traditional ball-groove couplings, or extension to inexact constraint quasi-kinematic couplings for which a minimum-energy configuration must be found, is straightforward future work.

3.2 Global Error Model of a Kinematic Coupling Interface

Recalling that the six-points of contact from a kinematic coupling exactly constrain a solid body, kinematic couplings can be exploited as minimum geometric error interfaces for two main reasons. First, the forced point-line contact of the ball triangle on the groove lines reduces the positional error of the coupling centroid to one-third the error of the coupling positions. Second, the deterministic point-line contact enables calculation of an error transformation between the nominal interface mating position and the true mating position, when the position and orientation offsets of the balls and grooves are known. Furthermore, at a very fine scale, the mechanical error motion of the interface from Hertzian contact between the balls and grooves can be determined [2]. However, at even extreme interface preloads and disturbances this error motion is very small compared to the magnitude of the kinematic transformation due to error in the coupling placements from typical CNC machining processes. Because of this determinism, the kinematic error of the coupling interface can be expressed in closed form.

To start the error model, consider a general machine design application in which two modules mate through an interface of canoe ball kinematic couplings, shown in Figure 3.1 for the base interface of an industrial robot. The grooves sit on a fixed floor-mounted lower module, and the mating balls are attached to the upper module. Reference coordinate frames are placed centroidally on the groove set (F_{groove}) and the ball set (F_{ball}), and the couplings are secured using a sufficient (bolted or magnetic) preload. For the machining task, the tool center point (TCP) and co-located coordinate frame (F_{TCP}) are offset from the ball

coordinate frame by a translation and rotation described by the homogeneous transformation matrix (HTM) $T_{Ball-TCP}$. Theoretically, the location of these coordinate frames is determined using a measurement system located near the machine. The measurement system also has an attached coordinate frame (F_{MS}) and is transformed to the groove frame through $T_{MS-Groove}$ and to the tool frame through T_{MS-TCP} . Furthermore, a work frame in the cell, F_{work} , is the absolute reference for positioning the tool and is hence known with certainty.



When the tool point is at the nominal position and orientation, F_{Work} and F_{TP} are identical; when the coupling balls and grooves are placed nominally, F_{ball} and F_{groove} are identical. However, when errors in the position and orientation (orientation of the balls in the case of non-spherical mounts, e.g. canoe balls)

of the balls and grooves exist, the frames are subject to translational and rotational error offsets. The translational errors are reflected exactly at the tool point, yet the rotational errors are magnified by the distance to the tool point. For example, when the tool point is 2 m from the coupling centroid, a 0.0001 radian error about one axis results in a sine error of 0.2 mm translation at the tool point. Hence, while this error may be repeatable to the micron level, its existence makes “out of the box” use of kinematic couplings without calibration impractical when reasonable errors of securing the balls and grooves to the modules are present. This presents a problem to the concept of complete modularity, in which interfaces should be “plug and play”, requiring no on-line measurement to eliminate the interface error after installation.

In establishing a deterministic error model, this work presents a method through which error of kinematic interface interchangeability can be minimized by a simple computerized calibration routine. Furthermore, the deterministic behavior can be parametrized in terms of the error contributions, enabling design decisions that minimize cost and maintain the desired error budget by optimally specifying manufacturing tolerances on the couplings and interface plates.

3.2.1 Components of Interface Error

The error at the interface can be broken into several causes and components, and then transformed into an error at the tool point by deriving the serial chain of HTM’s relating the position of the cell measurement system to the position of the tool. The sources of TCP error from the kinematic interface can be divided into random errors and systematic (hysteretic) errors. The components of error within these categories are:

Random Errors:

1. Positional tolerances of the mounting holes in the interface plate holding the balls and in the interface plate holding the grooves.
2. Flatness of the ball holding plate and groove holding plate.
3. Feature and form errors in the ball and groove mounts.
4. Error in the measurement system. For a standard laser tracker, this is a worst-case value of 0.01 mm per meter between the tracker head and the measurement point.
5. Errors in the process of fitting the ball and groove mounts to the pallets, predominately manifested

in translation error normal to the pallet (failure to press the coupling all the way into the hole, or stiction because of galling) and angular error about the insertion axis.

When specifying values for the random errors, it is customary to use 3-sigma levels, representing a 99.7% upper-bound on the actual error, within a zero-mean Gaussian density function.

Systematic/Hysteretic Errors:

1. Deflection at the coupling contact points due to applied static and dynamic disturbances.
2. Thermal expansion/contraction of the pallets and couplings due to environmental variation.

In this study, solely the random errors are parametrized and included in the mathematical model of the interface. For the canoe ball interface, the sum of the errors gives a positional error offset of each of the six centers of the coupling balls, a change in the radius of each of the coupling spheres, and base position and direction offsets of the planes defining the groove flats.

While important, the systematic error of direct coupling deflection is less significant in magnitude when machining applications requiring no less than 10 micron accuracy are considered. Furthermore, due to often complex interface and structure geometries, the thermal error is most easily estimated through a finite element simulation, and the only way to estimate it without simulation is to make a crude approximation based on the temperature distribution on the structure, or a bulk temperature change in the environment (e.g. from summer to winter). Incidentally, thermal error of modular structures can be minimized by using a segmented, symmetric, kinematically coupled structure, which is the case study of the next chapter.

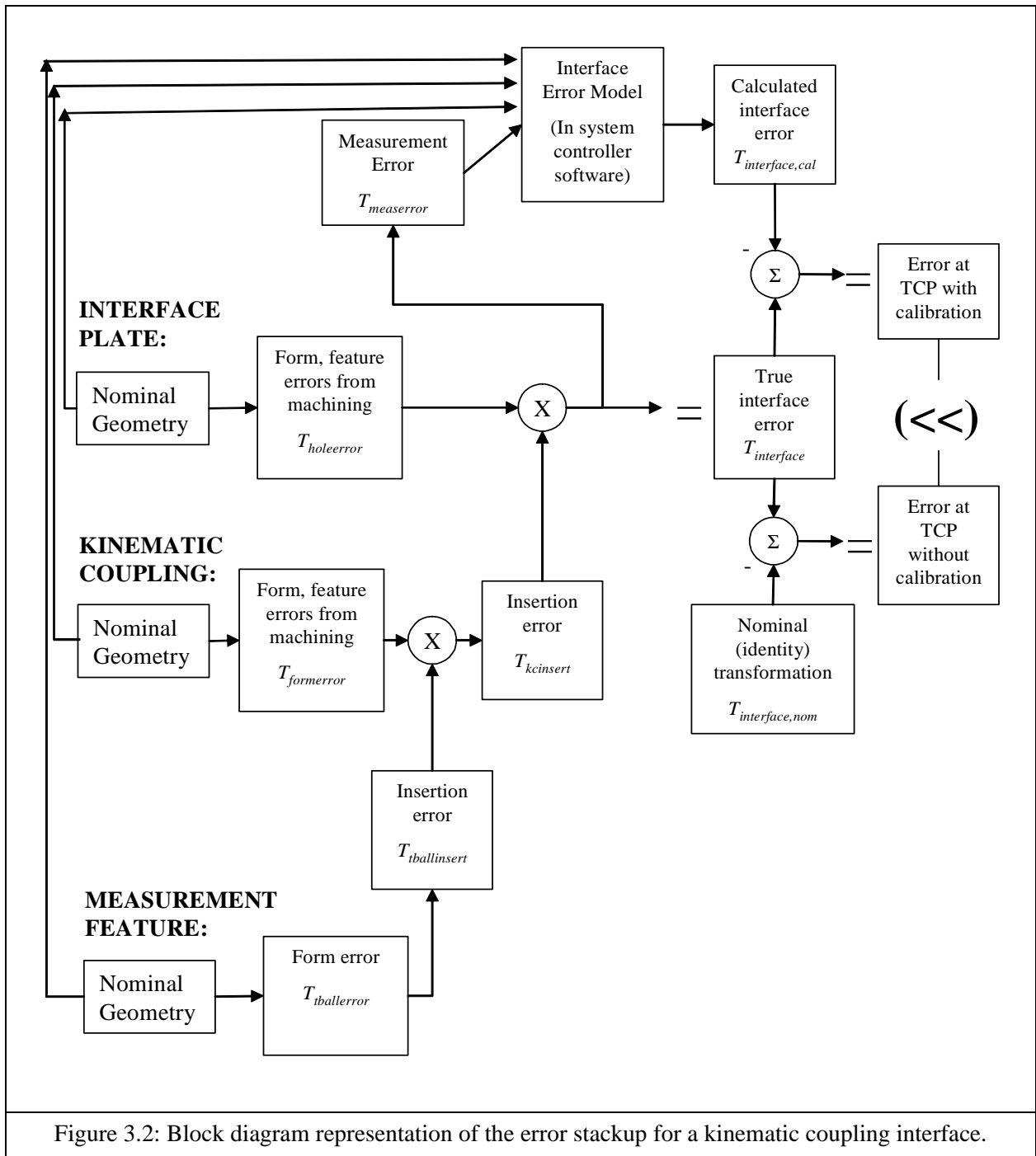
3.2.2 Error Chain Representation

The final discrepancy between the expected and the true position of the tool point is a chain of propagation from:

1. Error in machining of the kinematic coupling units;
2. Error in machining the interface plates that will hold the kinematic couplings;
3. Error in mating the kinematic couplings to their holding interface plates;
4. Error in measuring the placements of the contact points of the kinematic couplings after mounting.

This error chain is captured in Figure 3.2, expressing each component as a HTM from the nominal posi-

tion. The serial multiplication of the HTM's gives the total interface error at the TCP. First, the nominal geometries of the interface plates, the kinematic couplings, and the measurement feature are specified. The interface plates are perturbed by error in placement of the coupling mounting holes ($T_{holeerror}$), the kinematic coupling is perturbed by form error in machining ($T_{formerror}$), and the measurement feature (assumed modular) is perturbed by form error in machining ($T_{ballerror}$). Insertion error ($T_{tballinsert}$) between the measurement features and the kinematic couplings, and between the kinematic couplings and the interface plates ($T_{kcinsert}$) is added next. The serial addition of these transformations represents the true interface transformation ($T_{interface}$), which when extended to the TCP can be compared in magnitude with and without calibration. Assuming full measurement of the contact positions and orientations, the only difference between the true and the calibrated kinematic error of the interface comes from the error in the measurement feature form and offset, the inaccuracy of the measurement system ($T_{measerror}$) itself, and the non-modeled higher-order effects.



3.2.3 The Interface Transformation

If some of the dimensional perturbations in the error chain are known or can be measured, introduction of an interface transformation can reduce the error at the tool point. Normally, when a kinematic coupling interface is mounted, its interface transformation is an identity matrix; hence by the reciprocal path of coordinate transformations:

$$T_{Groove-Work} = T_{Ball-TP} \quad (3.1)$$

However, the existence of any error component in the chain means this equality is untrue, hence:

$$T_{Groove-Work} \neq T_{Ball-TP} \quad (3.2)$$

The mismatch is the error from the work point to the tool point, expressed in terms of the transformations as:

$$T_{Error-full} = (T_{Ball-TP})^{-1} T_{Groove-Work} \quad (3.3)$$

If the interface transformation is known exactly, the forward loop to the tool point including the interface transformation exactly matches the reverse loop. However, because error in the measurement system is a part of the error estimate, a residual error transformation exists:

$$T_{Error-resid} = (T_{interface} T_{Ball-TP})^{-1} T_{Groove-Work} \quad (3.4)$$

However, the residual error is far less in magnitude (expressed as a Cartesian distance by the $\arg()$ notation) than the full error:

$$\arg(T_{Error-resid}) < \arg(T_{Error-full}) \quad (3.5)$$

This chapter contends that the interface error transformation is in large part due to positional and rotational misalignments of the kinematic coupling's mating curved and flat contact surfaces. For a canoe ball interface the mating surfaces are the spherical canoe ball units and the vee grooves, and for a three-pin interface are the shouldered pins in the top interface plate and the mating vertical contact planes in the bottom interface plate. Once the positions and orientations of the contacting pieces are known, deducing the interface transformation from the kinematic constraints of the coupling is a simple deterministic calculation. Absent error of the measurement system, the interchangeability of calibrated kinematic coupling

interfaces can approach their individually paired repeatability, and a convenient, low-cost method of interface calibration can give interchangeability sufficient for most industrial applications.

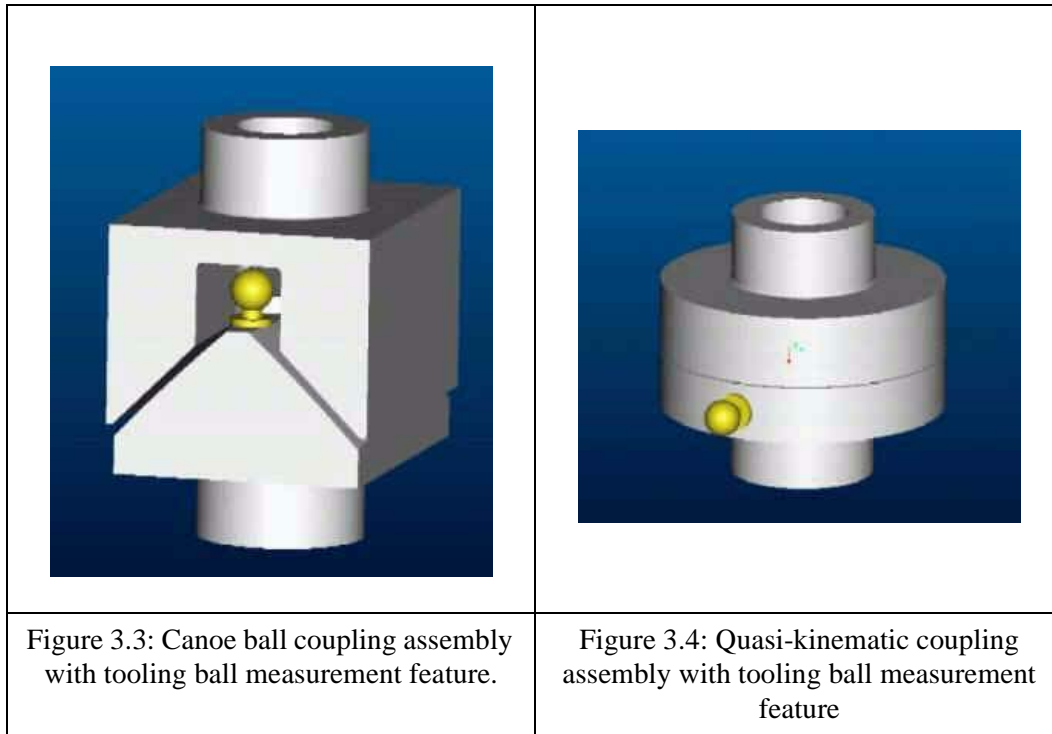
3.3 Kinematic Coupling Measurement and Calibration

This section presents a straightforward method of calibrating kinematic coupling interfaces, specifically sets of canoe balls and mating vee grooves. A similar model for a three-pin interfaces with line contacts mating directly to cuts in an interface plate is presented later in the chapter. Both interfaces are especially suited to modular placement of large- or heavy-load bearing machinery and material handling systems in manufacturing situations. Calibration is based on direct measurement of the ball and groove, and pin and contact, positions and orientations after they have been press-fit to or machined into the interface plates. To facilitate easy measurements in industrial settings, a novel, yet simple measurement feature is added to the canoe balls and grooves. The projected centers and radii of the curved contact surfaces and the plane-defining (point and normal vector) parameters of the flats become direct inputs to a programmed tool to calculate the interface transformation, and the magnitude of the residual error is dependent upon the detail and accuracy of the interface calibration measurements.

3.3.1 Integrated Measurement Feature

Before detailing the calibration procedure for a kinematic coupling interface, it is proposed that interfaces can be calibrated more easily by adapting non-traditional kinematic halves - including canoe coupling balls and grooves and quasi-kinematic couplings contactors and targets - to include a measurement feature to simplify the calibration process and improve interchangeability. This measurement feature may be a hemisphere machined to be homogeneous with the coupling unit, or a pre-fabricated tooling ball press-fit into a hole on the coupling unit. Representative of the idea, a canoe ball coupling assembly and a quasi-kinematic coupling assembly are shown with tooling balls in Figures 3.3 and 3.4. Figure 3.5 shows a canoe ball unit with an integrally machined measurement hemisphere. The feature enables direct measurement of the unit's location, with accuracy dependent primarily on the machining tolerances of the features on the coupling unit and the error of the measurement system. When using a standard laser tracker to locate the interface, it is much easier to measure the small sphere and apply nominal corrections than to measure

the large canoe sphere or groove surfaces. Incidentally, at equal costs, the accuracy of the method with homogeneous features will be superior to that when modular tooling balls are used.



When these special couplings are used in a planar interface for constraining six degrees of freedom of a body, measurement of the feature location on three planar coupling units gives the coordinate frame of the interface plane. The origin of the frame is the centroid of the coupling triangle. For an example application of mounting a machine, the kinematic coupling balls can be used on a floor-mounted interface plate. The coordinate system of the base can then be related to the coordinate system of a fixture in the work cell (perhaps assessed from a kinematic coupling interface on the tooling) through an HTM. Because of the customary high-precision manufacturing of the couplings, the relative locations of contact points on the plate and on the tool are known with high accuracy, and the method is not sensitive to errors prevalent in traditional mounting methods. The calibration accuracy is dependent only on the short error path from the measurement feature to the contact points between the coupling halves, and the parameters of the curved and flat contact surfaces are input to the transformation model by assuming nominal offsets from the measurement feature.

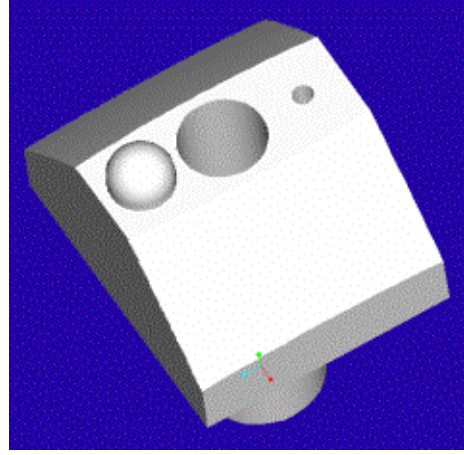


Figure 3.5: Canoe ball mount with integrally machined measurement hemisphere.

3.3.2 Determining the Centroidal Frame

The most basic computational element of the interface calibration procedure is positioning of the coordinate frame (F_{ball} or F_{groove}) at the centroid of the ball triangle or the groove triangle. The frame is determined directly from only the relative positions of the balls or grooves. At this point the method of acquiring the position is abstracted, as it could be an offset method using a measurement feature or a more complex algorithm directly locating the contact points. This description is stated in terms of placing the centroidal frame for three balls mounted to an interface plate fixed to the cell.

Given the locations of the three ball centers, the parameters of the plane containing them and a coordinate system with origin at ball 2 can be found. Defining two vectors in F_{MS} , one from b_1 (ball 1, as numbered in Figure 3.2) to b_2 and one from b_1 to b_3 , the cross-product of these vectors gives a vector parallel to the ball frame (vertical) z-axis:

$$z_{F_{ball}} = (b_2 - b_1) \times (b_3 - b_1) \quad (3.6)$$

Choosing to align the ball frame x-axis along the segment connecting balls 2 and 3, the y-axis vector direction is the cross-product of the x-axis and the z-axis:

$$y_{F_{ball}} = \underline{(b_3 - b_2)} \times z_{F_{ball}}. \quad (3.7)$$

Hence, the coordinates of ball 2 in F_{ball} are $(x, y, z) = (0, 0, 0)$ and of ball 3 are:

$$b_3 = (0, \|b_1 - b_2\|, 0). \quad (3.8)$$

To find the coordinates of ball 1 in F_{ball} , use dot products:

$$x_{1, F_{ball}} = \underline{(b_2 - b_1)} \cdot \underline{(b_3 - b_2)} \quad \text{and} \quad (3.9)$$

$$y_{1, F_{ball}} = \underline{(b_2 - b_1)} \cdot y_{F_{ball}}. \quad (3.10)$$

Next, the origin of F_{ball} is shifted to the location of the coupling centroid. Specifically, the coupling centroid is the point of intersection between two lines starting at the coupling locations and bisecting the respective angles of the coupling triangle. Hence, the coupling centroid is the solution of a system of two linear equations in the x-y plane of F_{ball} , each derived from applying the law of cosines to the triangle geometry. The included angles of the coupling triangle are:

$$\theta_{13} = \arccos\left(\frac{\|(b_2 - b_1)^2\| + \|(b_3 - b_2)^2\| - \|(b_3 - b_1)^2\|}{2\|(b_3 - b_2)\|\|(b_2 - b_1)\|}\right) \quad \text{and} \quad (3.11)$$

$$\theta_{12} = \arccos\left(\frac{\|(b_3 - b_1)^2\| + \|(b_3 - b_2)^2\| - \|(b_2 - b_1)^2\|}{2\|(b_3 - b_2)\|\|(b_2 - b_1)\|}\right). \quad (3.12)$$

And the pair of linear equations (suitably between any two balls), expressed relative to F_{ball} , is:

$$y_{C-ball} = \tan\left(\frac{\theta_{13}}{2}\right)x_{C-ball}. \quad (3.13)$$

$$y_{C-ball} = \tan\left(\frac{\theta_{12}}{2}\right)(x_{C-ball} - \|(b_3 - b_2)\|). \quad (3.14)$$

From this solution, the location of the coupling centroid in F_{ball} as initially placed at b_2 is denoted as $(x_{C-ball}, y_{C-ball}, 0)$. Note that even under perturbations in the vertex locations, which make the triangle no longer equilateral or isosceles, the angle bisectors of a triangle always intersect at a point; hence the intersection of the bisectors originating at balls 2 and 3 defines the in-plane location of the coupling centroid.

Now, sufficient information has been derived to calculate the HTM between the measurement system and the coupling interface. When the axis vectors of F_{ball} expressed in F_{MS} are normalized to unit vectors,

they directly become the rows of the 3 X 3 rotation portion of the 4 X 4 HTM, such that solely the rotation between frames is expressed by:

$$T_{MS-ball-Rot} = \begin{bmatrix} \frac{x_{F_{ball}}}{\|x_{F_{ball}}\|} & 0 \\ \frac{y_{F_{ball}}}{\|y_{F_{ball}}\|} & 0 \\ \frac{z_{F_{ball}}}{\|z_{F_{ball}}\|} & 0 \\ 0 & 1 \end{bmatrix}. \quad (3.15)$$

Next, the translation from the F_{MS} origin to the “temporary” origin of F_{ball} at ball 2 is expressed as another HTM:

$$T_{MS-ball-Transl} = \begin{bmatrix} 1 & 0 & 0 & b_{2,1} \\ 0 & 1 & 0 & b_{2,2} \\ 0 & 0 & 1 & b_{2,3} \\ 0 & 0 & 0 & 1 \end{bmatrix}. \quad (3.16)$$

Next, the translation from the “temporary” origin of F_{ball} to its final origin at the coupling centroid is a third HTM:

$$T_{-ball-Transl} = \begin{bmatrix} 1 & 0 & 0 & x_{C-ball} \\ 0 & 1 & 0 & y_{C-ball} \\ 0 & 0 & 1 & 0 \\ 0 & 0 & 0 & 1 \end{bmatrix}. \quad (3.17)$$

Finally, by the serial multiplication of the transforms, a single HTM defines the transformation from F_{MS} to F_{ball} :

$$T_{MS-ball} = T_{MS-ball-Transl} T_{MS-ball-Rot} T_{-ball-Transl} \quad (3.18)$$

This defines the centroidal coordinate system of a set of three balls. In a manufacturing cell, work objects can be calibrated to this frame, and this frame can be related to the machine coordinate system through the interface transformation after mounting the other half of the kinematic coupling interface.

The routine described in this section is handled by the MATLAB routine *baseframe_complete.m*, in Appendix C. The function takes the command line argument:

`[MCS_BCStrans] = baseframe_complete(xyz),`

where xyz is a 3 X 3 matrix with columns representing the cartesian coordinates of the hole centers of balls 1, 2, and 3 in F_{MS} . The transformation matrix result of Equation 3.19 is returned.

The centroidal frame of the coupling groove set is determined by the same method as that of the ball set. While the groove set is assumed fixed with an absolute transformation to the measurement system in the cell, the ball set is a “floating” module relative to the measurement system, for which only a definition of its centroidal frame relative to the tool frame makes sense. When the balls and grooves are set nominally to their interface plates and the coupling is assembled, their centroidal frames coincide; however, since these placements are never perfect, there are always small translational and rotational errors between F_{ball} and F_{groove} . If the exact relative positions and orientations of the balls and grooves are known, the transformation between these frames is kinematically closed. Note that in the prior section the balls were assumed fixed, but the assumption of fixed grooves in the next section makes no difference in the calculations.

3.3.3 Determining the Interface Error Transformation

In this section, the interface error transformation ($T_{interface}$) is calculated for a canoe ball coupling interface, assuming knowledge of the positions and orientations of the canoe balls relative to F_{MS} , and the positions and orientations of the vee grooves relative to an arbitrary frame. If standard ball-groove couplings were considered, the interface mating would be the simple forced mating of the balls upon the surfaces with normal vector directions imposed by the grooves without a secondary effect from the rotational misalignment of the canoe spheres. To build a deterministic model of the canoe ball interface, individual contacts between each spherical surface and each groove flat must be considered, such that:

1. The measured radius and projected center of each spherical surface defines normal, minimum distance contact with the measured plane defining the mating groove flat.
2. The distances from the projected sphere centers and the centroid of the ball frame constrain the triangular arrangement of balls, relating the rest position of each sphere center with respect to its mating flat to the error motion of the centroidal ball frame.

The mating transformation between a perturbed ball set and a perturbed groove set is depicted in Figure 3.6. The error motion of the centroidal ball frame upon mating with the grooves is the specific six-parameter interchangeability error:

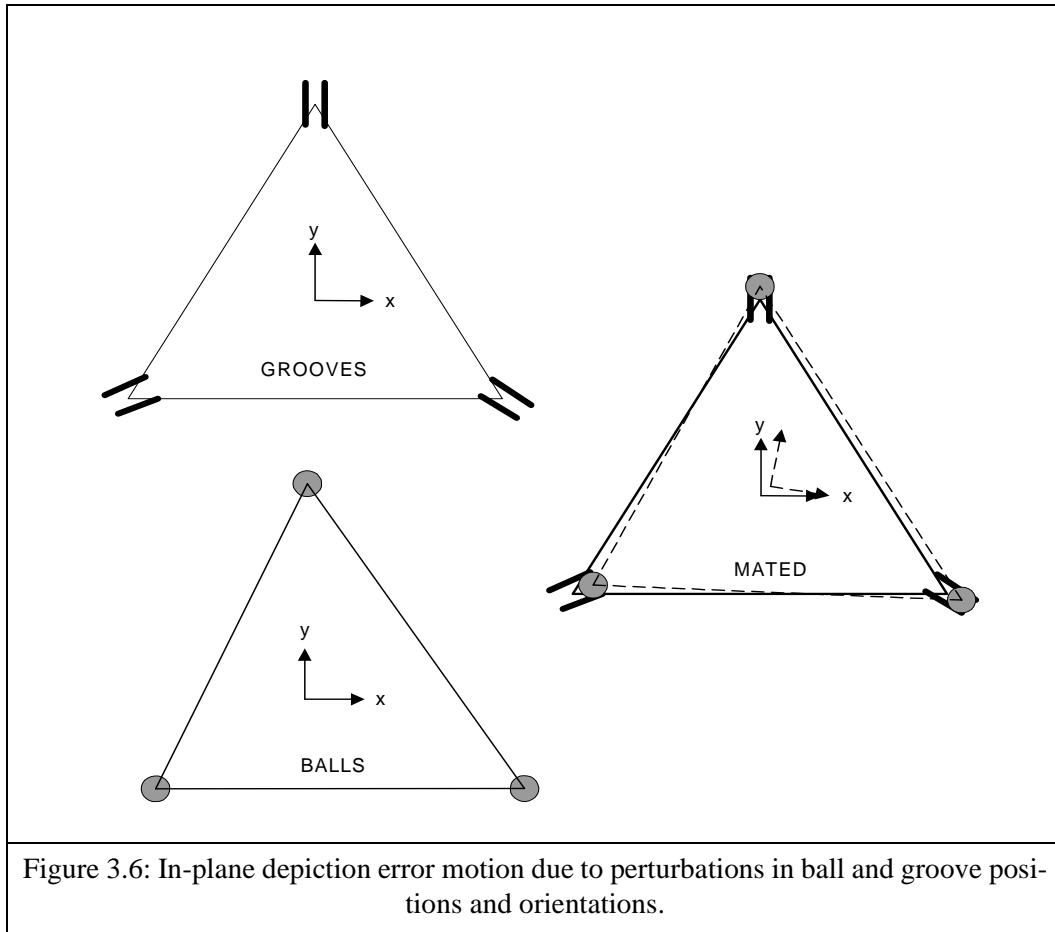
$$\boldsymbol{\varepsilon}_{interchange} = \begin{bmatrix} \delta_{x_c} \\ \delta_{y_c} \\ \delta_{z_c} \\ \theta_{x_c} \\ \theta_{y_c} \\ \theta_{z_c} \end{bmatrix} \quad (3.19)$$

Making small-angle approximations, the interchangeability error becomes the interface transformation between the ball frame and the groove frame:

$$T_{interface} = \begin{bmatrix} 1 & -\theta_{z_c} & \theta_{y_c} & \delta_{x_c} \\ \theta_{z_c} & 1 & -\theta_{x_c} & \delta_{y_c} \\ -\theta_{y_c} & \theta_{x_c} & 1 & \delta_{z_c} \\ 0 & 0 & 0 & 1 \end{bmatrix} \quad (3.20)$$

Then, the vector of interchange error at the TP, defined by the vector V_{TP} in the nominal ball frame, is calculated by taking:

$$E_{TP} = T_{interface} T_{Ball-TP} V_{TP} \quad (3.21)$$



Note that the centroidal frames are solely determined by the ball and groove positions, while their interface mating behavior is also determined by the orientations of the coupling units, manifested in angular perturbations of the groove flat planes, and positional perturbations of the sphere centers orthogonal to the nominal centerlines of the canoe ball units.

Knowing the parameters defining the groove flats and the radii and center locations of the spherical surfaces, the interface transformation between the groove set and ball set of a canoe ball interface is a deterministic calculation. The solution is that of a 24-equation linear system, with the following nomenclature used in derivation:

1. $R_{n,1}$, $R_{n,2}$, etc. = Measured radii of spherical contact surfaces ($n = 1, 2, 3$), numbered counter-clockwise between each pair.

2. $p_{Sn,1}, p_{Sn,2}$, etc. = Relative positions (projected from measured surface points) of sphere centers for a canoe ball unit, for example consisting of $(x_{Sn,1}, y_{Sn,1}, z_{Sn,1})$.

3. $p_{Sn,1}, p_{Sn,2}$, etc. = Final positions of sphere centers for a canoe ball unit after interface mating, for example consisting of $(x_{Sn,1}, y_{Sn,1}, z_{Sn,1})$.

4. $p_{0n,1}, p_{0n,2}$, etc. = Measured arbitrary base points on flats of each groove unit, for example consisting of $(x_{pon,1}, y_{pon,1}, z_{pon,1})$.

5. $N_{n,1}, N_{n,2}$, etc. = Measured normal vectors to flats of each groove unit, for example consisting of $\langle x_{Nn,1}, y_{Nn,1}, z_{Nn,1} \rangle$.

The measured coordinates of the sphere centers coordinates are transformed from F_{MS} to the nominal F_{ball} before determining the interface transformation.

First, the system of equations lists six linear constraints between the sphere center points and the planes representing the respective mating groove flats, defining the eighteen unknown final coordinates of the sphere centers. The distance from each sphere center to its contacting flat is to be the minimum (normal) distance between the point and the plane, equal to the measured radius of the spherical surface. For example, the constraint between the first sphere and mating flat for the first canoe ball to groove pair is:

$$\frac{(p_{S1,1} - p_{o1,1}) \cdot N_{1,1}}{\|N_{1,1}\|} = R_{1,1} \quad (3.22)$$

Performing the vector operations, this linear relation is:

$$\frac{(x_{S1,1} - x_{p01,1})x_{N1,1} + (y_{S1,1} - y_{p01,1})y_{N1,1} + (z_{S1,1} - z_{p01,1})z_{N1,1}}{\sqrt{x_{p01,1}^2 + y_{p01,1}^2 + z_{p01,1}^2}} = R_{1,1} \quad (3.23)$$

Next, the distance constraints between the sphere centers and the original, fixed centroid of the nominal ball triangle are listed. The final coordinates of the sphere centers are related to the nominal centroid by the translational and rotational error motions of a frame fixed to the ball triangle, coincident with the nominal centroidal frame before the ball positions are perturbed and the error of mating to the perturbed grooves is introduced. For example, the final position of the first sphere center of the first canoe ball unit is related to the components of $\mathcal{E}_{interchange}$ by (taking $s()$ as shorthand for $\sin()$ and $c()$ as shorthand for $\cos()$):

$$x_{S1,1} = \delta_{x_c} + x_{S1,1}[c(\theta_{z_c})c(\theta_{y_c})] + y_{S1,1}[c(\theta_{z_c})s(\theta_{y_c})s(\theta_{x_c}) - s(\theta_{z_c})c(\theta_{x_c})] + z_{S1,1}[c(\theta_{z_c})s(\theta_{y_c})c(\theta_{x_c}) - s(\theta_{z_c})s(\theta_{x_c})] \quad (3.24)$$

$$y_{S1,1} = \delta_{y_c} + x_{S1,1}[s(\theta_{z_c})c(\theta_{y_c})] + y_{S1,1}[s(\theta_{z_c})s(\theta_{y_c})s(\theta_{x_c}) + c(\theta_{z_c})c(\theta_{x_c})] + z_{S1,1}[s(\theta_{z_c})s(\theta_{y_c})c(\theta_{x_c}) - c(\theta_{z_c})s(\theta_{x_c})] \quad (3.25)$$

$$z_{S1,1} = \delta_{z_c} + x_{S1,1}[-s(\theta_{y_c})] + y_{S1,1}[c(\theta_{z_c})s(\theta_{x_c})] + z_{S1,1}[c(\theta_{y_c})c(\theta_{x_c})] \quad (3.26)$$

Making small angle approximations, the final coordinates are:

$$x_{S1,1} = \delta_{x_c} + x_{S1,1} + y_{S1,1}[-\theta_{z_c}] + z_{S1,1}[\theta_{y_c}] \quad (3.27)$$

$$y_{S1,1} = \delta_{y_c} + x_{S1,1}[\theta_{z_c}] + y_{S1,1} + z_{S1,1}[-\theta_{x_c}] \quad (3.28)$$

$$z_{S1,1} = \delta_{y_c} + x_{S1,1}[-\theta_{y_c}] + y_{S1,1}[-\theta_{x_c}] + 1 \quad (3.29)$$

Angular errors at the centroid are transferred to linear errors in positioning the sphere center in the z-y-x order dictated by the Euler angle convention.

Separating the variable coefficients and constant terms of the twenty-four equations, the system takes the matrix form:

$$AX = B, \quad (3.30)$$

with A as the 24 X 24 matrix of constant coefficient terms computed from the measured points and distances on the coupling halves, B as the 24-element column vector of constant position offsets (sphere radii and position offsets from the centroid to the nominal locations of the spheres), and X as the vector of the unknown rest positions of the spheres and error motions of the interface.

In production, knowing the parameters of the contact surfaces ahead of time, the calculation of $T_{interface}$ would be a step of the machine calibration routine. Ideally, the software would take the measurement values for the components (as discussed later, by direct input, floppy disk, or wireless transfer), calculate the interface HTM, and apply it to the global serial chain of transformations, placing it between the ball and groove frames.

The algorithm to calculate the interface transformation is implemented in MATLAB in the script *errortransform.m* and the aforementioned sub-routine *baseframe_complete.m*, both transcribed in Appendix C. The *errortransform.m* routine takes the function command format:

```
function [errorHTM] = errortransform(centers, radii, basepoints,
normal);
```

where `centers` and `radii` are the center positions and radii of the six canoe spheres, and `basepoints` and `normals` are points on and measured surface normals to the groove flats. Note that these

parameters are directly the points that would be returned by a coordinate measuring machine (CMM) that performed a plane fit to each groove surface and a sphere fit to each curved surface. The return object `errorHTM` is the interface transformation.

3.4 Applied Modeling of Error Components

The prior section placed the frames and transformations based upon exact knowledge of the ball and groove contact surface positions. Clearly, the accuracy of the calculation of the base frame, groove frame, and the interface transformation depends upon the accuracy of the measurement system and the level of precision in manufacturing the couplings and mounting plates. If an offset measurement feature is used, such measurements are still corrupted by the manufacturing tolerances of the placement of the measurement feature relative to the coupling contact points. Accordingly, this section extends the frame and transformation calculations to include each of the random error components listed in Section 3.2.1. Such a model enables prediction of the magnitude of the interface transformation correction when the distributions of the random errors are known; hence, a novel relationship between interface calibration intelligence and accuracy at the tool point is formed.

3.4.1 Modeling of Random Error Components

The error model is built as a serial combination of the random error components in the ball and groove center positions, the ball and groove orientations, the flatness of the interface plates, the machined form of the balls and grooves and associated placement of the measurement feature if present, and in the measurement system. Each component is characterized by a standard Gaussian distribution, with known mean and variance. Random variates are generated in a Monte Carlo simulation to assess the variability at the tool point at any chosen or measured magnitudes of the random error distributions.

3.4.1.1 Ball and Groove Position Error

When the balls and grooves are mounted to the interface plates, their positions vary because of in-plane positional errors in the locations of their mounting holes. The mounting holes are assumed to vary within a circular tolerance zone of their nominal location. The error of hole location is the error of the plate

drilling process; with the coupling centroid taken as a nominal reference, this variation is assumed to scale linearly with distance from the centroid. So, in cartesian coordinates relative to the centroidal frame, the true position of a mounting hole is e.g.:

$$x_{h_{b_1}} = x_{h_{b_1nom}} + R_{h_{b_1}} h_{tol} \text{RandN}() \cos(\theta_{rand}) \quad (3.31)$$

$$y_{h_{b_1}} = y_{h_{b_1nom}} + R_{h_{b_1}} h_{tol} \text{RandN}() \sin(\theta_{rand}) \quad (3.32)$$

$$\theta_{rand} = 2\pi \text{Rand}() \quad (3.33)$$

In these equations, h_{tol} is the one-sigma radial tolerance of the hole position for the circular tolerance zone, $\text{RandN}()$ is a normally distributed random number between -1 and 1, and $\text{Rand}()$ is a uniformly distributed random number between -1 and 1.

3.4.1.2 Ball and Groove Orientation Error

The angular variation in coupling alignment is calculated by assigning a random variate as an angular perturbation of the line through the coupling center and the triangle centroid. Hence, orientation error of the coupling results in a small rotation about its center point, for example sampled from:

$$\theta_{b_1} = \theta_{tol} \text{RandN}(). \quad (3.34)$$

θ_{tol} is the one-sigma tolerance of angular position of the couplings, reflecting the capability of the coupling-to-plate assembly process (usually using a dowel or spring pin through a secondary hole) to align the couplings such that their extended centerlines pass through the centroid of the coupling triangle. This error causes rotations of the normal vectors, base points, and sphere centers, about the central axes of the mounting holes of the balls and grooves.

3.4.1.3 Mounting Plate Flatness Error

In this simple case, error in the flatness of the plates to which the couplings are fitted results in a vertical shift in the contact points of the balls and grooves. The flatness error is modeled as a normally distributed variation in the plate thickness. The centroid of the coupling triangle is treated as a reference with

nominal thickness, and the magnitude of thickness variation scales linearly with distance from this point. Hence, the true plate thicknesses at the coupling positions are e.g.:

$$t_{b_1} = t_{nom} + t_{tol} \text{RandN}() R_{b_1} . \quad (3.35)$$

Note that the angular pitch of the plate due to this error would also tilt the coupling points out of plane; this effect is negligible and is neglected.

3.4.1.4 Coupling and Measurement Feature Form and Placement Error

There are also form errors from inaccuracies in machining the couplings, and in the machining and placement of the measurement feature if it is present. If the offset measurement feature described previously is used, error results in estimating the positions of the sphere centers, the sphere radii, and the groove plane parameters with respect to the measurement features. If the contact surfaces are measured directly, the error is reduced, yet is still present in predicting the locations of the sphere centers with respect to the canoe ball surfaces. In each case, the total error of each prediction is determined through a stackup of individual dimensional errors, referenced in terms of a local coordinate frame on each coupling ball or groove. This frame, F_{loc} , has its origin at the center of the bolt hole through the coupling, at the lower surface of the protrusion. The x-axis is normal to the coupling centerline, the y-axis along the coupling centerline, and the z-axis vertical along the mounting hole axis. Errors due to non-sphericity of the canoe surface and the measurement sphere surface are considered negligible, but could be several microns.

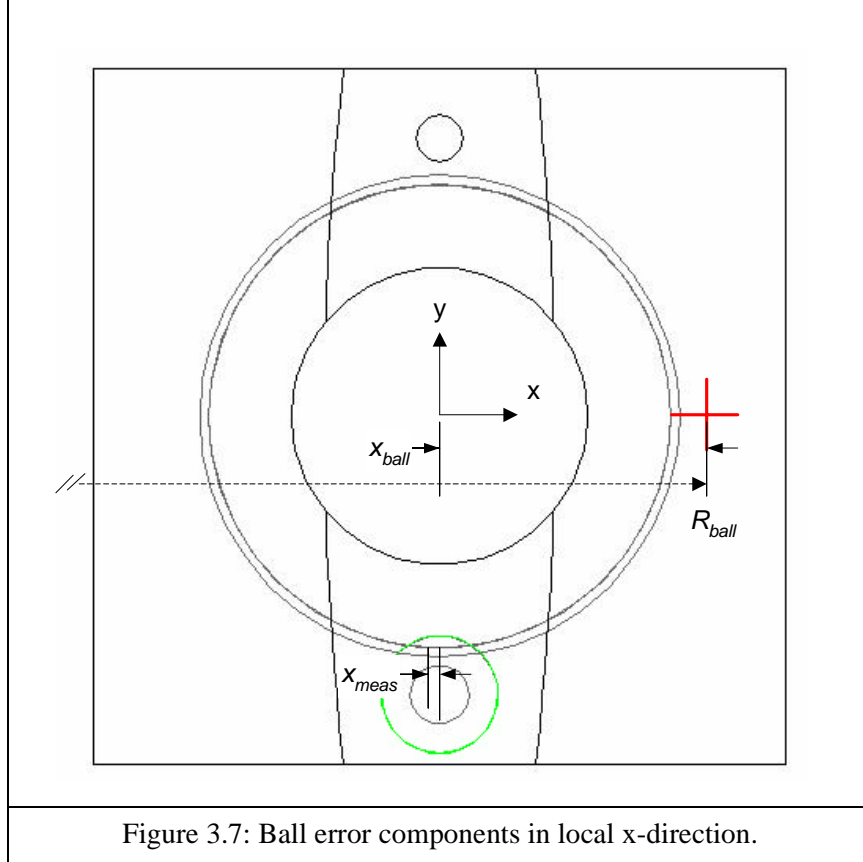
In the x-direction of F_{loc} , error in the predicted position of the sphere center with respect to the measurement feature is from error in:

1. R_{ball} = The surface radius of the canoe ball at the contact point.
2. x_{meas} = The position of the measurement feature along the x-axis.
3. x_{ball} = The position of the sphere center along the x-axis.

By convention that the stacked-up error is the average of a worst-case and root-sum-square (RSS) stack-up, the error in this direction is computed from:

$$\epsilon_x = \frac{1}{2} \left(2 \left(\frac{R_{ball}}{\sqrt{2}} \right) + 2x_{meas} + 2x_{ball} \right) + \sqrt{2 \left(\frac{R_{ball}}{\sqrt{2}} \right)^2 + 2x_{meas}^2 + 2x_{ball}^2}. \quad (3.36)$$

Note that when the measurement feature is used, the error in the ball radius can be absorbed into the stackup for the center position, hence the algorithm can use the nominal radius for each sphere in the matrix system.

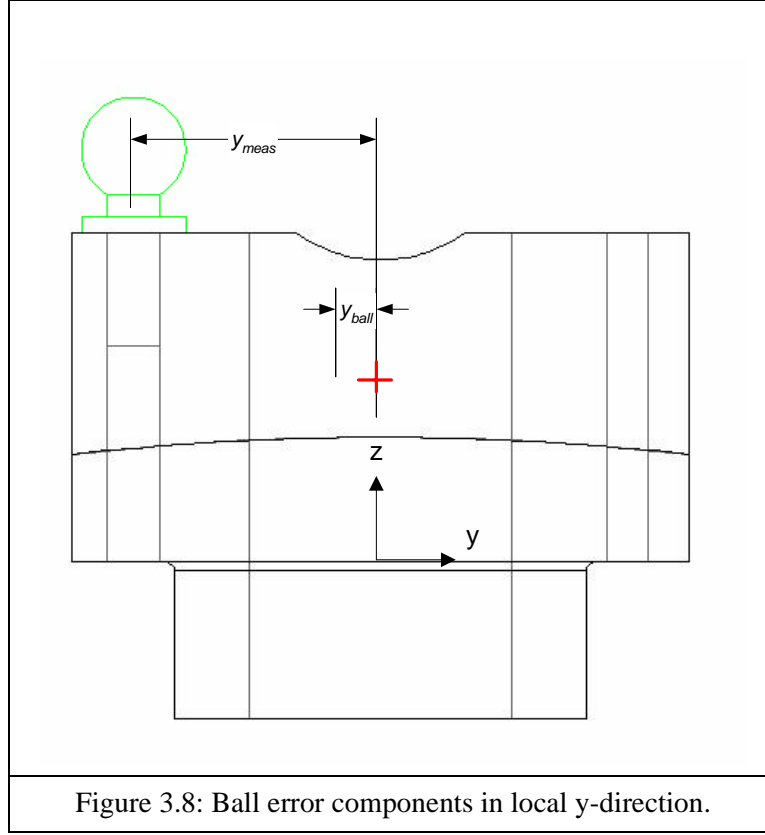


In the y-direction of F_{loc} , error in the predicted position of the sphere center is from error in:

1. y_{meas} = The position of the measurement feature along the y-axis.
2. y_{ball} = The position of the theoretical canoe ball center along the y-axis.

The stack-up of these components gives total y-direction error of:

$$\epsilon_y = \frac{1}{2} ((2y_{meas} + 2y_{ball}) + \sqrt{2y_{meas}^2 + 2y_{ball}^2}) \quad (3.37)$$

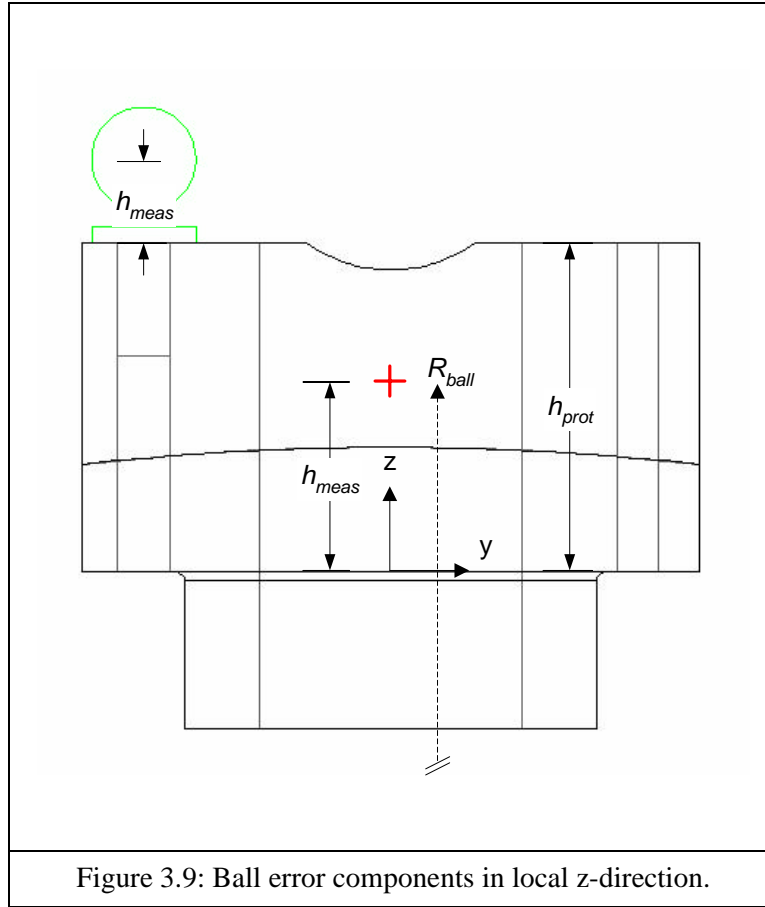


In the z-direction of F_{loc} , error in the predicted position of the sphere center is from:

1. R_{ball} .
2. h_R = The position of the contact point relative to the bottom of the bulk protrusion, along the z-axis.
3. h_{prot} = The height of the canoe ball bulk protrusion.
4. h_{meas} = The measurement feature relative to the canoe ball bulk protrusion.

Hence, the total z-direction error is:

$$\epsilon_z = \frac{1}{2} \left(2 \left(\frac{R_{ball}}{\sqrt{2}} \right) + h_R + h_{prot} + h_{meas} \right) + \sqrt{2 \left(\frac{R_{ball}}{\sqrt{2}} \right)^2 + h_R^2 + h_{prot}^2 + h_{meas}^2} \quad (3.38)$$



Note that the presence of these form errors after calibration is unique to the case of using an offset measurement feature. If the spherical surface is measured directly, first-order error contributions from the form error dimensions above are non-existent; however, measurement error in placement of the measurement point and in prediction of the sphere center location are present. Although the form errors are small in magnitude and measured over small distances, this shows how use of the measurement feature is a mild sacrifice of accuracy in estimating the contact point location, in exchange for ease of calibration.

The error stackup for location of the groove contact points is quite similar, only with the x-axis and z-axis contributions from R_{ball} replaced with contributions from the placement of the groove flat. When variability exists in both the groove angle and the distance of the flat from the centerline along the x-axis, the contribution is:

$$2x_{groove}\theta_{groove} \quad (3.39)$$

The angular alignment of the groove unit and variation in groove angle affect the alignment of the groove normal vector, while the form error offsets of the measurement feature and the positional error in the mounting holes affect the position of the base point of groove plane. When the groove surfaces are directly measured all these dependencies are removed, notwithstanding error of the measurement system.

3.4.1.5 Measurement System Error

Any reported value from the measurement system used in interface calibration has error from the measurement system itself. For 3-dimensional laser tracking systems often used in calibrating manufacturing cells, this error scales in an approximately linear fashion with distance of the objective reflector from the fixed tracking head, which emits the laser beam. At the measured point, this error is treated as normally distributed within a spherical tolerance zone of the nominal location, hence the measured cartesian position is:

$$x_{meas} = x_{nom} + R_{meas} \text{RandN}() \cos(\theta_{lat}) \cos(\theta_{long}) \quad (3.40)$$

$$y_{meas} = y_{nom} + R_{meas} \text{RandN}() \cos(\theta_{lat}) \sin(\theta_{long}) \quad (3.41)$$

$$z_{meas} = z_{nom} + R_{meas} \text{RandN}() \cos(\theta_{lat}) \quad (3.42)$$

$$\theta_{lat} = 2\pi \text{Rand1}() \quad (3.43)$$

$$\theta_{long} = 2\pi \text{Rand2}() \quad (3.44)$$

Here, R_{meas} is the one-sigma radius of the tolerance sphere, θ_{long} and θ_{lat} are angles in orthogonal directions and the stochastic parameters are as defined before. Rand1() and Rand2() simply indicate that two distinct uniformly-distributed random numbers are generated.

3.4.2 Assignment of Reasonable Error Magnitudes

Reasonable values for the error components discussed in the prior section are listed below, within ranges representative of mainstream high-volume machining processes for the couplings and plates, and state-of-the-art cell calibration systems. All values are to two-sided 3-sigma confidence.

Error Component [units]	Low Value	Mid Value	High Value
h_{tol} [mm/m]	0.05	0.10	0.15
t_{tol} [mm/m]	0.05	0.10	0.15
θ_{tol} [deg]	0.1	0.2	0.5
R_{ball} [mm]	0.01	0.02	0.04
x_{meas}, y_{meas} [mm]	0.01	0.02	0.04
x_{ball}, y_{ball} [mm]	0.01	0.02	0.02
h_R [mm]	0.01	0.02	0.02
x_{groove}, y_{groove} [mm]	0.01	0.02	0.02
h_{prot} [mm]	0.01	0.02	0.04
h_{meas} [mm]	0.005	0.01	0.015
R_{meas} [mm/m]	0.01	0.05	0.05
θ_{groove} [deg]	0.01	0.02	0.04

Table 3.1: Representative 3-sigma values for interface error components.

3.5 Parametric Relationship of Calibration Detail vs. Mating Accuracy

Using Monte Carlo simulations which generate large numbers of random variates for each error component, the interface model facilitates a parametric study of the relationship between the detail of interface calibration and the interface mating accuracy. If the distribution tolerances can be estimated accurately, this model can be used to predict interface performance before mass-production, enabling error-budgeting and choice of component tolerances to give the desired accuracy at minimal cost.

3.5.1 Interface Calibration Options

The random errors in the kinematic interface fall into two categories: those that can be reduced or eliminated through calculation of the interface transformation between the groove set and the ball set; and those that cannot be eliminated, and will persist in a mismatch between the true and calculated tool point locations. While a measurement system with minimum error can be chosen, its error will persist. Similarly,

while the couplings and measurement features can be machined to high accuracy, form error in terms of the offset dimensions between the measurement feature and the contact point will make the predicted contact points slightly from the true contact points.

A parametric model of the interface enables understanding of the effect of coupling calibration on the error at the tool point, and prediction of the residual error at the tool point when the measurement system and coupling form errors can be well-approximated. For canoe ball interface calibration using a measurement feature, six levels of intelligence are identified, listed in Table 3.2. When the contact surfaces are measured directly, the three levels of calibration listed in Table 3.3 are studied. If the lowest level of complexity is selected, the magnitude of error at the tool point will be maximum. Alternatively, if the greatest complexity is selected, the remaining “calibrateable” error shall be zero, and the only tool point error should be from the measurement system and coupling form errors.

Complexity	Example Calibration Procedure	Measurement Knowledge
0	Measure nothing, assuming fully nominal placement	$T_{interface}$ is identity transform between F_{ball} and F_{groove} . Perfect nominal deterministic match.
1	Measure groove positions: - Center slip-fit measurement tool into mounting hole - Perform sphere fit with laser tracker, gathering (X,Y,Z) coordinates	Groove locations define F_{groove} , from which $T_{MS-groove}$ is defined Calculate $T_{interface}$ using measured groove positions and assuming nominal groove orientations and nominal ball positions and orientations
2	Same as (1), plus: Measure groove orientations through having a second recorded point on each groove: - Use coupling with integrated secondary measurement feature	Groove locations define F_{groove} , from which $T_{MS-groove}$ is defined. Kinematic accuracy improved by knowledge of sliding directions. Calculate $T_{interface}$ using measured groove positions and orientations; assume nominal ball positions and orientations
3	Same as (2), plus: Measure ball positions.	Ball locations define F_{ball} , from which $T_{interface}$ is now calculated using measured values. Now the only assumption is of nominal ball orientations, with all other information known.
4	Measure groove positions and ball positions as before, but neither set of orientations.	F_{ball} and F_{groove} are known as accurately as possible, but kinematic algorithm for $T_{interface}$ assumes nominal orientations from the measured positions.
5	Same as (3), plus: Measure ball orientations using second recorded point on ball.	Calculate $T_{interface}$ with full knowledge of coupling positions and orientations; $\arg(T_{interface})$ extended at tool point is minimized for chosen manufacturing process and measurement system.

Table 3.2: Calibration options for canoe ball interface, using offset measurement feature.

Complexity	Example Calibration Procedure	Measurement Knowledge
0	Measure nothing, assuming fully nominal placement	$T_{interface}$ is identity transform between F_{ball} and F_{groove} . Perfect nominal deterministic match.
1	Measure ball parameters: - Perform sphere fit to curved surfaces of canoe ball, calculating center position and radius.	Calculate $T_{interface}$ using measured ball parameters (sphere center-to-radius constraints) and assuming nominal groove normal vectors.
2	Measure groove parameters: - Perform three-point plane fit to flats of vee grooves, calculating base point and normal vector.	Calculate $T_{interface}$ using measured groove parameters (plane placement and normal direction constraints) and assuming nominal ball parameters.
3	Measure ball parameters and groove parameters.	Calculate $T_{interface}$ with full parameter knowledge; $\arg(T_{interface})$ extended at tool point is minimized for chosen manufacturing process and measurement system.

Table 3.3: Calibration options for canoe ball interface, directly measuring contact surfaces.

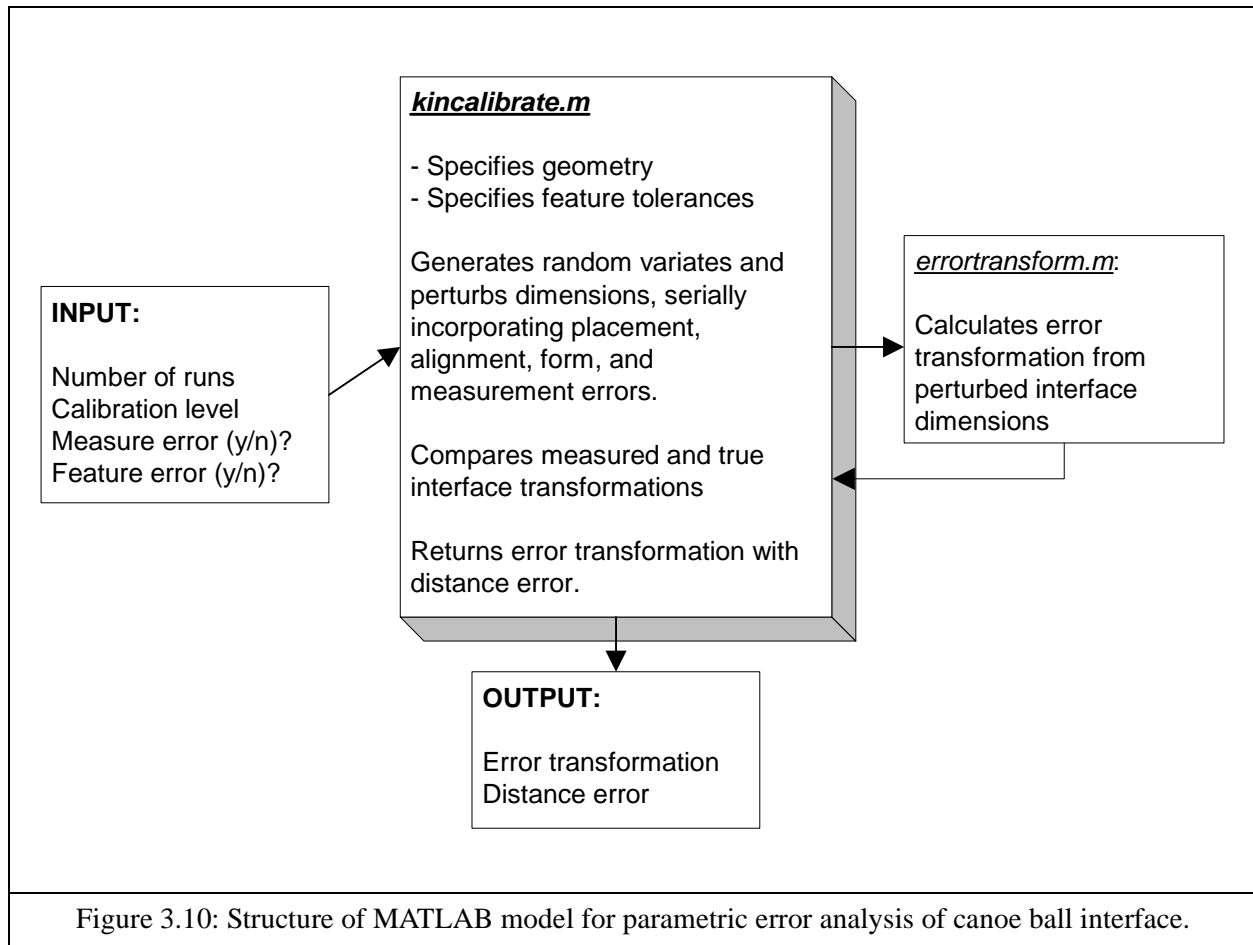
3.5.2 Model Structure and Procedure

The computer model for the parametric study is written as a series of MATLAB scripts, driven by the master routine *kincalibrate.m* and containing the sub-routines mentioned before for positioning the centroidal frame, computing the individual error components, and calculating the interface transformation. The structure of the computer model is explained by the block diagram below, excluding auxiliary matrix math functions specially defined for the model.

The *kincalibrate.m* routine takes the command line argument:

```
function [TCPerror, rmsavg] = kincalibrate(numruns, caltype).
```

Here, *numruns* is the number of Monte Carlo iterations and *caltype* is the complexity of calibration. All geometric parameters of the interface and values of the error parameters are configured by editing the values specified in the scripts.



This initial parametric study was simple, choosing fixed the values given in Table 3.3 for all the error components. The interface geometry was specified as listed in Table 3.4. A single 10,000-iteration Monte Carlo simulation was conducted for each level of calibration detail, and the series of resultant errors at the tool point was averaged to give the interchangeability at each level.

Error Component [units]	Value
h_{tol} [mm/m]	0.10
t_{tol} [mm/m]	0.10
R_{ball} [mm]	0.02
x_{meas}, y_{meas} [mm]	0.02
x_{ball}, y_{ball} [mm]	0.02
x_{groove}, y_{groove} [mm]	0.02
h_R [mm]	0.02
h_{prot} [mm]	0.02
h_{meas} [mm]	0.01
R_{meas} [mm/m]	0.004
θ_{tol} [deg]	0.2
θ_{groove} [deg]	0.02

Table 3.4: Error component values for parametric study with varied calibration complexity.

R_{canoe} [mm]	500
D_{beq} [mm]	30
R_{b1}, R_{g1} [mm]	500
R_{b2}, R_{g2} [mm]	500
R_{b3}, R_{g3} [mm]	500
θ_{b1}, θ_{g1} [deg]	90
θ_{b2}, θ_{g2} [deg]	210
θ_{b3}, θ_{g3} [deg]	330

Table 3.5: Canoe ball interface geometry for parametric study with varied calibration complexity.

Additionally, the tool point was specified at $(x,y,z) = (2.0, 2.0, 2.0)$ m with respect to F_{ball} , and the measurement system was placed approximately 3 m from the tool point.

3.5.3 Parametric Study Results

The parametric study was completed with eight full Monte Carlo simulations: six for the individual levels modeling offset measurement, and three for the levels modeling direct measurement of the contact surfaces. As shown in Figures 3.11 and 3.12, for the 3-sigma error parameter values chosen, use of the interface transformation eliminates approximately 49% or 0.11 mm of the 0.22 mm total error of interchangeability when full offset calibration is performed. When direct contact measurement is performed, the interchangeability analysis reduces the tool point error 88% to 0.02 mm. In the former case, the remaining error at full calibration is due to measurement system error and error in the offset distances from the measurement feature to the contact points on each coupling, and in the latter case the remaining error is solely due to measurement error.

With respect to detail of the calibration process using a measurement feature, the results also indicate that a negligible advantage in accuracy is gained by knowledge of the relative orientations of the balls and grooves, and nearly all of the measurable interface error is removed when only the positions are measured. The independent effect of angular misalignment is shown in 3.13, with a large error needed to generate significant variation at the tool point. Hence, unless the process of mounting the couplings to the plates is poorly controlled, only single-point (spot) position information is needed for best calibration performance when a measurement feature is used. From this position, nominal ball and groove orientations can be assumed for calculating the groove normal vector directions and projecting the positions of the canoe spheres.

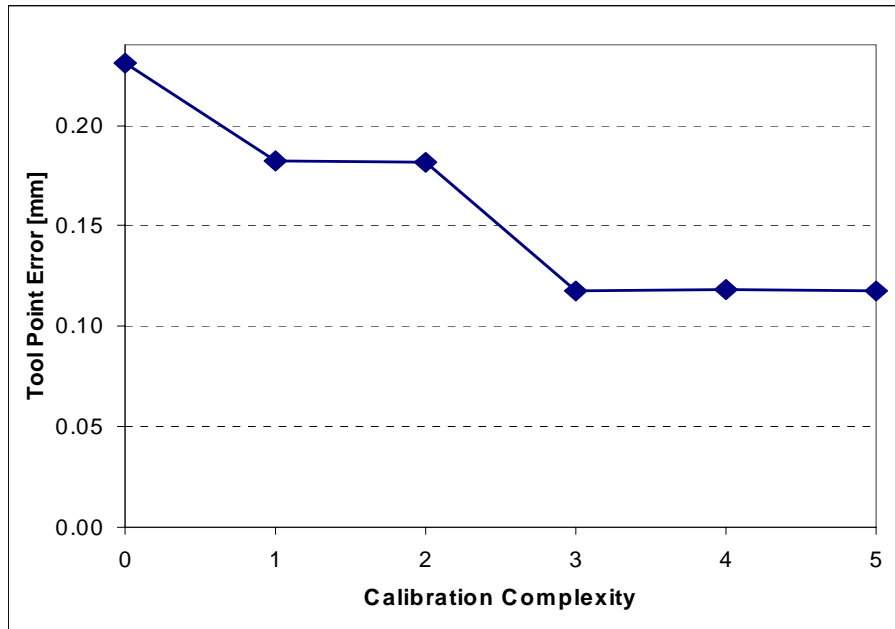


Figure 3.11: Tool point error versus interface calibration detail - calibration using offset measurement sphere.

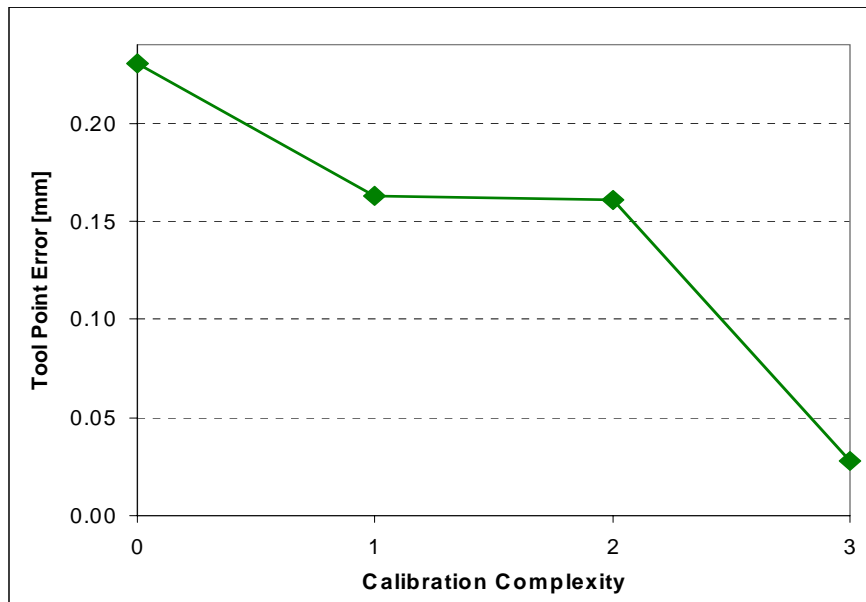
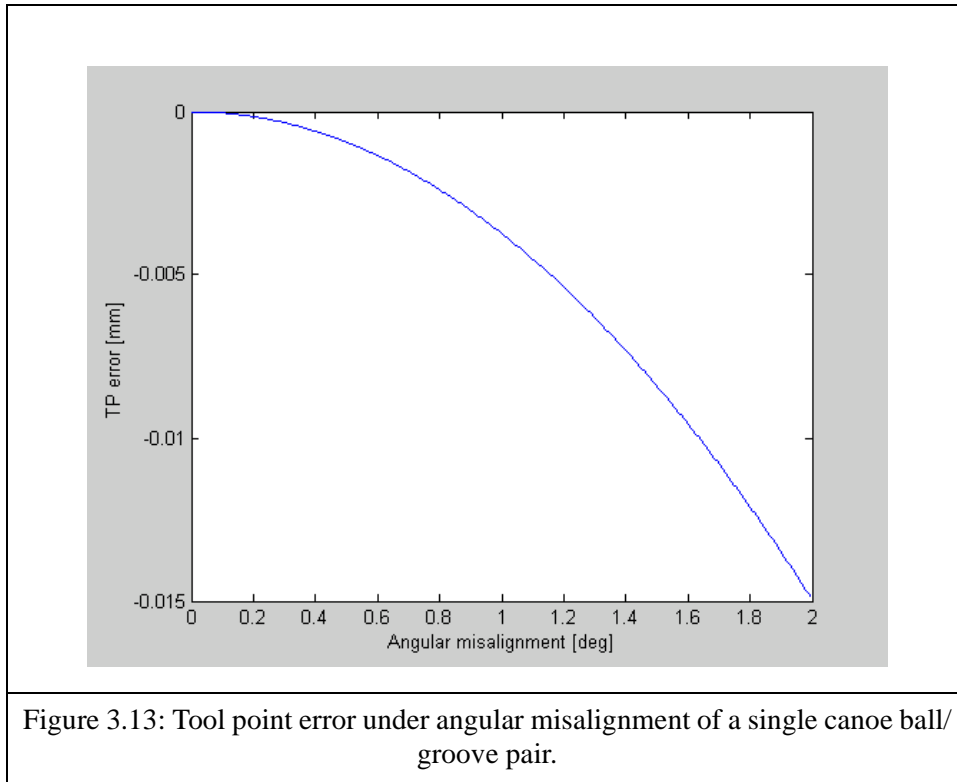


Figure 3.12: Tool point error versus interface calibration detail - calibration using direct measurement of ball and groove contact surfaces.



A more detailed parametric study using this model is part of Chapter 5, a case study of repeatability and interchangeability of a kinematic coupling factory interface for heavy-duty industrial robots.

3.6 Bench-Level Interchangeability Model

The interchangeability of the canoe ball interface as deterministically modeled here was demonstrated by building a series of small prototype models and measuring the error in their centroidal frame positions and orientations over all combinations of ball sets and groove sets. Figures 3.14, 3.15, and 3.16 show the interchangeability models, a large baseplate with two arrangements of six grooves at equal 60-degree angles around a center point, and ten smaller top pallets each with an equilateral ball arrangement. The plates were milled from 6061-T651 aluminum precision jig plate (flatness 0.02 mm/m), press-fitted with 420 stainless steel 250 mm surface radius canoe mounts at 106 mm from the coupling centroid. As seen below, the opposite side of the pallet was fitted with three steel measurement spheres, used for measuring the pallet location, upon interchange between the different groove sets.

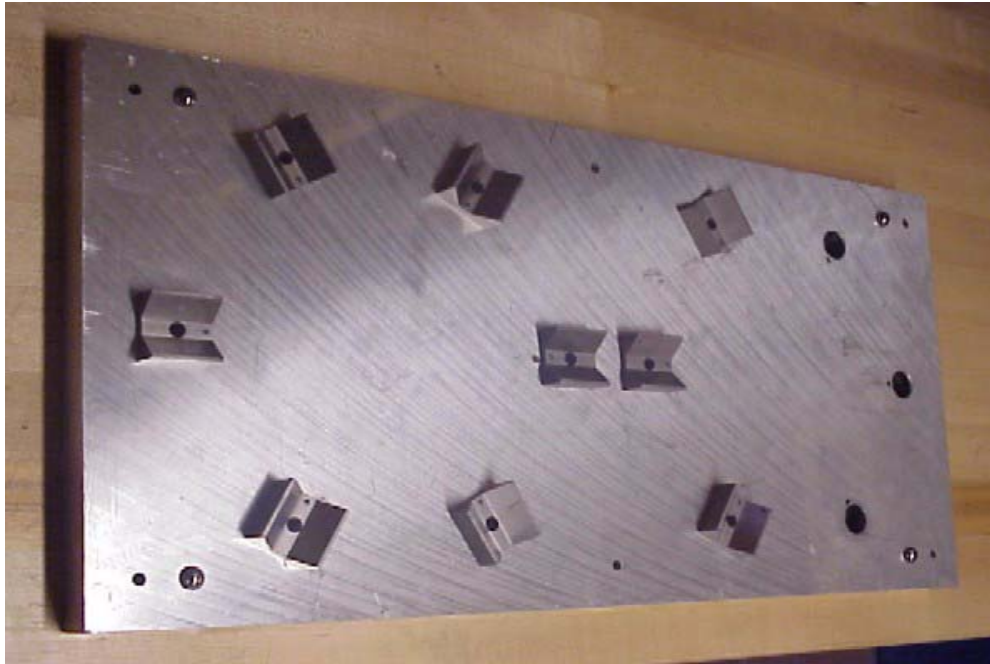


Figure 3.14: Prototype groove base for measurement of canoe ball interface interchangeability (three adjacent grooves removed).

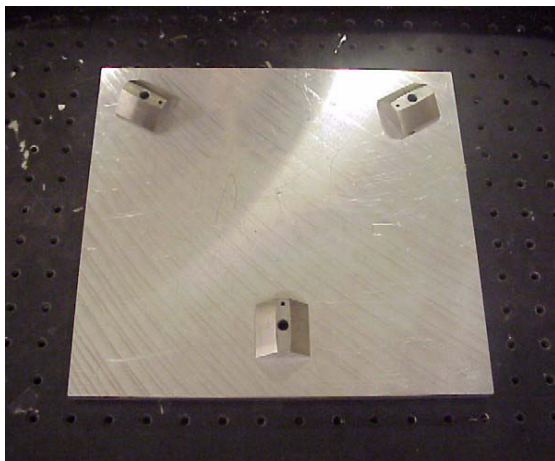


Figure 3.15: Prototype pallet for interchangeability measurements - canoe ball side.

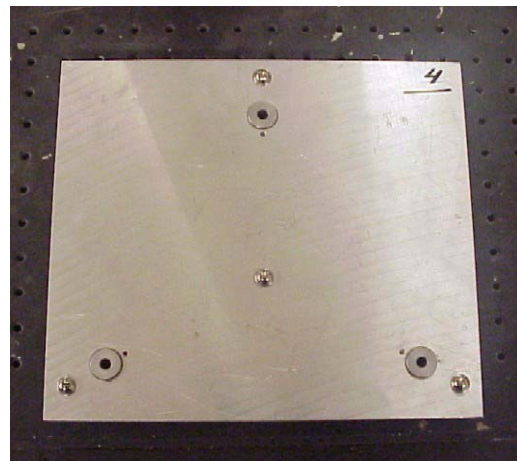


Figure 3.16: Prototype pallet for interchangeability measurements - measurement sphere side.

To ensure statistical confidence in the calibration-interchangeability relationship, the base and pallet plates were machined on a precision CNC mill with positional accuracy of 0.02 mm. The locations of the coupling mounting and alignment hole pairs were intentionally perturbed within circular tolerances zones of 3-sigma diameter 0.64 mm from their nominal positions relative to the coupling centroid, while the measurement spheres were always placed identically. This was guided toward making the interface variation between interchange positions almost solely due to individually measurable errors in the coupling locations, and not due to the error of the CNC machine or that of the measurement system. The latter could only be characterized in terms of statistical distributions and not assigned specific values for each machined part and measurement task.

3.6.1 Metrology Setup and Procedure

The interchangeability of the canoe ball pallet system was measured using a Brown & Sharpe MicroVal PFX coordinate measuring machine (CMM), shown in Figure 3.17. The three-axis CMM was fitted with a Renishaw touch-trigger sensor, with a 15 mm extension tip and side-touch-activated probe.



Figure 3.17: Interchangeability setup on Brown & Sharpe MicroVal PFx CMM

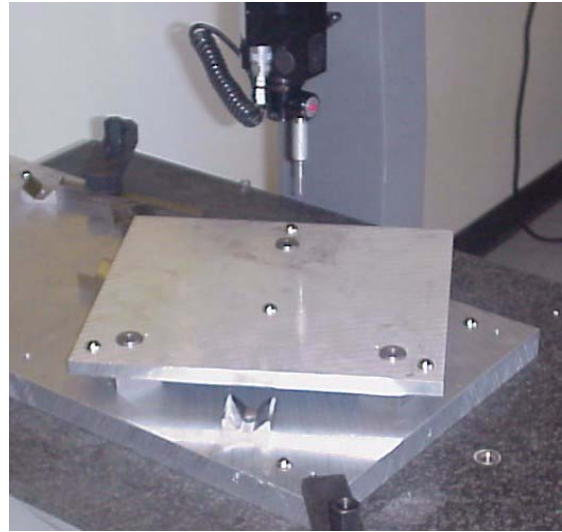


Figure 3.18: Pallet in 60 degree clockwise measurement position.

To begin the measurements, the probe was seated in the sensor, and the sensor was mounted to the CMM. The tip was calibrated using a standard 20 mm diameter reference sphere. Next, the repeatability of the machine was assessed by clamping the groove baseplate to the table, mounting a ball pallet to one of its groove sets, and taking twenty-five successive measurements of the measurement spheres on the pallet. This gave two-sigma repeatability of the centroidal frame of 0.005 mm (5 microns); since absolute accuracy was not a requirement, this was an adequate performance verification.

After checking mounting repeatability, the ball pallet was removed, and the positions and orientations of the twelve grooves on the base were measured. The positions were measured by finding the center of each groove through a three-point least-error circle fit. The orientations were measured by fitting three-point least-error in-plane vectors to the sides of each groove, and taking the average of the two directions

as the centerline. Each position and orientation was measured three times, and the average result for each of the canoe balls and grooves was used.

Next, the pallets were calibrated. Each was mounted to the CMM table, and the positions and orientations were assessed in the same fashion as the grooves. The planar side edges of the protrusions (below the spherical surface areas) were used for the vector fits. This enabled calculation of the distances between the ball centers and the vector orientations with respect to the arbitrary (since different pallets will be mounted in different places on the table) measurement frame.

Finally, the interchangeability of the five pallets was assessed. Each was mounted successively in each of the twelve groove set configurations, and its measurement spheres were located. Each sphere was measured using an eight-point least-error fit to the calculated center position. This scheme permitted analysis of the central frame variability when interchanged between groove sets, and calculation of the absolute correction by finding the interface transformation for each mating combination. Three measurements were taken and averaged for each pallet in each mounting place.

3.6.2 Result Validation of Interchangeability Model

To validate the interchangeability model for the canoe ball interface, the error transformation for each unique interface set (each pallet in each set of three grooves) was calculated using the measured groove positions on the baseplate and the distances between the canoe balls on the pallets. The positional and angular errors implied by the error transformation were compared to the transformations calculated using the centroidal frames of the groove sets and the tooling balls on the tops of the pallets. Hence, if the components of the measured interface transformation matched those of the predicted transformation based solely on the relative positions of the couplings, the kinematic model for interface calibration would be verified.

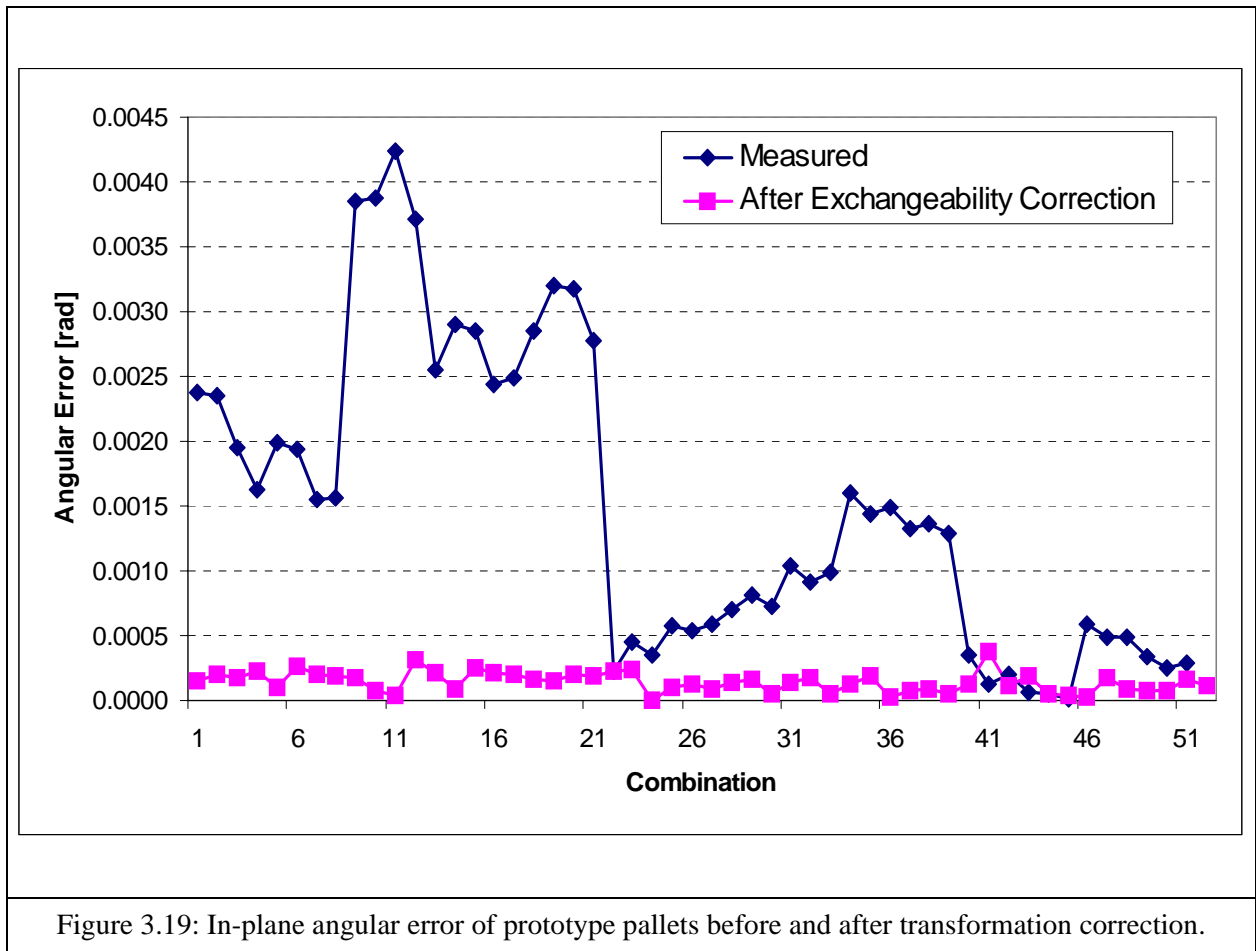


Figure 3.19 plots the in-plane angular error of each interface combination, as measured between the centroidal frames, and after the transformation correction was applied to the measurements. The combinations are grouped for each pallet, so the last ten measurements represent those of the fifth pallet, which was machined with no more than 0.01 mm deviation from the nominal mounting hole locations. So, within the resolution of the measurement system and the accuracy of placing the tooling balls as offset measurement features, the correction had little benefit in that instance. However over all trials, applying the interface transformation reduced the placement error by an average of 92%, specifically from 1.5×10^{-3} radians to 1.4×10^{-4} radians for in-plane rotation. The average total (positional + sine) error reported at a 100 mm circle from the coupling centroid was then 0.015 mm. Hence, within the accuracy limits imposed by the CMM and the tooling ball placements, the canoe ball interchangeability model had been validated.

3.7 Interchangeability Model of Three-Pin Interface

Having built and validated the interchangeability model of the canoe ball interface, the MATLAB routines were easily adapted to comparatively model the interchangeability of the three-pin interface, with in-plane location by forcing three vertical pins against three vertical contact surface, and vertical seating by engagement of preloaded horizontal contact surfaces. However, because the three vertical line contacts and three horizontal plane contacts make the three-pin arrangement technically quasi-kinematic or overconstrained, the model makes the following assumptions to ensure a deterministic solution of $T_{interface}$:

1. The vertical contacting surfaces of the pins are perfectly parallel to the mating vertical cuts in the bottom interface plate.
2. The horizontal contact surfaces surrounding the pins in the top interface assembly are all parallel to the horizontal contact surfaces on the top of the bottom interface plate. While vertical perturbations of the locations of the horizontal contact surfaces are modeled, resulting angular errors between the contact pairs imposed by mating of all three randomly offset pairs at once are ignored.
3. Sufficient preload is always applied to perfectly seat the interface, and manufacturing variation in the location of the preload has no effect on the interface mating behavior.

Considering these assumptions, a deterministic matrix system of nine linear equations gives the centroidal error motions of a three-pin interface when parameters of its pins and contact surfaces are perturbed:

1. Three in-plane constraints are established between the measured pin centers and the contact surfaces in the bottom plates. Similar to the method of (3.23) for the canoe balls, but here in two dimensions, the radii of the pins at the contact points are parallel to the measured normal vectors of the contact surfaces.
2. Six in-plane individual coordinate constraints are established between the pin centers and the error motions of the nominal centroidal frame of the pin arrangement.
3. Out-of-plane error is incorporated by adding the vertical offsets of the horizontal pin and plates surfaces at each of the three points. The total error at each point is considered as a decoupled normal motion, which individually causes a pure rotation of the centroidal frame. The average of the three normal motions is added as a normal motion of the centroidal frame.

Like the canoe ball model, this was built to model kinematic error only, ignoring motion of the reference point due to mechanical deflections of the contacts upon application of the preloads and/or disturbance forces. For simplicity, measurement error was not included here.

3.7.1 Variable Dimensions

The interchangeability model of the three-pin interface considers manufacturing variation in the following dimensions:

1. Positions of the pin mounting holes in the top interface plate, with variations expressed as diameters of circular tolerance zones scaled linearly from the centroid of the triangle of nominal pin locations. This is the same treatment as for the mounting holes for the canoe balls, with h_{tol} in [mm/m].
2. Radii of the pins [r_{pin} , mm].
3. Thicknesses of the pins [t_{pin} , mm], when shouldered pins are press-fit to the holes in the top interface plate.
4. Thickness of the top and bottom interface plates [t_{tol} , mm/m].
5. Positions of the vertical contact surfaces in the bottom interface plate. As directly machined features, these are treated the same as the holes in the top plate, assigning h_{tol} in [mm/m].

3.7.2 Interface Calibration Process

Note that unlike the canoe ball interface, where placement error of the couplings and form error in placement of the measurement feature and contact points are separate components of the model, the three-pin interface is modeled solely through direct measurement of the contact locations. Planar surface fits of three or more measurement points with a touch probe, or spot surface measurements with a tracked reflector, can locate the vertical contact surfaces in the bottom plate by assigning a base point and a normal vector. Circle fits to the pins mounted to the top plate can locate the pin centers and measure their radii. Planar surface fits to the horizontal contact surfaces (plate surfaces or pin shoulders) on both plates can assign a z-position to each contact.

Hence, direct measurement of the contact points and surfaces enables full interface calibration to significantly remove the dependence of interchangeability on placement error and form error of the couplings, notwithstanding the error of the measurement system. Table 3.5 lists the complexity levels of calibration for the three-pin interface, where F_{base} and F_{pin} are centroidal frames defined in the same manner from three measured Cartesian positions as F_{ball} and F_{groove} were before.

Complexity	Example Calibration Procedure	Measurement Knowledge
0	Measure nothing - assume fully nominal placement	$T_{interface}$ is identity transform between F_{base} and F_{pin} . Perfect nominal deterministic match.
1	Measure vertical and horizontal contact surfaces in baseplate: - Multi-point plane fits using touch-trigger probe CMM (e.g. fixed 3-axis multi-DOF FARO arm) or spot plane measurements using tracked reflector.	Contact locations define F_{base} , from which $T_{MS-base}$ is defined. Calculate $T_{interface}$ using measured base contact positions and assuming nominal pin contact positions in the top plate.
2	Same as (1), plus: Measure radii and center positions of pins in the top interface plate: - Multi-point circle fits using touch-trigger probe or continuous circle fits using tracked reflector.	Contact locations define F_{base} , from which $T_{MS-base}$ is defined. Pin locations define F_{pin} , from which $T_{interface}$ is defined assuming nominal pin contact heights.
3	Same as (2), plus: Measure relative heights of horizontal contacts around pins.	Full interface calibration.

Table 3.6: Calibration options for three-pin interface.

3.7.3 MATLAB Model Structure

The routine structure of the MATLAB model for three-pin interface interchangeability is almost identical to that of the canoe ball interchangeability model. All code is given in Appendix C, with the master routine *pincalibrate.m* driving the simulation, and the secondary routine *pintransform.m* calculating the interface transformation based on the level of calibration of the base contacts and pins. The *pincalibrate.m* routine takes the command line argument:

```
function [TCPerror, rmsavg] = pincalibrate(numruns, caltype)
```

Here, the input and output parameters hold the same definitions as for *kincalibrate.m*, and all geometric parameters of the interface and values of the error parameters are set by editing the values specified in the scripts.

This model is used in the next chapter to simulate the interchangeability of a three-pin interface for an industrial robot base.

3.8 A New, Interface-Driven Machine Module Calibration Process

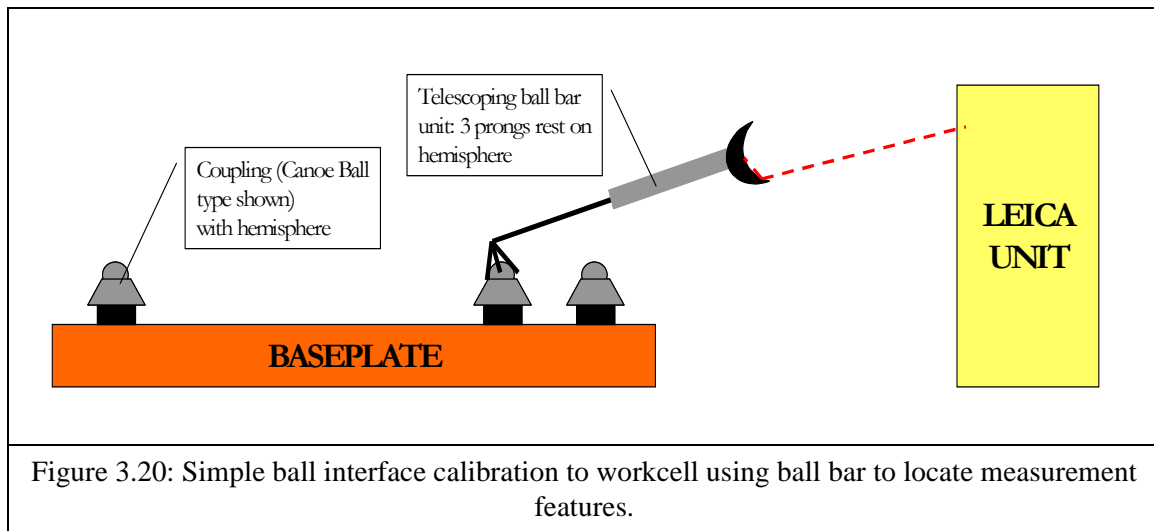
The work of this chapter simulates the ability to achieve near-perfect interchangeability of modular machine components using pre-calibrated kinematic interfaces. While exact-constraint kinematic couplings, namely the traditional ball-groove and canoe ball-groove types, were previously known mainly for their unprecedented repeatability, now interchangeability becomes a deterministic design parameter through introduction of the kinematic interface transformation. When interfaces are pre-calibrated by encoding the coupling positions and orientations with respect to individual interface plates, any combination of plates can perform with consistent, predictable accuracy when $T_{interface}$ is calculated and added within the serial kinematic chain of the machine's position. With simple calibration, interface interchangeability is not dependent on the manufacturing errors in the possibly large interface plates or in fitting of the couplings, but is instead more well controlled within the small error loop from the measurement feature to the contact point.

Hence, the interface transformation becomes sort of a universal kinematic handshake between interfaces with balls and grooves in different positions, and enables a conceptually new interface-centric calibration process for modular machines wherein:

1. Interface halves are pre-assembled and encoded with their coupling calibration information, relative to their centroidal coordinate frames.
2. These calibrated interface halves are attached to machine modules, and if necessary the modules are calibrated by mounting the assembly to a reference mating interface half. The coupling parameters of the reference interface is known; hence a calibration $T_{interface}$ is known.
3. When the machine modules are brought to the production installation site, the production $T_{interface}$ is calculated from knowing the coupling parameters of both production interfaces. A correction is applied to the machine module calibration for the difference between the calibration $T_{interface}$ and the production $T_{interface}$.

The last step is an essentially automated routine executing the interface transformation algorithm presented here; hence calibration online is conceptually non-existent with respect to the interface's contribution to the placement of the point of interest, and installation is "plug-and-play".

In addition, the innovation of the integrated measurement feature on the coupling half enables easy pre-installation of interface halves before installation of machine modules. For example, if a machine is to be kinematically mounted to a factory floor, the bottom interface half can be secured to the floor prior to arrival of the machine. Using the measurement features on the floor-mounted couplings, the centroidal frame of the floor interface can be used as a calibration reference for work objects in the cell. Hence, the fixtures and other equipment in the cell can be referenced to the base interface frame before the machine is installed, and the machine can be installed with respect to the base interface frame. Since $T_{interface}$ is known deterministically, the complete serial chain from the tool point to the work location can be found without physically calibrating the machine to the work tooling. Incidentally, the base interface frame could be assessed rapidly using a ball bar to locate the spherical measurement features integrally machined with the canoe balls, with respect to a laser-tracking measurement system, as shown below.



The ability to parametrize the interchangeability in terms of the random error components of the interface enables well-guided error budgeting of the interface manufacturing and calibration processes. One can only choose what is necessary to achieve the desired accuracy, which may be a decision to accept large manufacturing variation and measure the coupling placements, enforce low manufacturing variation in the plate and assembly processes and to not measure coupling placement, or enforce 'medium' variation and perform partial calibration. With the model here, these decisions can be made with best guidance, and

appropriate calibration procedures can be designed to provide the required accuracy given the capability of the interface manufacturing process. For example, if interface halves are made in high-volume, a specialized fixture with balls or grooves in free rotation and instrumented with single-axis linear and angular encoders could measure the relative positions and orientations of the opposite set. This measurement fixture would have higher accuracy than a non-contact system such as a laser tracker, reducing the impact of the caveat that the inherent error of the measurements would only be amplified to a tool point farther from the interface centroid than the couplings themselves.

The design of such a deterministic interface is well related to the principles of robust design, as a way of reducing the sensitivity of accuracy at the tool point to variation in the mounting interfaces, rather than reducing the variation in the interfaces themselves. This is exactly the idea of kinematic couplings - geometric averaging decreases the sensitivity of the system interface to individual component variances, and beyond that the deterministic behavior of the contact enables the remainder of the uncertainty to be filtered. The kinematic coupling interface is robust to the varying interface variables; the interface variables are measured, and the relationships between them are known. Between the interfaces, the variances of the linking components are no longer important to the system accuracy. The key determinants of the system accuracy are the variances between the measurement features and the primary locating features, which are comparable to the accuracy of state-of-the-art industrial measurement systems.

3.9 Conclusions and Future Work Plans

The work of this chapter is a straightforward extension of existing kinematic coupling theory to assess the mechanical interchangeability of interfaces for applications to modular machines where high accuracy at the tool point is needed in a fashion of rapid interchange. The parametric model for the canoe ball interface is a simple example of a method of how to use interface calibration and the interface transformation matrix to reduce error at the tool point, and predict interface interchangeability when distribution parameters for random manufacturing errors are known. The introduction of the integrated measurement feature makes inheritance of the centroidal frame of a triangular coupling set straightforward using standard measurement tools, and facilitates calibration of workcell objects directly to the interface. Such use of the kine-

matic interface as a mechanical handshake between components can make machine calibration independent of cell calibration, perhaps decoupling the applicability of machine work simulations from the often necessary condition that tool-to-workpiece relations be nearly identical between the real and virtual worlds.

As the parametric model of interchangeability is presented here for the canoe ball interface, and three-pin interfaces, extensions can be made to other types of kinematic interfaces including quasi-kinematic couplings. For quasi-kinematic couplings, the static interface transformation would be the minimum energy solution of the interface mating problem, considering the true positions of the contactors and targets. However, due to plastic deformation of the quasi-kinematic contactors or targets, the accuracy of the interchangeability model would degrade after a handful of repeated mounting cycles. Furthermore, the error detail of the model could be extended by considering mechanical deflections of the canoe ball interface under static preloads and dynamic disturbances, which were neglected here because of small order. In a parametric sense, an end-to-end model for all kinematic couplings could result; incorporating a wide range of tolerances, coupling types, and associated cost information, a cost-accuracy relationship for kinematic interface design would be formed. Mathematically, this could also extend to optimal geometric design of the interface, such as finding the optimal coupling placement angles to minimize the interchangeability error.

This interchangeability study gives positive implications for design of modular robots, instrumentation structures, and other structures that would benefit from separability but demand high accuracy on component interchange. Furthermore, standardization of a kinematic interface between equipment from different manufacturers and recognition of common interface design and performance parameters could improve flexibility of assembly operations with especial benefit to low-volume processes needing reconfigurable, quick-change style-differentiated tooling.

Chapter 4

Machine Case Study: Mechanical Performance of a Quick-Change Industrial Robot Factory Interface

This chapter applies the previously discussed kinematic coupling design, repeatability, and interchangeability theory to development of a new factory interface for base mounting of industrial robots, used primarily in automotive body assembly welding, sealing, and material handling. Because of the extreme forces and torques at the manipulator base during robot operation and the critical nature of interface stability, design choices are restricted to large-radius canoe ball couplings, and quasi-kinematic alternatives with larger contact areas. When the relative positions of the contact points are pre-recorded and the interface transformation is calculated, use of a kinematic base interface is a step toward installation of a replacement manipulator without need for online recalibration. The calibrated kinematic couplings reduce the resultant error at the tool center point (TCP) by over 85% relative to the best current design. This improvement is demonstrated through tests of a prototype interface for the ABB IRB6400R 150kg payload industrial robot.

4.1 Background and Problem Definition

Over the past three decades, advances in mechatronics, as well as increasing demand for high-precision, high-volume, heavy-duty manufacturing processes, have made use of robotics in industrial assembly commonplace. At the large scale, industrial robots are used most frequently in the automotive body shop, where in a single passenger vehicle or light truck plant, more than three hundred robots can be used for material handling, body sealing, sheet metal welding, and general assembly operations. Notwithstanding extreme competitive pressures in manufacturing efficiency and quality, minimizing production interruptions due to failures of automation is an a-priori objective, especially when a production facility is running at full scheduled capacity. For example, one minute of downtime of an average (60 JPH) automotive body shop costs at least \$10,000 to the manufacturer, in terms of unscheduled overtime wages paid to account for lost production. Here, reliability and flexibility of automation are sought to make production processes more efficient and reduce direct and indirect costs of automation installation, replacement, and repair.



Figure 4.1: Six-axis industrial robot manipulator commonly used in automotive assembly (ABB IRB6400R).

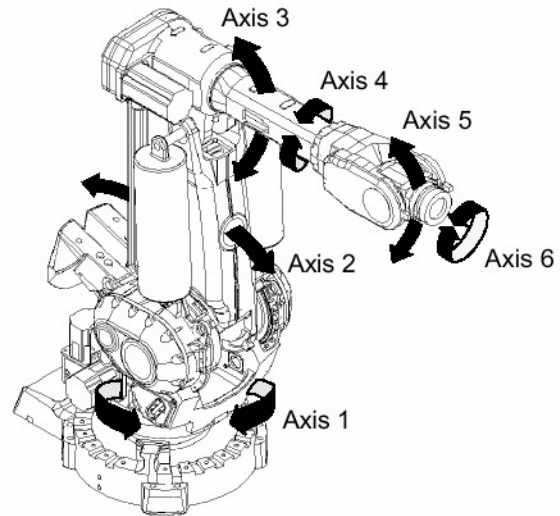


Figure 4.2: Nomenclature of ABB IRB6400R's six revolute axes [1].

In automotive assembly, industrial robots are installed at first construction of a facility, and replaced at regular intervals of 5-7 years, or following catastrophic failure during production. If necessitated by a coincident end of the life cycle, or if simply convenient in being near the end of the life cycle, robots are also replaced when a facility is re-tooled to accommodate a product change. If the product architecture is drastically different or if the production layout is changed, robots are not mounted in the same places as before. Furthermore, if a new robot manufacturer is chosen, a different working envelope or manipulator size will independently dictate a change of the mounting base.

The approximate \$80,000 cost of a new manipulator package is divided about equally between equipment and installation, and about one-quarter of the installation portion is for online programming, touch-up, and calibration. Furthermore, catastrophic (greater than 20 minutes of downtime per failure) robot fail-

ures empirically cause a per shift average of approximately 5% downtime, equaling twenty-five minutes and \$250,000 in unscheduled overtime per occurrence.

After installation and calibration are completed, robot operation involves control of the manipulator to repeated execution of a planned work task. When the manipulator is directed to a point in its workspace using this programmed plan, the real position of its end-effector always differs from the programmed (simulated) position. The main sources of this error are:

1. Gravitational effects on the gearboxes and structure, causing positional offsets of the revolute joints.
2. Inherent accuracy limitations of the calibration methods and the non-repeatability errors in the system.
3. Manufacturing tolerances on the components, resulting in slight misplacement of the interfaces from their nominal mating positions (e.g. exact alignment of mounting holes in foot to those in floor).

The positional offsets of the joints are corrected by directing the manipulator to a large number of points throughout its workspace, and synthesizing error coefficients for each joint using inverse kinematic relations for the serial chain. Determined at the robot factory, these coefficients are entered into the robot controller after line-side installation as a unique calibration signature for the manipulator. Clearly, the accuracy of the joint corrections is determined by the accuracy of the measurement system, the second source of error. Here, improving the accuracy and repeatability of the measurement system reduces the positional offset. Currently, laser-tracking measurement systems (e.g. the Leica LTD500), which use a motorized laser head to track the position of a retroreflector mounted to the manipulator, are used in calibration. The Leica LTD500 is accurate within 0.01 mm per meter from the retroreflector to the tracker head [2].

This work seeks to propose and validate a new, quick-change method of mounting industrial robots to the factory floor, using a pre-calibrated exchangeable kinematic coupling interface, with one set of coupling halves on a standard, floor-mounted baseplate and the other set on the manipulator base. By improving the dimensional accuracy of the robot replacement process through the use of the deterministic, repeatable, and exchangeable kinematic coupling interface, and through greater robot accuracy from software-based calibration routine in general, the following major advantages are envisioned:

1. A decrease in robot replacement and installation time, by reducing the need for online touch-up of part programs transferred from the prior manipulator or generated through simulation (initial installation).
2. An improvement in part dimensional quality, by increasing the margin of tool placement error that can be directly calibrated through the kinematic chain of the manipulator. This is especially salient for continuous path applications, which have higher dimensional requirements ($< 0.5\text{-}1\text{ mm}$) than spot welding ($< 2\text{-}3\text{ mm}$).
3. Encouragement of a paradigm for standardization of factory interfaces using kinematic couplings. If the same interface is used by different robot manufacturers, true interchangeability, flexibility, and compatibility of different manipulators will be realized. The mating behavior of the interface and representation of calibration data shall be independent of the equipment type or configuration. In a programming sense, the mechanical interface should be object-oriented.

Recall that a kinematic coupling interface improves the accuracy of mounting for two reasons: first, the triangular arrangement of coupling averages the geometric errors of the interface mounting locations; second, measurement of the coupling positions and orientations enables inclusion of the interface error transformation as a static component of the serial kinematic chain. This transformation shall be uniquely calculated from the positions and orientations of the couplings on the floor plate and the manipulator foot as a function of the on-line startup and calibration software. In this respect, inverse kinematic calibration of the revolute axes can be performed when the manipulator is mounted to a master baseplate at the robot factory, and correction to the true mounting position can be made by including measurements of the positions and orientations of contacts on the final mounting plate at the line site. The calibration data for the individual production mounting plates are measured and identified to (perhaps stored on) each plate by the plate manufacturer.

The goal of this study is to design and validate feasibility and mechanical repeatability of the kinematically coupled robot-to-factory interface. Mechanical interchangeability, which would require construction of a series of interfaces for testing that is too cumbersome and costly for a first prototype test, was simulated using the computer interface models presented in Chapter 3. For the project, ABB recommended an upper limit on the contribution of the kinematically coupled base interface to the TCP error at robot interchange, equaling 0.1 mm . Considering current interchangeability metrics of approximately $0.5\text{-}1\text{ mm}$, this is superior to many customer expectations and needs; however as process quality requirements tighten and robots are designed to carry larger and heavier payloads, the demands will become more stringent.

4.2 Current Interface Design and Robot Installation Procedure

The heavy-duty manipulator factory interface redesigned by this project holds the manipulator in place by bolts into a floor-mounted plate with threaded holes, or by bolts into a set of floor-mounted threaded anchors. Traditionally, between three and eight bolts are tightened through clearance holes in the manipulator foot. In some cases, when the manipulator is mounted to a floor plate, a pair of up-pointing hardened steel pins in the plate are manually seated into the foot to lock its position, and the bolts are tightened gradually and periodically until a specified tightening torque is reached.

This method, sometimes aligning the manipulator using dowel pins, and then tightening it to the floor using a set of bolts, overconstrains the interface. Because of manufacturing tolerances in the pin placements and mounting hole positions, the dimensional accuracy of the TCP with respect to the mounting location is highly sensitive to the angle at which the manipulator is contacted to the floor, the in-plane force with which the pins are engaged or the bolt holes are aligned directly, and the order in which the bolts are tightened. It is especially difficult to place the manipulator foot parallel to the floor for mounting, since it is usually held by a several of straps to an overhead crane, likely attached at a slight offset from the manipulator's center of gravity, or placed by a forklift.

4.2.1 Existing Base Designs and Interchangeability Performance

The existing three-point bolted foot of the ABB IRB6400 manipulator and the four-point bolted foot of the ABB IRB6400R manipulator were benchmarked. First, the foot of the 6400, shown in Figure 4.3, features three 32 mm diameter holes placed in an equilateral triangle with corner-to-centroid distance of 400 mm. The manufacturing specifications place 3-sigma tolerances of 0.10 mm on the mounting hole placements and the parallelism of the up-down mounting surfaces around the holes. While it was not possible to measure the mechanical interchangeability of manipulators with this interface, a static geometric tolerance analysis gave a worst-case interchangeability of 0.79 mm and root-sum-square interchangeability of 0.66 mm. Taking the average of these values, the interchangeability (distance error measured at the TCP) of the three-point bolted interface is 0.73 mm, far exceeding the design goal of 0.10 mm.

The four-point bolted foot of the ABB IRB6400R is diagrammed in Figure 4.4 and shown in Figure 4.5. This foot is positioned by engaging the two alignment pins in a floor-mounted baseplate to precision

holes in the foot, and anchored by tightening eight 20 mm bolts. The bolts rest uniformly 400 mm from the axis one of the manipulator. Manufacturing specifications place 3-sigma tolerances of 0.12 mm between the opposite hole locations, and of 0.10 mm on mounting surface parallelism



Figure 4.3: Three-point manipulator foot (ABB IRB6400).

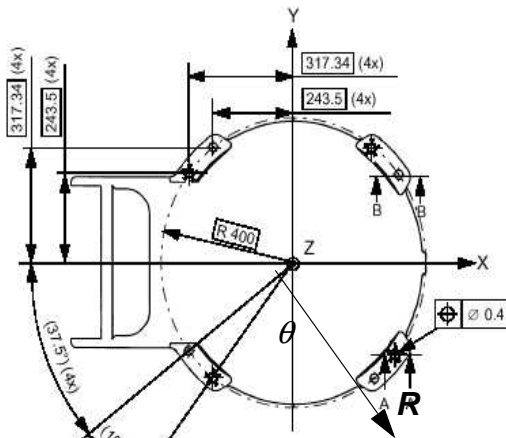


Figure 4.4: Schematic of four-point manipulator foot (ABB IRB6400R) [1].

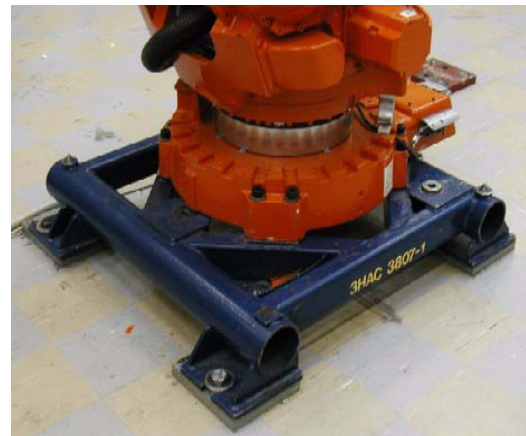


Figure 4.5: Four point, eight-bolt 6400R manipulator foot mounted on test pallet.

4.2.2 Current Robot Calibration Procedure

The high accuracy of the kinematically coupled interface can streamline the calibration process that follows manipulator installation. The current calibration process for the ABB IRB6400R is as follows:

1. At ABB, the manipulator is bolted to the floor in a cell with the Leica LTD500 laser-tracker positioning system in place.
2. The robot is moved to approximately 100 joint references throughout its workspace, with the Leica system measuring each location with respect to its own coordinate system using a retroreflector mounted at the end of the sixth axis.
3. The inverse kinematic signature of the robot is calculated, based on the solution to the Jacobian equation system. This also determines the frame relationship between the measurement system and base.
4. The error coefficients are loaded to the robot controller, and the reflector is manipulated to an additional 50 positions (cartesian references) to verify robot accuracy. The calibration is accepted if 95% of non singular positions are less than 0.1 mm from the desired positions.
5. The robot is shipped to the customer site. A cell alignment is performed by measuring 10 points (cartesian robot references) and aligning the Leica base coordinate system to the robot base coordinate system. Inherent in the procedure is an error indication for the 10 points. The tooling and other work objects in the cell must be similarly aligned, and the TCP of the end-effector, which is often installed at the line site, must be determined.
6. The robot program, generated offline, is loaded to the controller, and the robot is slowly run or stepped through the program sequence, performing the production operation with prototype or production parts in the tooling. If part quality is insufficient, the program must be manually touched-up online to correct for the dimensional error translated in mounting the robot.

A kinematically coupled interface has greatest potential to minimize or eliminate time spent performing steps five and six. If the coordinate relationships between the floor-mounted coupling plate and the in-cell work objects are measured and recorded prior to manipulator installation, there should be no need to align the robot to the cell upon installation. Furthermore, if the kinematic error transformation between the floor plate and foot is known, the full transformation from the tooling to the robot end-effector can be calculated by the controller, and the planned joint values in the path program generated by simulation can be corrected based upon this transformation. Note that error may remain at the interface between the end-effector and the axis-six tool-mounting flange however, with a smaller interface size, direct offset and Abbe error contributions will be much less than for the base.

In considering the existing designs, interchangeability performances, and example calibration process, some manufacturers are able to manufacture the robot foot with accuracy sufficient to enable full re-mounting without program touch-up. While this solves the problem of interchangeability, it still requires full robot-to-cell calibration upon installation, leading to expensive downtime by requiring the setup of a measurement system in the cell. Decoupling the cell calibration from robot calibration using the kinematic interface can help solve this problem.

4.3 Customer Attitudes Towards Interface-Based Modularity

The desirability of the modular factory interface solution is determined in large part by two factors: the accuracy requirement of the application and the end user's robot replacement strategy. For the first factor, on the one hand, some users replace robots in batches near the predicted end of their usable life cycles, and hence suffer few severe breakdowns during production that require replacement of the entire manipulator. On the other hand, some don't schedule batch replacements, and instead replace robots station-by-station and individually when the robots fail catastrophically (or begin to require inordinately excessive maintenance). Clearly, the modular base would be more attractive to the latter set of customers, who would be performing more random robot switches, hence requiring a strategy for rapid replacement. The customers who perform batch changes are likely to schedule these operations during planned downtimes, and can therefore take the extra time for full placement and calibration without penalty to production operations.

When a robot fails catastrophically during production, typically due to an internal mechanical malfunction (e.g. sensors, gearboxes, or drives) or a collision with an object in the workcell, the decision of whether to repair the manipulator or replace it is logically based upon the estimated time of repair. If the estimated time to repair exceeds the estimated time of replacement, the manipulator is replaced. Three manufacturers interviewed place this breakpoint at between two and four hours. If the kinematic solution can reduce the replacement time by improving the efficiency of calibration toward a "plug-and-play" standard, manufacturers will be willing to replace manipulators and repair broken ones offline. With lean manufacturing techniques leading to more linear body shop layouts to improve reconfigurability and material flow, it is becoming easier to replace a manipulator during production. Furthermore, while current interchangeability values of 1 mm are appropriate for spot welding applications, improved accuracy is gener-

ally demanded for continuous path applications such as body joining, body sealing, and arc welding. In point-to-point spot welding or painting applications, quality is often sufficient if the spot is placed within a 1-2 mm neighborhood of the nominal location. However, body architecture is changing to include more tubular aluminum frame parts, which are continuously arc brazed together; accordingly, frame welding is the most critical of body assembly applications, and improved interchangeability would be most beneficial here.

As part of a grand absolute accuracy strategy for robot positioning, it was stated that the optimum future solution for maintenance is to use mechanically interchangeable parts, without the need for re-calibration. Use of a measurement system to fully re-calibrate the robot with respect to the work objects and touch-up the path program can result in maintenance time of six to twelve hours, compared with one half hour at most for mechanical exchange. If a measurement system were efficiently integrated into the robot cell then this could also be an effective solution, but this would at least double the fixed equipment cost for the robot package. Manipulator exchange times under these varying levels of required calibration are listed in Table 4.1.

Alternative	Burdens	Exchange Time
Pre-calibrated manipulator - no calibration online	- (None)	2-4 h
Partial calibration online (moderate touch-up)	- Laser measurement system - Personnel trained for calibration	4-8h
Full calibration online	- Laser measurement system - Personnel trained for calibration	6-12h

Table 4.1: Manipulator exchange times under varying levels of on-line calibration.

Based on this sample, exchange of a pre-calibrated manipulator saves an average of six hours, or \$3,600,000 in unscheduled shop overtime (assuming a single serial flowpath). In any case, the customer choice of a replacement strategy is a cost-performance trade-off, framed in terms of general manufacturing strategy toward flexibility and constraints of facility layout and inventory space. While full manipulator exchange is a rare maintenance task, this survey has shown a demand for a quick-change solution among major automotive manufacturers.

4.4 Quick-Change Interface: Applied Kinematic Coupling Design Process

Beyond the conceptual shift of using a pre-calibrated factory interface and hence decoupling cell calibration from manipulator calibration, mechanical design of the components is a straightforward application of the kinematic coupling design theory for high load applications presented in Chapter 2. This section summarizes the design calculation results for three prototype coupling sets: canoe ball mounts, three-pin mounts, and quasi-kinematic groove/cylinder mounts.

4.4.1 Load Conditions

With the design manipulator accepting a payload of up to 150 kg, and having a maximum linear tool speed of several m/s, the resolved dynamic forces at the base represent the foremost boundary condition to the kinematic coupling design. Table 4.2 lists the loads for the ABB IRB 6400R design manipulator. Each load case is a six-tuple consisting of three forces acting along orthogonal axes, and a moment acting about each of these axes. The operation case is the maximum simultaneous disturbance that the base will experience during a maximum payload cycle at maximum speed, and the emergency stop is the peak effect of initiating maximum deceleration from the operation point.

	<u>Operation</u>	<u>Emergency Stop</u>
Force - x [kN]	9.9, -9.9	26.9, -26.9
Force - y [kN]	9.9, -9.9	26.9, -26.9
Force - z [kN]	5.0, -11.0	16.0, -22.0
Torque - x [kN-m]	24.0, -24.0	43.1, -43.1
Torque - y [kN-m]	24.0, -24.0	43.1, -43.1
Torque - z [kN-m]	7.0, -7.0	15, -15

Table 4.2: ABB IRB6400R dynamic loads at center of foot (max, min).

Considering the extreme forces in the design case, and the known trend toward higher payload capacity in future manipulator designs, the following design guidelines were established for the kinematic couplings:

1. Select preloads sufficient to prevent load reversal under the operation and emergency stop cases.

In the canoe ball case, design a preload to prevent reversal under a tensile emergency stop, yet still prevent yield under a compressive emergency stop.

2. Complete all designs with a safety factor of 1.5 against Hertzian contact pressure failure in the couplings, under all load cases.

3. Complete all designs with a safety factor of 3.0 against static failure in the bolts, under all load cases.

4. Complete all within the regime of infinite fatigue life for all components, considering tens of millions of potential cycles throughout the life of the robot.

4.4.2 Evaluation of 3/4-Scale Canoe Ball Base Model

Before designing and procuring the full-size prototype couplings for the factory interface, a scale model of the canoe ball design was built and tested statically using ABB's production robot calibration measurement system. In terms of the coupling placement relative to the triangle centroid, the model was a 3/4-scale version of the 3-point canoe ball adaptation to the 6400R, with 420 stainless steel couplings with 250 mm surface radius and 20 mm shank diameter (these were on hand for a separate project). The couplings were press-fit and aligned using 3 mm slotted stainless steel spring pins, to 3/4" 6061-T651 aluminum plates.

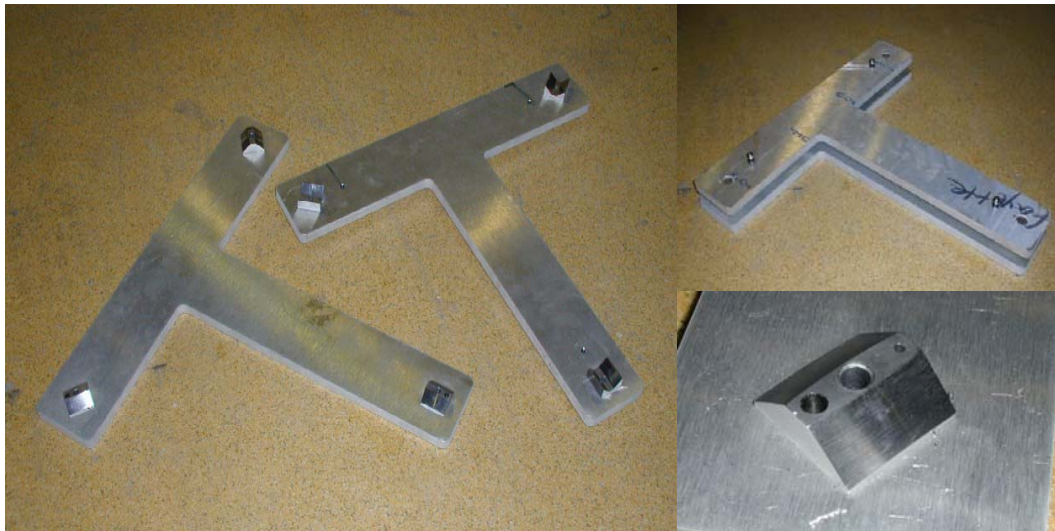


Figure 4.6: Scale prototype canoe coupling interface, with 3/4-scale placement relative to the full-size design.

Measurement of the interface repeatability was achieved by press-fitting 1/2" diameter shanked tooling balls near the couplings, facing upward from the assembly. Then, the repeatability was expressed in terms of that of the centroidal frame based upon the repeatability of the tooling ball placements when the top plate was disengaged and then reengaged from the bottom plate. Repeatability was measured using a Leica LTD-500 laser-tracking measurement system, shown in Figure 4.8. Each tooling ball was located using a hand-held spherical retro-reflector; the reflector was placed on the tooling ball surface and moved gently until the tracking head obtained an accurate minimum error spherical fit. The LTD-500 has repeatability of 0.01 mm (10 microns) per meter from the retro-reflector to the tracking head.



Figure 4.7: Tooling ball reference sphere.



Figure 4.8: Leica laser tracker with retro-reflector in calibration seat.

From a standpoint of functionality, the scale interface demonstrated the ease of seating the canoe balls precisely; the plates could be separated and replaced in partial contact with significant misalignment, and slide to the nominal full contact position very easily. This was important knowing the difficulty of precise initial seating of the manipulator on its base rests.

The repeatability of the measurement system was estimated to be 0.15 mm from ten successive measurements of the ball positions obtained without unseating the plate. From fifty successive procedures of

unseating, reseating, and measuring (via the tooling balls) the top plate, the RMS repeatability of the centroidal frame was 0.19 mm. Hence, nearly all the error in repeatability could be attributed to the measurement system, making the true coupling repeatability more than adequate for an application with this order of measurement accuracy. Incidentally, had these measurements been made with a repeatable preload greater than the self-weight of the interface, the coupling repeatability would likely have been even higher, since there would have been a greater restoring force to overcome frictional resistances between the balls and grooves.

4.4.3 Manipulator Interface Plate Design

To make the prototype design easily adaptable to the existing ABB IRB6400R, the couplings were designed to mount to the foot using an intermediate interface plate. The top interface plate accepts the balls (or pins) and mounts to the robot foot, and the bottom interface plate accepts the grooves (or provides engagement surfaces for the pins) and mounts to the floor. The top interface plate functions to convert the eight-bolt four-point mounting of the 6400R to the chosen three-point kinematic coupling configuration by bolting to the foot through the traditional eight mounting holes and accepting the couplings by a light press fit. The bottom plate accepts the mating three couplings through appropriately sized holes, and includes a pattern contact surfaces for the three pins. The interface mounting and engagement methods for each coupling type are detailed later. The plates were machined from standard mild steel. Each is 1.2 m square. the top plate is 40 mm thick and the bottom plate is 60 mm thick.



Figure 4.9: Prototype steel interface plate to manipulator foot - top side.



Figure 4.10: Prototype steel interface plate to manipulator foot - bottom side.

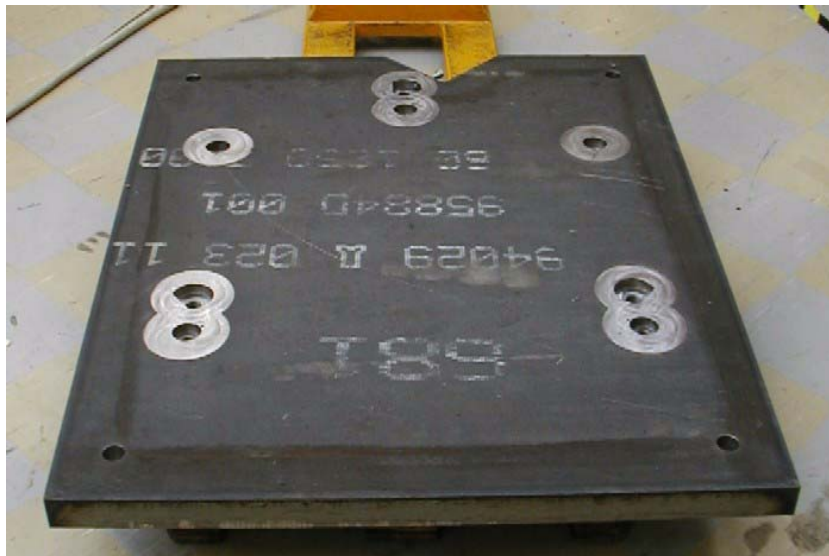


Figure 4.11: Prototype steel interface plate to manipulator foot - top side.

Although dynamic tests were not run on the prototype interface system, mechanical analyses confirmed that the interface dynamics would not affect the repeatability measurements or adversely affect performance of the manipulator. In the static case, the maximum load cases in Table 4.2 were applied to the top surface of the top solid body in Figure 4.12 representing the manipulator foot in the assembly shown. For the maximum fully-reversed operation load case, the maximum stress in the prototype interface model is 50.6 MPa, and for the maximum emergency-stop load case, it is 54.7 MPa. Both are well below the yield stress limits of the steel interface plates. The plate deflections were also studied, showing approximately 0.005 mm at the coupling points in the operation case, and 0.01 mm at the coupling points in the emergency stop case.

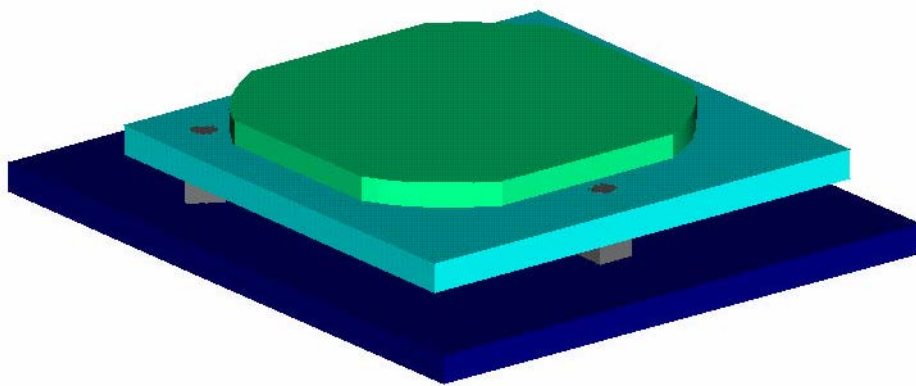


Figure 4.12: Solid model of interface assembly for static stress analysis.

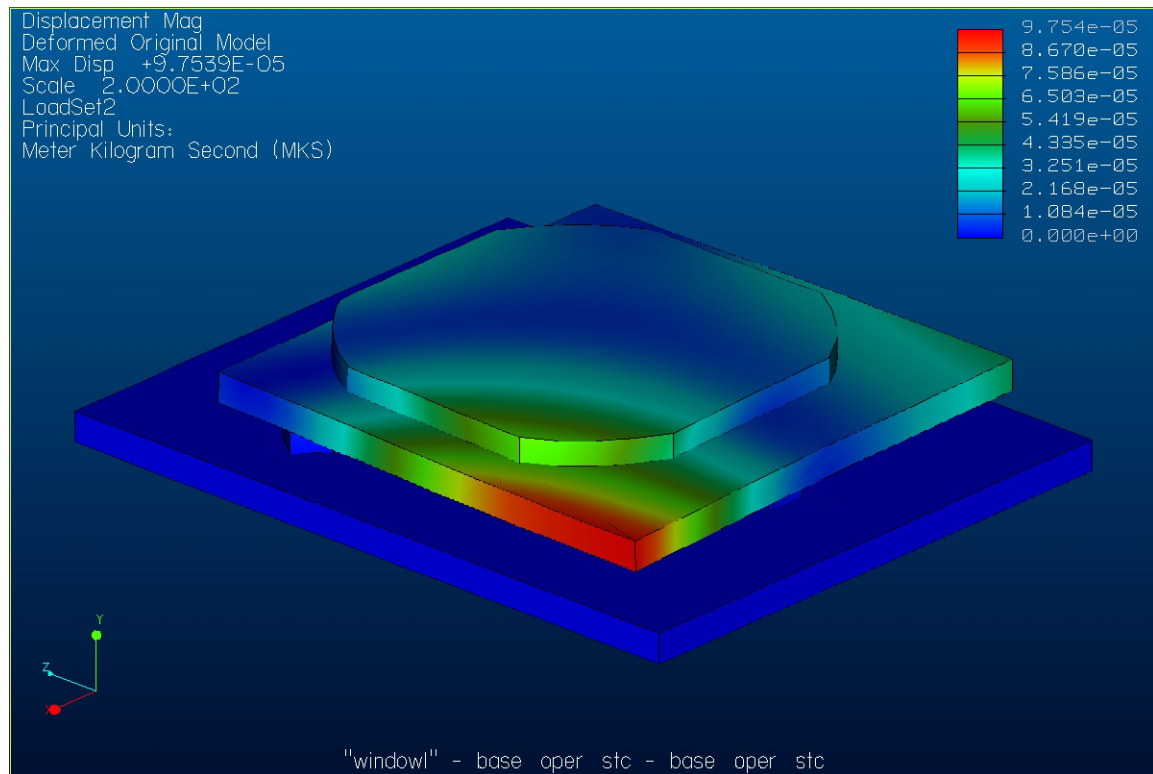


Figure 4.13: Deformation of prototype interface assembly under fully-reversed operation cycle loading.

4.4.4 Canoe Ball Coupling Design

As the sole coupling method considered in which the spot contact zones handle the full disturbance, the canoe ball couplings were designed considering the stability and strength of the coupling arrangement, subjected to the operation case and emergency stop case disturbance forces for the 6400R manipulator.

Recalling the discussion in Chapter 2, the process for designing the canoe ball couplings was to:

1. Determine the necessary preload to maintain stability, knowing the disturbance forces and the locations of the couplings.
2. Determine the ball surface radius necessary to support the preload throughout the disturbance force space, specifying a material for the couplings.
3. Verify the high-cycle performance of the interface based upon fatigue-life relations, choosing a different material if necessary. Recalculate the necessary surface radius if desired and re-check for durability.

For the first step, the coupling locations were specified to be outboard of the nominal foot mounting bolts, and placed along lines stretching from the manipulator's base axis (axis one) to the foot mounting bolts. Hence, the centroid of the coupling triangle was offset slightly from the rotation axis of the foot. The initial design parameters (including ranges) for the canoe ball couplings are given in Table 4.3. These were specified as inputs to the MATLAB code for kinematic coupling design presented in Chapter 2.

Location, coupling 1 - R [mm], θ [deg]	450, 90
Location, coupling 2 - R [mm], θ [deg]	500, 217.5
Location, coupling 2 - R [mm], θ [deg]	500, 323.5
Ball surface radius [mm]	500 - 750
Equivalent sphere diameter at same contacts [mm]	75
Downward preload force [N]	50000 - 250000

Table 4.3: Initial design parameters for canoe ball couplings

Since the contact force solution for kinematic couplings is that of a linear system, the disturbance space could be fully explored by examining all of its corner points. Hence, the first step was to solve for the contact reaction forces at each corner point of the disturbance space, incrementing the preload force until the contact force vector was fully positive at all corner points of the disturbance space. From this, the minimum preload was set to -130,000 N over each of the three coupling points, with the nearest limiting disturbance case being the six-tuple of $[F_x, F_y, F_z, M_x, M_y, M_z] = [-26.9, -26.9, -22.0, -43.1, -43.1, -25.0]$. Next, with the preload fixed, the ball surface radius was incremented until all the contact stress ratios did not exceed 0.67 (accounting for the factor of safety) at all corner points of the disturbance space. The appropriate radius was 0.55 m. The largest contact ellipse between the balls and grooves with preload and full emergency stop loading is approximately 20 mm in diameter.

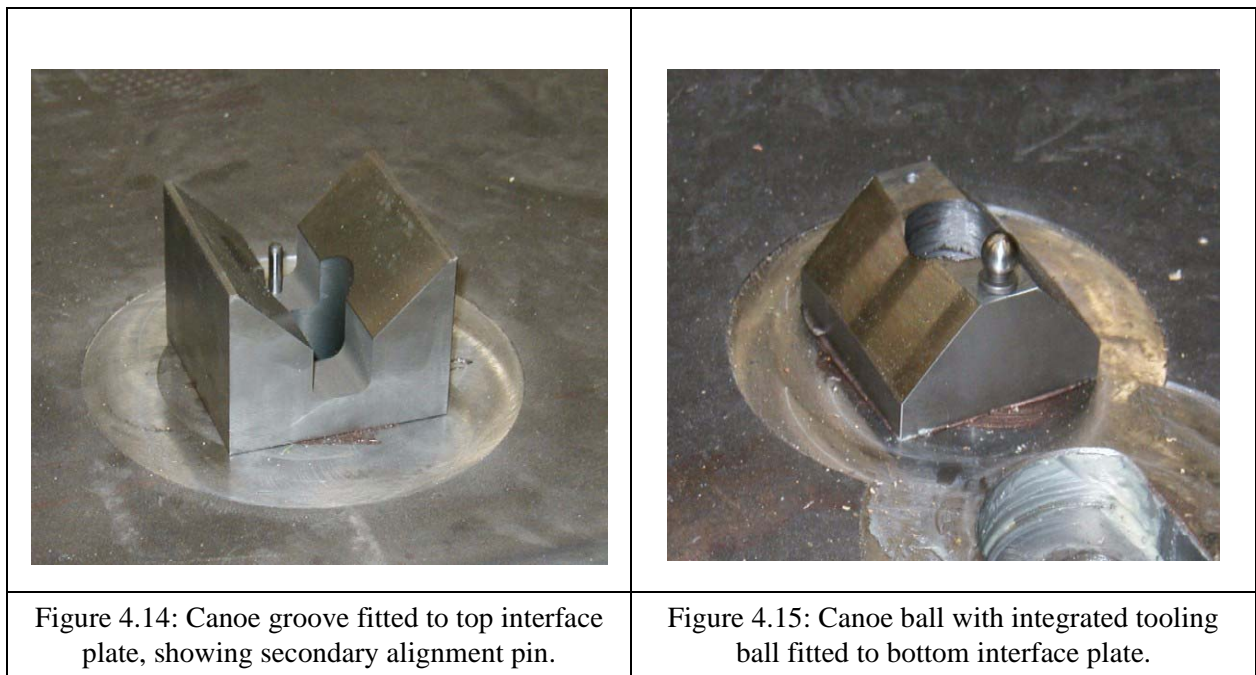
The final specifications of the canoe ball and groove mounts for the 6400R prototype, shown below, are as listed in Table 4.4. The couplings were blank CNC machined from AISI 420 stainless steel, hardened, then the groove flats and ball surfaces were precision CNC ground. To complete the assembly, a

hardened steel shanked tooling ball was press-fit to each coupling ball unit after the couplings were ground.

Material	AISI 420 stainless steel, hardened to RC 50-55
Ball surface radius [mm]	550
Equivalent sphere diameter at same contacts [mm]	75
Groove flat angle [deg]	45
Coupling plan length [mm]	100
Coupling plan width [mm]	100
Shank diameter [mm]	50
Thru hole diameter [mm]	32

Table 4.4: Final Specifications of prototype canoe ball coupling

With copper anti-seize lubricant applied to their shafts and insertion holes, the couplings were manually press-fit to the interface plates. Proper alignment was guaranteed by locking a 5 mm hardened steel alignment hole in a secondary hole through each kinematic element at the mounting location.



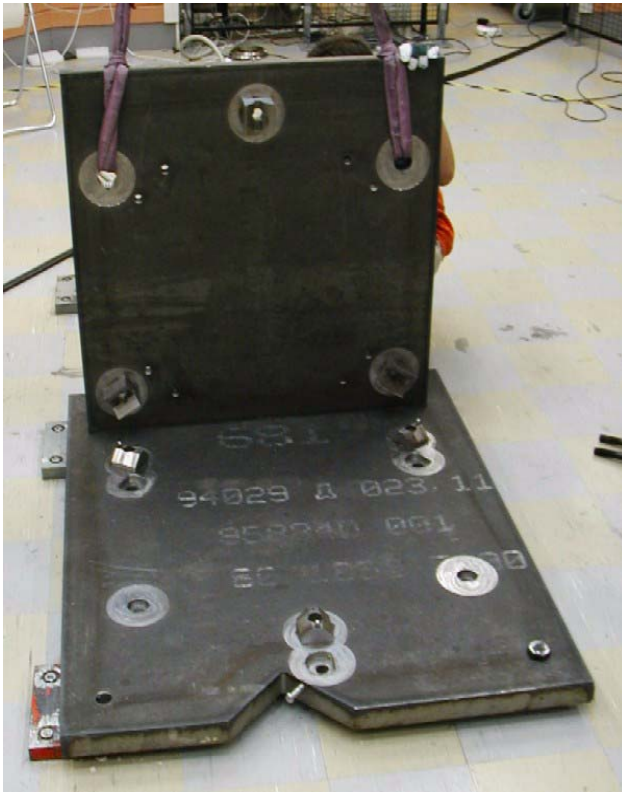


Figure 4.16: Interface plates fitted with canoe ball couplings.

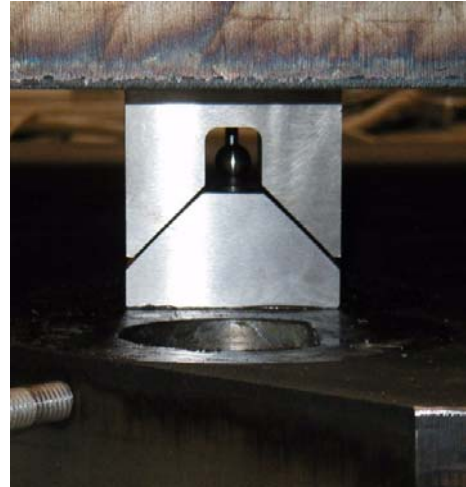


Figure 4.17: Mounted canoe ball joint with tooling ball.

4.4.5 Three-Pin Coupling Design

Next, the three-pin contacting couplings were designed with the major guidelines:

1. Choose the pin diameter and in-plane preload force to guarantee stability of the interface under the static weight of the manipulator.
2. Choose the bolt preload to guarantee sufficient vertical resistance and in-plane friction against the dynamic disturbances, without causing yield of the vertical contact surfaces.

The first choice was made using the frictional engagement model discussed in Chapter 3, specifying a static coefficient of friction of 0.15 between the pin surfaces and plate surfaces, and the approximately 22500 N static weight of the manipulator as the normal force. The geometric layout was specified to be the same as for the canoe balls, so both types of couplings could share the same hole set (with pull removal of

the press fit to exchange coupling types) in the top interface plate. The preload angle was chosen to be 45 degrees. The friction model gave the maximum necessary preload forces as listed by pin/surface contact case in Table 4.5. Hence, the seating would be guaranteed with 16.8 kN applied to the preloaded pin.

Pins in contact	Minimum preload for slip (kN)
(none)	3.7
1	6.1
2	11.1
3	16.8
1, 2	11.2
1, 3	7.2
2, 3	6.6

Table 4.5: Required preloads to pin interface in cases of partial contact.

The shouldered pins insert to the top interface plate and mate to flat contact surfaces on the perimeters of oversized clearances in the bottom plate. In this way, the robot could easily be lowered to clear the pins into the holes, and the preload could be applied to seat the interface in the deterministic interface position. The interface was designed to apply the preload through a bolt fixed to the bottom interface plate as shown below, and pushing the preload pin by applying the torque necessary to give the required axial force. This is achievable through 38 N-m of torque to an M12-1.75 bolt, which was specified at a final level of 50 N-m to guarantee seating under trial-to-trial variability in surface conditions.



Figure 4.18: Prototype shouldered coupling pin - side view.



Figure 4.19: Prototype shouldered coupling pin - perspective view.



Preload

Figure 4.20: Application of preload through threaded hole in floor interface plate.



Figure 4.21: Preload screw in prototype floor interface plate.



Figure 4.22: Shoulder pin fitted to top interface plate.

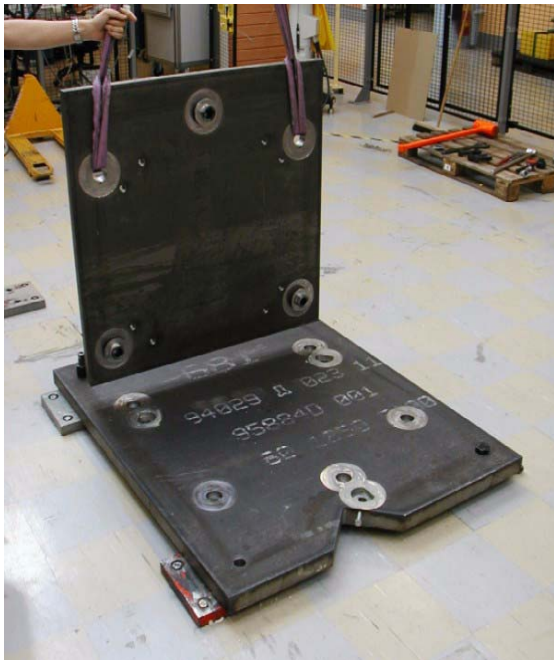


Figure 4.23: Interface plates fitted with three-pin couplings.

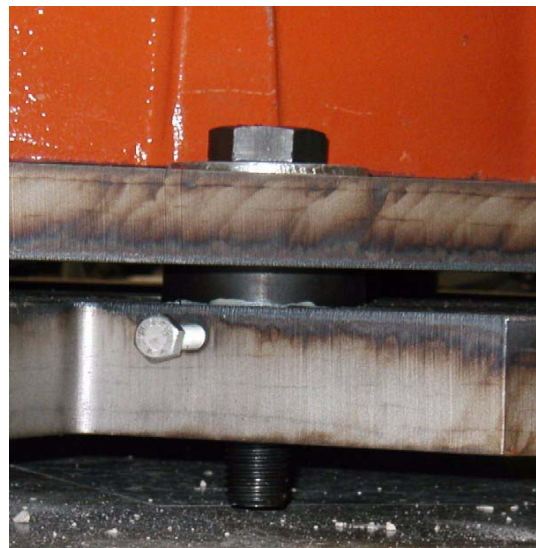


Figure 4.24: Mounted three-pin joint.

Knowing 50 N-m of torque would be applied to seat the interface, the chosen 50 mm diameter pin sizes were verified to offer an appropriate margin of safety against yield along their line contacts. Similarly, to maintain consistency of material and surface properties with the canoe ball couplings for comparison of results, the pins were machined from AISI 420 stainless steel, although a softer and less expensive material could have been chosen. The contact forces against each pin were calculated using the reaction force model presented in Chapter 2, and the Hertzian contact ratios at pins 1, 2, and 3 were respectively found to be 0.55, 0.57, and 0.57.

Finally, it was necessary to determine the minimum vertical preload at each of the pins to guarantee stability of the interface. Since the layout of the pins was the same as the layout of the canoe balls, -130 kN was used as an initial guess. After resolving the normal disturbances a compressive force is needed at each of the pin seats to provide in-plane frictional resistance against sliding of the pins from the equilibrium location. This was verified for the -130 kN value at all load combinations for operation and emergency stop loads, and actually no more than -100 kN was needed, but the -130 kN load was specified for consistency with the canoe ball case. Furthermore, because of the large contact area between the pin shoulders and floor interface plate, increasing the preload reasonable can only boost the margin of safety as long as the yield limit between the surfaces is not crossed.

4.4.6 Cylinder-Groove Coupling Design

The third type of prototype coupling for the base was simple placement of aluminum cylinders as kinematic locators between mild steel flanged vee grooves, press-fitted to the interface plates in the same triangular hole patterns as the canoe coupling balls and grooves. To minimize machining variety, the grooves were specified to be geometrically similar to the stainless steel grooves for the canoe balls, only with extended side flanges to bear contact stresses after the preload was applied.

As discussed in Chapter 2, the locating principle here is to use the twelve line contacts (four per cylinder) to near-exactly constrain the groove sets together in static mounting, and then apply an axial preload by tightening bolts that pass through the groove pairs and cylinders to elastically compress the cylinders and bring the groove flanges in contact. Like the pin shoulders for the three-pin coupling, the groove flanges bear the significant dynamic loads. For the prototype geometry shown below, a cylinder diameter

of 57 mm gave a nominal unloaded gap of 0.61 mm between the groove flanges. Clearly, in a production case of cylinder/groove interfaces, dimensional control of the groove depths, groove flange heights, and cylinder diameters, would be necessary to prevent the true gap size from exceeding the deflection capability of the preload, and prevent plastic deformation of the cylinders should a greater preload be applied to close a larger than nominal gap. Similarly, far limiting cases must be prevented from having negligible or no unloaded gap, which would cause contact too early and limit the preloaded restoring force that locks the cylinders into place.



Figure 4.25: Flanged mild steel groove.



Figure 4.26: Aluminum cylinder mounted statically between pair of grooves.

Due to machining constraints at the test site, it was not possible to drill bolt holes through the prototype cylinders, so the manipulator was simply mounted statically without bolt preload.

4.4.7 Quasi-Kinematic Coupling Design

A fourth type of coupling, the quasi-kinematic coupling, was designed for the base interface but not manufactured and tested due to time and cost constraints for the project. Recall that the general quasi-kinematic locating principle is the same as for the groove-cylinder couplings - establishing in-plane near-exact

constraint, then applying a preload to seat the mating halves and engage large vertical contact surfaces to bear the disturbance loads. However, since the traditional quasi-kinematic locators would be fixed to the interface plates, plastic deformation of the contactor or target is permitted (and favored) before the gap is closed. Solid model images and high-level dimensions of the designed quasi-kinematic couplings are provided. The design steps were a straightforward application of Culpepper's analysis for estimating elastic contact deflections and yield points of circular line contacts, of which specific discussion is not given here.

Contactor material	420 stainless steel
Target material	Mild steel
Contactor and target protrusion diameter [mm]	100
Target groove angle [deg]	45
Contactor primary radius of curvature [mm]	100
Contact circle diameter [mm]	40
Unloaded (static) gap between contactor and target flanges [mm]	0.30
Deflection limit of plastic deformation [mm]	0.10

Table 4.6: Specifications of designed prototype quasi-kinematic couplings.

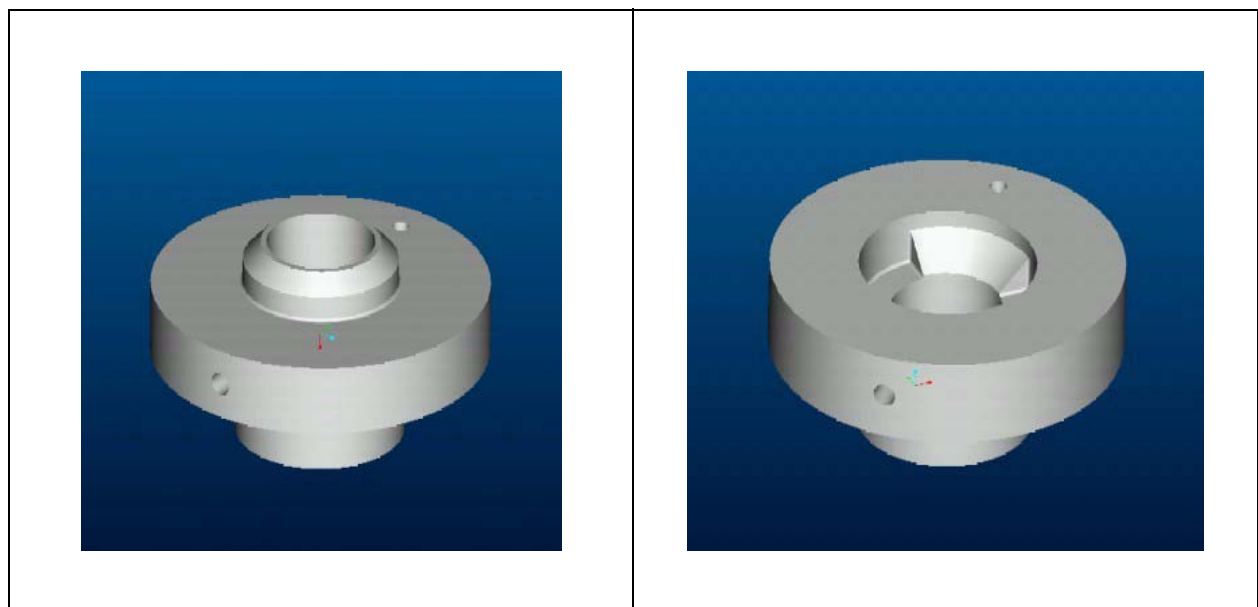


Figure 4.27: Solid model of prototype quasi-kinematic contactor

Figure 4.28: Solid model of prototype quasi-kinematic target.

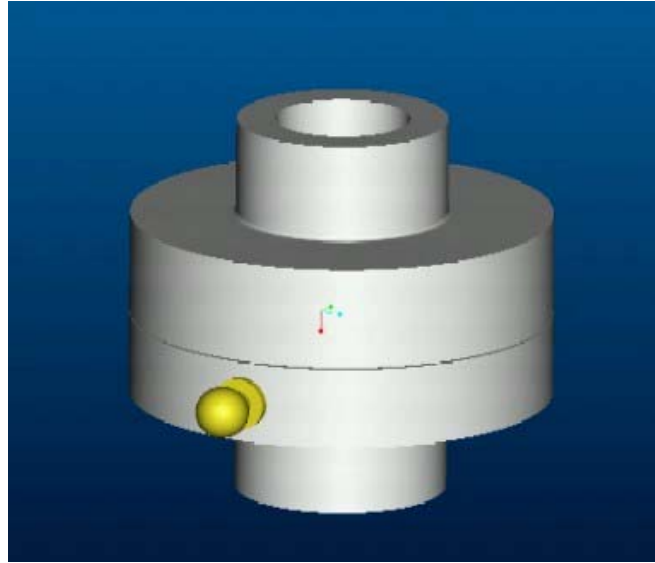


Figure 4.29: Solid model of quasi-kinematic coupling assembly with measurement ball.

4.4.8 Bolt Selection and Torque Specification

Finally, appropriate bolts were chosen for fastening the canoe ball and three-pin interfaces. To package reasonably within the chosen coupling sizes, and provide sufficient strength to hold the 130,000 N preloads, M30-3.75 hex head bolts with quality of 10.9 were chosen. Three bolts of 200 mm length were needed to fasten the canoe balls, while 160 mm length was sufficient for the pins. The choice of 30 mm diameter bolts was corroborated by ABB's specification of 28 mm bolts for mounting the 6400 manipulator to the floor at three points.

The necessary preload torque was determined using the bolt equation from Chapter 2, and calculations were handled by the MATLAB script *bolttorque.m*. A friction coefficient of 0.20 and thread efficiency of 0.3 were specified, giving 565 N-m as required to generate the 130 kN of force in the bolt. This torque is equivalent to application of 258 pounds of force at the end of a wrench 0.5 meters long.

4.5 Prototype Repeatability Tests

With the foot and floor interface plates serving as a reconfigurable test fixture, the repeatability values of the canoe ball, three-pin, and cylinder/groove couplings as factory interfaces for the 6400R manipulator were measured at ABB Robotics Research in Vasteras, Sweden. While safety concerns prohibited dynamic exercises at full speeds and emergency stop cases of the manipulator, the robot was successfully dismounted and remounted, and repeatability was measured at a series of points in the workspace reached by gentle movement at 250 mm/s.

4.5.1 Test Procedures

Having press-fitted the first set of kinematic couplings, the three pins, to the top interface plate, the plate was mounted to the manipulator and placed in the measurement cell. A Leica LTD-500 Laser Tracker was placed at the corner of the cell (approximately 3m from the manipulator foot) and the robot tool flange was fitted with a magnetic holder for the Leica cat's eye retroreflector as shown below.

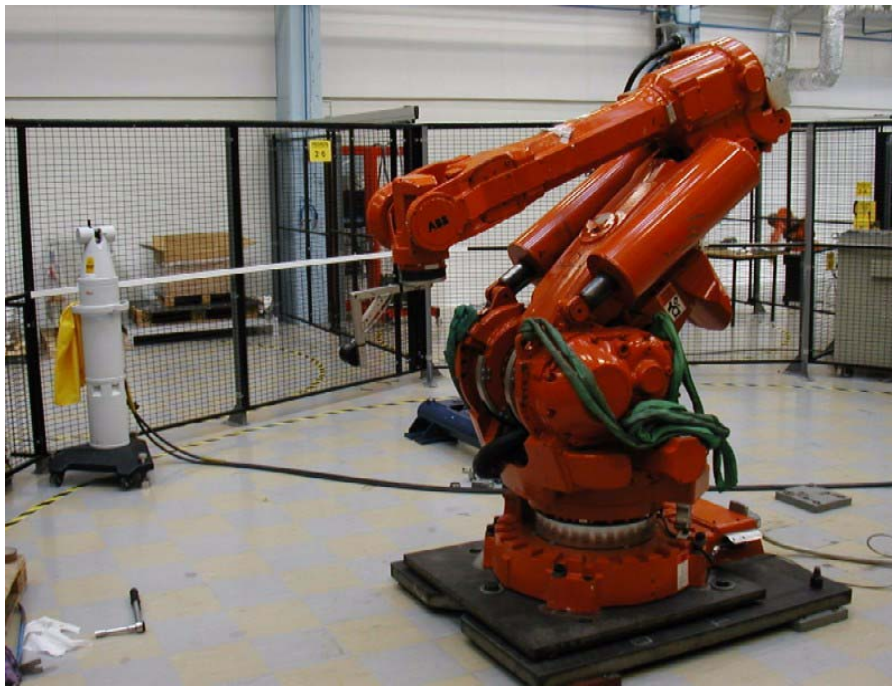


Figure 4.30: Cell setup for repeatability measurements, showing mounted manipulator in crouched home position and laser tracker.

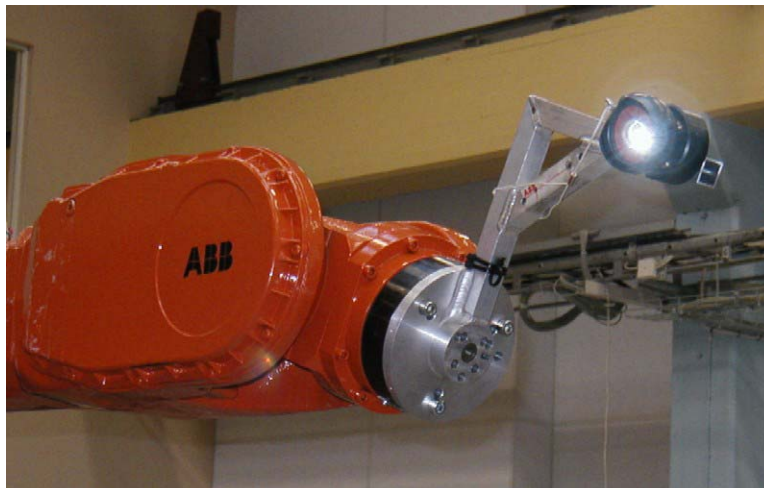


Figure 4.31: Leica cat's eye retroreflector mounted on robot tool flange.

Two test procedures were established for each interface set: first a “basic” procedure involving tightening the bolts to approximately the specified torque, and second a “refined” mounting procedure involving incremental bolt tightening using a torque wrench, and cleaning of the couplings and bolts between mountings.

For the canoe ball and three-pin interfaces, the high-level steps of the re-mounting procedure were to:

1. Attach four nylon lift straps to the manipulator’s lift hooks, attach the straps to an overhead crane hook, and pull the straps taut by winching the hook upward.
2. Loosen and fully remove the interface bolts.
3. Lift the manipulator with the crane so the couplings clear contact and the manipulator can swing freely.
4. Visually inspect the coupling contacts, and clean if appropriate. Also clean and re-grease the bolts if appropriate.
5. Slowly (measured by the slow setting of the crane winch) lower the manipulator and statically seat the couplings, attempting to manually align the coupling contacts to minimize asymmetric seating of the interface.
6. Tighten the interface bolts.
7. Lower the crane harness to a free-hanging position and detach the lift straps from the hook.
8. Raise the crane hook beyond the work envelope of the manipulator.
9. Measure the mounted position using the Leica laser tracker as described below.

Measurements were taken each time with the reflector in each of the eight positions shown below: one at the TCP with the robot in the crouched (lift) position, with power to the robot controller off; two with the reflector statically seated in holes in the top interface plate; and five at the TCP with the robot at points in a programmed path. Comparison of the repeatabilities between the interface plate points and tool positions in the sample path gave elementary insight on the effects of dynamic flexibility of the mounts and distance of the measurement position from the base origin on the measurements.



Figure 4.32: Manipulator harnessed to crane, hanging unbolted over floor interface.



Figure 4.33: Retroreflector seated in measurement hole in top interface plate.

For the basic mounting procedure, step 4 excluded cleaning of the couplings. For the refined mounting procedure, the canoe ball spherical surfaces and groove flats were each deposited with a few drops of methanol and wiped clean with a clean paper towel. For the three-pin interface, the contacting areas of the shouldered pins and the bottom interface plate were sprinkled with methanol and wiped. Also under the refined process, the mounting bolts were wiped clean with paper towels and the threads were uniformly filled with standard axle grease. The bolts and holes were numbered and re-matched after cleaning and greasing. For the three-pin interface, the M12 preload application bolt was also cleaned and re-greased with each interface mounting.

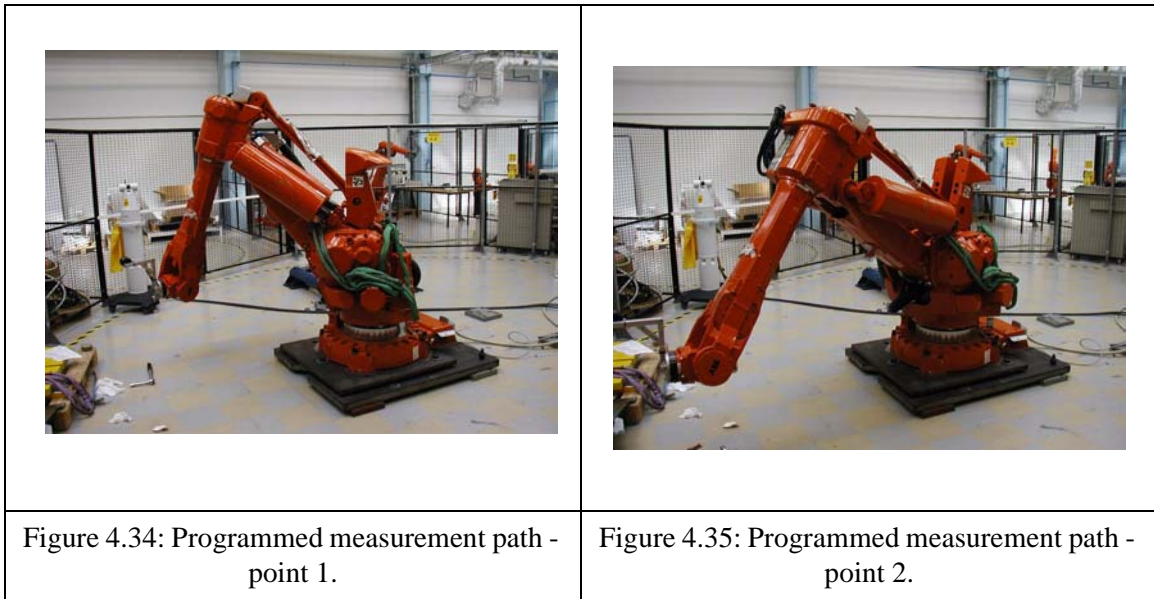




Figure 4.36: Programmed measurement path - point 3.



Figure 4.37: Programmed measurement path - point 4.



Figure 4.38: Programmed measurement path - point 5.

The coupling bolts were numbered (1, 2, 3) and always tightened in the same order. For basic mounting, the bolts were first inserted and finger-tightened in order, then tightened in order to the torque limit of a standard air wrench. With refined mounting, the finger-tightening was followed by three ordered cycles of tightening the bolts to 10%, 50%, and 100% of the preload using a manual torque wrench. Only a 300 N-m limit wrench was available, so the incremental torque values were 30 N-m, 150 N-m, and 300 N-m; because the manipulator was only run at slow speed (0.25 m/s at TCP) without emergency stops, this

torque was more than sufficient to maintain interface stability. Prior to inserting and tightening the coupling bolts for the three pins, the preload bolt was inserted and tightened to 50 N-m. This established the in-plane kinematic seating before application of the vertical preload.

Because of the inability to drill bolt holes through the aluminum cylinders for the cylinder/groove couplings, the manipulator was re-seated by simply static rest of the top grooves on the triangular arrangement of cylinders, resting in the bottom grooves. In basic mounting of this interface, the cylinders, which sat freely in the grooves, were not moved between placements. In refined mounting, the cylinders were removed, cleaned, and re-seated. The grooves were also cleaned according to the refined procedure.

Between six and fifteen trials of each interface were conducted for each of the two mounting procedures. Each trial, including dismounting, cleaning, remounting, robot initialization, and measurement, took approximately twenty minutes for the canoe ball and three-pin interfaces. Static re-mountings and measurements of the groove/cylinder interfaces took no more than ten minutes each.

By running the manipulator through the measurement path ten times without re-mounting the base, the repeatability of the measurement system and manipulator was estimated to be a combined 0.02 ± 0.02 mm.

4.5.2 Prototype Repeatability Results

When a robot is replaced, the error of the replacement is the deviation of the TCP from its new to old location, hence the most useful analysis of the prototype repeatability measurements takes the average differences from the prior mounting locations. The initial mounting is taken only as a reference for the next measurement, subsequent trials give a deviation relative to the prior measurement and a reference value for the next measurement, and the last trial gives only a deviation relative to the prior measurement. Table 4.7 lists the average relative repeatabilities of each prototype interface, under basic and refined mounting when appropriate. Baseline measurements were taken for standard 8-bolt mounting of the 6400R to the blue pallet shown in Figure 4.5. Repeatability of the 8-bolt mounting using the 2-pin alignment method is reported as measured by ABB at a prior date; these measurements were taken with two different robots under undocumented conditions and should only be considered a rough performance of the best current solution.

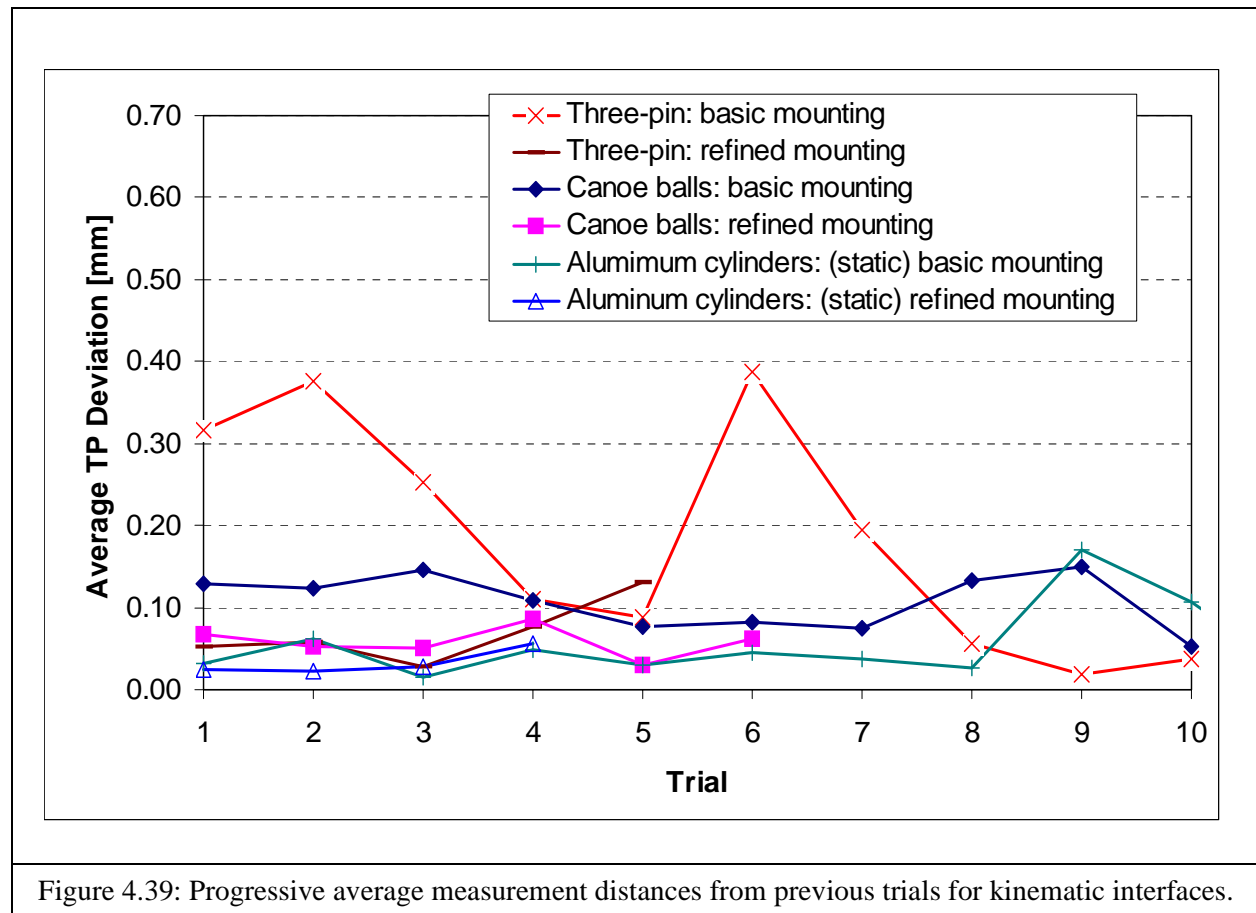
Uncertainties are reported within upper and lower bands of two standard deviations, estimating a 95% confidence interval.

For both the basic and refined mounting procedures, the kinematic coupling prototypes demonstrate significant improvements in tool point mounting repeatability, of no less than a factor of ten, and as much as a factor of fifty improvement over the 8-bolt pallet in all instances. When the basic procedure is followed, the three-pin coupling shows a 52% improvement over the 2-pin engagement, and a 89% improvement over the bolt-only pallet. The canoe balls are a 41% reduction with respect to the three-pin average, hence 72% better than the 2-pin method and 93% better than the 8-bolt pallet. When the mounting process is refined to include cleaning the couplings before replacement and follows an incremental preload schedule using a torque wrench, the benefit is even greater: the 69 micron repeatability of the three-pin mounting is 83% improved from the 2-pin value and a 96% reduction from the 8-bolt pallet; and the 57 micron repeatability of the canoe ball couplings represents 85% and 97% reductions, respectively. The factor of two-to-three improvement between the average relative repeatabilities under basic and refined mounting demonstrates the critical nature of properly seating the kinematic interfaces; unequal torques applied to the bolts, as well as uneven patterns of torque application can severely degrade performance by increasing nonrepeatability due to friction between the contacts and static deflections of the couplings. These results show that to achieve high accuracy, mounting a kinematic interface properly is nearly as important as using a kinematic interface in the first place.

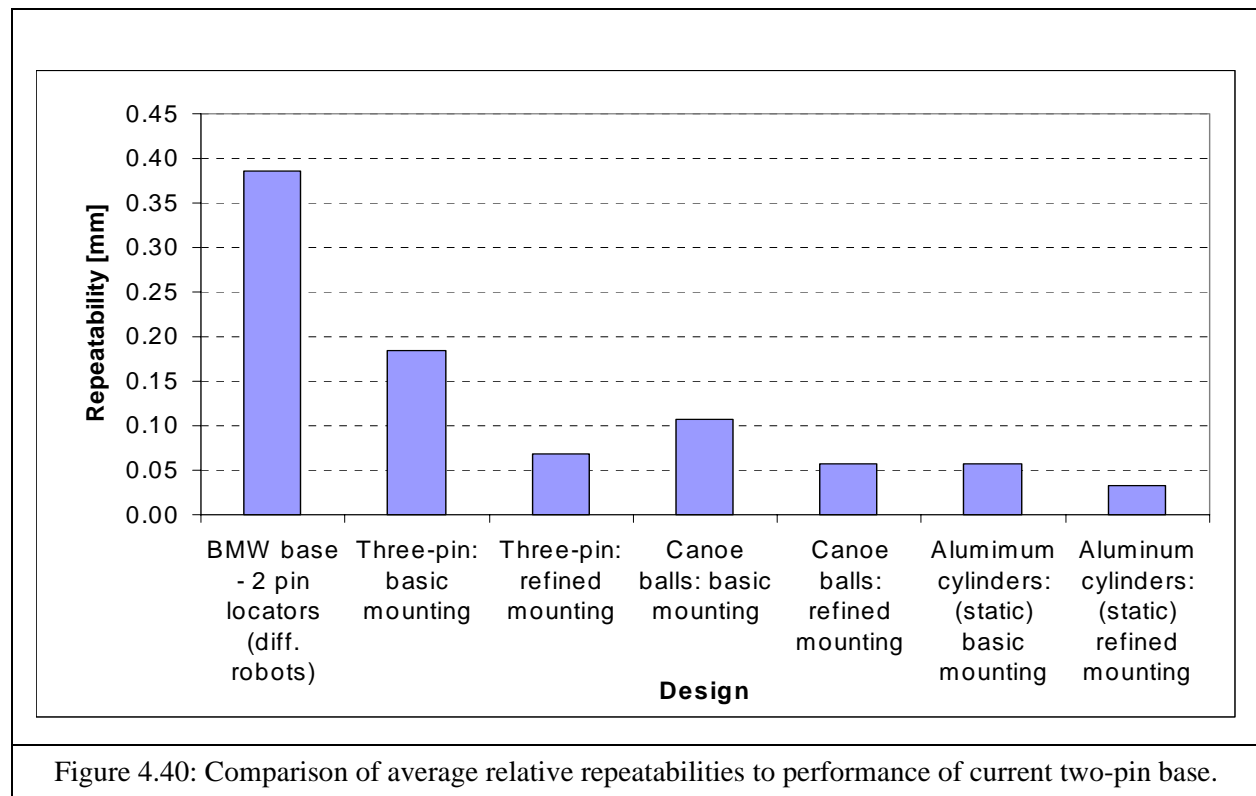
Mounting	Interface				
	ABB 8-bolt blue pallet	ABB 2-pin engagement (diff. robots)	Canoe ball couplings	Three-pin coupling	Groove/cylinder mounts
Basic	1.627 +/- 3.088	0.386 +/- 0.421	0.108 +/- 0.067	0.184 +/- 0.284	0.057 +/- 0.092
Refined	-	-	0.057 +/- 0.038	0.069 +/- 0.077	0.033 +/- 0.032

Table 4.7: Average tool point path repeatabilities [mm] of current ABB and new kinematic coupling base designs, relative to previous trials.

The measurements of static quasi-kinematic mounting of the aluminum cylinders mating to mild steel grooves show even greater improvement: 57 microns for basic mounting and 33 microns (approaching the inherent error of the robot and measurement system) for refined mounting. However, there are two important disclaimers to these values. First, the static mounting process itself is likely more repeatable than when bolts are used, because errors in the torque application and measurement by the wrench make the preload deflections of the joints unequally contribute to the tool point error. Second, the results are reported only in the crouch position of the tool. Since this is the closer to the base than any of the five points in the measurement path, the effect of angular misalignment of the couplings (Abbe error) is not fully seen. This can only justify further testing of the groove/cylinder solution with bolt preload and measurement throughout the coordinate path.



The results also show that the kinematic couplings give less variation in repeatability than the existing designs, shown by Figure 4.39. In order of increasing robustness come the three-pin coupling, groove-cylinder mounts, and canoe ball couplings for basic mounting, and the groove/cylinder mounts, three-pin couplings, and canoe ball coupling for refined mounting. The improvement in robustness between the mounting procedures is nearly the same as the improvement in relative repeatability: near a factor of two for the canoe balls and near a factor of three for the three-pin and groove/cylinder interfaces.



The repeatability of each interface and mounting method is reported in terms of the mean deviation relative to an average value of all the measured trials, in Table 4.8. In most cases, this reporting method shows better results than the calculation of mean relative repeatabilities. When relative values are used, a trial that outlies from the neighborhood of most of the other values (perhaps because of loose debris, or mis-tightening of one bolt) counts doubly against the mean repeatability; there is one large deviation from the outlying value to the prior point, and a second large deviation from the following improved (closer to the global

neighborhood) trial to the outlying point. However, considering single robot replacements where deviation to the previous is all that matters, the relative repeatabilities are far more instructive.

Mounting	Interface				
	ABB 8-bolt blue pallet	ABB 2-pin engagement	Canoe ball couplings	Three-pin coupling	Groove/ cylinder mounts
Basic	1.146 +/- 1.426	N/A	0.080 +/- 0.070	0.274 +/- 0.117	0.095 +/- 0.093
Refined	-	-	0.053 +/- 0.040	0.067 +/- 0.050	0.022 +/- 0.020

Table 4.8: Average tool point path repeatabilities [mm] of current and new designs, relative to nominal average of all trials.

Figures 4.41, 4.42, and 4.43 show the cartesian component deviations of each measurement point with respect to the first measurement taken. Over the small number of trials in each case - five total per trial for three-pin and canoe balls, and three per trial for the groove/cylinder mounts - consistent drift is seen in the x (along the manipulator centerline) and z (vertical) directions for refined mounting of the three-pin interface, and in the y and z directions for basic mounting of the groove/cylinder interface. Moderately widening variability is seen for refined mounting of the canoe ball interface. The drift of the three-pin interface could be due to thermal growth, as it was noticed that the ambient temperature of the cell increased six degrees fahrenheit during the measurements. Also, the decreasing z-values of the groove/cylinder mounts could be because of settling of the soft aluminum into the unpolished machining marks in the steel grooves. Nothing more can be drawn from such limited data; analysis would be more instructive over a greater number of trials, with more direct monitoring of environmental conditions.

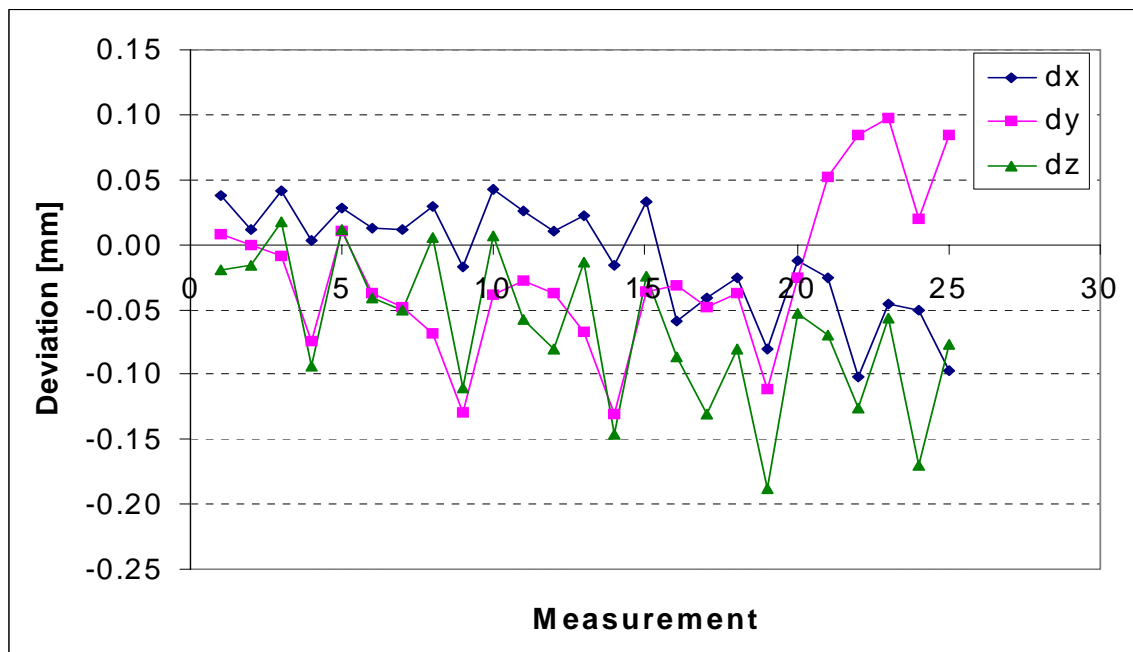


Figure 4.41: Cartesian TCP deviations from first trial - three-pin interface, refined mounting.

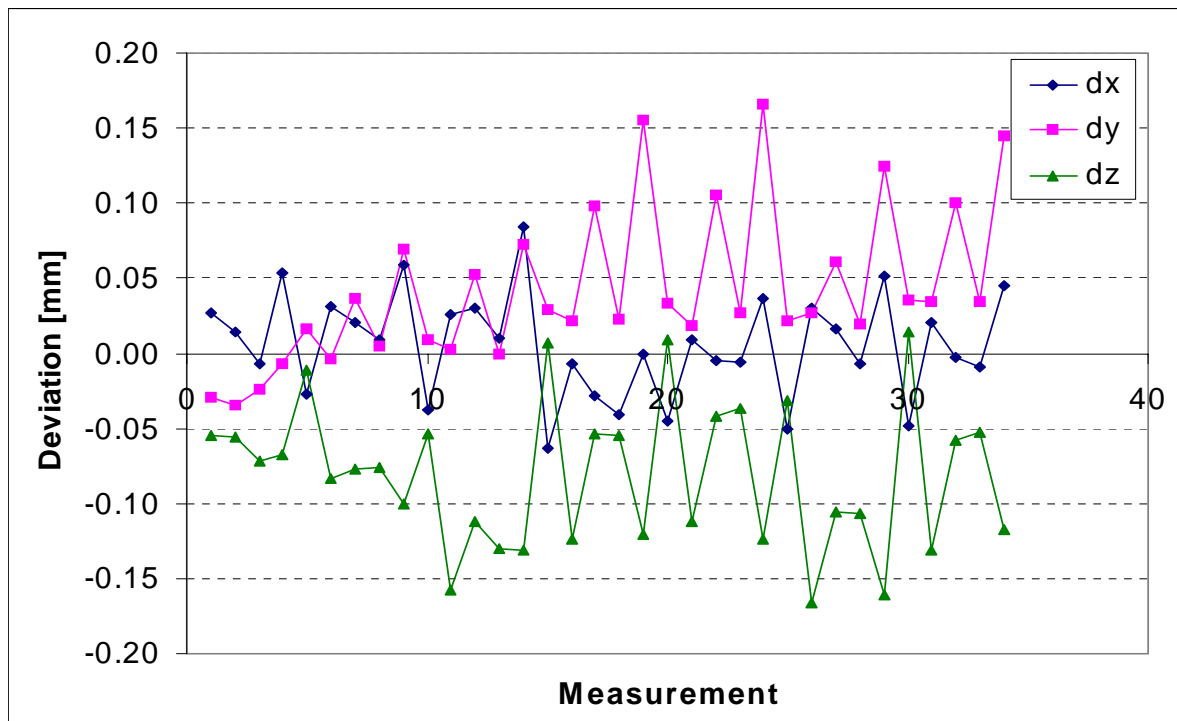


Figure 4.42: Cartesian TCP deviations from first trial - canoe ball interface, refined mounting.

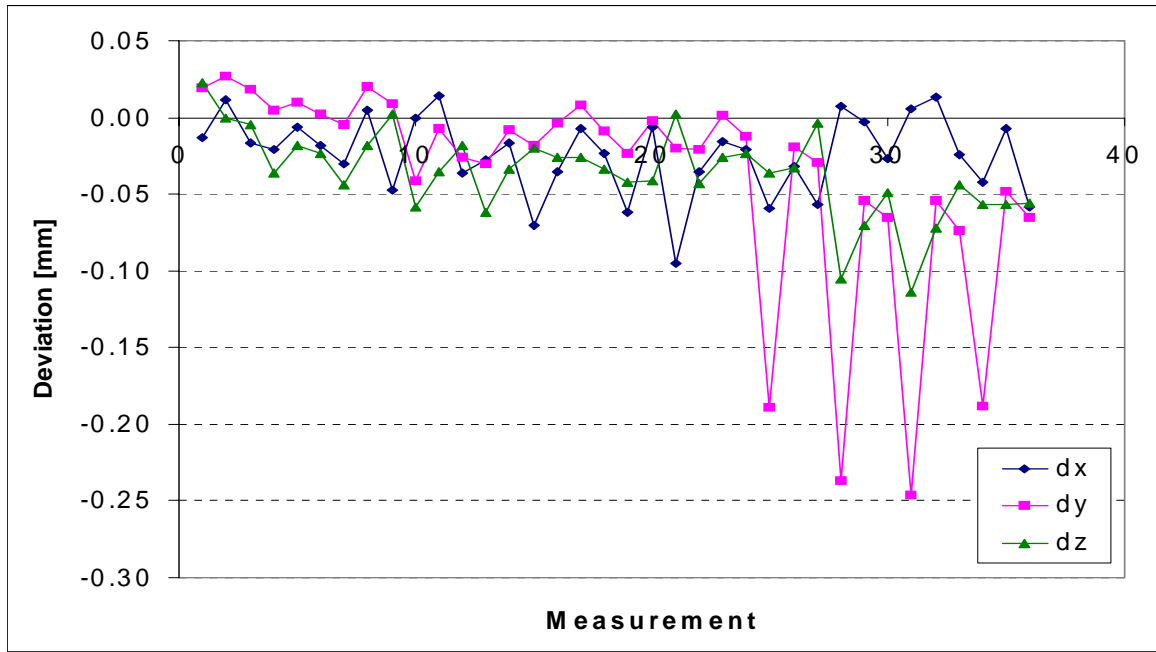


Figure 4.43: Cartesian TCP deviations from first trial - groove-cylinder interface, refined mounting.

Finally, the couplings were examined for wear marks after the repeatability tests were completed. When wiped clean, the vertical and in-plane contacts of the shoulder pins showed no visible scratches or indentations. On the other hand, the canoe ball mounts, one of which is shown in Figure 4.44, clearly indicated the contact areas of elastic deformation by dark spots, and showed small scratches from contact with the groove edges due to asymmetric lowering of the manipulator with the crane. The main contact spots measured approximately 15 mm in diameter, and a second, smaller contact spot existed nearby on one side of the coupling shown, from improper seating of the interface when the manipulator was twice lowered in an abrupt fashion. The aluminum cylinders, one pictured in Figure 4.45, showed patterns of small indentations from the machining marks of the unpolished steel grooves. The stainless steel and mild steel grooves were intact to the naked eye.

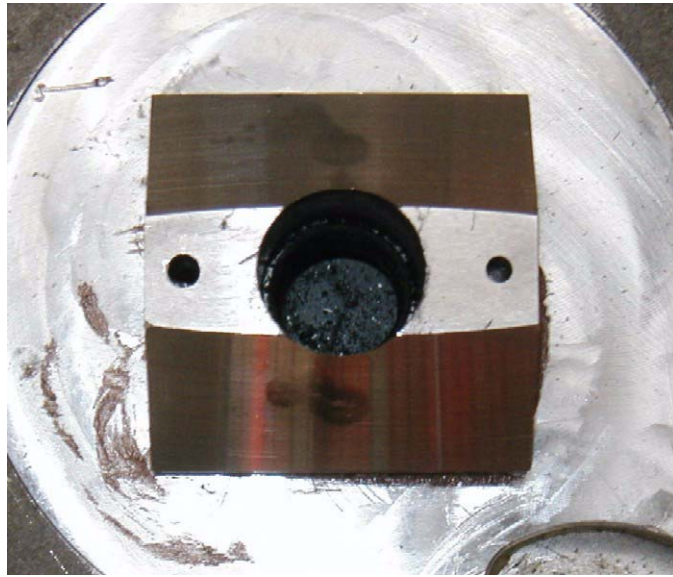


Figure 4.44: Canoe ball surface after eleven base mountings.



Figure 4.45: Aluminum cylinder after fifteen static base mountings.

It is anticipated that repeatability could be improved further, by as much as a factor of two, by augmenting the mounting process to include adding a few drops of oil to the contact surfaces before mounting, and by vibrating the interface (e.g. hitting the side of the top interface plate with a hammer) before tightening the bolts. These would overcome frictional non-repeatability between the contacts.

4.6 Factory Interface Interchangeability Simulations

In addition to the physical prototype repeatability experiments, parametric interchangeability assessments of the canoe ball and three-pin interfaces were made using the numerical models presented in Chapter 3. Here, the geometry of the interfaces was specified as built for the prototypes, and the error at a nominal TCP position relative to the coupling centroid was calculated as related to the manufacturing and placement tolerances of the couplings and the measurement features, the level of detail of the calibration process, and the error of the measurement system itself. These results can predict the interchangeability performance as a step of the design process, enabling choice of the coupling manufacturing tolerances and the calibration process steps to ensure the desired accuracy at minimal cost.

4.6.1 Canoe Ball interchangeability Simulation

4.6.1.1 Model Input Parameters

The MATLAB-based numerical model presented in Chapter 3 was used to simulate interchangeability of the manipulator factory interface. The nominal coupling dimensions and three-sigma manufacturing tolerances were specified exactly as for the prototype canoe balls and grooves. For a parametric study, the manufacturing tolerances on the plates (hole position and thickness), and the error of the measurement system were also specified at “low”, “medium”, and “high” levels as listed in Table 4.9. For each of the error levels, the interchangeability was simulated with no calibration, at each of the five levels of calibration detail for offset measurement, and at each of the three detail levels for direct measurement of the contact surfaces.

Error Component [units]	Value - Low	Value - Med	Value - High
h_{tol} [mm/m]	0.12	0.24	0.36
t_{tol} [mm/m]	0.10	0.20	0.30
θ_{tol} [deg]	0.1	0.2	0.4
R_{ball} [mm]	0.05	-	-
x_{meas}, y_{meas} [mm]	0.02	-	-
x_{ball}, y_{ball} [mm]	0.02	-	-
h_R [mm]	0.02	-	-
x_{groove}, y_{groove} [mm]	0.02	-	-
h_{prot} [mm]	0.02	-	-
h_{meas} [mm]	0.01	-	-
θ_{groove} [deg]	0.02	-	-
R_{meas} [mm/m]	0.01	0.05	0.1

Table 4.9: Error component values for canoe ball interchangeability simulation.

4.6.1.2 Results

At the dimensional tolerances of the prototype canoe ball interface - coupling mounting plate tolerances of $h_{tol} = 0.12$ mm/m, $t_{tol} = 0.10$ mm/m, and $\theta_{tol} = 0.10$ degrees, and the error of the standard laser measurement system of $R_{meas} = 0.01$ mm/m - the interchangeability simulation yielded the following results:

1. Approximately 0.23 mm interchangeability at the TCP when the interface is not calibrated, and nominal positions of the contacts are assumed.
2. At full interface calibration by offset measurement of the canoe ball and groove flat surfaces, interchangeability is reduced to 0.12 mm. 0.09 mm of this is introduced by form inaccuracies in the couplings and error the projections of the contact points from the offset location. The remaining 0.03 mm is due to error of the measurement system.
3. At full interface calibration by direct contact surface measurement, 0.03 mm interchangeability is achieved. Within this first-order model, the residual error here is only from the measurement system.

Hence, for this example, interface calibration using an offset measurement feature reduces the TCP error by approximately 50%, and interface calibration by direct measurement reduces it by approximately 85%.

Recall from Chapter 3 that the numerical designations for the levels of calibration of the canoe ball interface under offset calibration are:

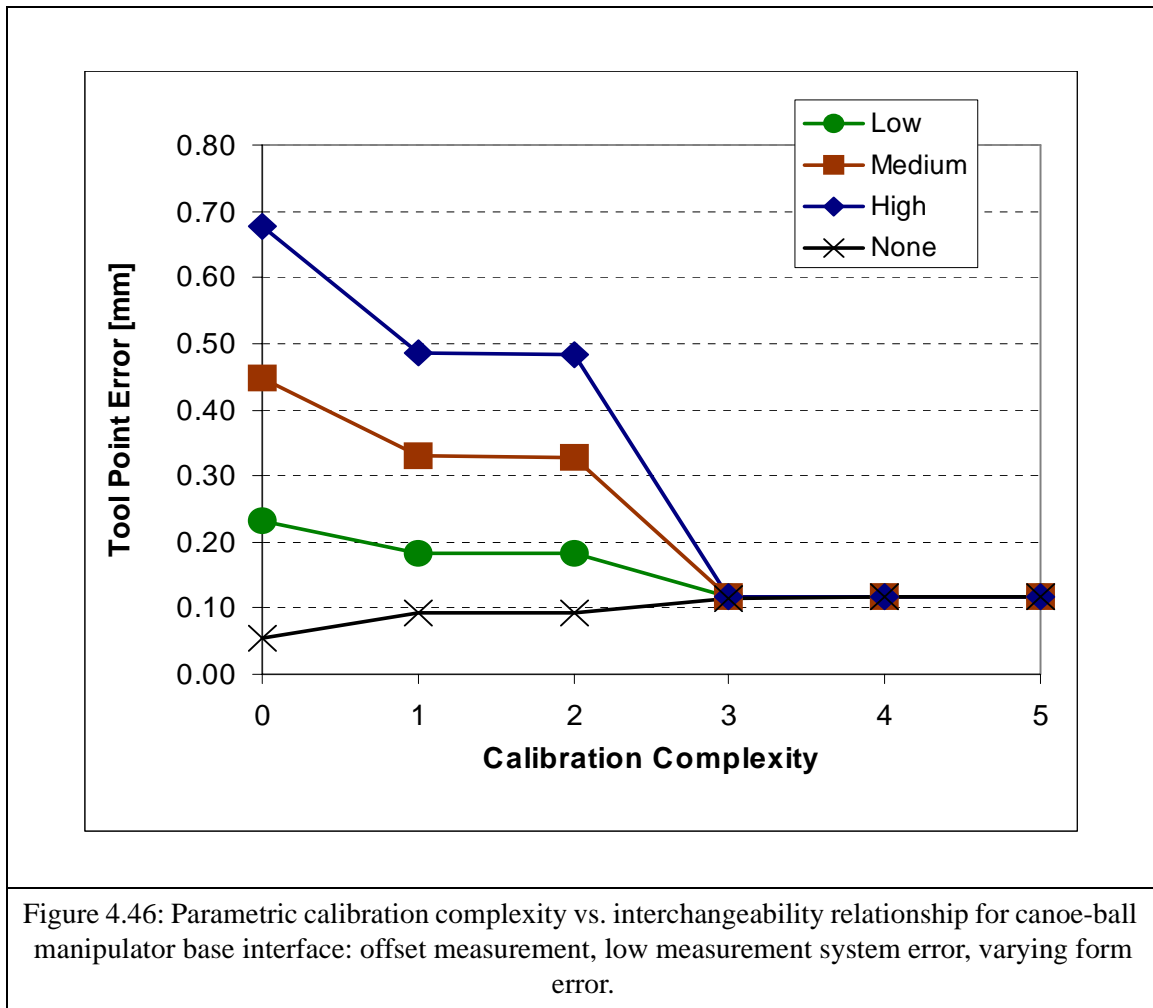
0. Assumption of fully nominal placement;
1. Measurement of the positions of the floor-mounted grooves;
2. Measurement of the groove positions and orientations;
3. Measurement of the groove positions and orientations, and the ball positions;
4. Measurement of the groove positions and the ball positions;
5. Measurement of the groove positions and orientations, and the ball positions and orientations.

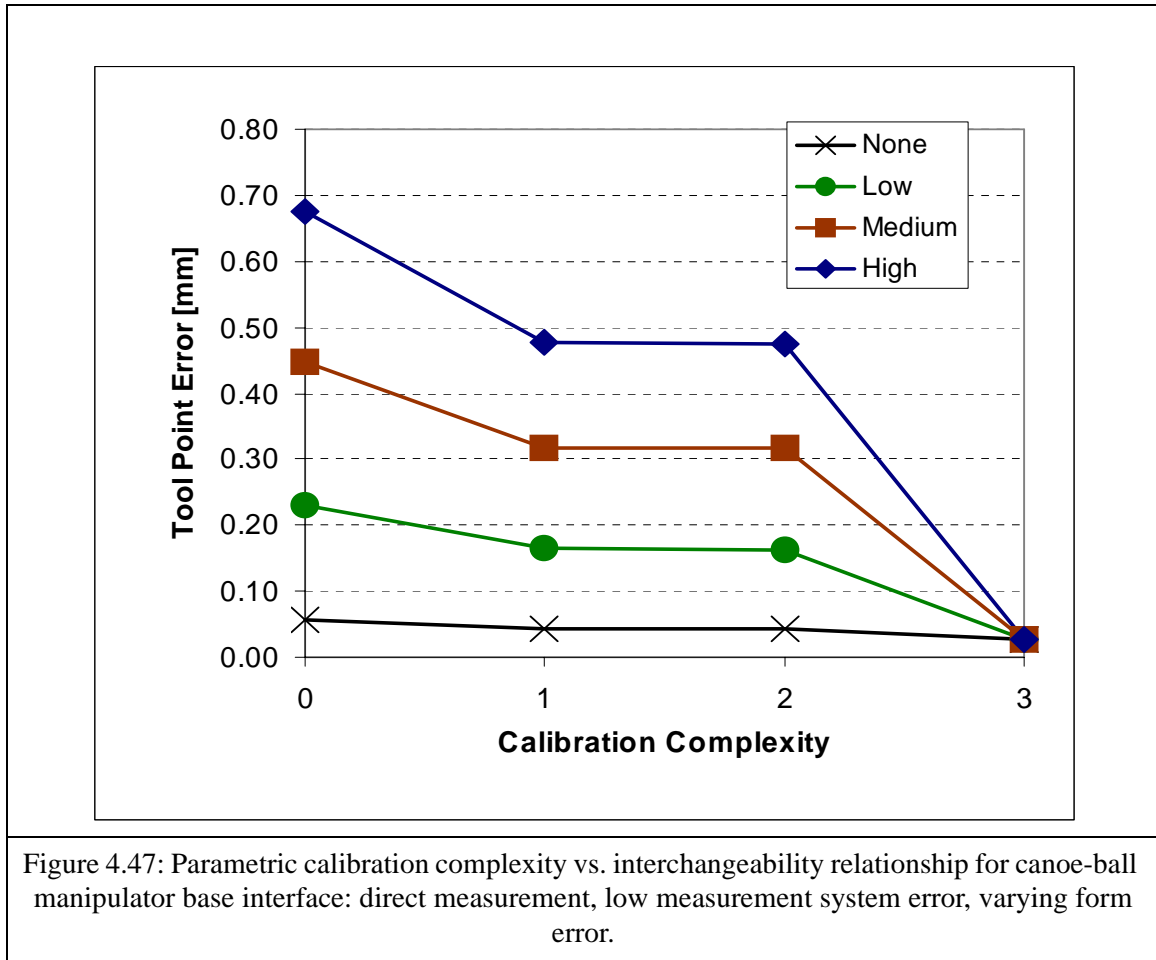
Here, position measurement is simulated by locating an offset measurement feature, such as a tooling ball press-fit into a secondary hole in the ball or groove mount. When the model considers calibration by direct surface fits to the canoe spheres and the groove flats, the levels of calibration are:

0. Assumption of fully nominal placement;
1. Surface fits to the canoe spheres, measuring the radii and projecting the center positions;
2. Surface fits to the groove flats, measuring plane base points and normal vectors;
3. Surface fits to the canoe spheres and the groove flats (minimum error calibration).

Figures 4.46 and 4.47 show the parametric variation of error as a function of calibration complexity at the dimensional tolerance levels listed in Table 4.9. TCP error is shown to scale linearly with overall magnitude of the coupling placement feature and position measurement feature tolerances. With measurement system error remaining nominal, relaxation of the placement tolerances to the medium level increases the total TCP interchangeability error to 0.45 mm without calibration, and relaxation to the high level increases the TCP interchangeability to 0.68 mm. However, the error with full interface calibration remains the same, 0.12 mm with offset measurement and 0.03 mm with direct measurement, when the ball and groove positions are measured. Hence, within the greater limits of kinematic seating (e.g. tolerances of +/- 2-5 mm), the tolerances on manufacturing the interface plates and placing the couplings have no effect on

the accuracy of the base interface when the interface is calibrated as proposed. Note that for the idealized case when there is no form error (or when form error is nearly zero), measurement and prediction can decrease the accuracy of the interface; when measurement system error is greater than form error, the variation between the predicted and true transformations will be greater than the difference between the nominal and true transformations. Here, it would be best to assume nominal parameters and ignore the calibration step.





4.6.2 Three-Pin Interchangeability Simulation

4.6.2.1 Model Input Parameters

For comparison to the canoe ball interchangeability results, simulations of the three-pin interface performance were conducted. As with the canoe ball model, each dimension was specified at “low”, “medium” and “high” levels, with the three-sigma input values given in the table below. For each level, one 10,000-trial simulation was executed at each of the levels of measurement calibration described in Chapter 3. Recall that measurement system error was not a component of this model, and coupling positions (pin diameters and contact surfaces in the floor plate) are measured directly, so form error has no modeled influence on the accuracy of the calibration. Hence, calibration with full measurement of the

interface produces perfect interchangeability, with zero modeled error between the true interface transformation and that predicted by the calibration.

Error Component [units]	Value - Low	Value - Med	Value - High
h_{tol} [mm/m]	0.06	0.12	0.24
t_{tol} [mm/m]	0.05	0.10	0.20
r_{pin} [mm]	0.01	0.02	0.04
t_{pin} [mm]	0.01	0.05	0.10
θ_{flat} [deg]	0.01	0.02	0.04

Table 4.10: Error component values for three-pin interchangeability simulation.

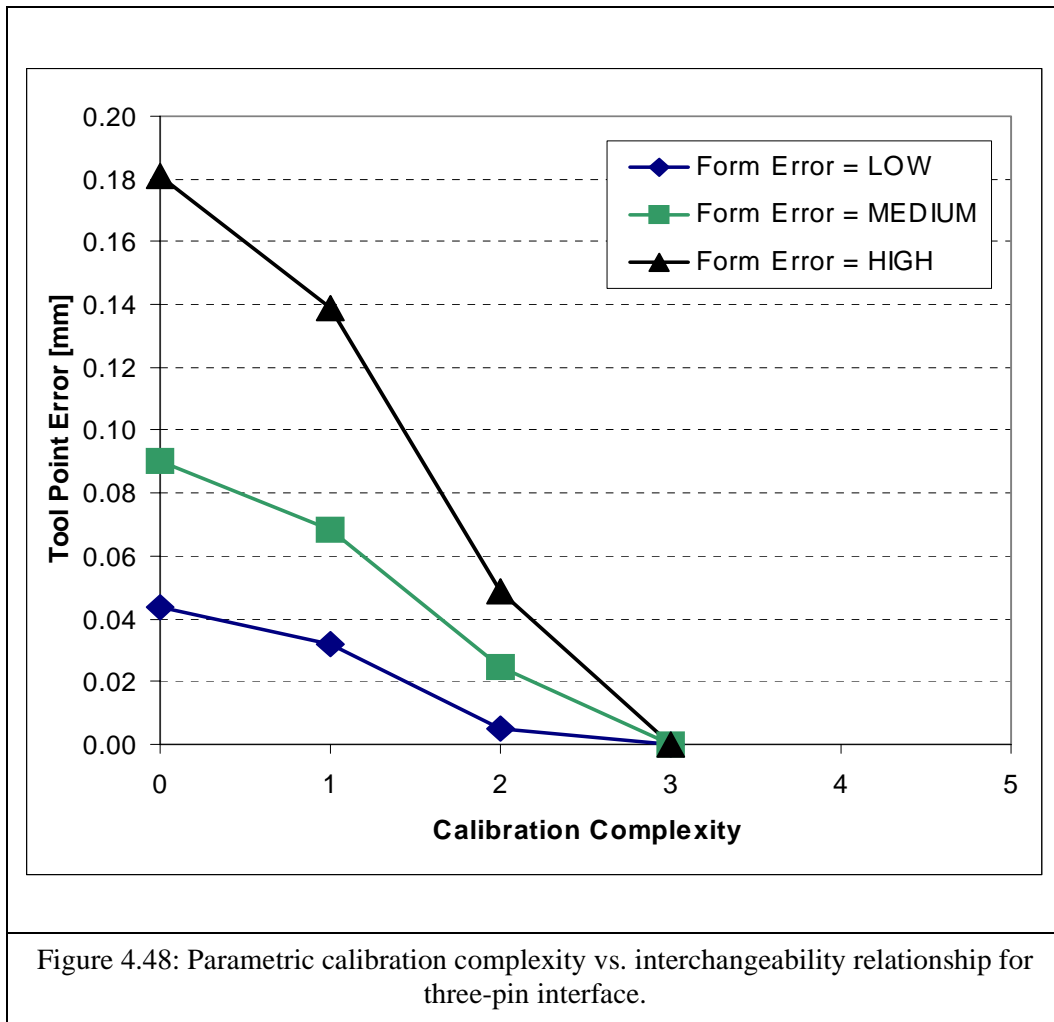
4.6.2.2 Results

Figure 4.47 displays the relationship between calibration complexity and TCP interchangeability error for the three-pin interface, at the three form error levels quantified in the previous section. Recall from Chapter 3 that the numerical levels of calibration complexity correspond to:

0. Assumption of fully nominal placement;
1. Measurement of the positions and relative heights of the contact surfaces in the floor plate;
2. Measurement of (1) plus the contact point locations of the foot-mounted pins;
3. Measurement of (2) plus the relative heights of the pin shoulders.

For the medium level of dimensional tolerances - approximately equivalent to the nominal precision of the canoe ball interface studied previously - interface interchangeability without calibration is 0.09 mm, decreases to 0.07 mm with measurement of the vertical contact flats in the baseplate, decreases to 0.03 mm with knowledge of the in-plane pin contact locations, and is zero when the interface is fully calibrated. This of course ignores error of the measurement system, but since the contact surface and pin locations are measured directly, form error (ignoring out-of-roundness of the pins, and local skewness of the contact planes) of the coupling contacts is absorbed into the calibration. Taking a 0.03 mm value for measurement error from the prior section, total interface interchangeability including the 0.07 mm measured repeatability is 0.10 mm, meeting the 0.10 mm goal for the project. This value can only be improved by decreasing the

measurement system error expressed in calibration, or improving the interface repeatability, a combination of the non-deterministic components of the interface kinematics, and the refinement of the mounting process. Based on dimensional accuracy alone, the combination of simulated interchangeability and measured repeatability shows that the three-pin interface with full direct calibration of the contact points is much more desirable than the canoe ball interface with full offset calibration of the contact points.



4.6.3 Interchangeability as a Component of an Accuracy Menu

Beyond the individual simulated interchangeability values given here, the interchangeability models are an important component of an accuracy menu for kinematic interfaces, from which engineers can design kinematic interfaces to produce needed accuracy, and trade-off the error of individual components to minimize cost. With the models presented, a designer can compare the performance of the canoe ball and three-pin interfaces when interface geometry, error reporting location, coupling placement tolerances, coupling form tolerances, and measurement system tolerances are varied. Combined with the basic repeatability data from the prototype tests, the performance of the robot factory interface can be estimated with good confidence at any reasonable level of manufacturing precision. The concept of interface calibration

also eliminates dependence of interface accuracy on placement of contact points, and illustrates how kinematic couplings can be calibrated in a standard representation. This encoding means that different suppliers can make the same components, and use standard error parameters to measured locations, reducing the sensitivity of overall product quality to the symmetry of quality from component sources.

Hence, the most valuable contribution of the interchangeability study is not a fixed design recommendation, rather a deterministic engineering process which improves both mean accuracy and variation of the final solution by being able to predict the accuracy and robustness of a given kinematic interface given input error parameters. A more intelligent model could operate inversely, taking the accuracy requirements and interface geometry and producing interface requirements with optimal allocation of the error budget between the random error components. This could be extended to include cost relations, long-term interface performance data as it becomes available, and certain rules of thumb in logical format to make the interface design process a nearly automated, minimum uncertainty life-cycle decision. The breadth and depth of the information on repeatability can also be improved by testing and simulating the performance of other quasi-kinematic couplings, and all solutions at long-term periods of manipulator operation.

4.7 Conceptual Extension to Four-Point Mounting

Although three-point mounting is used here and almost always in other applications for the kinematic couplings, canoe balls can also be used in a kinematic four-point “split-groove” fashion [3]. To accommodate this, the coupling normally placed along the centerline of the foot is split into two single-contact couplings, which are shifted outboard in opposite directions as indicated in Figure 4.49. Because there are still six contact points, the constraint is kinematic, and the greater average distance between the couplings and the center of the foot increases the dynamic moment-holding capacity of the interface.

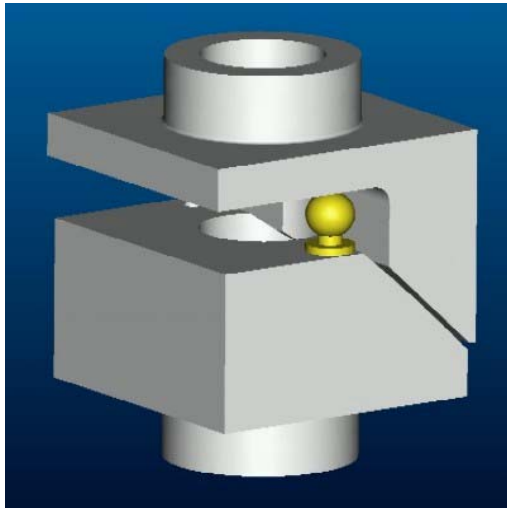


Figure 4.49: Split groove canoe ball to accommodate kinematic mounting using all four corners of a bolt rectangle.

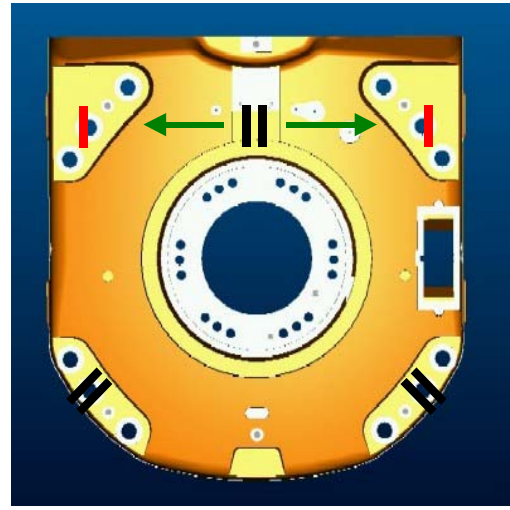


Figure 4.50: Four-point coupling locations on four-corner mounting base.

A direct interchangeability model for this configuration is a straightforward extension to the three-point interchangeability analysis for canoe ball couplings, although the measurement of the central coordinate frame would be a least-fit process to the four measurement points on the coupling balls, rather than an exact fit to three locations.

The four-point solution is presented here only as a concept for easiest retro-fitting of existing designs to accommodate couplings, and to show adaptability of kinematic couplings to a four-point configuration. Detailed work by Ryan Vallance applied four-point mounts to a material handling pallet system [3].

4.8 Improvements to Robot Accuracy

In all configurations tested, the canoe ball and three-pin kinematic couplings demonstrate significant improvements in mounting accuracy of the robot factory interface when compared to the current ABB manipulator base designs. In terms of measured repeatability, both interfaces offer nearly the same average relative repeatability, the canoe balls show less variation in repeatability over the full set of trials, and static

mounting of mild steel grooves gives results that warrant further tests of this possible third improved solution. In terms of simulated interchangeability, the interface calibration by standardized measurement of the coupling contact points and calculation of an interface error transformation makes the accuracy of complete robot replacement independent of the position tolerances of the mounting holes in the interface plates. The measured repeatability values are considered as a random error superimposed upon the predicted interchangeability from Monte Carlo simulation to give the “Total Mechanical Accuracy” (TMA) of the interface. The three-pin solution guarantees placement of the TCP with no more than 0.10 mm of error due to the base interface, and the canoe ball solution gives 0.08 mm TMA with direct measurement of the spherical surfaces and flats, and 0.18 mm with offset single-point measurement. Using the models presented in this thesis, the interchangeability performances can be predicted as functions of the interface component tolerances, and the repeatabilities are known under two distinct procedures of basic and refined interface mounting.

Interface	Repeatability	Interchangeability	TMA [mm]
Canoe balls - offset measurement	0.06	0.12	0.18
Canoe balls - direct measurement	0.06	0.03	0.09
Three-pin (direct measurement)	0.07	0.03	0.10
Cylinder/groove	0.03	Not simulated	N/A

Table 4.11: Total Mechanical Accuracy (TMA) of manipulator base solutions.

The three-pin interface clearly is the least expensive of the two solutions here, requiring simply turned steel shouldered pins pressed to the foot, and simple-to-machine mating contact holes in the floor interface plate. On the contrary, the high cost of grinding and polishing the large radius canoe spheres makes the solution impractical for production as designed for the prototype. The existing ABB IRB6400R foot can be fitted with the three pins, mated to an appropriate interface plate with in-plane preload application, and bolted vertically using the eight current bolts in an incremental, patterned process using a torque wrench.

Generally, the concept of a deterministic mechanical interface is a step toward streamlined robot replacement and installation procedures, resting on three main concepts:

1. The position of the floor-mounted kinematic baseplate relative to the cell components is known by pre-installing the baseplate and measuring its coordinate frame relative to the work objects in the cell.
2. The position of the end-effector relative to the kinematic foot is known by calibrating the robot relative to this foot at the robot factory.
3. The mounting of robot foot relative to the baseplate is deterministic, based upon the positions of the coupling locators and contacts as measured at the robot manufacturing facility.

Hence, by summing this chain, calibration of the robot is decoupled from calibration of the cell through a known deterministic transformation. Upon manipulator component exchange, this decoupled calibration is much more accurate than the coupled, full cell calibration that is currently performed.

In the future, the pre-calibrated kinematic interface would be a key part of a server-based management system for modular robots and other instances of modular automation, such as that described in detail in Chapter 6. For initial implementation of the intelligent interface technology:

1. The robot user purchases standard, kinematically coupled base plate and wrist plates with each robot, with an appropriate increase to the robot package cost. Standard costs are maintained for piping, wiring, and robot rigging. Baseplates are installed on the factory floor and dimensioned to tooling.
2. The robot user purchases a centralized control server/system (per cell or area) for data management and system analysis.
3. The calibration “fingerprint” of each robot and end effector is determined in standard form at the appropriate manufacturer, enabling accurate math-based simulation of the robot work path. Robots and end effectors can be “plugged” into the base plates and wrist plates with little or no debug and tryout, tremendously saving time and cost of plant installation, integration, and programming.

For equipment selection, the interface also introduces the concept of an accuracy “menu” to customers; for example, kinematic mounting can be chosen if high accuracy is desired, or bolted mounting with encoded module identification can be chosen if lesser accuracy is sufficient.

At the subsequent robot replacement at this facility:

1. Assuming new robots are in the same size/payload class as existing robots, the standard baseplates are reused and kept in the same locations. These interfaces are standard among major equipment manufacturers.

2. The hardware and software of the central server system is upgraded (open-architecture design), and accepts all new information. The application design is transparent to information format, and interfaces with appropriate equipment-specific control applications.
3. Robots and end-effectors are calibrated at the manufacturer and programmed accurately through simulation, simplifying system and plant integration, installation, and debugging.
4. Calibration data and programs are stored in the central server, and can be mapped by station and device object address (e.g. station10a.robot1.weldgun1) through the system to each piece of equipment, whether programs are reused or are new.

And in routine system operation or maintenance:

1. Since calibration data and programs are housed centrally, failure downtime can be reduced by replacing a damaged end-effector or even a catastrophically-failed robot (given each is a standard spare part, e.g. a bill of process specified sealer wand or pinch weld gun) with a new component and repairing the damage offline.
2. Equipment can be optimally rotated and control signals can be intelligently re-mapped using the centralized information system.
3. Plus, the new replacement and maintenance processes are faster and more efficient, reducing frequent replacement schedule overruns, and increasing schedule flexibility.

4.9 Caveats and Needs for Future Work

Including the quick-change smart factory interface, the grand prize for the robot customer such as a major automotive manufacturer is a fully integrated absolute robot tool point positioning system. Using current technologies, attempts to build such a system using accuracy components from different manufacturers have been like forcing non-adjacent pieces of a jigsaw puzzle to fit together. In this sense, the full reliability of simulation-generated robot programs, and the “plug-and-play” notion that accompanies no need for on-line path touch-up and calibration, will not be realized without such a system. However, the kinematic factory interface is a significant step towards standardization of mechanical interfaces; its simple and general nature implies compatibility with most all calibration schemes. Furthermore, notwithstanding the mechanical mounting standard, common power, air, water, and control connections would be extremely helpful in exchange, at least with intermediate quick hose disconnects.

Additionally, the kinematic analysis presented here neglects other persisting mounting errors to the interface performance, such as thermal expansion under daily or seasonal temperature cycles (as much as

20 C) and dirt buildup and harsh treatment in the manufacturing environment. These concerns have been found as very salient to potential customers, and should be investigated before a production design is established. Furthermore, process refinements such as cleaning the kinematic contacts before re-mounting, can minimize external error influences.

When integrating the factory interface with the calibration system, information storage of the calibration parameters, such as the positions and orientations of the coupling balls and grooves, is a critical issue. In some present systems, robot calibration coefficients are shipped on a floppy diskette packaged with the manipulator, intended to be loaded at the line site when the robot is matched with a controller cabinet and installed. This is because all robots are hooked to a fixed cabinet when calibrated at the robot manufacturer; production cabinets are shipped separately. These floppy disks are often lost, causing days of delay in receiving a backup copy from the manufacturer, if the manufacturer even keeps a backup copy. In other systems, the axis-by-axis inverse kinematic corrections are stored individually in memory on serial communication boards on the manipulator. If the robot is unpowered for an excessive duration, such as that during shipping, the battery backup of the memory can fail, losing the data. In both cases, a static, indefinite storage mechanism attached to the manipulator would alleviate these problems. For the base, this could take the form of a non-contact smart radio frequency identification device (RFID) attached to the manipulator foot, which wirelessly dispatches its data to the control cabinet when brought into the production cell.

One manufacturer gave a “wish list” of future improvements in robot replacement and calibration technologies which included:

1. Efficient robot placement using a quick-change base system, with accuracy of the floor mounting plate.
2. A simpler, more portable laser measurement system for calibrating the workcell
3. Easier, and more accurate installation, calibration, and exchange of the end effector tool.
4. Total calibration of the robot at the line site, including the tool, in an automatic mode.

The first item is a direct application of the quick-change base interface. The second is an extension to measurement system technology, and would be ideally served by integrating the measurement system with the robot. Such is currently cost and size limited, as laser tracking systems are floor-standing and cost over

\$150,000 each. The third item is a direct extension of the base interface; a smaller, pre-calibrated kinematic coupling set can be used at all robot interfaces. Standardization between the wide variety of end effector types and manufacturers is the challenge here; an intermediate step would be building a kinematic adaptor kit which can be attached to a tool, calibrated to a standard (offline) mating interface, and encoded with the positions and orientations. The fourth item requires integration, including full software packages for absolute accuracy. A small part of this software would be an optimized routine for choosing the sequence of calibration points in the workspace. A brief study of this problem was done as a course project and is discussed in Appendix E.

Overall, the concept of the quick-change factory interface seems very likely to improve flexibility during production by reducing the uncertainty involved in the repair/replace decision for robot manipulators. More importantly, the solution must add minimal cost to the manipulator, and without standardization, ease of scheduled replacement becomes little greater considering that automotive manufacturers often change manipulator manufacturers between subsequent retoolings of a facility. Scheduled replacement must not be deterred, as new manipulators often incorporate cycle time-improving upgrades, which business cases show to have financial benefit from increased throughput that is several times the cost of the automation itself.

Chapter 5

Instrumentation Case Study: Thermal Performance of a Modular Structure for a High-Precision Microscope

This chapter describes a novel segmented design for an instrumentation structure based on modules connected by canoe ball kinematic couplings. The design is applied to a high-precision microscope for single-molecule experiments, under primary development at the University of Illinois. The modular segmented design is a series of metallic rings, and is shown to be significantly less sensitive to deformation from uneven thermal disturbances than a similar structure consisting of a single full-length ring, or a traditional non-symmetric microscope structure. Sub-micron repeatability of the kinematic coupling interfaces enables the structure to be disassembled and reassembled without re-calibration, and pre-calibrated ring modules with different optical components can be installed for quick changeover between experiments. The design and thermal experiment results are presented here, with the repeatability assessments as ongoing work to be presented in a future publication.

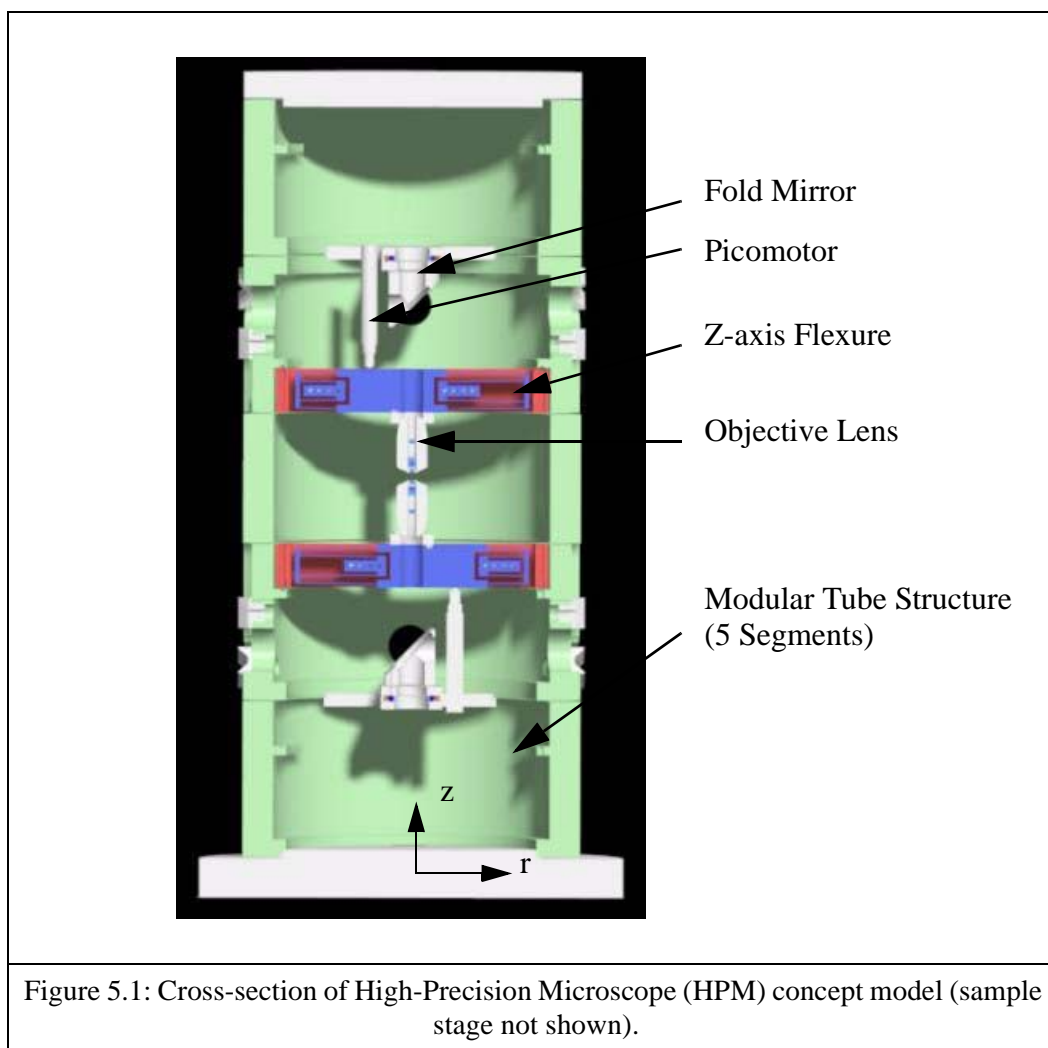
5.1 Overview of the High Precision Microscope Project

Recent developments in microscopy have focused on using microscopes for quantitative measurements in addition to imaging. Spectroscopy has also become an important tool in microscopy, requiring the use of additional optical devices in conjunction with the microscope itself. Furthermore, technological advances have made single molecule detection possible, driving interest in measurements with sub-nanometer precision [1].

These new applications require performance beyond the capabilities of conventional microscopes, and have revealed the need for improvement in the optomechanics of microscopes, in three main areas:

1. Resolution - The ability to adjust the optics and sample on a nanometer scale
2. Flexibility - The ability to use a wide assortment of peripheral optics and devices; the ability to use several different experimental modes simultaneously; and the ability to rapidly reconfigure the microscope without the need for re-alignment.
3. Stability - Resistance to vibration, acoustic, and thermal noise; hence the ability to maintain an

optical alignment within nanometers over the course of hours [1].



The High Precision Microscope (HPM) project, headquartered at the University of Illinois Laboratory for Fluorescence Dynamics (LFD) and funded by the National Institutes of Health (NIH), is developing a novel system and a set of optics modules to address each of these shortcomings through the construction of a new microscope for high resolution, single molecule experiments. The microscope will be equipped with the experimental capabilities of being a symmetric upright and inverted microscope, and support advanced optical capabilities such as wide field Differential Interference Contrast (DIC) imaging, wide field fluorescence imaging, scanning fluorescence imaging, Laser DIC microinterferometry, quadrant position detection, and Total Internal Reflection (TIR) illumination [1]. These capabilities are integrated together such

that many of them may be used simultaneously. Ideally, optical modules will be interchangeable with sufficient accuracy to require no calibration upon reconfiguration of the setup. A concept model of the HPM is shown in Figure 5.1.

When this microscope is used for single molecule experiments, the most important specification is the position stability of a spot on the object plane, formed by the focus of the laser. UIUC LFD is collaborating with the MIT Precision Engineering Research Group (PERG) in mechanical design and packaging of the microscope. The MIT PERG is working to design and test a modular, kinematically coupled segmented structure, verifying its improved thermal stability and mechanical repeatability over both traditional and single-piece tubular microscope structure designs.

This chapter presents the segmented structural design for the HPM, and methodology and results for assessments of its dimensional stability under asymmetric thermal disturbances. Its goal of mechanical repeatability and exchangeability on disassembly, reassembly and reconfiguration is well grounded in past assessments of canoe ball kinematic coupling performance, and detailed assessments of the performance of the serial kinematic chain of the microscope are underway and will be presented at a later date.

5.2 Design and Theoretical Basis of the Modular Structure

The HPM structure is the assembly that will hold all of the optical elements in place, thus determining their position and fit, and the relative alignment pass-through of optical signals. In this respect, the primary requirements of the structure are to:

1. Hold the optical and mechanical elements precisely together and minimize their sensitivity to thermal drift, mechanical vibration, and acoustic noise.
2. Support several optical paths for the peripheral optics and devices.
3. Allow easy access to the components so they may be aligned, adjusted, and cleaned without removal.
4. Be air and light tight, although being vacuum tight is not required.
5. Be arranged in such a way as to reduce stray light within the system.

To meet these requirements, a modular tubular structure was proposed, with canoe ball kinematic couplings connecting the structural segments. The three main projected advantages of this design are:

1. Stability with respect to thermal creep because the tube structure distributes heat so that the tube expands with significantly less circumferential thermal gradient than a one-piece tubular structure.
2. Precision alignment of the optical axes, enforced by the inherent repeatability and geometric error averaging behavior of the kinematic couplings between the segments.
3. Easy reconfiguration to accommodate different optical assemblies.

Under normal laboratory conditions, this design seeks to meet performance goals of:

1. Less than 5 nm deviation of the optical beam at the sample stage from angular drift of the stack structure, caused by gradual room temperature fluctuations of less than 0.5 °C.
2. Relative radial repeatability of the optical axes of 0.2 microns when the stack is disassembled and reassembled in an identical serial configuration. If interchangeable modules are calibrated with position and orientation errors of the ball and groove placements, 0.2 micron exchangeability shall be achievable when these error offsets are considered.

The design breaks the structure into vertical sections, a series of aluminum tube rings connected by highly repeatable canoe ball kinematic couplings, as shown in Figure 5.2. By segmenting the structure, it is hypothesized that an incident asymmetric thermal disturbance will be directed circumferentially around the structure, and significant axial heat flow will be prevented by the air gaps between the tubes and the minimal coupling point contacts between the tubes. Hence, by maximizing the angular uniformity of the temperature distribution of the structure, the asymmetry of axial thermal expansion of the structure will be minimized. In a microscope, non-uniform axial thermal expansion causes in-plane misalignment of the optical beam axes at the point of examination; even drift of a few nanometers can cause loss of the image in single molecule experiments. In this respect, the infinity corrective objectives used in present microscopes can deal with uniform axial expansion, and radial expansion is not an issue as long as the center point where the objectives reside remains in the same radial position as the stage below it. Here, an equal angle three-groove arrangement of kinematic couplings would provide uniform radial expansion and geometrically-averaged motion of the center point by constraining the ball sets to slide in the grooves when the tubes expand.

5.2.1 Specifications of Prototype Structures

The prototype segmented stack structure for the thermal stability and mechanical repeatability experiments consists of five hollow cylindrical 6061-T651 Aluminum tubes, 12" outside diameter and 9" inside

diameter, with equilaterally triangular hole and spot-face patterns on each end to accommodate the kinematic couplings. The center tube is 2.56" long, while the remaining four tubes are identical in feature geometry, but 4.24" long. These dimensions were scaled down (to decrease manufacturing cost) from the original dimension set with 16" outside diameter, proposed by the UIUC LFD for the operational microscope; however, critical dimensionless ratios relating to heat flow through the geometry were preserved. The geometrically similar control structure, a single tube with the same inner diameter, outer diameter, and total length as the coupled series of segments, was also procured.

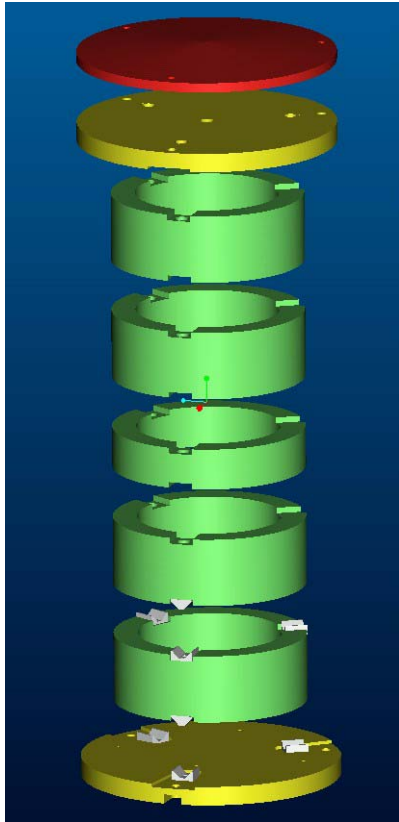


Figure 5.2: Exploded model of segmented structure including two canoe ball sets.

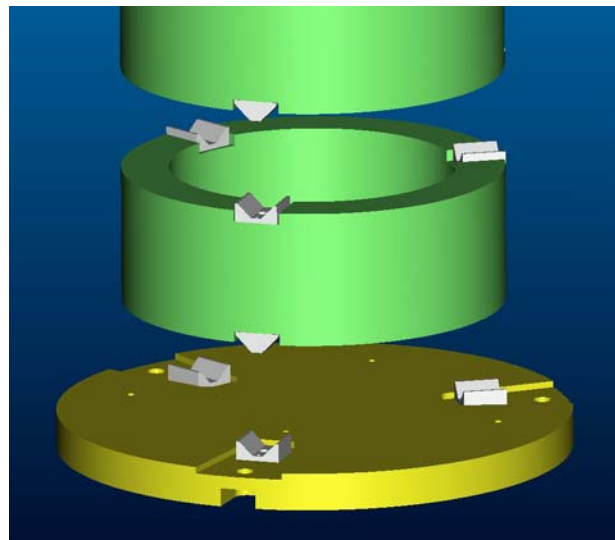


Figure 5.3: Close view of canoe ball interfaces between segments.

The canoe ball couplings, used as interconnects between the segments of the former structure, and between the ends of the tube regions and the mounting plates of both structures, were machined from AISI 420 stainless steel, hardened to Rockwell C50-55 and CNC precision ground to fine surface roughness. The male ball units have a spherical surface radius of 0.25 m, and the female groove units are standard 45-degree flat vees. The couplings were aligned to the seat mounts using 3.0 mm diameter spring pins, and lightly (0.02 mm Δd) press-fit into place. Contrary to the robot interface application, stress-limiting design of the couplings was not a factor; sizes were chosen to take advantage of high repeatability with large surface radius and fine surface finish, and for stiffness to maintain high natural frequencies.

For testing, both tube assemblies were placed between the same set of identical top and base plates, and tightened in compression with full-length threaded rods. To distribute the compressive load equally among the couplings, an additional plate was added at the top of the structure, to which the threaded rods were bolted through stacks of belleville spring washers, and the load was transmitted to the stack by a centrally seated 1" diameter steel tooling ball.

5.2.2 Supporting Heat Transfer Theory

Having presented the concept of a segmented, kinematically coupled design for instrumentation structures, its performance characteristics can now be explained in terms of general heat transfer and mechanics relations. First, the theorized ability of the segments to enforce greater circumferential uniformity of temperature than the single-piece structure is seen by examining the constant temperature profiles when an ideal point-located disturbance is applied to one side. As shown in Figure 5.4, the temperature profiles on the single-piece tube (considering length far greater than diameter) are nearly circular in side view, and flow the disturbance equally in axial and circumferential directions. On the other hand, the far lesser length to diameter ratio of the short segment constrains the axial heat flow, forcing the contours to show constant temperature bands in the circumferential direction. Hence, the difference in average temperature between the heated and non-heated sides of the long tube is greater than that on the short tube, and the greater total variance in temperature between the distant sides of the single-piece structure creates a greater discrepancy in the non-uniformity of thermal expansion.

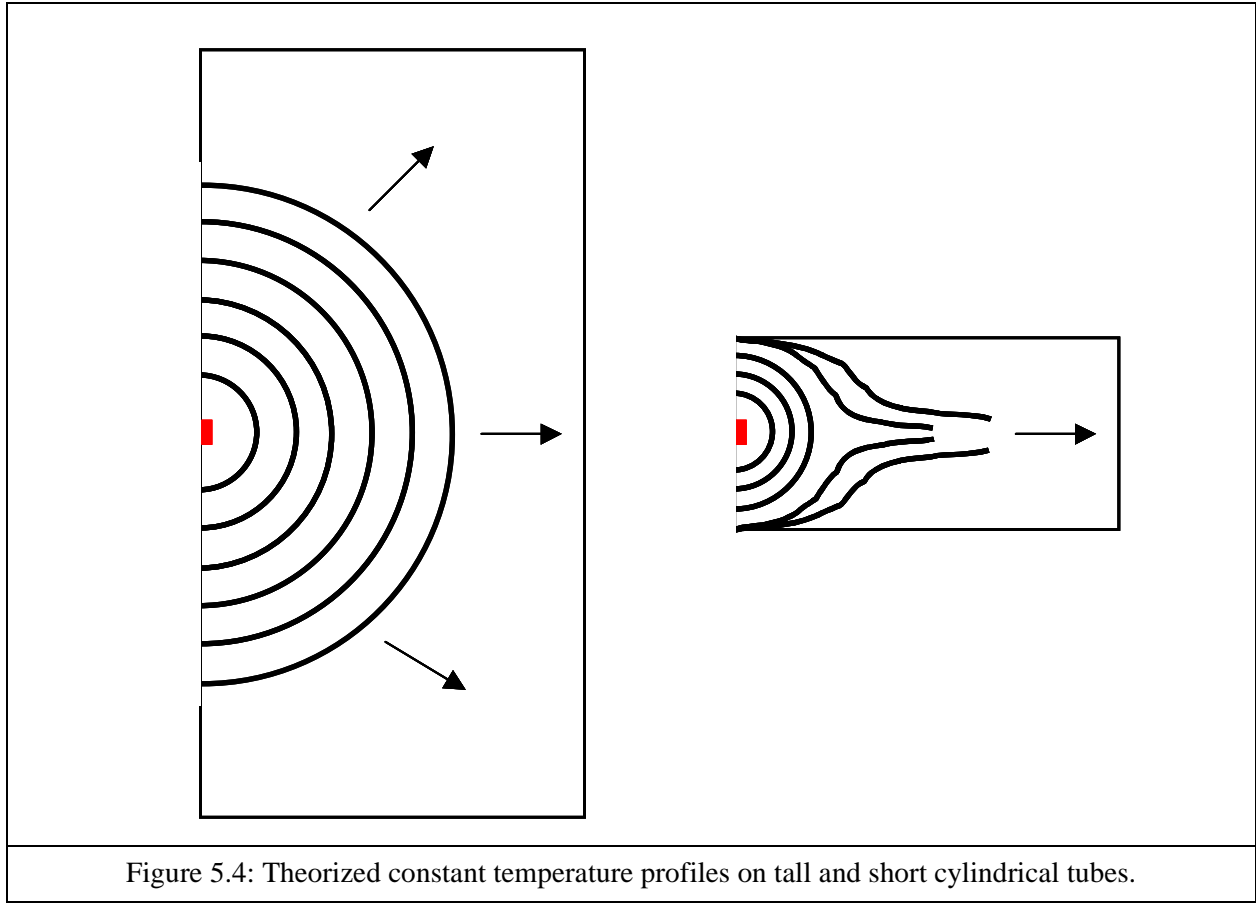


Figure 5.4: Theorized constant temperature profiles on tall and short cylindrical tubes.

The one-dimensional thermal expansion of a body with length L_o , subject to a uniform temperature increase ΔT , is:

$$\frac{\Delta L}{L} = \epsilon_{thermal} = \alpha_t \Delta T, \quad (5.1)$$

where α_t is the material coefficient of thermal expansion. Relating this to the difference in length δ between opposite sides of a cylinder when a thermal disturbance is applied to one side:

$$\delta = \alpha_t L_o (\overline{T_h} - \overline{T_n}) = \alpha_t \left(\int_0^{L_o} (T_h(z) - T_n(z)) dz \right), \quad (5.2)$$

where the temperatures on the heated (T_h) and non-heated (T_n) sides are expressed as averages or definite integrals.

The gross error motion that causes misalignment of the optical axes is tilt of the top of the structure relative to a fixed bottom plane. Geometrically, this angle relates to δ by:

$$\theta_{tilt} = \text{atan}\left(\frac{\delta}{D_s}\right), \quad (5.3)$$

where D_s is the diameter of the structure at the supports of the top plate. θ_{tilt} equals the angle of misalignment of the optical axes; hence, δ_{obj} , the translational error of the objectives at the sample stage is:

$$\delta_{obj} = L_S \frac{\delta}{D_s}, \quad (5.4)$$

where L_S is the axial length from the top plate to the sample position. Combining relations (5.2) and (5.4), the translational error at the sample position relates to the mean temperature difference through:

$$\delta_{obj} = L_S \frac{\alpha_t L_o (\overline{T_h} - \overline{T_n})}{D_s}. \quad (5.5)$$

Substituting values for the prototype design, the mean temperature difference causing 5 nm drift at the objectives is 0.00047 °C. Although this is an extremely small difference, one which would be extremely difficult to control for experimentation, the primary goal of this study is to show the magnitude of benefit of the segmented design over the one-piece design; this is not complicated by applying an artificially large thermal disturbance since the error motion scales linearly with the temperature difference across the structure.

Next, the steady-state temperature difference is related to the magnitude of the thermal disturbance, Q , by the generalized thermal resistance, R , through:

$$Q = \frac{(\overline{T_h} - \overline{T_n})}{R}. \quad (5.6)$$

Treating the circumferential path of heat flow as one through a generalized linear body with effective area A , effective length L , and material thermal conductivity k ,

$$Q = \frac{(\overline{T_h} - \overline{T_n})}{L} A k. \quad (5.7)$$

Rearranging (5.7) and substituting into (5.5):

$$\delta_{obj} = L_s \frac{\alpha_t L_o L Q}{D_s A k}. \quad (5.8)$$

Therefore, with the goal to minimize δ_{obj} for a chosen structure geometry, the best material for steady-state performance is one with maximum thermal conductivity per unit of tendency to thermally expand, k/α_t . Higher k decreases the steady-state temperature difference between sides of the structure, while higher α_t represents a greater magnification into translational error at the sample.

However, since in a normal laboratory the structure will conceivably never reach a steady-state, constantly being subject to small thermal disturbances convected by air currents, the transient performance of the design is of greater importance. While it is cumbersome to express the transient temperature profile for the annular geometry of this structure in closed form, it is known that the penetration depth of temperature change through the structure t seconds after the thermal disturbance begins is related to the Fourier number, Fo:

$$Fo = \frac{t\alpha}{L^2}, \alpha = \frac{k}{\rho c_p}, \quad (5.9)$$

where α is the material thermal diffusivity and L is a generalized characteristic length. Assuming fixed geometry, the optimal structure material for transient performance is one with maximum α/α_t . Values of the steady-state and transient performance indices, k/α_t and α/α_t , are given for candidate metals in Table 5.1.

Material	Steady-state (k/α_t), W/m-K	Transient (α/α_t), m ² /s
Aluminum (6061-T651)	7.0×10^6	2.8
Copper	2.4×10^7	6.9
Brass	5.8×10^6	1.8
Stainless Steel (AISI 410)	1.9×10^6	0.54

Table 5.1: Steady-state and transient performance index values for various metals.

Among the materials surveyed, copper is conclusively the best choice, with over twice the transient performance index value of aluminum. Although for material and manufacturing cost reasons, aluminum was chosen for the prototype setup, superior performance would result if copper is chosen for the final HPM. This is confirmed by simulation results presented later.

To justify choice of boundary conditions for finite element simulations to be discussed later, free convection approximations from the structure are now presented. When the structure sits in a relatively calm ambient environment, with surface temperature greater than the surrounding air, the dominant mode of heat loss is through thermobuoyant free convection. Since the center of the structure is closed by the top and base plates, it is assumed to behave like a solid cylinder with uniform surface temperature (ignoring local gradients due to application of the disturbance), for which the following closed-form relations are well known:

$$Q_{ku} = \frac{Ak_f(\text{Nu}_L)(T_s - T_\infty)}{L} \quad (5.10)$$

$$(\text{Nu}_L) = [(\text{Nu}_{L,l})^6 + (\text{Nu}_{L,t})^6]^{\frac{1}{6}} \quad (5.11)$$

$$(\text{Nu}_{L,l}) = \frac{2.8}{\ln \left(1 + \frac{2.8}{a_1(\text{Ra}_L)^{\frac{1}{4}}} \right)} \quad (5.12)$$

$$(\text{Nu}_{L,t}) = \frac{0.13\text{Pr}^{0.22}}{(1 + 0.61\text{Pr}^{0.81})^{0.42}}(\text{Ra}_L)^{\frac{1}{3}} \quad (5.13)$$

$$a_1 = \frac{4}{3} \frac{0.503}{\left[1 + \left(\frac{0.492}{\text{Pr}} \right)^{\frac{9}{16}} \right]^{\frac{4}{9}}} \quad (5.14)$$

$$(\text{Ra}_L) = \frac{g\beta_f(T_s - T_\infty)L^3}{\alpha_f\nu_f} \quad (5.15)$$

$$h = \frac{Q_{ku}}{A(T_s - T_\infty)} \quad (5.16)$$

Here, g is the gravitational constant, β_f is the fluid coefficient of thermal expansion (reciprocal of absolute temperature for ideal gases), α_f is the fluid thermal diffusivity, ν_f is the fluid viscosity, and Pr is the fluid Prandtl number (0.69 for air at 300 K). Iteratively specifying a value for T_s using a spreadsheet, the steady-state convection coefficient h can be found for which the total surface convection loss Q_{ku} equals the magnitude of the thermal disturbance. For example, if 3W is applied, $T_s = 296.8$ K (for $T_{inf} = 295$ K) and $h = 1.93$ mK/W.

All heat transfer relations are referenced from Kaviany [2].

5.3 Thermal Stability Evaluation

The thermal stability of the HPM design was evaluated by applying circumferentially non-uniform thermal disturbances to the structures, and measuring the resulting circumferential and axial temperature distributions, and angular distortion of the top mounting plate. While the enforced disturbances were far stronger than those customary for a normal laboratory environment for a microscope, the results give an ordinal performance comparison between the designs, and validate a finite element model used for subsequent experiments and design optimization.

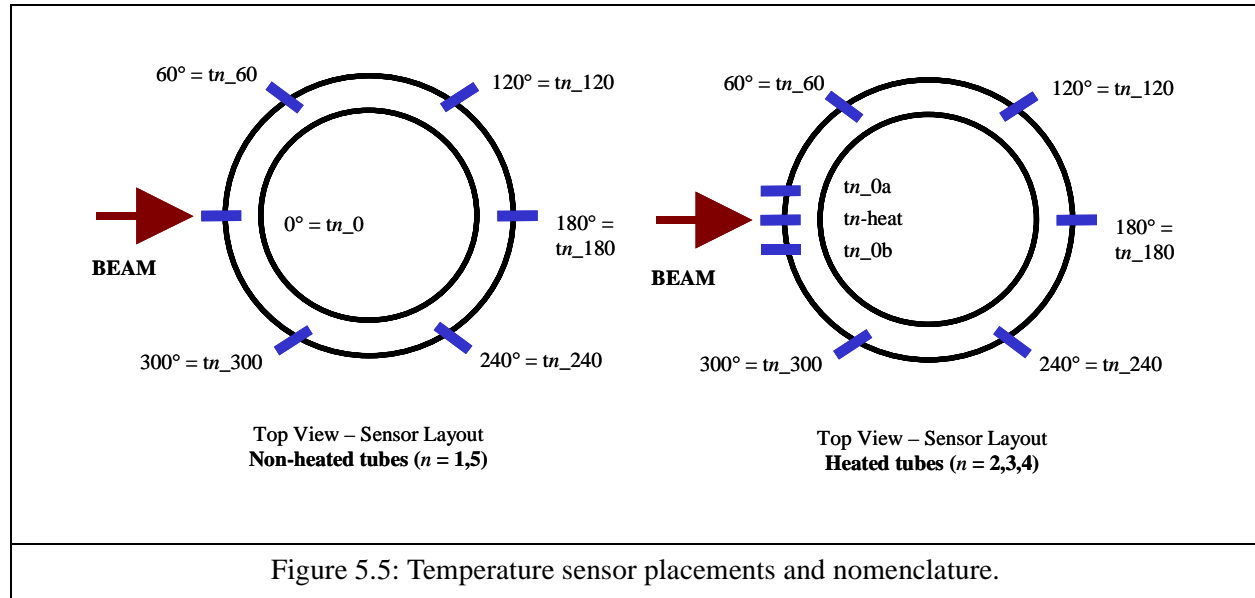
5.3.1 Experimentation Setup and Procedure

5.3.1.1 Temperature Metrology

The temperature distribution on the structure was monitored using fifty-two three-wire platinum RTDs (resistive temperature detectors), procured pre-assembled from National Instruments. The RTD's were wired to a 16-bit PCMCIA computer data acquisition card through a NI SCXI-1000 chassis containing four SCXI-1122 multiplexer modules with SCXI-1322 terminal blocks, each with sixteen differential measurement channels. A RTD is conditioned by applying a small excitation current through its terminals, then measuring the voltage across the terminals and calculating the RTD resistance, which is pre-calibrated as a function of temperature. The chosen sensors have nominal resistance of 100 ohms at 0 °C and fit the standard European RTD polynomial curve ($\alpha=0.00385$). The RTD's have an operating range from -50 °C to 204 °C, accurate to within ± 0.45 °C, and with resolution (dictated by the input voltage limits and the 16-bit nature of the DAQ card) of 0.0078 °C [3]. Temperatures were taken from each sensor once each minute, recorded using National Instruments Labview software, logged into a standard tab-delimited text file, and analyzed using Microsoft Excel.

Thirty-six RTD's were mounted to the stack structure, six on each of the non-heated tubes, and eight on each of the heated tubes. On the heated tubes, one sensor was placed directly on the heat source, and two neighboring sensors were placed 1" to the left and right of the source. The remaining sensors were placed at equally-spaced 60 degree circumferential intervals, named and located as shown below. The RTD's were

mounted in equivalent positions on the single-tube structure. The mounting locations and adopted nomenclature are given in Figure 5.5.



Additionally, seven RTD's were mounted to the central column; four equally spaced vertically in a single line up the column, and four equally spaced circumferentially just below the interferometer mount (one RTD shared between both sets of four). Eight RTD's were placed to monitor the air temperature near the structure, four sets of two each at 90-degree placements, 4" from the surface of the structure. Each set was hung from a PVC pipe support, with one at the level of the gap between tubes 1 and 2 and one at the level of the gap between tubes 4 and 5. This was intended to capture the circumferential and vertical (heat rises) heating phenomena of the air, and validate through this trend that the tube sensors predominately measure the metal temperature.

One RTD was placed outside the isolation chamber to monitor the temperature fluctuations within the test area. All RTD's mounted to metal were contacted to a dab of thermally-conductive paste, secured to the surface using Kapton tape, and insulated from the air using a small section of 1-1/4" X 1/2" standard household foam tape. The RTD's measuring air temperature were hung freely from their supports.

5.3.1.2 Dimensional Metrology

Angular drift of the stack was measured using a Sago differential plane mirror interferometer (DPMI), mounted to a 5" diameter aluminum column placed within the stack assembly, and measuring the tilt of a reference mirror mounted to a horizontal reference plate attached to the top of the tube set. The optics were placed as shown in Figures 5.6 and 5.7. The interferometer laser was located outside of the thermal isolation chamber, and the 6 mm diameter beam from the laser entered the chamber through a 1" diameter, 0.5" thick optical window. The beam then was bent 90 degrees by a fold mirror, traveling upward parallel to the axis of the reference column, and entering the interferometer. At that point, the beam was polarized and split sequentially twice, into two source measurement beams for taking differential linear measurements of the motion of the top plate, and two reference beams for comparison. These beams were processed into a single optical signal, directed out the back of the interferometer to a fiberoptic pickup mount, and into a flexible fiberoptic cable routed to the measurement board. The ZMI 1000 measurement board connected to a Windows PC running the ZMI 1000 software, and the interferometer output was displayed on the screen and recorded to a text file as an angular value, in arcseconds. Single-point values were saved to disk once each minute during testing.

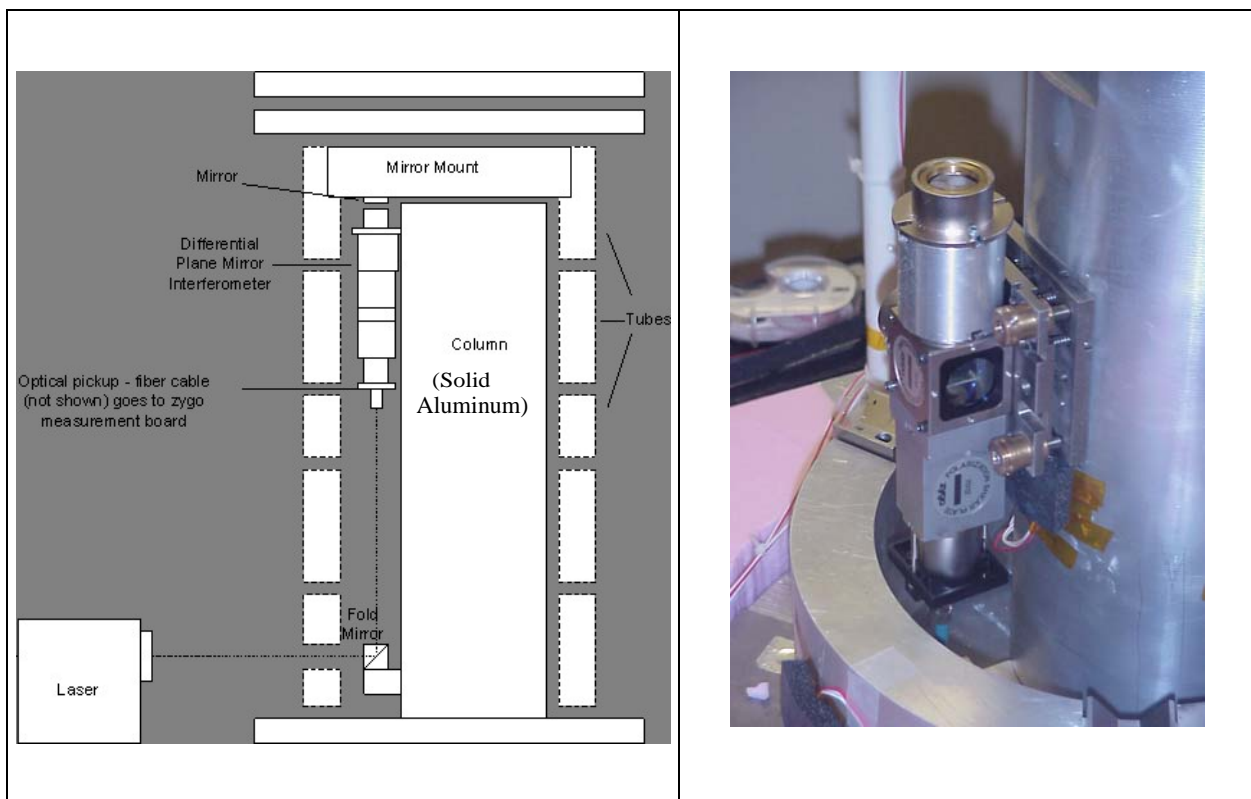


Figure 5.6: Optical beam path and laser metrology setup.	Figure 5.7: DPPI assembly on 5" diameter central reference column.
--	--

5.3.1.3 Application of Thermal Disturbances

Thermal disturbances were applied to the structure using Minco copper thin film heating elements, powered by a Xantrex XT 30-2 regulated DC power supply with a maximum nominal output of 60 W. Each source measured 1/2" x 1/2", with a maximum operating temperature of approximately 80 °C.

For the initial tests, three sources were mounted directly to the structure, one each at the vertical mid-points of the three center tubes, parallel to the axis of the interferometer. This placement maximized the ability of the single-axis interferometer to capture the gross error motion from thermal expansion, as ideally the maximum differential expansion of the stack was seen by the measurement beams. The three sources were wired in a simple parallel circuit, so each was supplied the same voltage. The voltage across the circuit was monitored continuously throughout the test, and the power was calculated directly from

knowledge of the resistance across each heat source. Nominally, 3W (5V, 0.6A) was applied to the circuit, such that each source emitted nearly 1W.

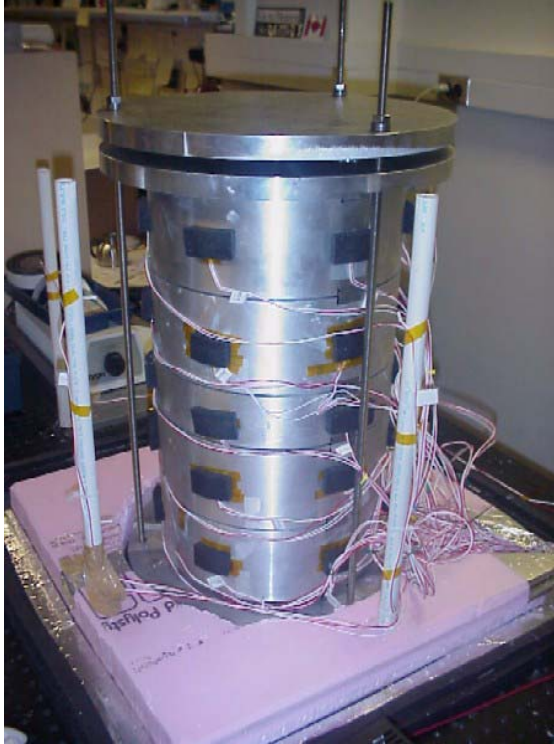


Figure 5.8: Final test assembly - segmented structure.

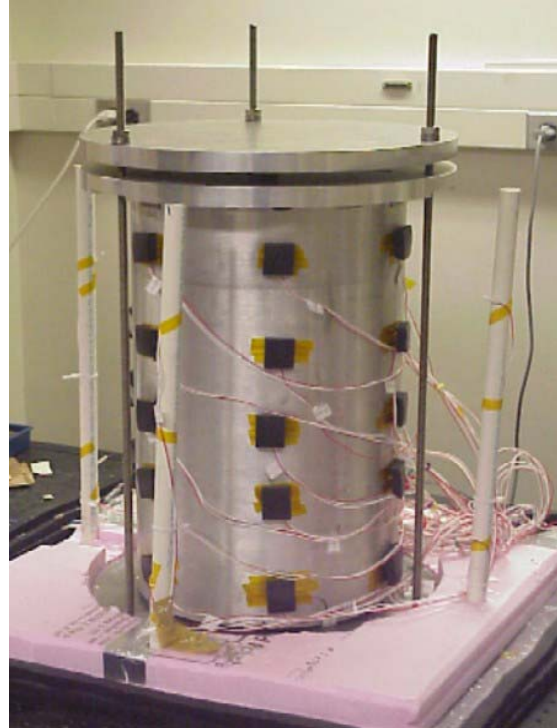
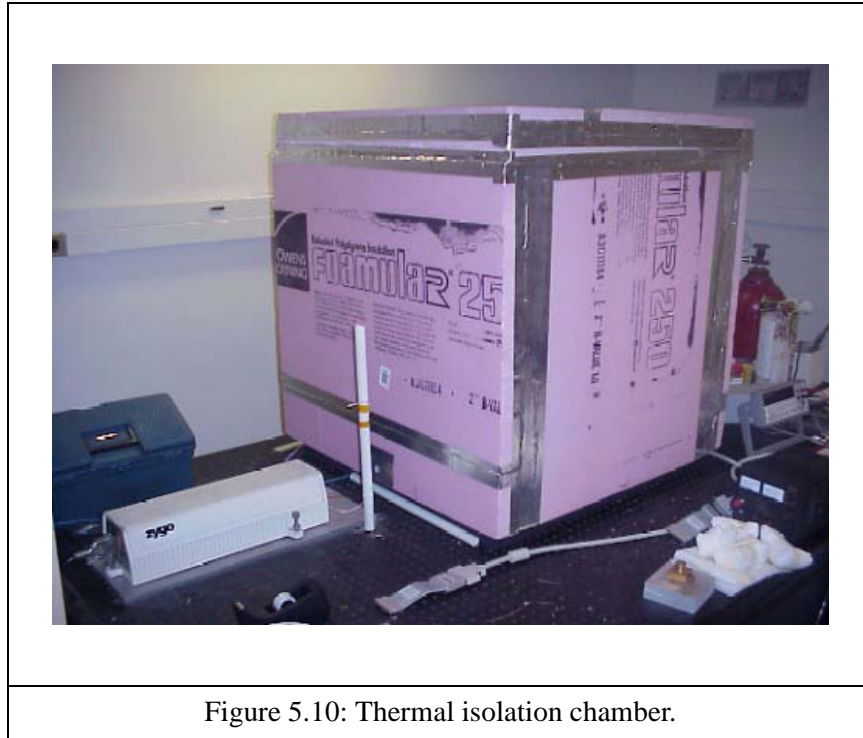


Figure 5.9: Final test assembly - one-piece control structure.

5.3.1.4 Thermal Isolation Chamber

In order to isolate the structure from temperature disturbances, which can occur due to heating, cooling and air currents in the room, the test apparatus was placed in an insulated chamber. The chamber, with internal dimensions of 24" x 24" x 30" (L x W x H), was constructed of 4" thick extruded polystyrene (Styrofoam) with an R-value of 20 ($k = .029$ W/m K). The walls and top of the chamber were butt-jointed together and bonded using hot melt glue. All joints were sealed with Reflectix tape and silicone sealant. The seal along the bottom of the chamber was achieved by placing the chamber on a perimeter of 1.5" thick open cell neoprene, which deformed under the weight of the chamber. A two-inch thick layer of polystyrene insulated the exposed area of the table around the stack structure with a dimension of just under 24

in. X. 24 in. The stack itself was placed on top of a 1/16 in. thick layer of Buna-N rubber to isolate it from any thermal disturbances that were transmitted through the threaded holes in the optical table.



5.3.1.5 Test Procedure

For the initial tests using three contacting heat sources each emitting 1W, the following test procedure was established:

1. Seal the structure in the thermal chamber for at least four hours before testing, to allow any prior thermal non-uniformities from exposure to room air to attenuate.
2. Following this period, begin acquisition of interferometer and temperature data. Take a single-point reading from the Zygo measurement board once each minute, and cycle through all temperature sensors once each minute. Each cycle of temperature measurements consisted of a single-point reading from each sensor, with subsequent readings separated by a one-second delay.
3. After one hour of such data acquisition, activate the heat sources. Continue data acquisition with heating for the next six hours.

4. After these six hours of heating, deactivate the heat sources and continue data acquisition for the next hour.

5. After this one hour, terminate data acquisition and remove the thermal chamber to speed dissipation of heat from the structure in preparation for the next test. Leave the structure uncovered for at least four hours.

Hence, this '1/6/1' test specifies eight hours of continuous data acquisition, with one-hour non-heated periods preceding and following a six-hour heated period.

5.3.2 Finite Element Simulation Setup and Procedure

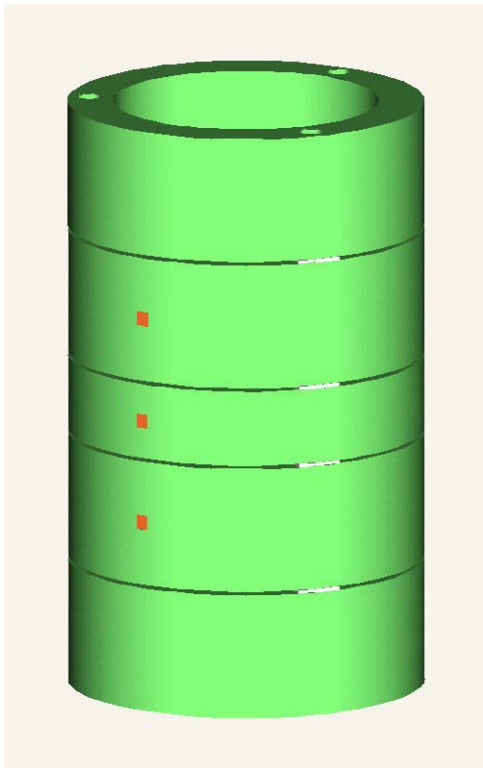
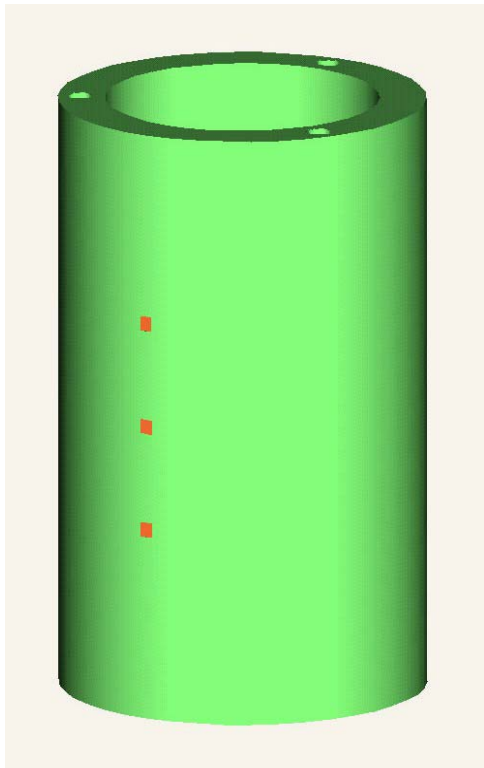
Prior to conducting the physical thermal stability experiments, a performance comparison between the segmented and one-piece control structures was made using finite element models in Pro/MECHANICATM. The structural solid models were simplified for simulation to those shown in Figures, 5.11 and 5.12, treating the tube sections as the only significant bodies, and replacing the kinematic coupling balls and grooves on the segmented structure with sets of 1.4" square (a very liberal estimate given the true nearly point contact) contacts between the nearly 1/8" (3 mm) tube-to-tube gaps.

Consistent with the laboratory test procedure, three 1/2" square heat sources were placed in a column at the horizontal centerlines of the second, third, and fourth segments, and at equivalent positions on the one-piece structure. Shown in red, these surfaces were defined as heat loads with input of 1W each. Using the thermobuoyant convection relations in Section 5.2.2, a uniform steady-state loss coefficient of 2 m-K/W was defined on the external cylindrical surfaces of the model, balancing the heat input of 3 W.

After building the solid model and defining the thermal loads and boundary condition, the thermally-induced deformation of the structure was determined by running consecutive Pro/MECHANICATM thermal and structural analyses, using the results of the thermal analysis as the boundary condition for the structural analysis. Because this stepped analysis is unique, it is worthwhile to detail the simulation procedure:

1. Within the thermal module of Pro/MECHANICATM, the thermal simulation was executed using the aforementioned heat load and convection boundary conditions. A multi-pass adaptive analysis was defined, with 8th-order maximum convergence to within 10% of global and local energy norms. Given the heat source magnitudes, this convergence metric ensured the steady-state results exhibited a mature gradient.

2. After the thermal analysis completed, the solid model was opened in the Structure module of Pro/MECHANICA.
3. The bottom ring face was constrained in all six degrees of freedom.
4. A temperature load of type MEC/T Temp was defined, specifying the Analysis input as the thermal analysis of the structure, and the Load Set as the 3 X 1W load set. The option to Use Previous Design Study was not chosen, as it was found necessary to have Pro/MECHANICA generate a new mesh for the structural analysis rather than use the thermal analysis mesh from before. Consistent with the thermal analysis, the reference temperature was left to the default of zero.
5. The structural simulation was executed, defining the same analysis parameters as described in step 1 for the thermal simulation.

 <p>A 3D rendering of a segmented cylindrical structure. The cylinder is composed of several horizontal rings, each separated by a thin gap. The entire structure is colored in a bright green. There are three small red square markers on the side of the cylinder, one on each of three different segments.</p>	 <p>A 3D rendering of a one-piece cylindrical structure. It is a solid, continuous cylinder with a uniform green color. There are three small red square markers on the side of the cylinder, arranged vertically.</p>
<p>Figure 5.11: Solid model of segmented structure for finite element simulation.</p>	<p>Figure 5.12: Solid model of one-piece control structure for finite element simulation.</p>

Each simulation converged within thirty minutes, using a 850 MHz Pentium III notebook, with 250 of the total of 512 MB system RAM allocated to the solver. Solution for the segmented model took approximately 75% longer than for the one-piece model.

5.3.3 Results

5.3.3.1 Finite Element Simulations

Having executed combined thermal and structural simulations, Figures 5.13 and 5.14 depict the solved steady-state constant temperature contours for the segmented and one-piece simplified models. Here, the hypotheses advanced in Section 5.2.2 are corroborated, with the heat disturbances directed prominently in the circumferential direction on the segments, while nearly equally in the axial radial directions on the one-piece structure. Within the range and resolution displayed, the contours remain elliptical on the one-piece structure, and approach the suggested hyperbolic form near the unheated side of the segmented structure. Significant temperature change within this resolution propagates nearly fully (180 degrees) around the segments, yet no more than 60 degrees around the tall single piece structure. The unheated segments show near perfect uniformity, being well-isolated from the disturbances by the stainless steel kinematic couplings.

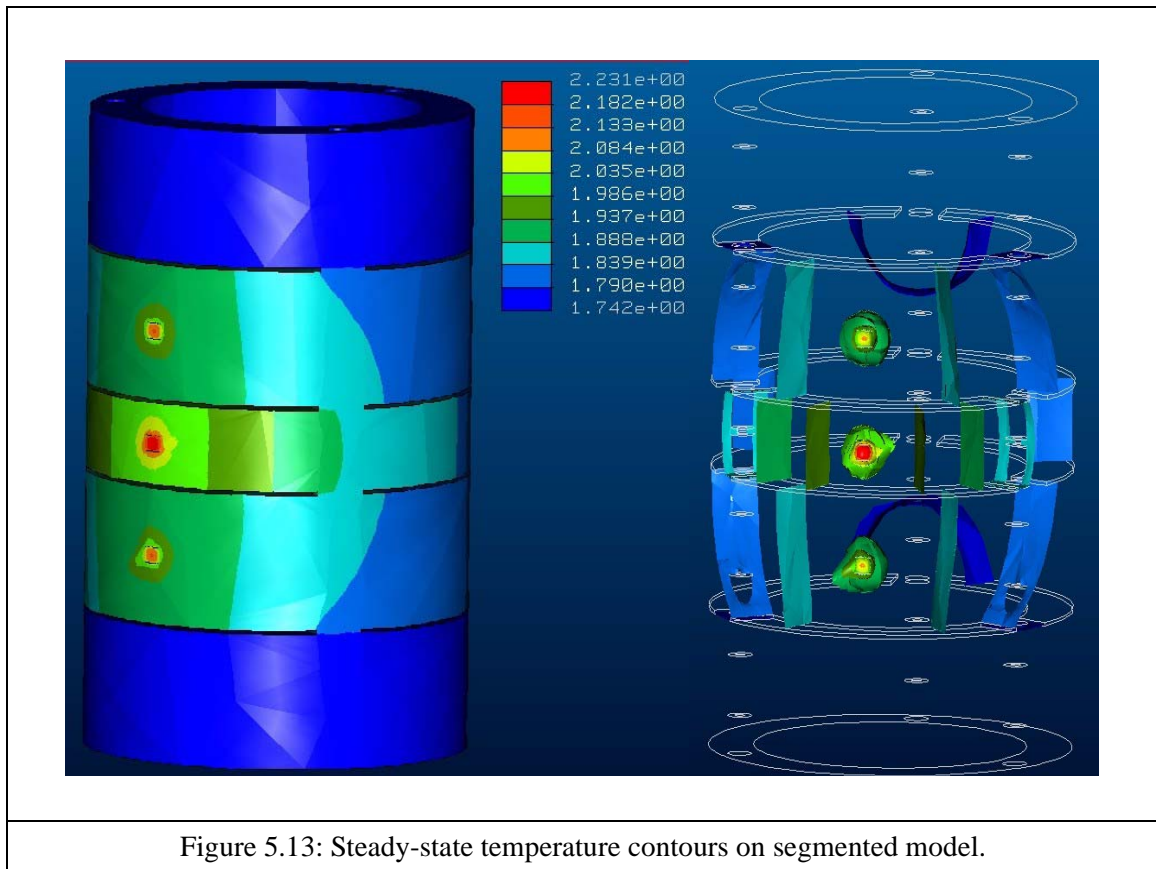


Figure 5.13: Steady-state temperature contours on segmented model.

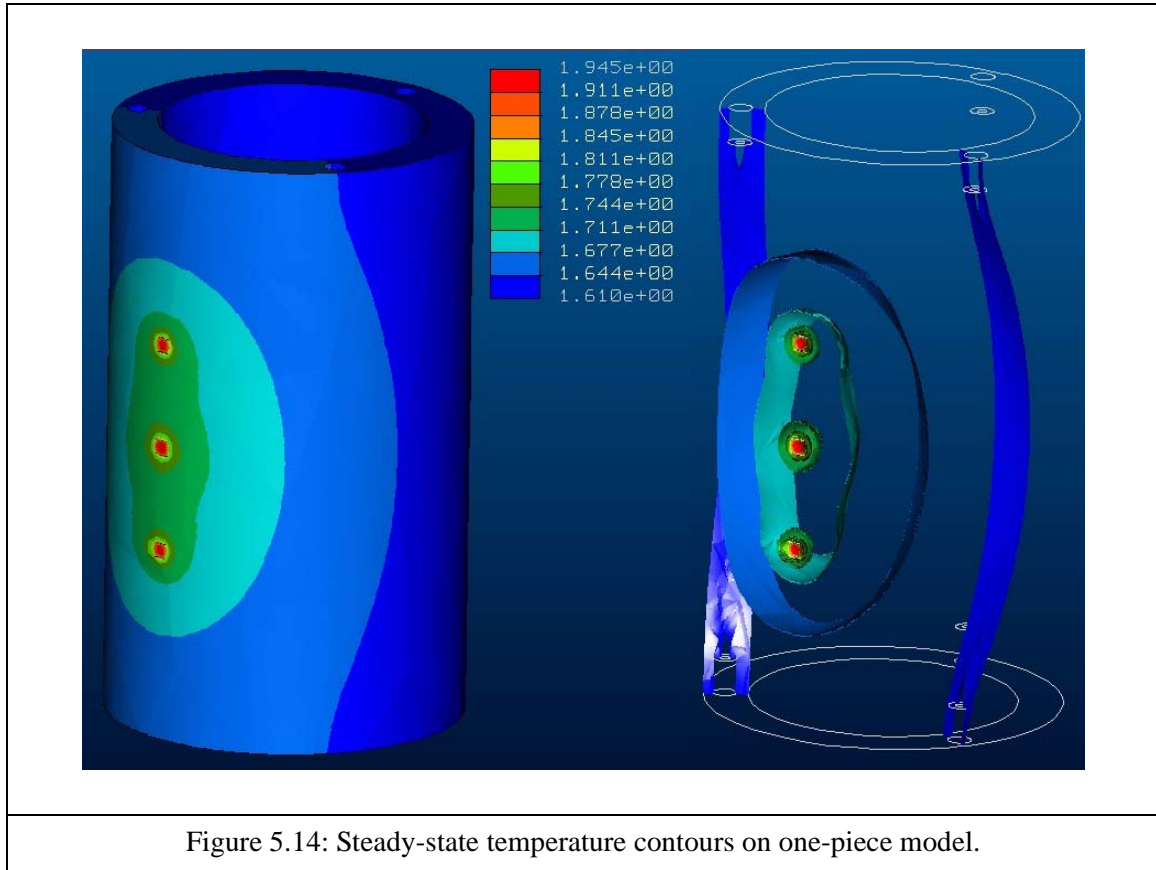
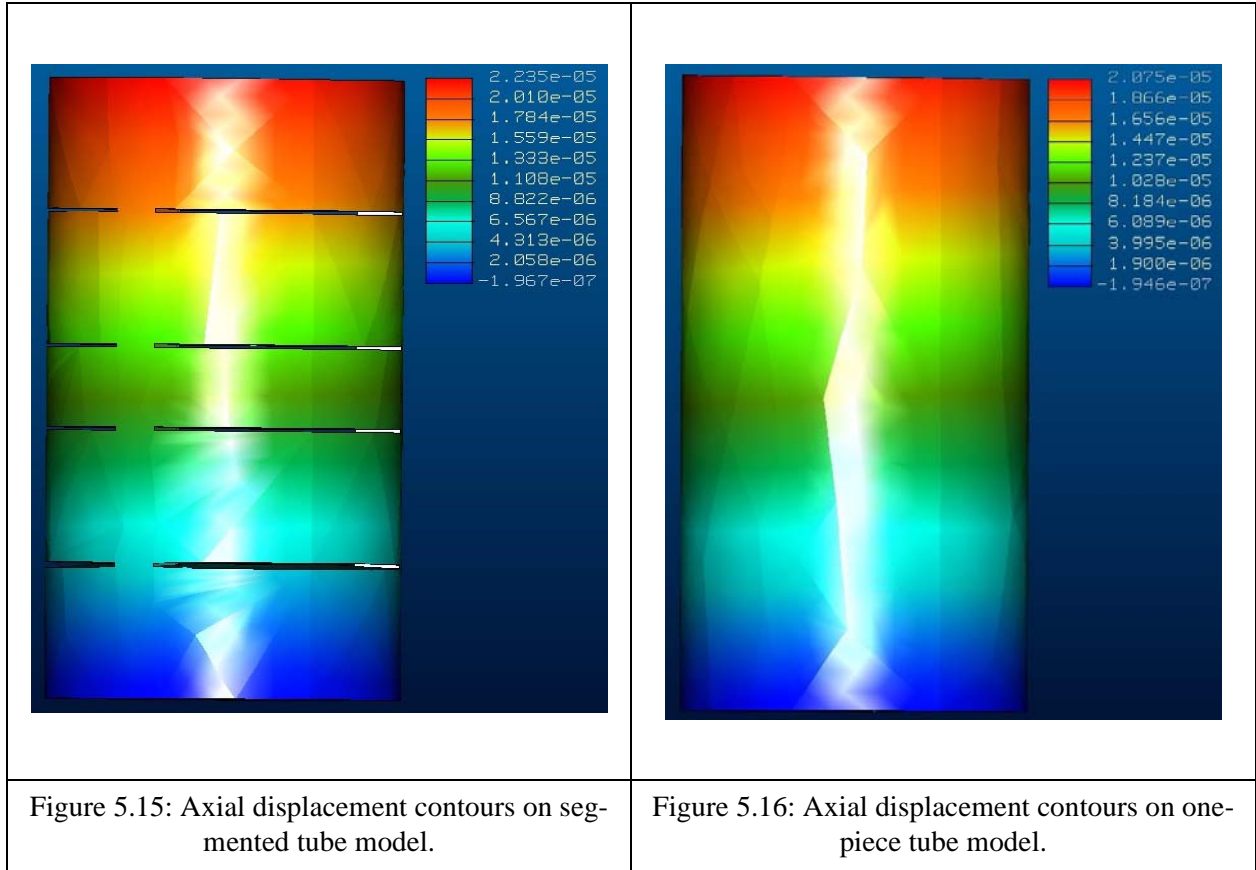


Figure 5.14: Steady-state temperature contours on one-piece model.

Figures 5.15 and 5.16 show the axial displacement distribution on the structures. In both cases, the axial displacement of the top surface of the assembly is slightly greater on the heated side than on the non-heated side, and this difference is greater for the one-piece structure. Specifically, the top of the heated face of the segmented structure displaces 22.3 microns, and the top of the non-heated face displaces 21.7 microns, equaling a uniaxial tilt of 0.46 arcseconds. Conversely, the top of the heated face of the one-piece structure extends 20.7 microns, while the non-heated face extends 19.8 microns, equaling a uniaxial tilt of 0.70 arcseconds. Thus, by simulation, the one-piece structure is 52% more thermally sensitive than the segmented design.



It is also important to consider the thermally-induced deformation in the radial direction. While uniform radial expansion would keep the axes aligned perfectly, consistent with kinematic coupling theory, non-uniform expansion would lead to translation at the sample position of no less than one third the magnitude of the non-uniformity. However, assuming excess of static friction between the coupling ball and groove at a particular joint, the advantage of the coupling is manifested in the ability for relative motion between segments, hence keeping their central axes aligned while also thermally isolating them. Capability for relative motion was not built into the structural models presented, but differences in radial expansion at the outer surfaces were queried to be as much as 0.1 micron, approximately 20% of the equivalent objective plane deformation caused by the asymmetric axial expansion.

5.3.3.2 Laboratory Experiments

Three sets of measurements were taken on each of the two structures, following the 1/6/1 hour schedule of heating with three 1 W sources described in Section 5.3.1.5. This section presents the angular interferometer measurements and selected temperature measurements for one trial on each structure; the metrics reported were repeatable within 0.1 arcsecond and 0.01 °C between the respective sets of trials.

Each plot is accompanied by a short explanation. In advance summary, the results demonstrate:

1. Maximum angular deflection of 0.6 arcsec for the segmented structure and 1.0 arcsec for the one-piece structure, translating to linear drift of approximately 675 and 1090 nm at the central objective position. These values represent a 60% performance degradation, or vice-versa a 40% performance improvement, between the segmented and one-piece designs.
2. Circumferential temperature differences of 0.10-0.25 °C across the heated tubes of the segmented structure, which are nearly constant over the heated duration of the experiments. Differences across all levels of the one-piece structure are 0.05-0.13 °C.
3. Nearly perfect circumferential temperature uniformity in the chamber air, around the non-heated tubes, and around the central column reference. Hence, the tubes act as thermally isolated bodies, and the interferometer readings are not subject to error from angular drift of the central column.

These results are largely consistent with the Pro/MECHANICA simulations; specific comparisons are given in the next section.

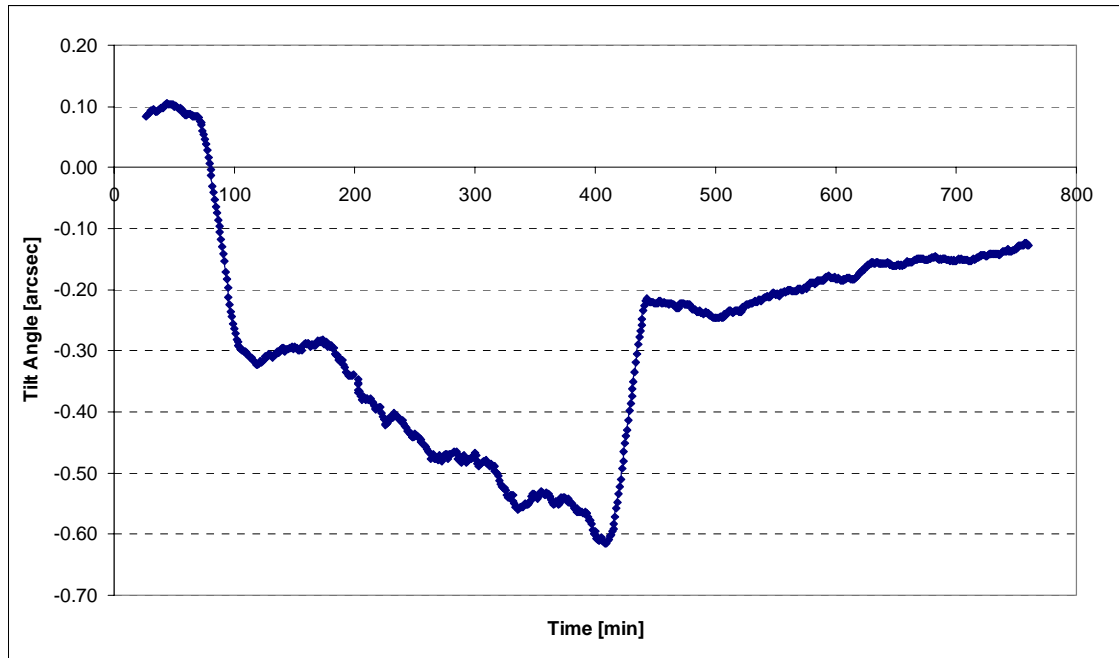


Figure 5.17: Deflection of segmented structure versus time (measurement duration extended to 13 hours to show thermal relaxation).

The interferometer values shown in Figures 5.17 and 5.18 are taken as 30-minute (30-sample) moving averages, which smooth the 0.06 arcsec resolution of the differential measurement. The steeper gradients are seen at the commencement (at $t = 60$ min) and termination (at $t = 360$ min) of heating. Maximum drifts of 0.60 arcsec and 0.87 arcsec are seen respectively for the segmented and one-piece structures, corresponding to linear movements of approximately 725 nm and 1050 nm at the central objective position. When the disturbance is applied, the deflection rapidly moves to an intermediate value as heat is reaching the sensors on the heated side before it flows around the circumference and affects the sensors on the non-heated side. When the sensors on the non-heated side are disturbed - when the iso-temperature contours drawing in Figure 5.4 are advancing at nearly the same rate at the heated and non-heated sensor positions - the rate of increasing deflection stabilizes. When the disturbance terminates, analogous rapid relaxation occurs, and then the relaxation slows and trends toward zero.

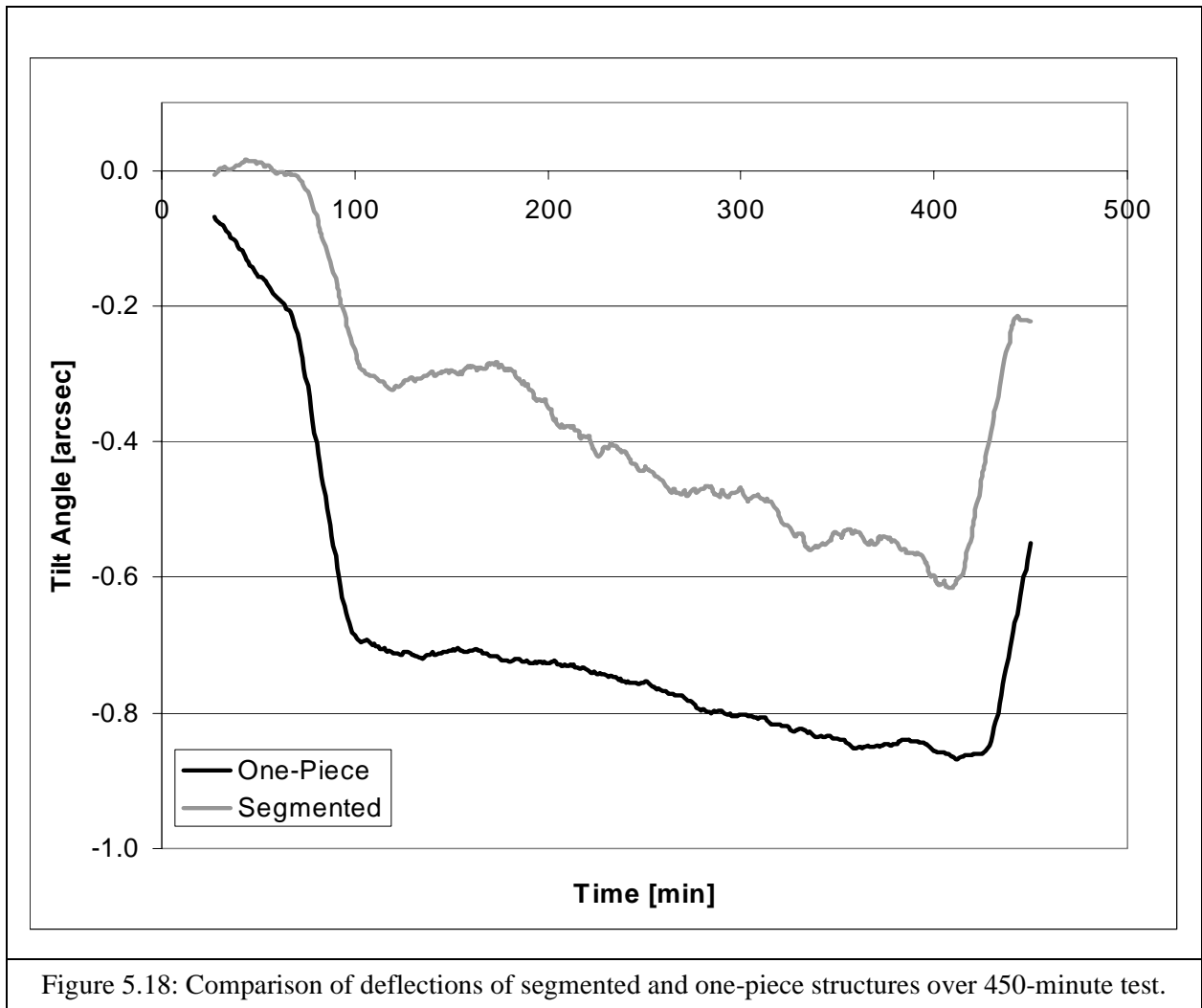


Figure 5.18: Comparison of deflections of segmented and one-piece structures over 450-minute test.

Comparing the transient profiles of the two structures as in Figure 5.18, the response of the one-piece structure during the first hour of heating is greater than the segmented structure; 120 minutes after measurement starts, the one-piece structure has drifted approximately 0.7 arcsec, while the segmented structure has drifted approximately 0.3 arcsec. This is a much greater discrepancy than after 8 hours of measurement, as after the initial heating period roles reverse and the one-piece structure continues to drift at a considerably slower pace than the segmented structure. This can be rationalized in terms of the ratios of axial to radial dimensions of the structures. Upon application of heat, the axial flow in the one-piece structure is continuous over a greater distance than in the segmented structure, hence more heat is directed circumferentially around the segments than around the one-piece tube. This shows that the segmented structure is far

superior in disturbance rejection, being 60% less sensitive to thermal input than the one-piece structure during the first hour of heating. Although the performance gap closes to only a 30% advantage over the course of several hours, the microscope design seeks stability of the image spot over approximately one hour, making the initial transient performance most important.

Several sets of interferometer data were also taken under identical experimental conditions, only without heat applied to the structure. These results verify the stability of the interferometer readings within 0.12 arcsec over several hours, subject to noise equal to the resolution magnitude of 0.06 arcsec.

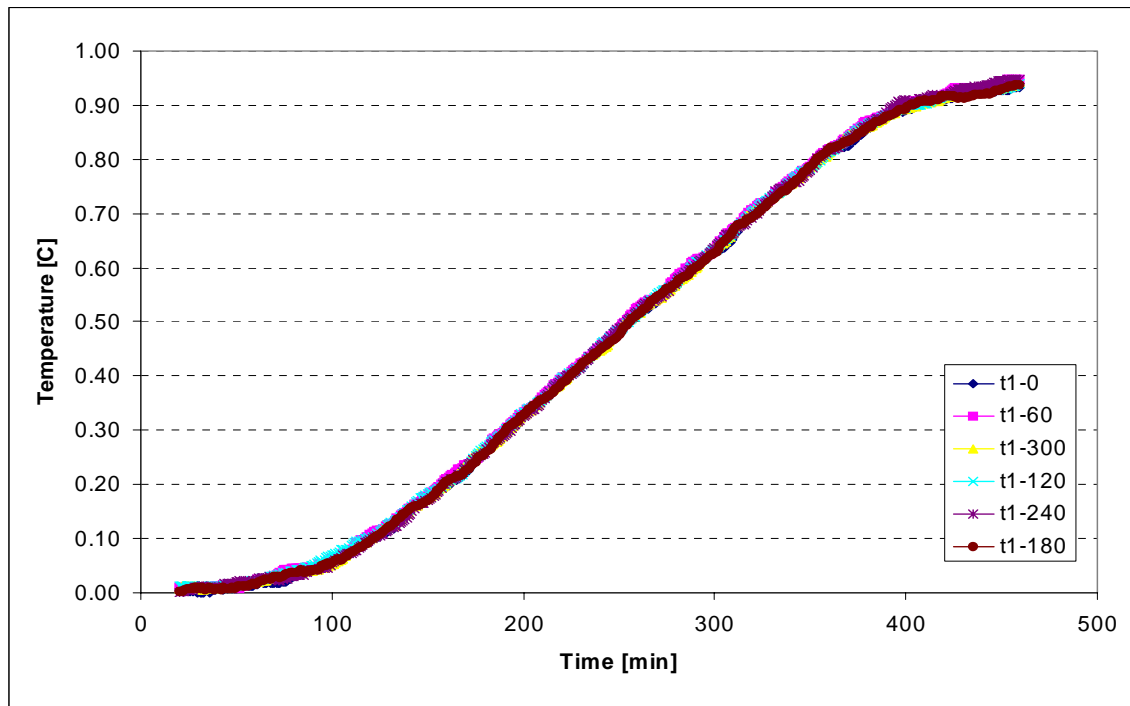


Figure 5.19: Normalized temperatures (10-minute averages) around tube 1 (non-heated) of segmented structure.

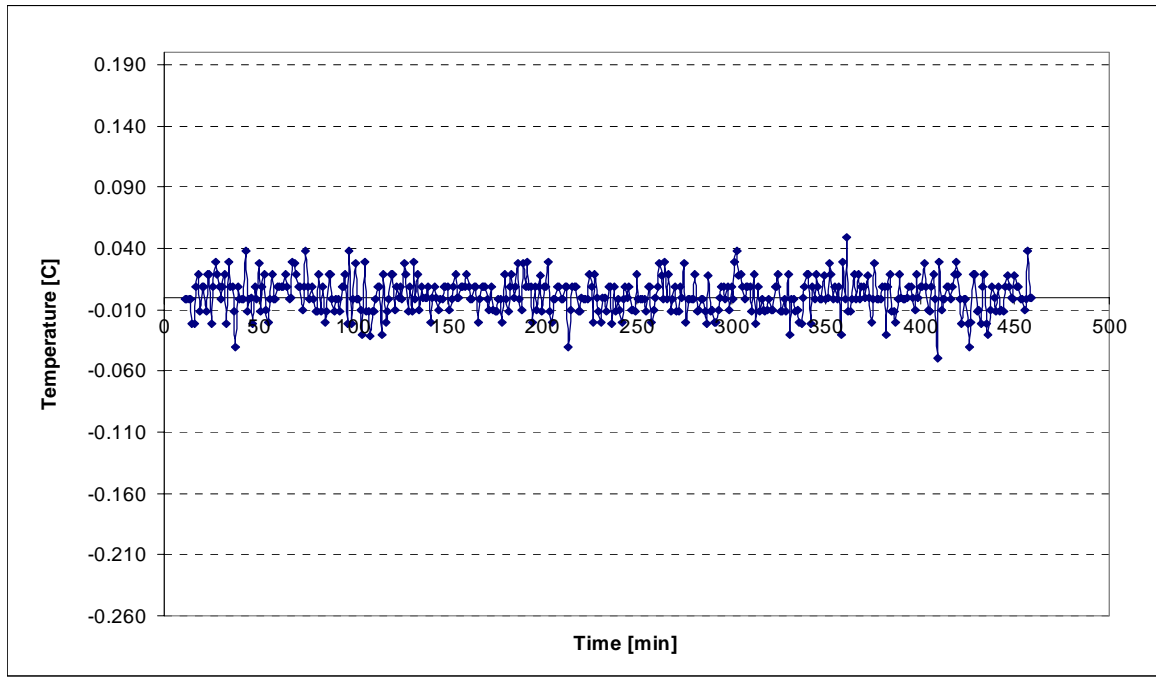


Figure 5.20: End-to-end normalized temperature difference on tube 1 (non-heated) of segmented structure.

Figures 5.19 and 5.20 show how the non-heated tubes of the segmented structure maintained almost perfect circumferential symmetry of temperature throughout the experiments; hence the air gaps and spot kinematic contacts between the tubes are excellent thermal isolators. The tubes heated uniformly by approximately 0.7°C during the test duration, yet the end-to-end range remained stable and centered at zero with RMS deviation of 0.02°C .

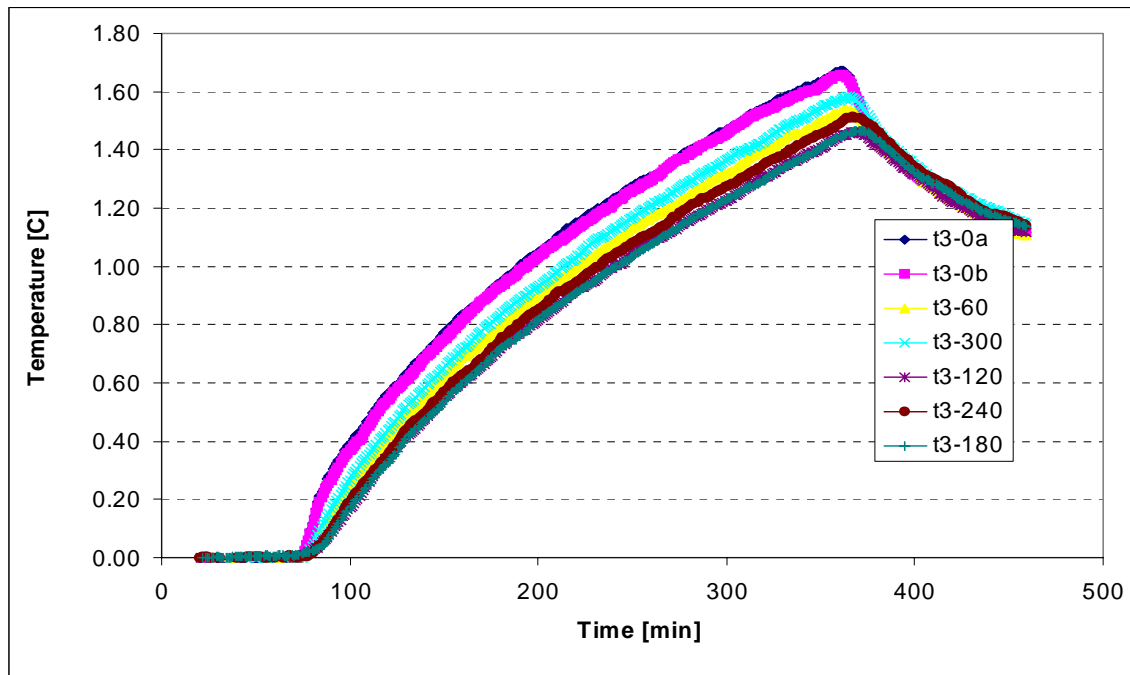


Figure 5.21: Normalized temperatures (10-minute average) around tube 3 (heated) of segmented structure.

Figure 5.21 displays the delayed circumferential heating pattern of the heated segments, as the sensors near the heat source show initial temperature changes approximately ten minutes after the start of heating, and the heat then flows around the tube. The farthest sensor is activated approximately ten minutes after the start of heating, after which all sensor temperatures increase at nearly constant and identical rates until heating is discontinued.

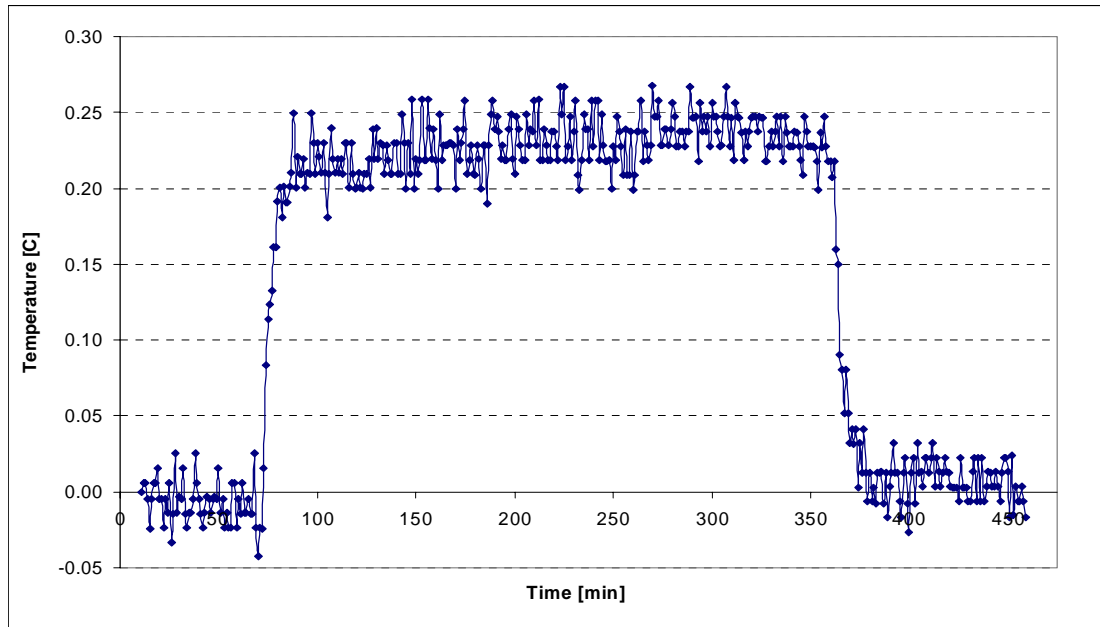


Figure 5.22: End-to-end normalized temperature difference on tube 3 (heated) of segmented structure.

Ten minutes after heating started, the end-to-end temperature range increased to 0.22 °C, gradually increased to 0.24 °C, and then gradually decreased until heating ends. This gradual decline is a motion toward a long-term steady-state circumferential gradient, predicted by simple calculations to be achieved after approximately 20 hours of constant heating.

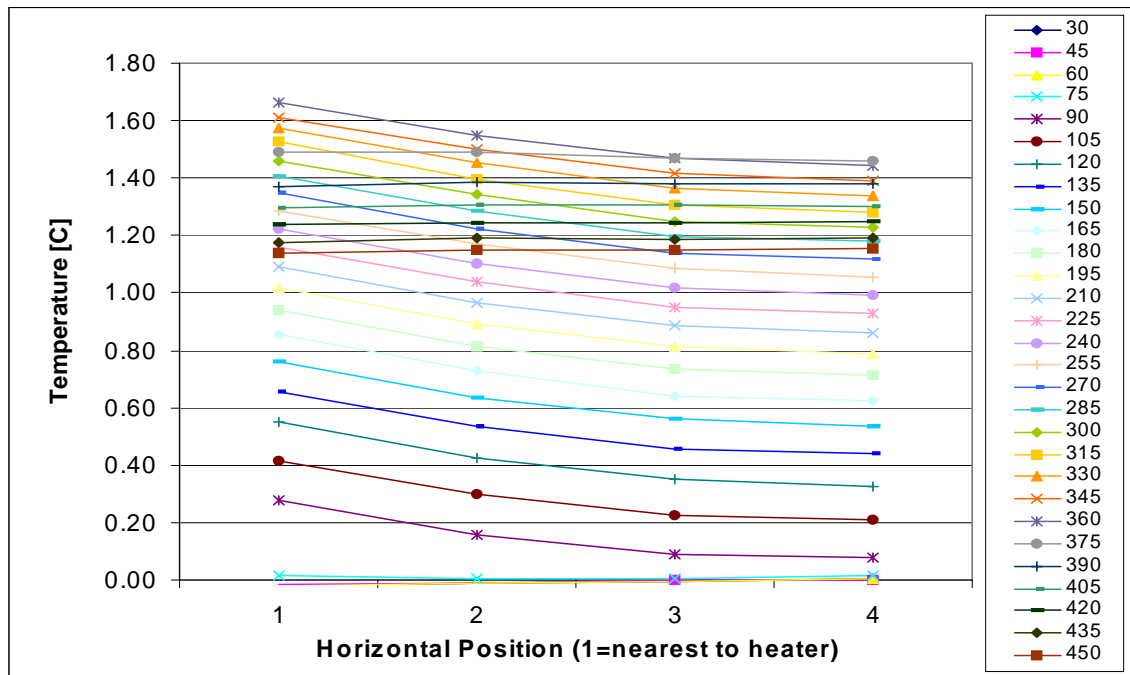


Figure 5.23: Circumferential normalized temperature profiles for tube 3 of segmented structure.

Figure 5.23 emphasizes the constancy of shape in the circumferential profiles starting approximately thirty minutes after heating begins. Once the steady-state gradient is established, relative temperature changes are uniform around the tube.

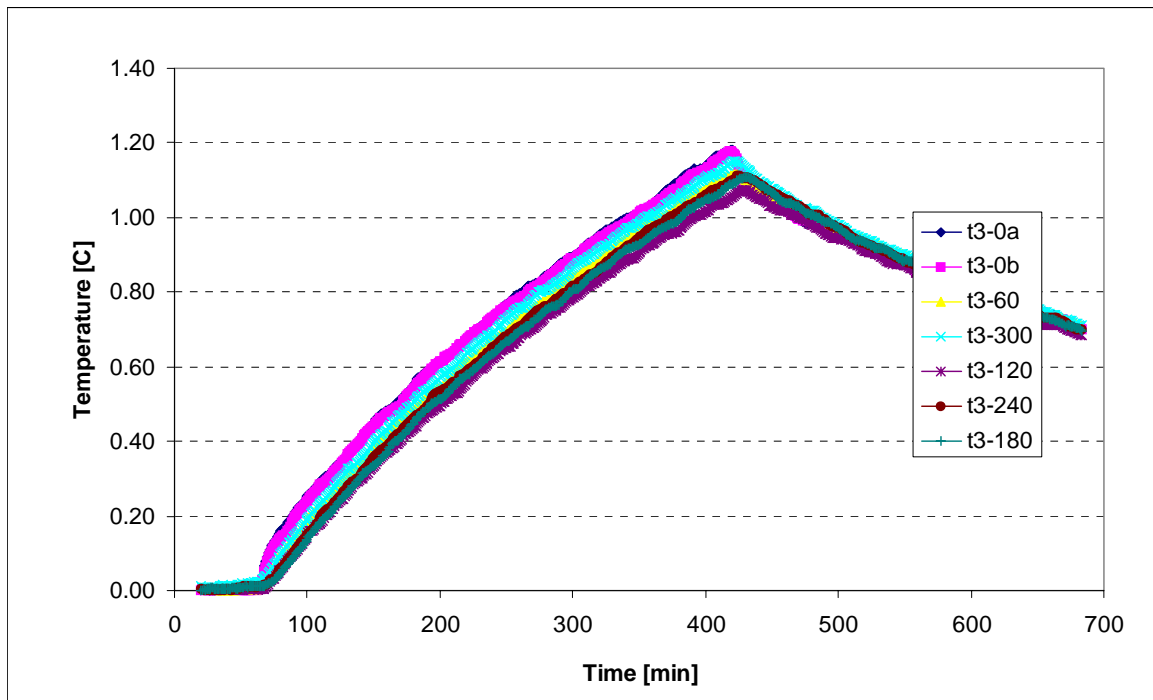


Figure 5.24: Normalized temperatures (10-minute average) around level 3 of one-piece structure.

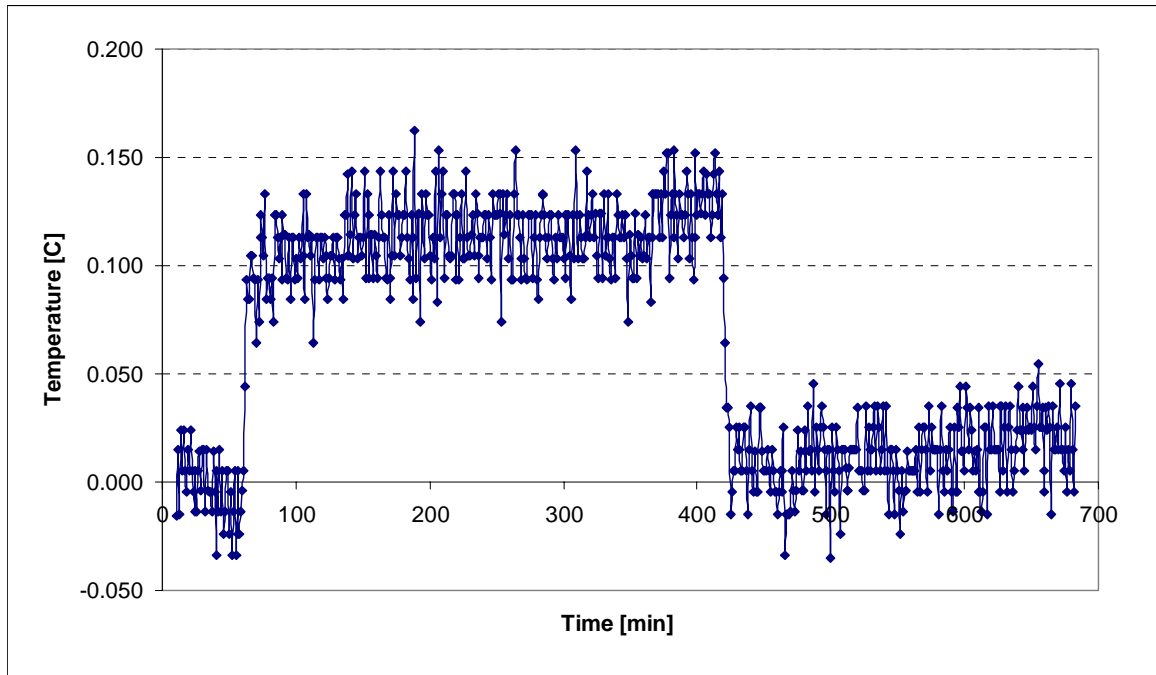


Figure 5.25: End-to-end normalized temperature difference at level 3 of one-piece structure.

Figures 5.24 and 5.25 show the characteristic thermal evolution of the levels of the one-piece structure. Trends for the third level are shown in Figure 5.25 with a steady non-uniformity of $0.12\text{ }^{\circ}\text{C}$. The behavior of all levels of the one-piece structure is similar to that of the heated tubes of the segmented structure, as the heat spreads radially from the sources and is not constrained in the axial direction until it flows to the absolute ends of the structure. Because of the lack of axial constraint, the total circumferential heating at this level is $1.2\text{ }^{\circ}\text{C}$, compared to $1.6\text{ }^{\circ}\text{C}$ for the third segment. Similarly, the $0.12\text{ }^{\circ}\text{C}$ steady circumferential non-uniformity here is approximately half of the $0.23\text{ }^{\circ}\text{C}$ value for the third segment. However, the one-piece structure carries such a difference fully along its length, whereas the segmented design restricts it to the heated segments. Because the segments channel the disturbances around the tubes, and prevent axial transmission between segments, the error motion of the segmented structure is significantly diminished.

Charts in Appendix C show that the air temperature inside the chamber was circumferentially uniform at both levels of measurement, and insensitive to fluctuations in the external laboratory temperature. The

air temperatures near and far from the heaters tracked almost perfectly upon application of the heat sources, confirming that the tube-mounted sensors were effectively recording the metal temperatures. Furthermore, the central reference column, to which the interferometer was mounted, exhibited uniform heating with circumferential temperature differences no greater than 0.02 °C, significantly less (less than approximately 0.05 arcsec) than the non-uniformity around the structure. Therefore, expansion of the central column had a negligible effect on the interferometer readings of the structural tilt.

5.3.3.3 Comparison - Validation of Simulation Models

To this point, qualitative similarities between the simulation results and the experimental results are evident; as predicted by Pro/MECHANICA, the non-heated segments exhibited near-perfect circumferential uniformity throughout the tests, while the heated segments and all levels of the one-piece structure showed considerable steady-state temperature differences. Quantitatively, Table 5.2 compares the temperature differences (heated side minus non-heated side) at each tube centerline level for both structures, when simulated using Pro/MECHANICA and when measured in the laboratory. At the heated levels, values are averages of those from the two sensors placed 1” from the sources.

Level (1 = bottom)	ΔT Segmented - Simulated	ΔT Segmented - Measured	ΔT One-Piece - Simulated	ΔT One-Piece - Measured
1	0.01	0.00 +/- 0.01	0.07	0.06 +/- 0.01
2	0.12	0.13 +/- 0.02	0.12	0.09 +/- 0.02
3	0.18	0.21 +/- 0.03	0.12	0.12 +/- 0.01
4	0.12	0.12 +/- 0.02	0.12	0.09 +/- 0.02
5	0.01	0.00 +/- 0.01	0.07	0.06 +/- 0.01

Table 5.2: Simulated and measured end-to-end circumferential temperature differences [C].

Within the levels of uncertainty (the 2-sigma confidence intervals between trials) of the experiments, the simulated and measured temperature differences are within 0.01 °C at all levels of both structures. The simulation reports steady-state results after at least 20 hours of heating, while the experimental measurements are transient values after only 4-6 hours of heating. However, with exponential transient progression

of heat, the temperature difference across a solid body subject to a constant heat input is nearly stable soon after application of the disturbance, as confirmed by the end-to-end difference progressions in Figures 5.21 and 5.24. Furthermore, the simulation model assumes that the coupling contacts are the only heat flow between the segments; since for simplicity no boundary volume is defined around the segmented structure and no outflow condition is specified for the intermediate top and bottom faces of the tubes, there is no convection flow across these interfaces. The specification of a uniform convection coefficient across the entire outer surface of the structures, which clearly inaccurately assumes uniform temperature distributions, is another small, yet permissible discrepancy.

Beyond these reasons, the true goal of this study is an ordinal optimization in two respects: first to establish the approximate advantage of the segmented design over the one-piece design; and second to ordinally determine the best geometry for the segments. Especially in the second case, the absolute performance values are less important than the relative rankings of the candidate designs.

5.3.3.3 Analytical Model of Thermal Expansion

It is also instructive to compare the time-varying laboratory interferometer measurements to predictions of the thermal expansion of the segmented structure. Using the thirty-six temperature measurements from the surfaces of the segmented structure as inputs, two predictions of the deflection were made: one assuming a constant vertical temperature distribution on each segment; and the other using a conventional transient approximation for spatial and temporal deviation. The two predicted trends and the measured trend are shown in Figure 5.26.

The first prediction is a good approximation of the steady-state tilt of the structure, yet fails to capture the behavior of gradual expansion which precedes the steady state. In assuming constant vertical temperature profiles on each segment (taking the RTD measured value at each location), this method ignores the transient delay associated with heat flow in the vertical direction. By using the direct measurements along the horizontal centerlines of the tubes the delay in circumferential flow is directly accounted for, yet the results over-estimate the deflection due to vertical heat flow until the vertical temperature profiles are truly constant at a near steady-state at $t = 350$ minutes. This estimate is based on a simple finite sum of the ther-

mal expansions of each segment, differenced between the heated and non-heated sides. The difference in linear expansion is calculated as:

$$\delta = \alpha \left[\left(\sum_{i=1}^5 L_i T_i \right)_{heated} - \left(\sum_{i=1}^5 L_i T_i \right)_{nheated} \right] \quad (5.17)$$

where L_i is the length of each segment, and T_i is the measured temperature at its horizontal centerline. From this linear difference, the angle is found using Equation 5.3. In providing a good steady-state estimate, this relation can be useful in macroscopically comparing designs when only the surface temperatures are recorded.

The second method is a good prediction of the shape of the transient deflection profile, yet overestimates the magnitude of the deflection by as much as a factor of two. In this method, the vertical temperature profiles in the segments take the shape of the depthwise profiles in a semi-infinite solid body, given by the relations [2]:

$$T_{norm} = \frac{T(x, t) - T(0)}{T_s - T(0)} \left(1 - \operatorname{erf} \left(\frac{x}{2\sqrt{\alpha t}} \right) \right) \quad (5.18)$$

$$\operatorname{erf}(\eta) = \frac{2}{\sqrt{\pi}} \int_0^{\eta} e^{-z^2} dz \quad (5.19)$$

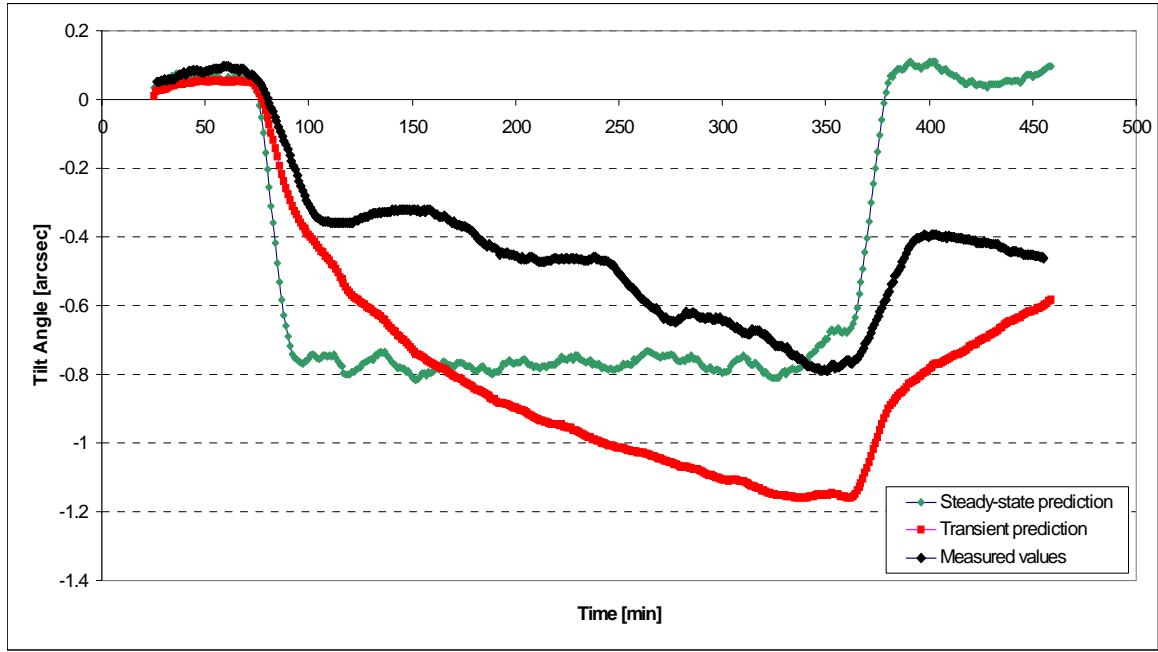


Figure 5.26: Comparison of measured and predicted angular deflections of segmented structure.

In Equation 5.18, the heated surface temperature, T_s , is invariant with time. To adapt the experimental data to this relation, T_s was specified as time-varying, with an instantaneous value equal to the temporal average of the measured value to that time. For ease of computation in a spreadsheet, the averages were updated incrementally with each time step [4]:

$$\overline{T_{s,n}} = \left(\frac{n-1}{n}\right)\overline{T_{s,n-1}} + \frac{T_{s,n}}{n}, \quad (5.20)$$

where $T_{s,n}$ is the instantaneous measured value along the horizontal centerline of each segment at time instance n . To make computation manageable, each segment was discretized into five piecewise constant sections, over which the transient profile was superimposed. This method of averaging roughly accounts for the latency in vertical heat flow due to changes in the disturbance temperature, T_s .

The semi-infinite body transient approximation is definitely crude, but is by far the simplest transient relationship available in closed form. A more appropriate closed-form solution could be one for a finite

prismatic solid body; however, that solution is based on an infinite series, and the increased complexity would not justify the slightly better (seen from $Fo = 0.08$ for semi-infinite body vs. $Fo = 0.07$ for finite body) solution. In either case, these methods are one-dimensional solutions, ignoring that the real case is one of two-dimensional conduction (vertical and circumferential) along the surface from the thin-film sources used in the tests. Furthermore, these methods assume that the heat source is uniform and time-averaged over the disturbed surface, while really it is localized and instantaneously variant.

A more accurate method would be to treat each segment as a series of slices, with each slice a finite thin volume with lumped (constant temperature) capacitance. However, this is approaching the finite element method, which enables appropriate assignment of boundary conditions and localized heat sources. Knowing the accuracy of the steady-state simulations from Pro/MECHANICA, similar transient simulations would be the best way of estimating the time-variant deflection absent direct experimental measurements.

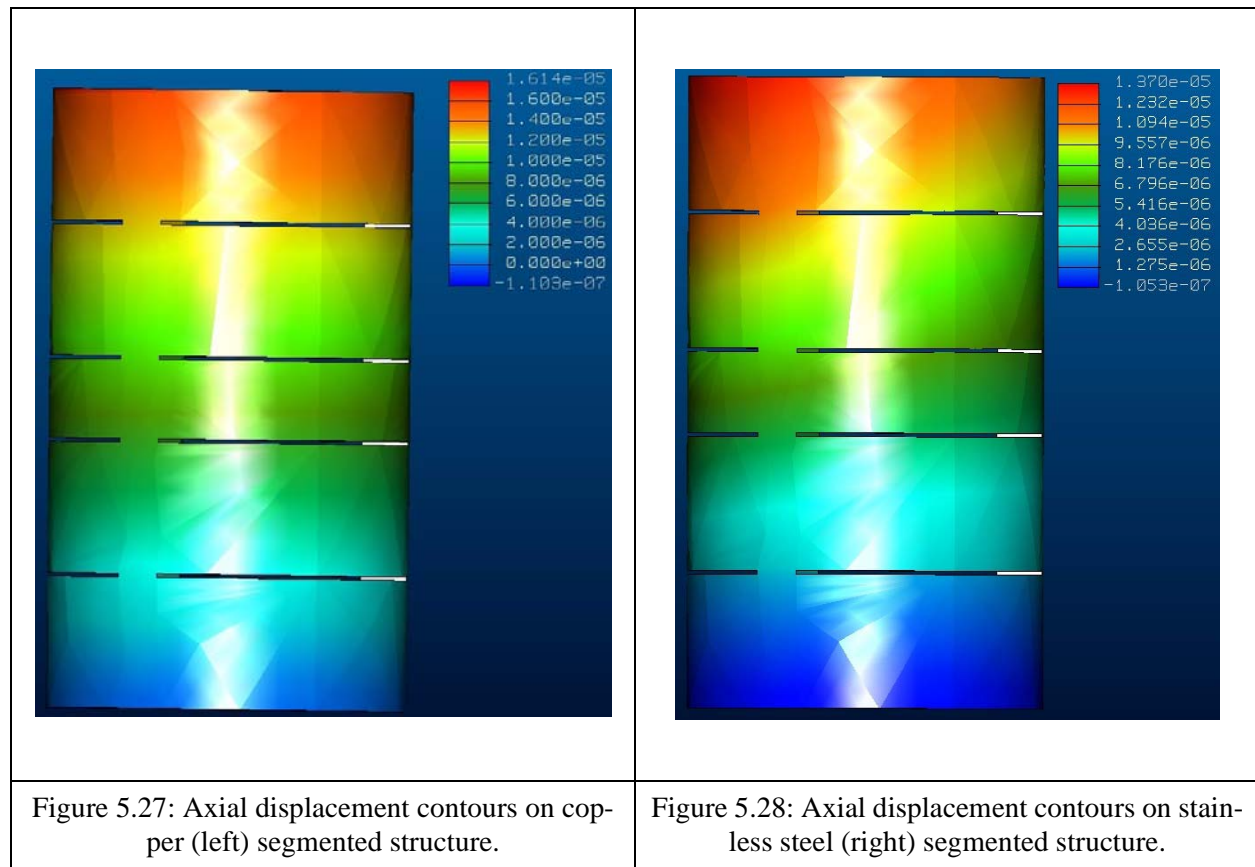
5.3.4 Design Optimization

Validation of the finite element model for the test configurations permitted its use for design optimization with respect to tube materials, tube thickness, and the number of structural segments. First, with the prototype dimensions, a performance comparison between the materials listed in Table 5.1 was made. Second, choosing the optimal material from this analysis and keeping the total length and inside diameter of the structure fixed (both packaging constraints), tube thickness and the number of segments were varied within reasonable bounds.

Material	Average ΔT [°C] - segmented	Tilt [arcsec] - segmented	Average ΔT [°C] - one-piece	Tilt [arcsec] - one-piece
Aluminum (6061-T651)	0.08	0.46	0.10	0.70
Copper	0.04	0.16	0.05	0.23
Brass	0.13	0.64	0.14	0.90
Stainless Steel (AISI 410)	0.59	1.93	0.60	2.62

Table 5.3: Tube material optimization study results (ΔT = heated minus non-heated).

Table 5.3 gives the results of the tube material optimization study, showing that the error motion of a copper tube segmented structure is 0.16 arcsec, versus 0.46 arcsec for the prior simulated aluminum tube structure, a reduction of 65%. Among the four materials studied, copper is best, aluminum is second best, brass is third best, and stainless steel is in a distant fourth place. For all materials, the ratio of tilt of the segmented structure to tilt of the one-piece structure is approximately constant at 1.45. The axial displacement contours for segmented copper and fully stainless steel structures are contrasted by Figure 5.27 and 5.28, showing a much greater angular nonuniformity in the stainless steel model.



Hence, in applications such as single molecule experiments where material and manufacturing costs are less important design variables than thermal performance, pure copper, or a copper alloy with a transient performance index value greater than that of aluminum, should definitely be chosen. For a low-cost structure with high thermal performance, for which strength and stiffness are not most critical, the aluminum segmented design should be elected. When strength requirements mandate a steel structure, placing

air gaps between modules will provide at least a 30% performance improvement in terms of the error motion studied here. In this case, more novel alternatives such as insulating the outside of the structure or placing a high-conductivity shield over the low conductivity steel (with a gap between the two to prevent transfer of thermal strains) can be studied.

Having optimized the material choice among four candidates, next a geometric design study was performed, with copper as the material choice. Keeping the total tube length and the inside diameter as packaging constraints, the tube thickness of both structures was varied within reasonable bounds of 1.0” and 2.5”. Next, for the segmented structure, total length, inside diameter, and thickness were held constant and the number of segments was varied. For simplicity of the analysis, one 3W heat source was applied at the horizontal centerline of the structure during the geometric optimization studies. The total length, including the kinematic couplings between segments, was shortened to 500.0 mm from 508.6 mm, and the segments were all equal in length. In this model, the segment length [mm] was calculated using:

$$L_s = \frac{500 - 3(n - 1)}{n}, \quad (5.21)$$

where n is the number of segments and 3 mm is the gap height between the segments.

Figure 5.29 shows that the error motion monotonically decreases with increasing tube thickness for the one-piece structure and for the structure with five segments. Hence, a better design is one with five thick segments, and a structure with five segments always outperforms a one-piece structure of the same thickness. The data series marked by triangles shows the error motion with thickness fixed at 1.5”, with the number of segments varying (in increments of two) from one to nine. The relationship here is better shown in Figure 5.30, indicating that the error motion is minimized with five segments, and increases in both bounding directions. When the results with varying thickness and with varying number of segments are collapsed onto the same plot in terms of the segment height to thickness ratio, Figure 5.31 results. Here, the (green and blue) curves for when thickness is varied are similar in shape (within the convergence confidence of the simulation), and are simple translations along the black curve for when the number of segments is varied.

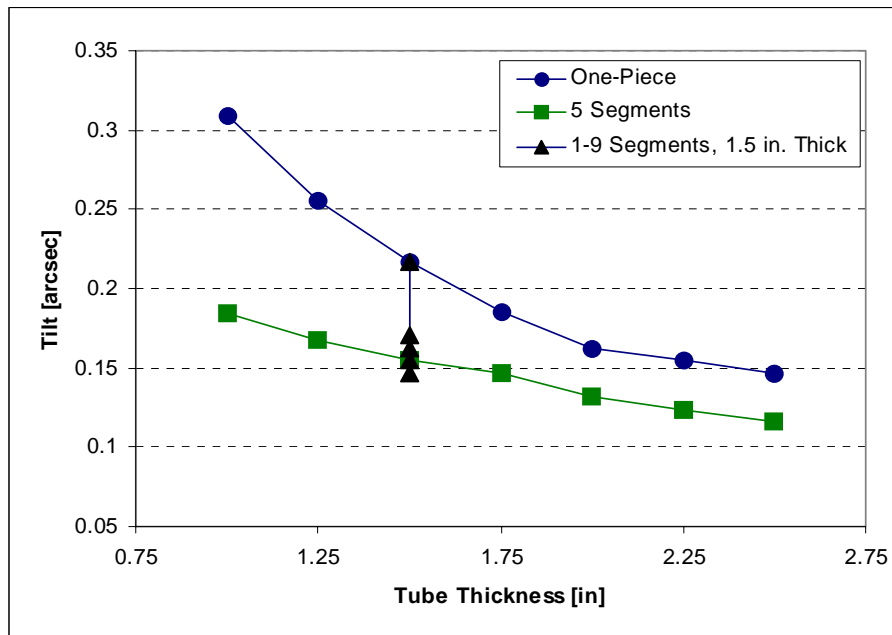


Figure 5.29: Angular deflection of segmented and one-piece copper structures with varying thickness.

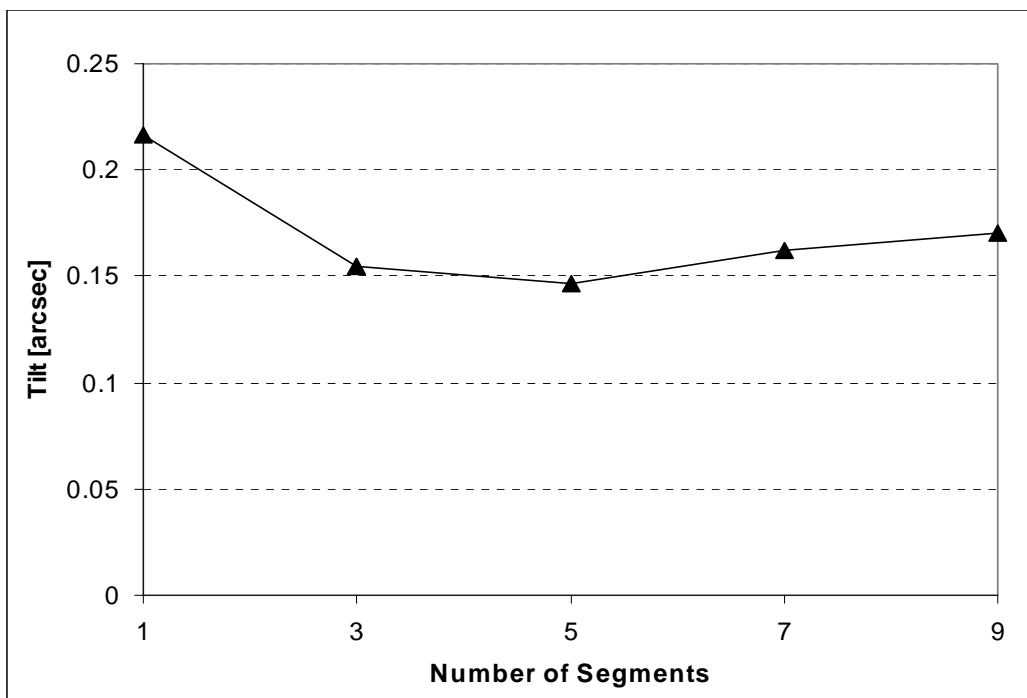
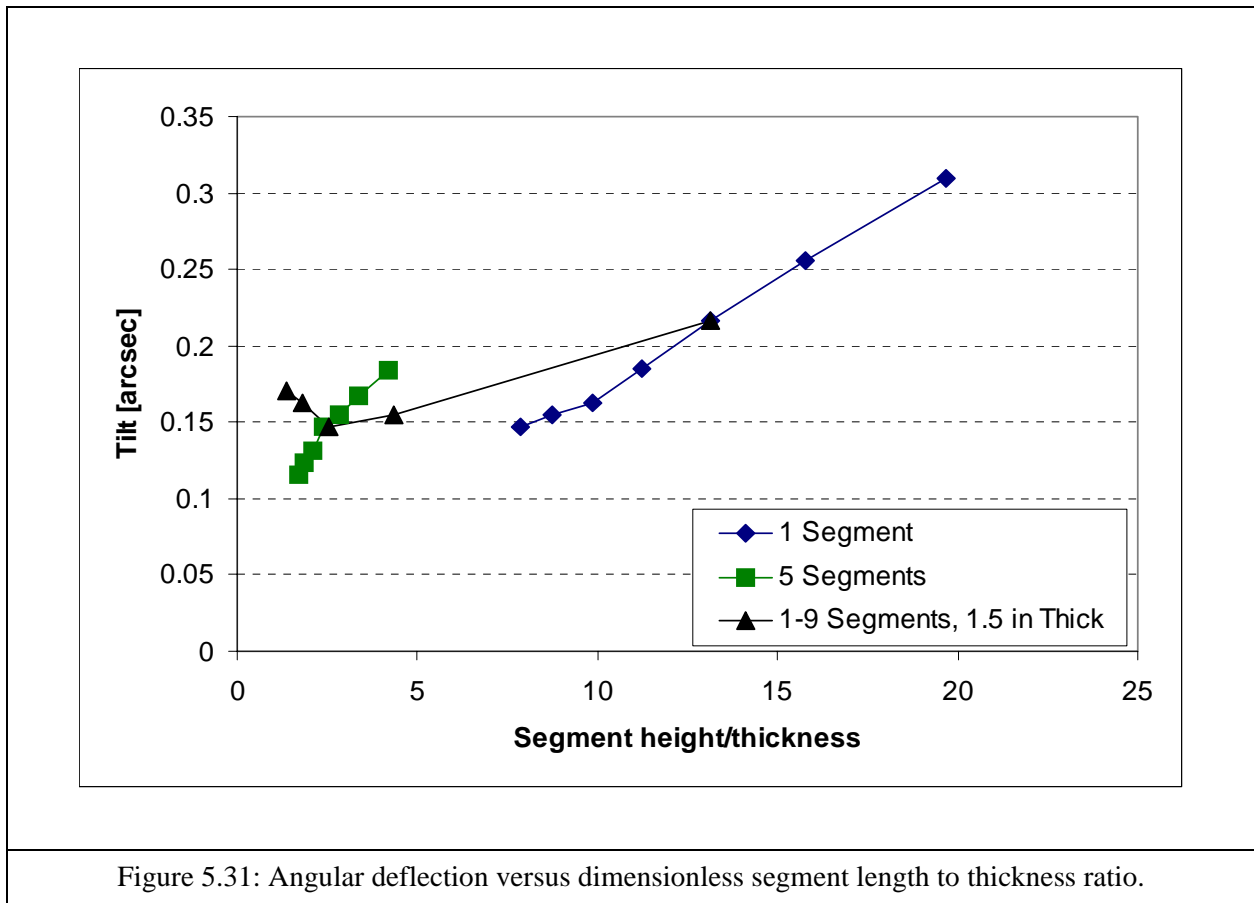


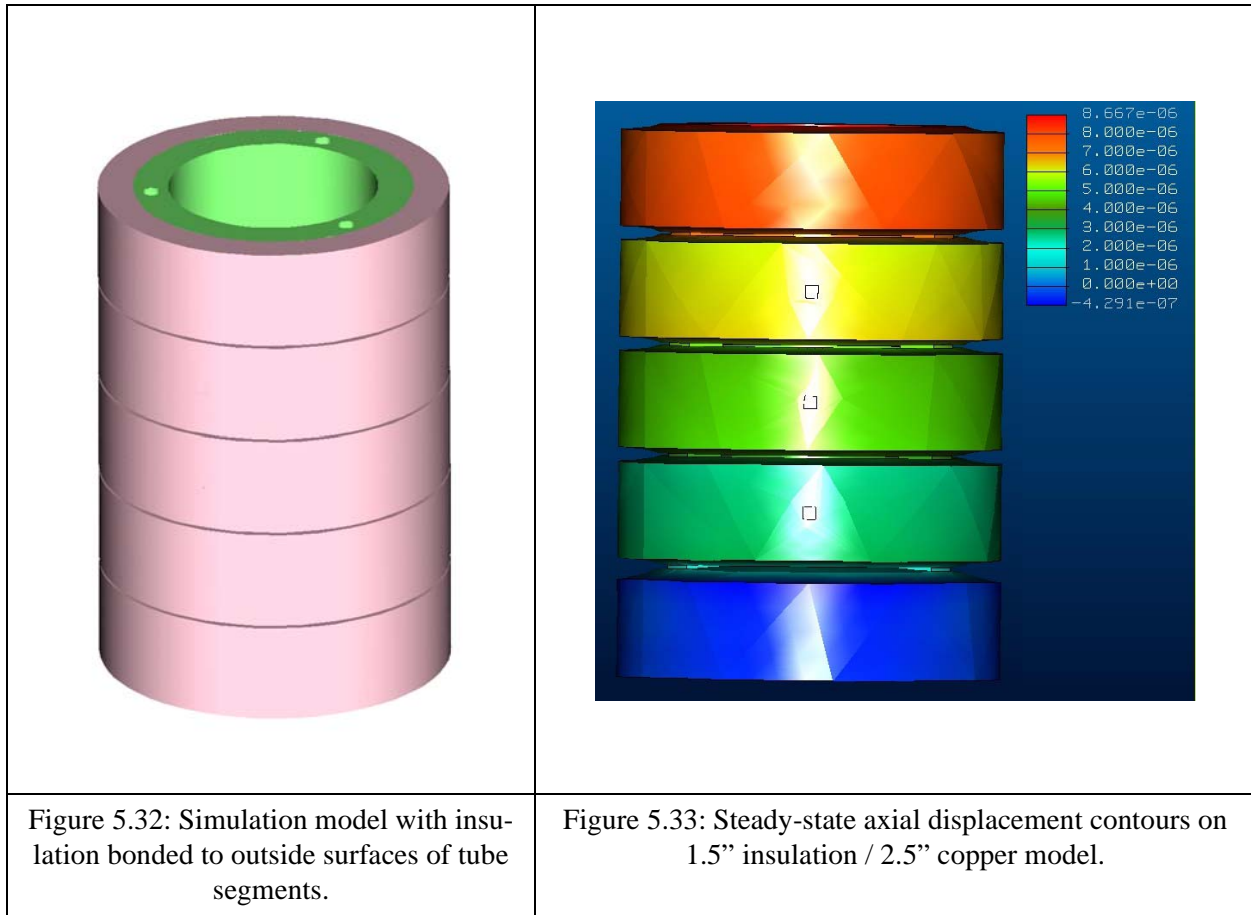
Figure 5.30: Angular deflection of structure with varying number of segments.



It was not intuitive that the error motion would decrease with increasing thickness; however, it is reasoned that a thicker tube presents greater thermal capacitance to absorb the constant disturbance, therefore decreasing the overall temperature change of the structure. The thermal expansion is directly related to the temperature difference between the heated and non-heated sides, which is a function of the magnitude of the overall temperature change, and the ease with which heat flows in the circumferential direction relative to the axial direction. Constraining the axial flow using a shorter segment is advantageous only until the effect of the decreased thermal capacitance of the segment takes over, after which the greater overall heating of the segment increases the magnitude of the thermal expansion.

The final iteration was to model a structure with uniform layers of foam insulation ($k = 0.026 \text{ W/m-K}$) bonded to the outside segment surfaces, and apply the thermal disturbances. Figure 5.32 shows the insulated model of the segmented structure with 1.5" thick bands of insulation constrained to the 2.5" thick

copper tube segments. Individual 1W total flux heat sources were applied at the usual locations of the second, third, and fourth segments. The insulation acts as an excellent primary dissipator; not only does the thermal mass of the insulation absorb some of the disturbances by bulk heating, but by the time the temperature gradient reaches the outer metal surfaces, it is significantly more distributed (both circumferentially and axially) than when directly applied.



Hence, within the bounds tested, the best design is a five-segment structure with copper metal tube segment thickness of 2.5", covered with a 1.5" thickness of foam insulation. With three 1W heat sources applied as before, this structure has simulated angular deflection of 0.04 arcsec, a 93% reduction from the 0.46 arcsec value for the 1.5" thick prototype aluminum structure. While there is confidence in the results of this optimal design study, given more time it would be useful to evaluate robustness by testing a varying number of segments at thicknesses other than 1.5", and with varying heat source magnitudes and distribu-

tions. It also seems like a more unified analysis could be achieved by normalizing parameters in terms of the thermal capacitance of the rings, rather than just the dimensions of segment length and thickness.

5.4 Future Work and Conclusions

While optimization through iterative finite element simulation significantly enhanced the performance of the design recommendation, additional bench-level thermal experiments would also be useful. Specifically, it would be instructive to assess performance with a layer of foam or fiberglass insulation mounted to the outside tube surfaces and relate the results to the simulations with insulation presented before.

Furthermore, in these experiments, the limited resolution of the interferometer necessitated that relatively large thermal disturbances be applied to generate well-measured deflection trends. More realistic thermal performance measurements, using lesser disturbances or exposing the structure directly to a well-controlled ambient, could be made by using high-precision capacitance probes mounted on the central reference, and measuring the deflection of the top of the structure. With three capacitive sensor pairs mounted vertically, one could sense biaxial rotation and axial extension of the top reference. With two to four additional sensor pairs mounted radially, one could sense in-plane drift of the structure. Capacitive sensors are available with linear resolution of less than 1 nm; sensors of this capability could improve the resolution of angular measurements by a factor of 60.

This work presented and validated the concept of a segmented, modular tube, kinematically-coupled structure as applied to a high-precision microscope for single molecule experiments. The structure was shown to be significantly less sensitive to asymmetric thermal disturbances than a single-piece tube alternative, and the kinematic interfaces between the segments offer significant functionality in disassembly, reconfiguration, and reassembly of the system without need for re-calibration.

More generally, these results demonstrate the feasibility of the segmented design for modular serial assemblies, in instrumentation structures including microscopes and high-precision reconfigurable measurement equipment such as large coordinate measuring machines, and in machine structures such as the industrial robot studied in the previous chapter. For robots, modules can be removable, perhaps wirelessly presence sensed and controlled, motor-driven axes. With different modules, the manipulator can easily be reconfigured to multiple end-effectors, extended reach kits, and even different numbers and types of joints.

Fixed-base parallel manipulators can be built from elementary structural sections similar to those of the segmented microscope structure, with links mounted to the outside tube surfaces extending parallel to ground. Results of the forthcoming repeatability and exchangeability experiments on the segmented prototype will quantify the mechanical modularity performance of such a design.

Chapter 6

Toward Standard, Low-Cost, Intelligent, Modular Interface Systems

The demonstration of high-accuracy, near-deterministic mechanical performance of kinematic coupling interfaces presented in this thesis is a building block toward defining standards for design of quick-change machine modules, using kinematic couplings as a universal mechanical handshake. Through simple measurement of the contact locations, manufacturing variation in the couplings can be parametrized through a series of discrete measurements, and this data can be packaged as a standard object to be wirelessly communicated to machine controllers upon interface mounting. Knowing this calibration procedure, couplings can be designed to optimize accuracy at minimum cost, allocating the interface error budget based upon measured repeatability and simulated interchangeability relations. Concepts are presented for low-cost contactors, which if performance-proven could make quasi-kinematic interfaces order-of-magnitudes cheaper than the current canoe ball design. In all, these processes of standard representations, deterministic detailed design, object data representation, and auto-calibration, can build an intelligently modular manufacturing system, potentially improving product dimensional quality, increasing production flexibility for multiple part styles, and reducing downtime required for replacement of failed automation components.

6.1 The Interface Design Process

6.1.1 Kinematic Coupling Standards

For nearly all industrial manufacturing and automation applications, the repeatability of any type of kinematic or quasi-kinematic coupling will meet or exceed the desired level of accuracy. The adaptability of the technology to an interface standard, with ease of quick-change modularity, is the driving reason to implement a kinematic coupling standard. An easy-to-change, deterministic interface lends itself to performance characterization via a discrete set of parameters. Then, as the module is used in large-scale implementations, the discrete parameter set enables a standard information representation, making interchangeability more efficient.

An essential element of a kinematic coupling standard is the characterization of the kinematic coupling performance in terms of a discrete set of parameters. These parameters should completely and universally describe the interface performance and suitability to all standardized applications, and maximum independence between the performance parameters should be established. To this end, Table 6.1 identifies a sample set of performance parameters, along with their primary and secondary related design parameters.

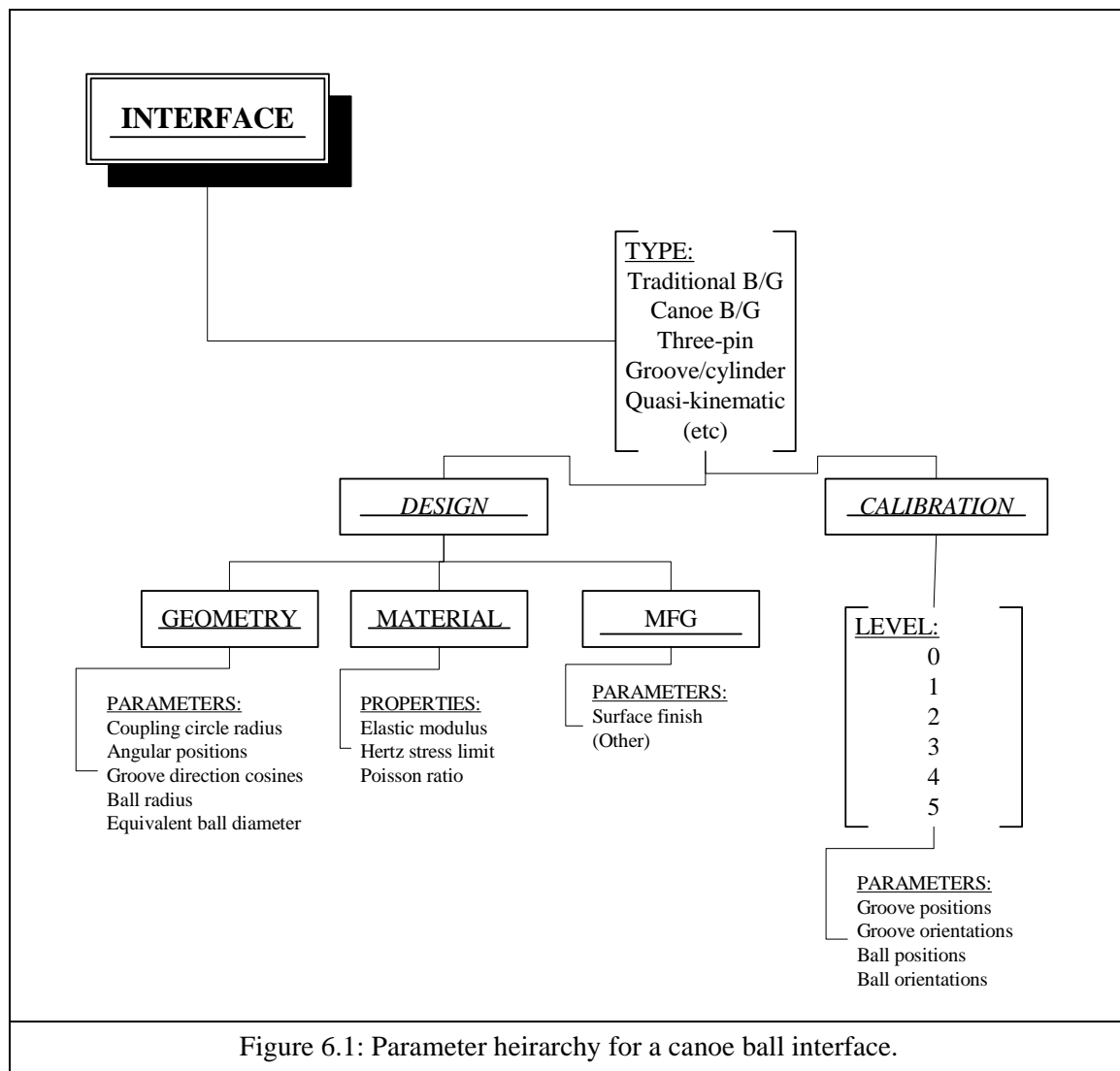
Performance Parameter	Primary Driver(s)	Secondary Driver(s)
Repeatability	Kinematic coupling type, materials, surface finish	Mounting procedure
Fatigue of repeatability	Material, surface finish, environmental conditions	Load condition
Interchangeability	Manufacturing process precision (feature tolerances)	
Load capacity	Coupling type, material	Geometry (within coupling type)
Cost	Coupling type, geometry, manufacturing process and precision	Material, assembly process and precision

Table 6.1: Suggested performance parameters for a standard kinematic interface.

For an example application to a pallet for material handling, the interface size can be chosen based upon geometric constraints of the pallet, while the load capacity of the coupling can be suited to the magnitude of disturbance forces by choosing the radius of curvature of the contactor, knowing the properties of the desired material. Note however that the priority of effects is dependent on the application; for example in a low-duty or static application, the mounting process will have a much smaller effect on repeatability than demonstrated before with high-preload industrial robot mounting.

When interfaces are standardized across manufacturers of similar automation components, such as between robot manufacturers for the factory interface studied earlier, the kinematic interface becomes a simple mechanical handshake. Attachment and calibration to the system interface is a deterministic process.

The efficiency of the standard mechanical representation is well complemented by a standard representation for the interface calibration data, such as the positions and orientations of the canoe balls and grooves on the robot foot and floor mounting plate. Like the design definition, the calibration parameters are discrete for each type of coupling. When quick installation of components is a-priori, the pre-determined (at the automation factory) coupling calibration data can be stored on the replacement automation module, and communicated wirelessly in short-range to the cell computer (e.g. robot controller). The calibration data identifies the new model uniquely, and error corrections are made in the controller by calculating the error transformation as discussed previously.



The standard should place minimal limits on innovation of compatible modules, while ensuring interchangeability at all interfaces. A suitable standard hierarchy of design and calibration parameters, branched for canoe ball kinematic coupling interface, is given in Figure 6.1. First, the interface is distinguished by coupling type, then parameters are separated into specified design parameters and measured calibration parameters. The design parameters are the geometry of the interface including the form dimensions of the couplings and their locations in the interface plane, the properties of the coupling material, and the parameters of the coupling manufacturing process. The calibration parameters are defined by level of calibration, and then the measurements made are sub-objects with sets of cartesian positions and/or orientations. The design geometry and calibration level parameter field names will obviously differ by coupling type; for example, a three-pin interface would still list the coupling circle radius and angular positions, but the remainder of the parameters would appropriately define cylindrical line contacts between the pins and contact planes. A similar data structure could be built to characterize the dimensional performance of an interface over a large number of instances; rather than list measured calibration data, this would assign tolerance magnitudes and distributions to each dimension, and leave the placement accuracy as an output parameter when simulated for each of the calibration levels. Example canoe ball interface specification based on standard parameter hierarchy.

With sufficient knowledge of the design relations and past experimental performance results, these design parameters can be derived in an inverse fashion based on the standard performance parameters listed in Table 6.1. Since the standard representation is transparent to the type of ball and groove within the specified coupling type (e.g. press-fit spheres, press-fit shanked tooling balls, or press-fit hemisphere-ended cylinders; e.g. modular groove inserts or directly machine grooves) placement tolerances can be expressed in the appropriate interchangeability model of form error. Notwithstanding a mechanical model of the full interface structure, load capacity is assumed to be constrained by the contact stress at the coupling points. Since cost is a function of the manufacturing and assembly processes, it can be estimated after selection of components to meet the other performance requirements.

Lessons on standardization of mounting interfaces can be taken from the semiconductor industry, specifically the SEMATECH standard SEMI-E57-0299 for standard three-ball to three-groove mounting of silicon wafer-holding pods to automated carrier vehicles used in fabrication plants [1].

6.1.2 Building and Using a Web-Based Design Community

The Internet and the World Wide Web have created a new paradigm for sharing of information and growth of communities through electronic interaction and collaboration that, has flourished in terms of interpersonal collaboration, business-to-consumer retailing, and business-to-business dealings, yet is still in early stages of cultivating interactive online engineering design and education platforms.

The base component of interactive websites is the relational database management system (RDBMS, e.g. Oracle 9i), which warehouses large sets of textual information and enables custom user-defined or provider pre-defined queries of its content for almost instantaneous results display in a browser. Display pages can be written in fixed-format hypertext markup language (HTML) or the newer standard of extensible markup language (XML) and dynamic content can be created using a variety of scripting languages (e.g. TCL, CGI, ASP, JSP, etc.). Another main feature of database-driven sites is hosting of discussion forums. These discussion groups aim to create a sense of community among website users, enabling collaboration of ideas on usually website-specific content, message, or popular issues, and for businesses are valuable tools for gathering customer input on product acceptance and website functionality [2].

Websites are moving away from fixed-format pages to more flexible content presentation standards such as XML and JSP, reducing the barrier of resources and expertise needed to express rich, custom content through a website. For example, the XML standard and newer XML-Schema format adds object significance to text by encoding it in custom-defined fields, and separates this text from its formatting by building separate document structure templates. Hence, the result of a database query can be placed in a field-designated text (.xml) file, and passed through a style sheet for display. This distinction enables style templates to conditionally format according to the fields within the content file, and makes updating content and updating format a very scalable, independent process.

To establish an efficient method for design selection, an information repository for kinematic coupling designs is needed. This should be a catalog of data on kinematic coupling performance, such as experimental and theoretical relations between manufacturing tolerances and coupling repeatability, as well as a database of existing coupling designs. Making this an industry member consortium-based or public design web community achieves easy, direct advancement of the technology. This community would have access to

the aforementioned repository, as well as open-source programmed tools for designing custom kinematic coupling interfaces for specific applications. As with many well-known collaborative web efforts, this environment would facilitate sharing of design ideas, analytical tools, and lessons learned, resulting in the collective benefit of the membership. This sharing should be without concerns of competitive confidentiality, as designs will be based on the interface standard, and disclosure of implementation and specific performance benefits will be at the discretion of the member.

A primitive kinematic couplings website was built in 2000 by the MIT Precision Engineering Research Group at <http://www.kinematiccouplings.com> or <http://pergatory.mit.edu/kinematiccouplings>. Here, spreadsheet design tools are available, research updates from the group are posted, and a comprehensive reference list to past work, patents, and suppliers of kinematic couplings and components has been built. A primitive, text archive-based message board interface is also present. In the coming year or two, the site will be enhanced to include integrated java-based design tools, with connectivity to a MATLAB engine on the web server for online calculations and rich display of graphical results. The site could become membership-based, with user ability to post or submit case study descriptions and design experience in a database-driven threaded discussion structure. A simple integrated application can enable hierarchical specification of standard design parameters by a user as inputs, and subsequent calculation of performance estimates, and queried results of a search of databased literature and discussion items related to the specified interface type, as outputs.

6.1.3 An “Expert System” for Optimal Cost/Accuracy Decisions

The standard interface representation and the open-access web repository of designs, design tools, and performance data can be integrated into an “Expert System” for best choice of a kinematic coupling design, manufacturing process, and calibration process, given the overall accuracy requirement. With sufficient archives of measured repeatability data, and design code modules predicting load capacity, static error motions, interchangeability, frictional non-repeatability, machining cost, calibration cost, installation cost, replacement cost, and so on, this “best choice” can be any objective function goal such as minimizing total cost, minimizing a cost component (e.g. replacement cost), minimizing variation in performance about the nominal accuracy requirement. An accomplished application, the Cambridge Engineering Selec-

tor, offers similar design guidance for materials selection in terms of strength requirements, manufacturing process requirements, expressed performance indices, and other factors.

With the repeatability results known to date and presented here for traditional, canoe ball, and three-pin interfaces, standard performance levels can be translated into relationships between interface cost and interface accuracy as the first level of an expert system. For a customer to a manufacturer of machines (e.g.) robots with many interfaced modules, this is a very useful "accuracy menu"; the ability to choose the standard interface suited most closely to the application error budget, through a near-deterministic design process eliminating uncertainty between the design goal and the measured performance upon start-of-production.

If the improvement in flexibility gained using a quick-change interface can be estimated, the following simple relation gives the maximum total cost of the solution per machine that justifies use of the interface:

$$C_{max} = (t_{normal} - t_{kinematic})(C_t)(S_{life}) \quad (6.1)$$

Here, t_{normal} is the module exchange time (including dismounting, mounting, and calibration) using the old interface design, $t_{kinematic}$ is the exchange time using the kinematic interface, C_t is the unit cost of machine downtime, and S_{life} is the number of failures per machine life (often < 1). In a more sophisticated form, the failures of a single machine can be assumed to follow a particular distribution throughout the machine's lifetime (e.g. few failures early, more failures later), and the cost can be discounted to a present-value savings on the capital cost of the equipment, which itself would be discounted to reflect periodic cash flows and tax savings from standard depreciation writeoffs.

6.2 Fundamental Hardware and Software

6.2.1 Low-Cost Locators

For widespread adoption of kinematic interfaces, high accuracy must be accompanied by reasonable component cost, competitive with that of existing bolt and pin interfaces. Notwithstanding the life-cycle methodology just proposed, in competitive manufacturing industries where primary producers continually demand lower equipment costs in spite of relatively constant costs of materials, manufacturing, and

machine assembly, even a component that enables an order-of-magnitude increase in individual accuracy over the prior design must come with only marginal increase in its contribution to the machine cost. For extreme-load interface applications, canoe balls have been shown to perform with highest accuracy and greatest robustness, yet cost of machining the high-radius spherical surfaces is nearly prohibitive, at \$100-\$1,000 per locator depending on surface size and production volume. This is ten to one-hundred times the cost of traditional anchoring methods. While individual, ultra-accuracy applications such as the high-precision microscope may allow for such expensive locators, mainstream designs must focus on dramatically reducing cost while marginally decreasing accuracy from the canoe ball standard; hence, a high gradient value of cost-to-accuracy is sought within the neighborhood of the accuracy-maximizing solution.

6.2.1.1 Low-Cost Machined Locators

Most notably for the canoe balls, the primary cost component of kinematic couplings is the cost of machining; hence first attempts to reduce cost can design locators with simpler machined geometries, or geometries machined directly into the mating machine interfaces. Two low-cost options, the three-pin interface and the quasi-kinematic couplings, have already been discussed in context of the robot base interface. The three-pin locating method requires only three, rotationally-symmetric locators, which can easily be turned in high volume, press-fitted to simple holes in the top interface plate, and mated to contact surfaces directly cut into the bottom interface plate. Recall that the tests of the robot base demonstrated only a 14% decrease in repeatability from the three-pin to the canoe ball interface, and combination with simulated interchangeability results rendered the three-pin to have comparable total accuracy to the canoe ball interface. The dependence of total accuracy of the canoe balls on placement error of the measurement feature could be eliminated by directly calibrating the spherical surfaces. With repeatability as the sole determinant of total accuracy when full calibration is performed, the canoe balls would regain a small performance advantage, but now requiring a more sophisticated calibration process.

Similarly, quasi-kinematic locators of the type designed but not evaluated for the robot base, are a simple rotationally symmetric geometry. If the contactors and targets are made of the same material, both can be machined into the interface plates using custom-shaped rotating tools. If the contactors and targets are made of different materials, one interface half can be a modular, rotationally-symmetric unit, while the

other unit can be homogeneous with the interface plate. Based upon Culpepper's results from the first quasi-kinematic application to engine block assembly, interface repeatability would be competitive with the other interface designs. interchangeability could be investigated using a simulation model based on elastic averaging of contactors and targets with slightly perturbed positions.

For traditional and canoe ball couplings, at least a marginal cost improvement can be gained by machining the vee grooves directly to the interface plates using a vee-mill, assuming applicability of the plate material and machined surface finish to the application. A lower-cost design of the cylinder/groove interface is also possible, where the six grooves are machined directly to the interface plates and the cylinders are simple dowel pins laid in the grooves before mounting. Bolting just radially outboard of these couplings can eliminate the need for holes through the cylinders, with negligible sacrifice of interface stability.

6.2.1.2 Low-Cost Extruded Locators

A last concept of a low-cost interface proposes that quasi-kinematic locators be extruded from aluminum and placed between steel grooves, an extension of the cylinder/groove concept. The extruded shape, shown in Figure 6.2, is that of a double canoe ball section in two dimensions, stretched along the centerline axis of the mating groove. The extruded section can be optimized to produce the desired interface normal stiffness, as determined by the design of the mid-section between the grooves, and the desired load capacity, as determined by the contact radius and the design of the contact stress-bearing section. Section design parameters are as indicated in Figure 6.4.

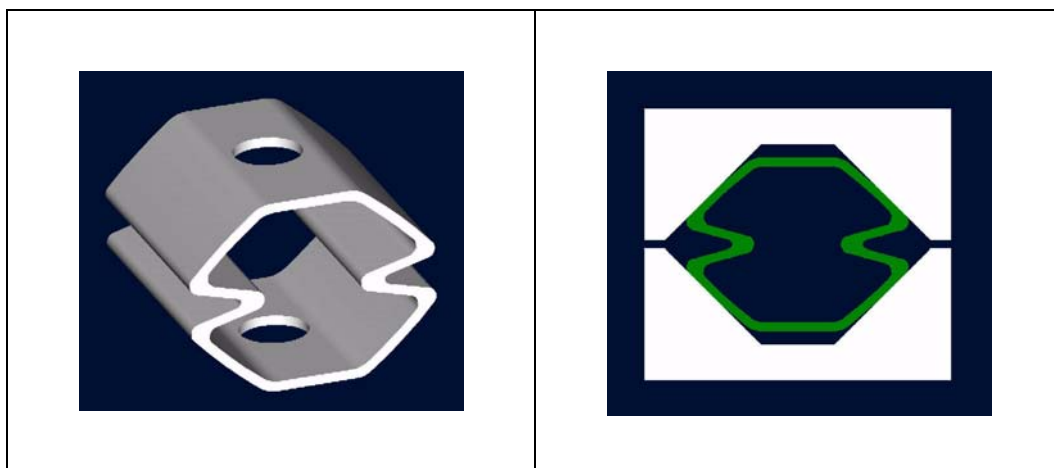
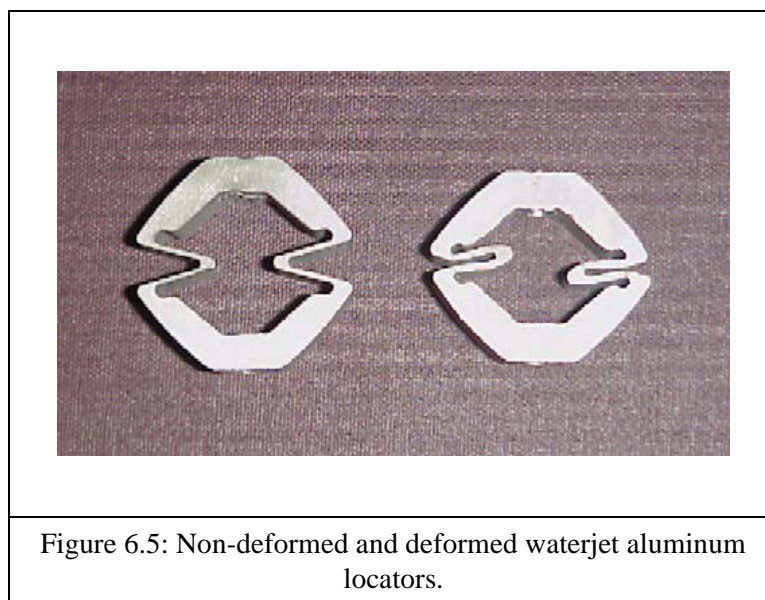
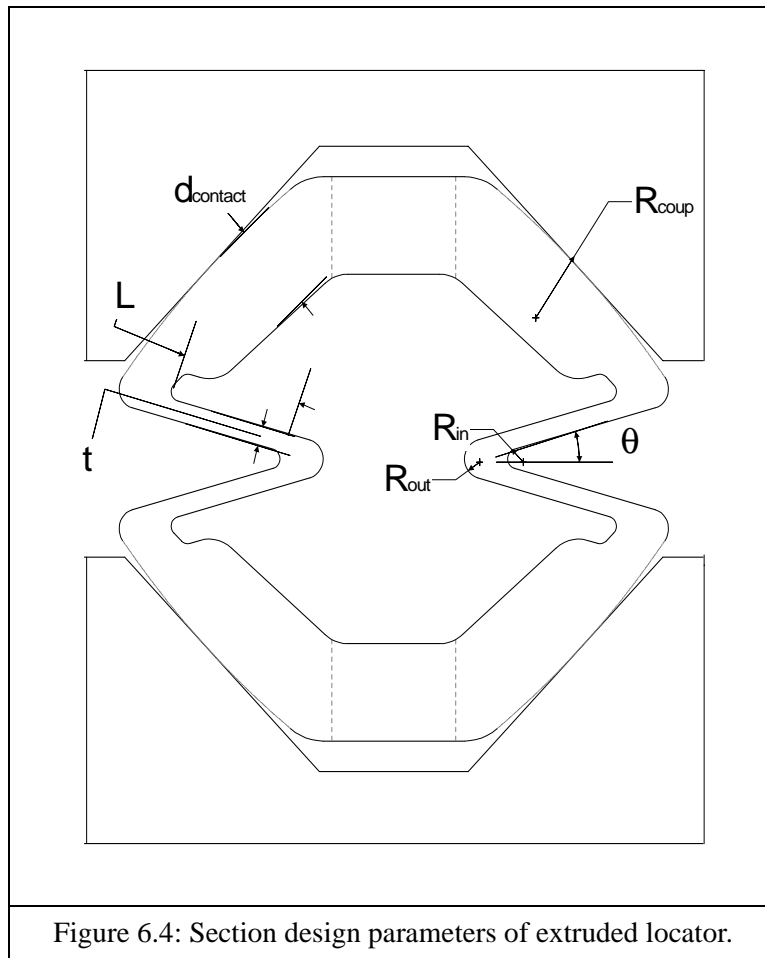


Figure 6.2: Isometric model view of extruded locator with central hole for clamping bolt.	Figure 6.3: End view of extruded locator in double mating vee grooves.
---	--

The coupling is designed such that the center section deforms elastically and plastically upon application of a compressive preload. Both ball ends mate to vee grooves, which engage significant normal contact areas when the preload reaches its limit. These contact areas handle the dynamic interface disturbance; hence the interface location is quasi-kinematic from the twelve short line contacts along the six grooves, and the dynamic stiffness is sufficiently high to handle large disturbance loads. Upon closure of the gap, the horizontal flanges of the grooves meet, and the stiffness of the interface is well approximated by the normal stiffness of the groove surfaces, excluding the contact stiffness of the quasi-kinematic unit at that deflection. The deflection of the groove surfaces will essentially command the deflection of the midsection of the coupling, and the contact stresses along the line contacts of the curved surfaces will remain approximately constant under dynamic operation.

To estimate the repeatability of the extruded locator, the 3/4-scale model test fixture for the canoe ball interface discussed in Chapter 4 was adapted to hold opposing triangular arrangements of hardened stainless steel vee grooves. 3/4" square air-hardened tool steel blocks were fastened along both sides of each groove to provide large normal contact areas. Figure 6.5 shows a prototype aluminum locator that was waterjet machined from 1/2" 6061-T651 aluminum plate. Figure 6.6 shows this coupling seated in the test fixture.



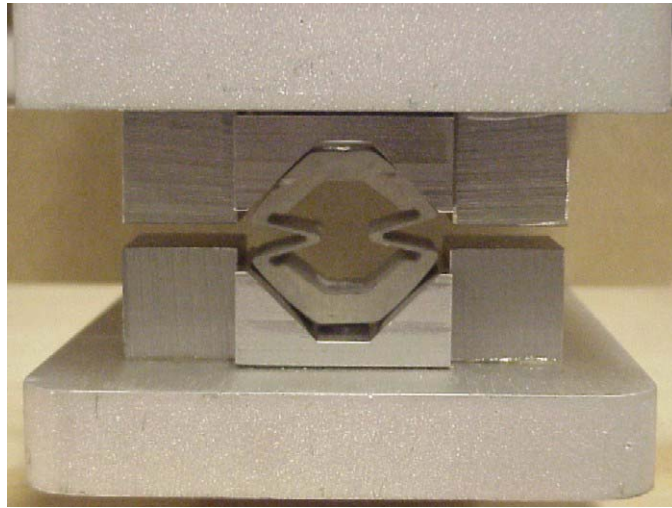


Figure 6.6: Aluminum locator clamped between vee grooves with side datum blocks on test fixture.

The test interface was initially seated by tightening each of the three mounting bolts in an incremental and sequential periodic fashion until the datum blocks seated in contact. This tightening process immediately revealed an inadequacy in the coupling design, as slight misalignments in the coupling placements and the applied preload caused uneven deformation of the thin sections. This is seen in Figure 6.5, as the uneven deformation caused a side-to-side shift of the canoe-like sections, resulting in an undesirable in-plane error motion upon initial seating of the interface. It is thought that this can be corrected by a design with double-parallel beam flexures in the center section. Similarly, solid couplings of this shape would be worth testing; the much higher in-plane stiffness would better resist non-deterministic error motions due to misalignments of the grooves, but the greater normal stiffness would be undesirable.

CMM measurements showed static repeatability of approximately 30 microns at the central frame. This is several times that for a comparable canoe ball interface and likely owed to the misaligned plastic deformation of the parts tested, yet still within a reasonable range for machine mounting. Furthermore, it is hypothesized that measurement of the positions of the groove sets can provide nearly the same interchangeability as the canoe interfaces. This interchangeability model would treat the elastic averaging as a

parallel arrangement of springs for the couplings, and neglecting frictional nonrepeatability the minimum strain energy configuration would give the static rest location of the central frame of the upper interface.

Additional design iterations and tests are clearly needed. When the magnitudes of the disturbance forces permit thin-walled extrusions, the individual couplings could be subsequently cold-formed with a second radius of curvature, creating near-kinematic spot contact. With a well-controlled extrusion process, interchangeability of these interfaces would be dependent mostly upon the placement of the pair of grooves (corrected by position and orientation measurement), and the extruded locators would act to elastically average the misalignments between the groove pairs.

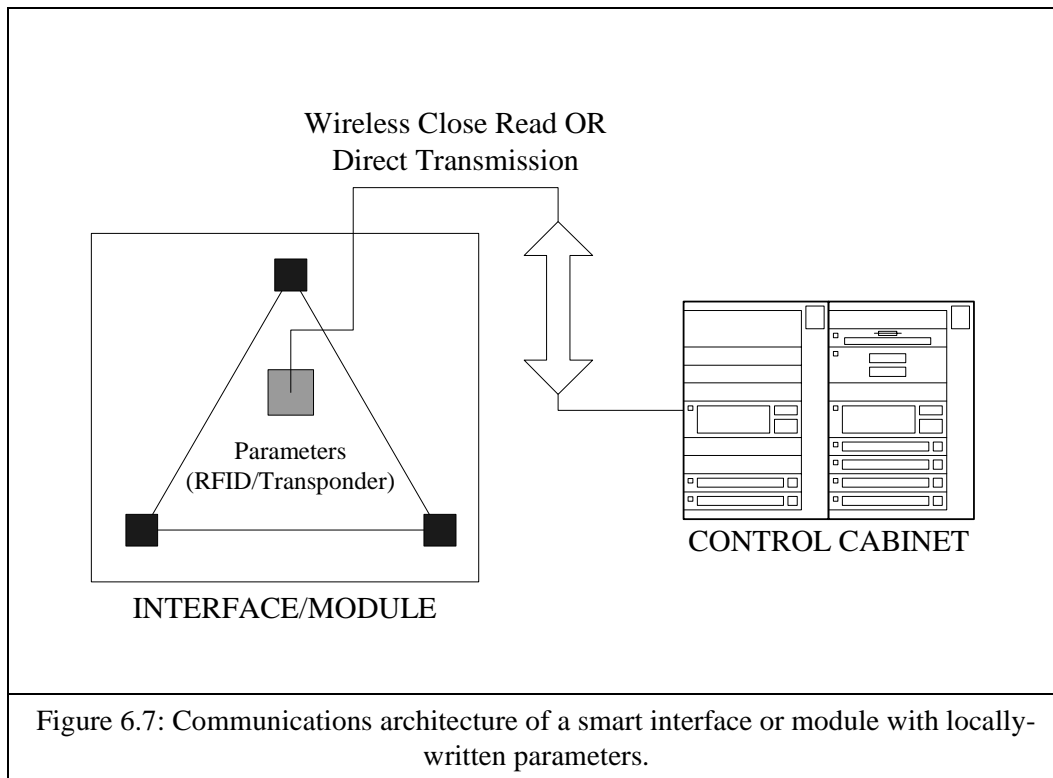
6.2.2 Distributed Storage and Handling of Calibration and Process Data

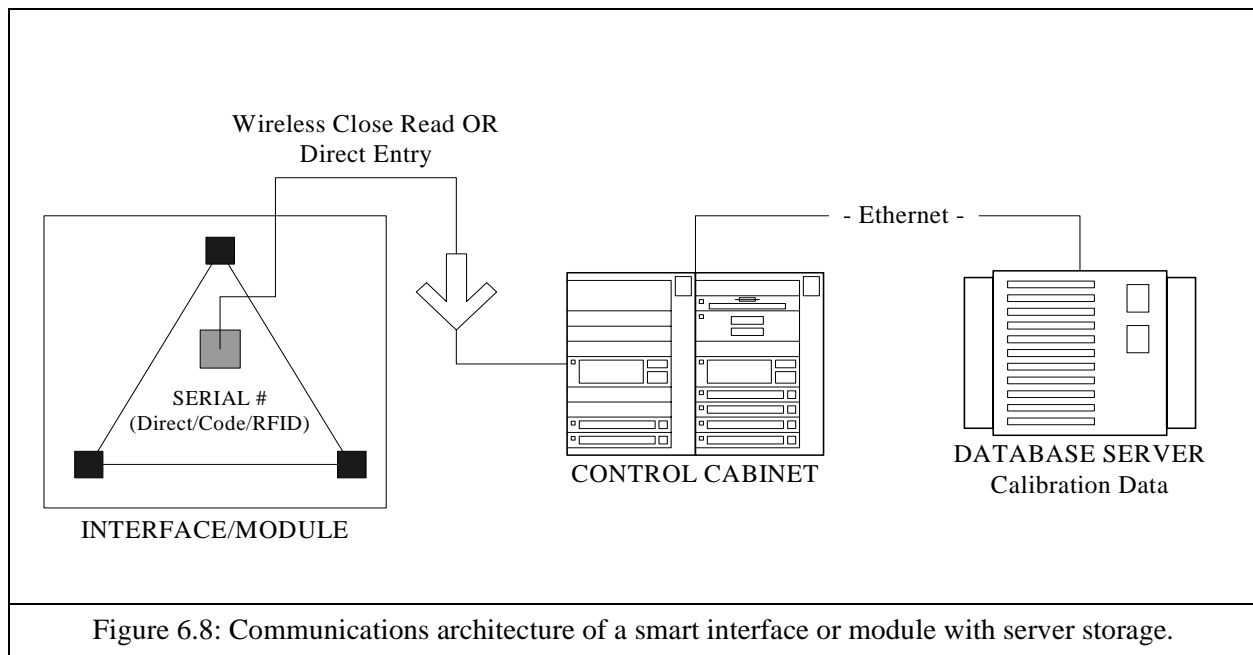
With calibration data needed to determine the interface transformation for mating interface halves, location and method of storage becomes an important issue. Traditionally for robots, since manipulators are shipped undesignated to control cabinets, calibration parameters are shipped on a floppy diskette and installed when a manipulator is paired to a control cabinet after installation at the line site. If the manipulator base is fitted with a calibrated interface, the positions of the locators could easily be loaded onto the calibration diskette. However, customer feedback to robot manufacturers indicates that diskettes are frequently misplaced; furthermore, when a robot or other machine with multiple modules is considered, diskettes would have to be shipped with each replacement module, requiring manual loading of the interface parameters as a first step in module calibration.

Simple wireless communications technology can be used to automate the installation of calibration parameters, through module identification using a serial number and retrieval of parameters from storage on a central server, or direct storage of the parameters in a read-only memory or read-write transponder device on the module interface. Sample architecture diagrams of server-based and fully module-based systems are shown in Figures 6.7 and 6.8. The stored calibration data could consist of the only interface parameters, or the full calibration set for the replacement machine module or initially the complete machine.

In the server-based case, each interface or module would be printed with a unique serial number, alphanumerically encoded on the piece, written into a bar code, or contained on a small-memory read-only

radio frequency identification (RFID) chip. Upon installation of the interface, the serial number would be read to the control cabinet, which being networked already, could contact the data server and retrieve the parameter files. In the case of local storage on the interface, a handheld or cabinet-held read device would retrieve the parameter files when the interface is brought to the installation position. If the storage device is an active transponder with sufficient range, the interface can form an ad-hoc local network with a similar transponder in the cabinet, identify itself, and embed the calibration data in object-oriented messages. When an active read/write device is used on a high-precision pallets with kinematic docking, its functionality can extend to hold part measurement data, and transmit it to each station for active correction of machine path programs or positions of the in-station locators to account for dimensional variation between parts. Additionally, wireless transponders can be used as control feedback devices within machines, such as to compare motor position to cartesian position on a robot, and save the cost of distributing sensor wires in cramped areas of the machine, or validating the durability of sensor cables.





The upperbound cost of the wireless storage method can be calculated in the same way as that for the interface itself, considering the time savings and potential loss savings over using diskettes in each installation. At the machine manufacturer, a wireless storage method would be more of a potential savings; an automated calibration procedure could build a transponder write device into the measurement system and use it to issue the calibration parameters to each interface directly after calibration, or a routine could save them in the manufacturer's database of calibration parameters. When the data is directly written to the interface, no supervision of its placement during packing and shipping would be needed. In the second case, extra cost would result from building and hosting the database, yet concerns of losing the data or even damaging the storage device on the interface would be eliminated.

For storing positions of three locators, nearly negligible storage capacity is required, making RFID tags and smart cards (which can perform elementary on-board computation) most suitable; however, these devices also have limited transmission ranges, requiring a closer proximity near-contact read process to load the parameters to the machine controller. At the opposite extreme, Bluetooth and 802.11 wireless ethernet transponders are certainly excessive designs, with adaptability to supplemental processors and bulk storage devices, at ten to one-hundred times the cost of the simplest option. Clearly, choice of the a wireless device is a cost-convenience and cost-expandability (in terms of application to active storage of part-

in-process data) trade-off, with directional capability, range, and storage capacity scaled to the modularity level of the application.

6.2.3 Object-Oriented Interface Protocol

When a module-based transponder is used for wireless communication of calibration parameters upon installation, and possibly for sending other feedback signals during machine operation, the messaging protocol between the server (the control cabinet) and the client (the transponder) should be object-oriented. Using an object-oriented protocol would best facilitate addition of interface types or measurement procedures that would require new message formats between the server and the client. When such an instance occurs, the API at the server, or at many servers at different manufacturing stations, can be patched incrementally from an authorized point on the corporate Intranet, and a replacement module can be brought in and can start sending messages according to the new format. This contrasts a non object-oriented architecture in which message formats would be standardized for different types of information exchange; hence, scaling the protocol would require detailed re-programming of the standard message definitions.

In the context of communicating calibration parameters for kinematic interfaces between an interface-resident transponder and a machine control cabinet, separate messages would be defined for communicating each level of calibration data from each type of interface. For example, when a new robot manipulator is brought to its destination cell, the transponder on the base establishes an ad-hoc network with the control cabinet, and communicates its calibration parameters for calculation of the interface transformation. A suitable sequence would be:

1. The robot is brought to the cell, and the transponder on the base detects the presence of the control cabinet. The transponder sends a **InterfaceConnect** message to the cabinet to notify it of its presence.
2. The cabinet acknowledges the connection by sending an **Ack** message to the base, containing the identification code of the connection message.
3. The base transmits its calibration parameters to the cabinet. For example, if the base has fully calibrated vee grooves, it could send a **VGrooveLevel5Send** message containing the data.
4. The cabinet acknowledges the receipt of the calibration parameters by sending an appropriately coded **Ack** message to the base.

Message retry policies and timeout handling flows can be easily constructed. These messages could be for-

matted as XML schemas and broadcast over any standard wireless protocol. The XML formatting would also facilitate easy, rich formatting for logging of messages in a database table, and for display of calibration data via a web interface.

6.3 Intelligent Manufacturing Systems Using Kinematic Couplings

6.3.1 Structure of a Modular System

In sum, the straightforward standard design process for high-accuracy kinematic interfaces, the technology of distributed low-cost realizations of contactor geometries, and the intelligent representation and communication of interface calibration data to speed interface installation and replacement, can be built into an intelligent manufacturing system networking modular machines with a server-based management and monitoring system. Beyond smart interfaces, availability and cost/performance enhancements of several other technologies make this system possible, a few of which are:

1. The advancement of communications standards makes automation easily networkable to information systems. Machine controllers today are often Ethernet-networkable, with PC interfaces. RFID memory systems enable distributed storage and non-contact reading of data, and emerging standards such as Bluetooth enable ad-hoc proximity-based networking between several transponders.
2. Several off-the-shelf applications exist for intelligent monitoring of manufacturing processes and equipment, and are networkable to accept and broadcast data over these standard protocols.
3. The decrease in cost of wired and wireless binary proximity and continuous value (e.g. position, temperature) sensors enables process monitoring on a wide scale.
4. The emergence of XML and open-architecture application development and web visualization tools enables modular web applications; common web site frameworks can be applied to numerous related applications, requiring minimal custom programming and setup.
5. Event-driven entries to relational databases of process data can allow remote, up-to-the-minute generation of custom process reports.
6. Simple artificial intelligence algorithms can learn process trends and generate feedback for automated tuning of machines and systems.

An example of an integrated system is given for the factory interface case study of automotive assembly robots with quick-change baseplates and full accuracy calibration software, diagrammed in Figure 6.9. First, the baseplate serves as a robust mechanical interface for placing the robot on the factory floor, as well as a power and information interface to drive the robot. As the main enabler of modularity, the base-

plates would be placed at each robot location in the manufacturing system, which would be calibrated to on-line tooling or automation. Baseplates would incorporate locating features, such as tooling balls, for precise measurement of their location with respect to work pieces using portable measurement equipment. In turn, robots would be calibrated and programmed with respect to a standard baseplate located off-line or in simulation, and each robot's calibration data and programs would be stored in a central server. The server would recognize the placement of each robot and end-effector in a specific base plate and wrist plate, and would enable reconfiguration of the system without re-programming of different controllers. When a robot is placed on the line, the robot software would synthesize the location of the robot end-effector with respect to the robot base, the location of the robot base with respect to the base plate, and the location of the robot baseplate with respect to the tooling and work piece. Hence, calibration and programming performed off-line (or programming in a virtual environment, e.g. ROBCAD), could be reliably successful with little or no required tryout or touch-up on the production line.

The back-office information infrastructure would be more of an integration than a development effort; existing database and process-monitoring software could form the basis of the information system, and one could manage these applications using a custom web interface built using open-architecture, open-source techniques. This way, the website interface would be specific to management of a system of modular robots, yet its underlying architecture would be relevant to building similar websites to manage modular technology in other, future applications such as reconfigurable fixturing. XML would be useful for defining common input/output and display formats for calibration information, specifications, reports, and other relevant data. Engineers could browse process performance data from throughout a corporate Intranet. Failure instances could generate automatic alerts to appropriate engineering and maintenance personnel, and failure statistics could be centrally archived in a database table for more efficient system-wide analysis.

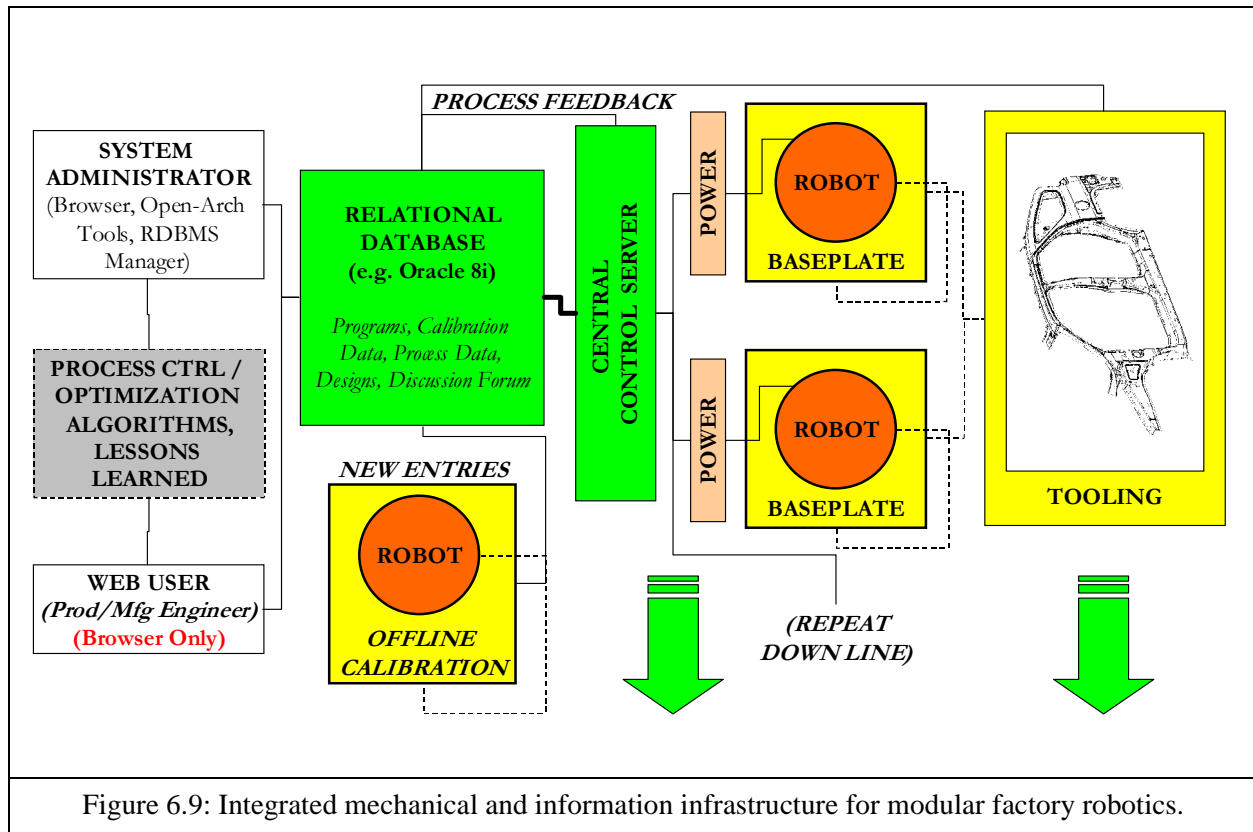


Figure 6.9: Integrated mechanical and information infrastructure for modular factory robotics.

Specifically, it is anticipated that the integration of an information infrastructure with a series of modular robots would have three distinct advantages:

1. A web-based tool for kinematic coupling design would facilitate easy design of coupling interfaces, incorporating design rules as discussed before, and staging a forum for electronic communication of design lessons learned and comments, etc. Hence, through discussion forums, the web can create a community to enable wide-scale acceptance of this new equipment at the development and plant engineering levels.
2. The database-driven web site would enable efficient management of the reconfiguration system. The database would be a warehouse for all robot specifications, component specifications, location histories, calibration data, robot path programs, and so on.
3. The information system would enable active process monitoring and change management. Dimensional and other statistical-based process management can be achieved by plugging in current applications. Perhaps a new area of technical interest is robot rotation. If switching robots is easy and repeatable, how can one analyze process performance data to optimally switch robots from station-to-station to even-out wear and extend the life cycle? Furthermore, can switching be coincident with routine maintenance, and how often should a switch take place?

The control and information servers and wireless hardware would make the initial cost of this system greater than stand-alone independently controlled robots of today, yet use of open-architecture hardware would necessitate only software upgrades throughout the life of the plant. The benefit of improved process management would likely more than payback the initial financial burden.

6.3.2 Case Study: Application to the Automotive Body Shop

Including the present work on automotive assembly robots, a second suitable application of standard kinematic interfaces is the automotive body shop. While the robot example is focused on how an information system networking robots can leverage common handling of control signals, programs, and calibration data, this section focuses on how the deterministic interfaces can improve intelligence and quality of the assembly operations when used to locate parts and machines. In terms of three distinct categories of kinematic interfaces, based on load capacity and size, potential automotive body shop applications include:

1. **Factory interfaces:** between robots and the floor, between modular full fixtures and bases (for high style differentiation in low-volume plants), and between large dies and presses.
2. **Structural interfaces:** between robot axis modules, between modular robotic locators (reconfigurable tooling) and tool bases.
3. **Measurement interfaces:** for placement of measurement devices on tooling, such as small wireless laser units (mini-Perceptron [3]) and inclinometer units.

These interfaces can define a new, higher-value process for calibrating automation and tooling:

1. Kinematic couplings incorporate measurement features, or are shapes (e.g. three-pin) that enable direct measurement of contact locations.
2. Because of exact or near-exact constraint, the interfaces are deterministic: once the couplings are measured, an error correction transformation can be used to eliminate Abbe error of fixtured parts or machine modules caused by manufacturing variation in the couplings.
3. The calibration data can be stored in an intelligent fashion, making installation of a new model a "plug and play" process. The serial chain of transformations is a trivial calculation in the station controller.
4. A more flexible measurement system architecture enables more targeted investigation of in-production dimensional issues, enabling faster, more direct resolution. When end-of-line vision systems show a critical dimension is out of specification, modular measurement devices allow essentially immediate measurement of suspect stations, with minimal interruption to production.

Furthermore, a fourth class of interface, the **part interface** can be used for kinematically locating compliant sheet metal components. In the case of large, flexible components (e.g. thin floor skins), compliance and the large number of spot welds per station make over-constraint necessary by using several clamps. However, small components are much more rigid, but current usage of clamps with large contact areas deforms the components through overconstraint, deteriorating the repeatability of assembly fits.

A potential solution to overconstraint is to stamp kinematic features such as grooves into sheet metal components. For large parts, the kinematic features would be the primary in-plane locators; these can be stamped with high accuracy and repeatability, then auxiliary clamps are needed for proper stiffness in areas to be welded. For small parts, the kinematic features are the sole constraints (with clamped z-preload). This can also apply to large, stiff parts, such as side rails, underbody cross-members, and body side pillars. Based on these locators, research can explore active interface correction, such as movement of tool-mounted balls to match individual part form errors in critical components. Centrally, the coupling triangle already averages errors in locators. Movable locators with one rotational and one positional degree of freedom can be used in elementary active interfaces, with the correction transform derived from the deterministic match between the fixture balls and the grooves in the sheet metal.

This proposition takes a top-down strategy to improving dimensional quality, while many current quality control processes seek to eliminate total body variation by reducing station-by-station variation. Here, kinematic locators built into rigid components (mainly bottom rails) become the primary, common locators for the major sub-assembly lines, with a process to:

1. At vision stations, measure the relative dimensions between the primary kinematic locators and the major datum points (surface and/or fit defining points).
2. In framing (sub-assembly and welding of side-frames to underbody), and in attachment of closure assemblies, each part has its vision data mapped to its vehicle sequence ID. Active kinematic balls in the framing station can shift each frame relative to the underbody so proper alignment is ensured.
3. In attachment of closure assemblies, design the hinge surfaces to accept variation in the relative placement of the closure relative to the hinge. Use the body vision data to predict how the assembly will hang (e.g. tailgate being fore/aft), and correct the placement for welding through active path correction of the material handling robot.

From the author's experience, significant time is spent attempting to reduce total automotive body variation by optimizing dimensional performance at individual stations. Perhaps a worthwhile thought experi-

ment is to instead accept the individual station and resulting sub-assembly variation and design the major assembly to accept high-level corrections for the sub-assembly variation. This becomes more important as automakers seek to outsource major sub-assemblies; these suppliers are now less experienced in sheet metal assembly than the automakers and subassembly quality has often been below expectations. Kinematic locators can provide an easy method of active correction for major sub-assembly variation, driven by intelligent handling of part-by-part measurement data. With standard stamped groove sizes and locations on parts, and intelligent measurement tools to support quality control, features can be common among styles. Furthermore, for high variety between multiple low-volume production styles, kinematic structural interfaces can be used between modular locators to make repeatable reconfigurable fixtures.

A noteworthy concept applying the measurement interface in the automotive factory would be use of a wireless measurement unit for flexible, in-station measurement of critical part features. This is thought of as a useful supplement to end-of-line vision and statistical process control (SPC) based techniques; when the dimensional engineer wants to monitor point variation at an intermediate station, the handheld unit could be easily placed at the desired point in the line, minimizing interruption to production. The unit would be a standard low-power non-contact laser camera (e.g. a Perceptron camera), and would recognize its position on the tool by communication by sensing a radio-frequency identification (RFID) chip on the tool mount. Measurement data would be sent wirelessly to a nearby computer (e.g. laptop or the central vision station computer), and could also be stored on a non-volatile memory chip on each part or part carrier for proximity reference by later manufacturing operations. Quick, micron-repeatable attachment to tooling would be guaranteed by magnetically preloaded ball/groove kinematic couplings between the measurement unit and the tool-mounted interfaces.

The wireless unit could also be used to improve the intelligence of manual part measurement, such as use of checking fixtures. Groove locators could be placed at the measurement locations around a checking fixture, and the measurement unit could be used to measure parts manually and transmit data directly to an offline workstation. Traditional checking fixtures are binary, indicating acceptability or unacceptability of features such as flange tab positions through manual inspection with over-sized and under-sized pins; however, the wireless camera could collect numerical values to be conditioned in the traditional fashion of SPC by the offline computer

For datum point (rather than custom location) measurements, this system would only require one operator. Buttons placed on the handheld unit can control starting/stopping of an individual measurement, and status lights (e.g. Red/Yellow/Green) can inform the operator of the measurement status. This simple interface can wirelessly drive the data collection console at the offline computer.

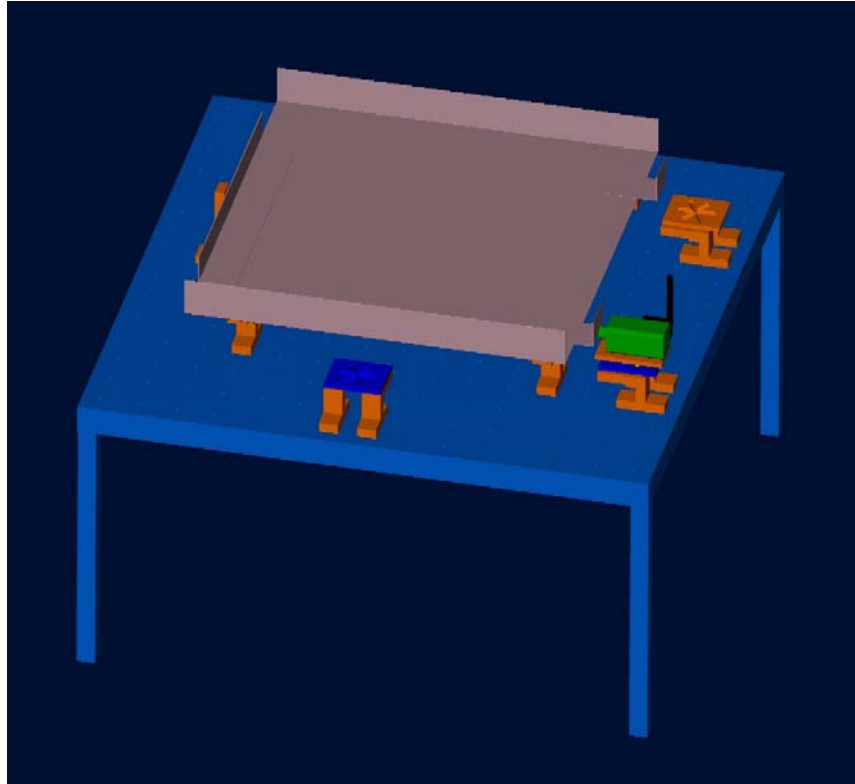


Figure 6.10: Model of wireless measurement tool kinematically coupled to groove plate on body subassembly welding fixture.

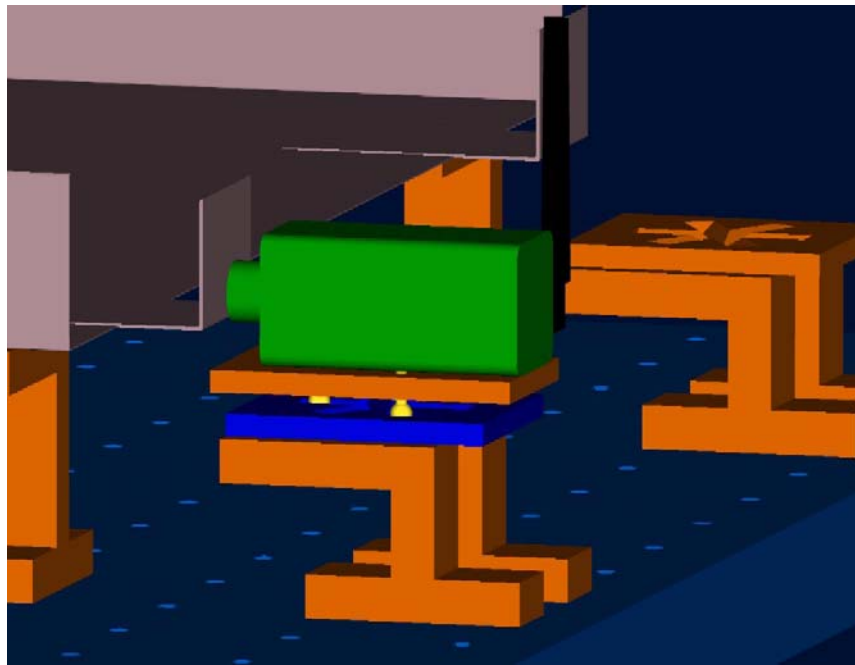
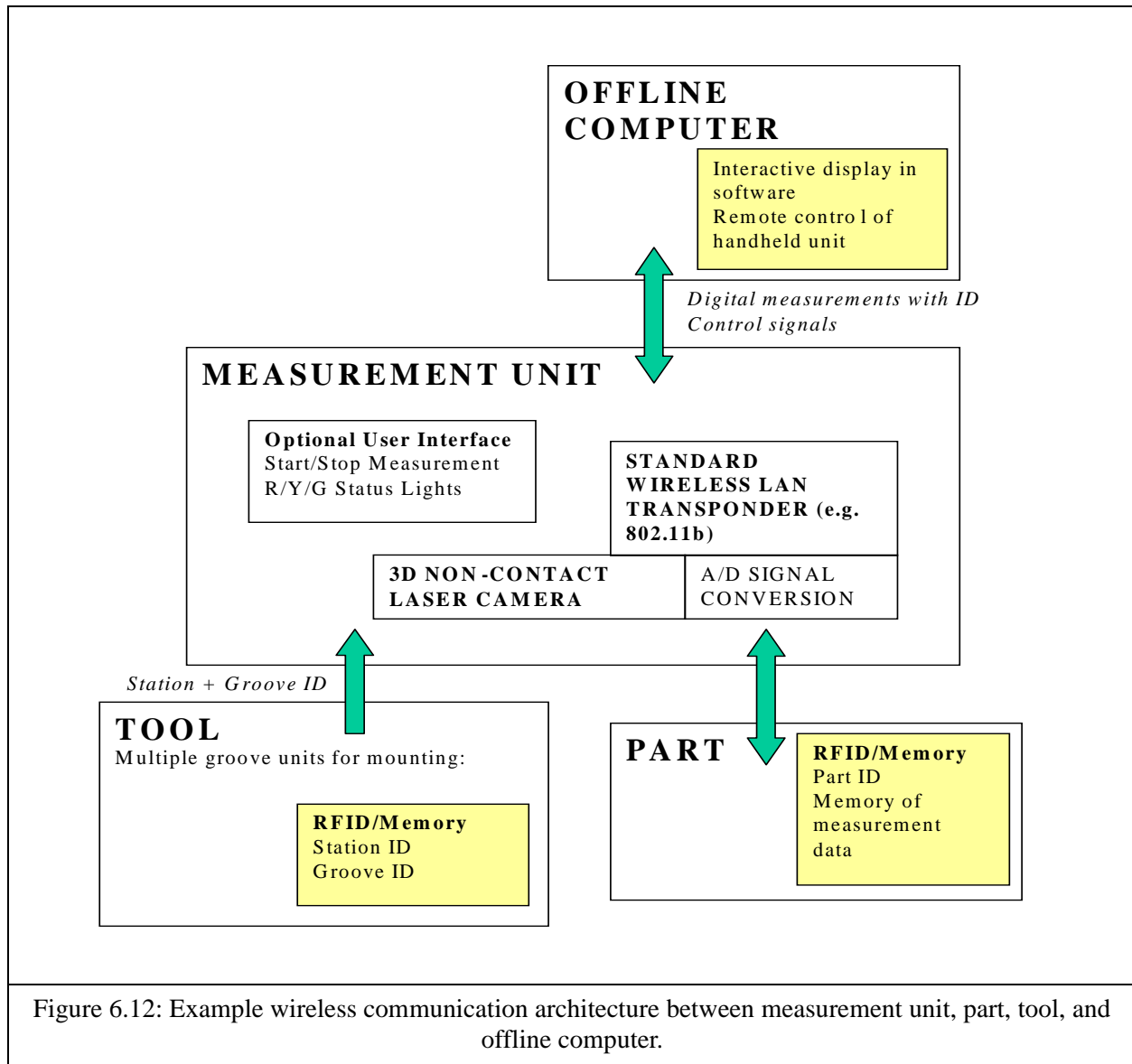


Figure 6.11: Ball-groove interface holding measurement tool in non-contact evaluation of flange position.

While building a subassembly vision station to check each minor sub-assembly in the automotive body is financially prohibitive, checking fixtures are always constructed for each sub-assembly at smaller levels; this tool would be a low-cost method of collecting and cataloguing checking fixture data. This would be especially useful, with proper agreements, for subassembly check data at the automotive suppliers to be transmitted directly to dimensional engineers at the major assembly plant. Another suited application would be to checking and rework of parts at stamping facilities, where binary checking fixtures are the primary method of part verification before and after rework (if needed).



One can also consider using electronics in vehicles or on material handling carriers as repeaters for a peer-to-peer wireless network in the factory. While modernization of existing plants to accommodate fully connected measurement data networks between parts, tooling, automation, and computers, via wired LAN's is sometimes considered too costly, using in-vehicle electronics as repeaters would require essentially no investment for the wired infrastructure. The only investment would be in scaling the network by adding measurement and active data handling capability to additional stations. Furthermore, the proximity and number of repeaters would conceivably eliminate concerns of signal shielding and limited wireless range

due to prominent electromagnetic interferences. An appropriate algorithm for repeating could dynamically correct a message's path if interference interrupts a transmission.

Furthermore, once the wireless infrastructure is built in terms of the desired number of fixed monitoring terminals, the system is easily scalable within reasonable bounds. Associated with each part ID, measurement data can be stored individually on each part and/or in a central database. Within the network in the plant, and bridged beyond the plant through a corporate intranet, measurement data can be monitored in real-time.

The concepts of wireless communication between the groove interface and the measurement unit, between the part and the measurement unit, and between the measurement unit and the offline computer are independent. Hence, the wired architecture of the major subassembly vision station can be maintained, yet each part's vision data can be simultaneously communicated to a self-contained memory chip. Then, active correction for part variation at later critical manufacturing operations is also possible, without cumbersome tracking of the production sequence among non style-specific parts. A part can communicate its variation data upon entry to a production station, making a formerly passive system active, without need for direct communication between measurement systems and active tooling. The deterministic nature of kinematic interfaces provides a simple method of interface measurement and control, which is well suited to a standard, discrete parameter representation for communication between measurement instrumentation, automation, fixtures, and parts in process.

Chapter 7

Conclusion

This thesis sought to present a clear methodology for using kinematic couplings as deterministic interfaces for modular machine and instrumentation structures. Design theory has been presented for traditional ball/groove, canoe ball, traditional quasi-kinematic, three-pin quasi-kinematic, and cylinder/groove quasi-kinematic couplings. This theory was also presented in terms of a design process for using kinematic couplings in high load applications, where rigorous analysis of the disturbance force space and appropriate selections of preload, surface condition, and fastener type are important steps.

The ability to parametrize kinematic coupling performance has been extended from reliance on experimental repeatability analysis to an estimate of Total Mechanical Accuracy, by presenting a closed-form computer model for determining the interchangeability of canoe ball and three-pin interfaces. Now, the total accuracy of a kinematic coupling is estimated well by summing its measured repeatability with its simulated interchangeability. With calibration of the interface by measurement of the perturbed locations of its contact points, introduction of an interface transformation to a machine's structural loop can reduce the deterministic interchangeability error to essentially that inherent in the measurement system's routine. Hence, the total accuracy of a kinematic coupling with full calibration is nearly equal to its repeatability. Perhaps more powerfully, a parametric model of interchangeability allows engineers to predict the accuracy of an interface, based on tolerance distribution parameters assigned to the coupling manufacturing process, plate manufacturing process, interface assembly process, and interface calibration process. This predictive ability enables choice of manufacturing process precision and calibration detail to give the desired interface accuracy at minimum cost.

The application of canoe ball, three-pin, and cylinder/groove couplings to an industrial robot factory interface demonstrated how kinematic coupling can benefit interchangeability of factory automation when downtime must be minimized when catastrophic equipment failures warrant robot replacement. Using an integrated measurement feature on the kinematic coupling, a new interface-centric calibration process is possible. The repeatability assessments of the factory interface pointed to potential limits of mechanical

accuracy for high-precision large-load situations, where the mounting process itself primarily dictates the repeatability of the deterministic interface. When large preloads are needed to counteract large disturbance forces, the non-deterministic effects of frictional sliding resistance between the contactors potentially limit the accuracy, and as demonstrated make lower-cost quasi-kinematic interfaces comparable in performance to higher-cost kinematic canoe ball couplings.

The presentation of a modular structure for a high-precision microscope demonstrated how kinematic couplings can be used to segment a structure to give dramatically improved thermal stability, while also providing enhanced mechanical functionality via the ability to interchange different optical modules with little or no need for re-calibration. The benefit of a segmented cylindrical structure can be extended in concept to other applications, including “Lego-like” robot structures with one or two axes per module.

Looking forward to future research, the ability to characterize performance of kinematic couplings in a closed form makes them well-suited for development of a standard representation for kinematic couplings. Most powerfully, kinematic couplings can be envisioned as an ideal handshake between precision mechanics and information technology. At the most basic level, encoding of interface calibration data on a wireless tag can initiate communication between the interface and a calibration computer when the interface is in proximity to the machine. Furthermore, kinematic couplings would be an ideal mechanical homing station for autonomous material handling vehicles. Given local positioning technology for such vehicles, docking stations using kinematic couplings could serve as absolute position references within a large system, and identification of location at the homing station could be made based on simple (e.g. RFID) proximity identification. In defining the framework for system-wide applications of kinematic couplings, based on deterministic predictions of total accuracy and a standard design representation, this thesis is a framework for further thinking in convergence of quick-change interfaces and thin-client information interfaces to build low-cost, intelligent, flexible, automation processes.

Appendix A

References

Chapter 2

- [1] Slocum, Alexander H. “Method of and Apparatus for Locating and Orientating a Part on a Gripper and Transferring it to a Tool While Maintaining Location and Orientation on the Tool”, U.S. Patent 5,711,647, January 27, 1998.
- [2] Culpepper, Martin L. and Alexander H. Slocum. “Quasi-Kinematic Coupling and Method for Use in Assembling and Locating Mechanical Components and the Like”, U.S. Patent 6,193,430, February 27, 2001.
- [3] Hale, Layton C. “Three-Tooth Kinematic Coupling”, U.S. Patent 6,065,898, May 23, 2000.
- [4] Slocum, Alexander H. Precision Machine Design, Prentice-Hall, Englewood Cliffs, NJ, 1992.
- [5] Hale, Layton C. and Alexander H. Slocum. “Optimal Design Techniques for Kinematic Couplings”, *Precision Engineering*, 25, 114-127, 2000.
- [6] Maxwell, J.C. “General Considerations Concerning Scientific Apparatus”, *The Scientific Papers of James Clerk Maxwell*, ed. W.C. Nivens, Dover Press, 1890.
- [7] Johnson, K.L. Contact Mechanics, Cambridge University Press, Cambridge, UK, 1985.
- [8] Slocum, Alexander H. “Kinematic Couplings for Precision Fixturing -- Part I: Formulation of Design Parameters”, *Precision Engineering*, 10.2, 85-91, 1988.
- [9] Slocum, Alexander H. “Design of Three-Groove Kinematic Couplings”, *Precision Engineering*, 14.2, 67-76, 1992.
- [10] Mullenheld, Bernard. “Prinzipien der kinematischen Kopplung als Schnittstelle zwischen Spindel und Schleifscheibe mit praktischer Erprobung im Vergleich zum Kegel-Hohlschaft” (Application of kinematic couplings to a grinding wheel interface), SM Thesis, Aachen, Germany, 1999.
- [11] Culpepper, Martin L. “Design and Application of Compliant Quasi-Kinematic Couplings”, Ph.D. Thesis, Massachusetts Institute of Technology, Cambridge, MA, 2000.
- [12] Matweb, <http://www.matweb.com>.
- [13] Mischke, Charles R. and Joseph E. Shigley. Mechanical Engineering Design, McGraw-Hill, New York, NY, 1989.

Chapter 3

- [1] Slocum, Alexander H. and Alkan Donmez. “Kinematic Couplings for Precision Fixturing - Part 2: Experimental Determination of Repeatability and Stiffness”, Precision Engineering, 10.3, July 1988.
- [2] Slocum, Alexander H. “Design of Three-Groove Kinematic Couplings”, Precision Engineering, 14.2, 67-76, 1992.

Chapter 4

- [1] ABB IRB6400R Product Manual.
- [2] Leica LTD500 Product Information, <http://www.leica.com>.
- [3] Vallance, Robert R. “Precision Connector Assembly Automation”, Ph.D. Thesis, Massachusetts Institute of Technology, Cambridge, MA, 1999.

Chapter 5

- [1] “Overview of the High Precision Microscope Project”, University of Illinois Laboratory for Fluorescence Dynamics, 2000.
- [2] Kaviany, Massoud. Principles of Heat Transfer, University of Michigan, Ann Arbor, Michigan, 1999.
- [3] National Instruments LabView and DAQ Reference, <http://www.ni.com>.
- [4] Ho, Y.C. Engineering Sciences 205 Class Notes, Harvard University, Cambridge, MA, 2001.

Chapter 6

- [1] SEMI E57-0299, “Provisional Mechanical Specification for Kinematic Couplings Used to Align and Support 300 mm Wafer Carriers,” SEMI, 1999.
- [2] Greenspun, Philip. Philip and Alex’s Guide to Web Publishing, Morgan Kaufmann, San Francisco, CA, 1999.
- [3] Perceptron, Incorporated. <http://www.perceptron.com>.

Appendix B

Kinematic Coupling Design Code

B.1 Design of Traditional and Canoe Ball Couplings

```
% kcggen.m - code for parametric design studies of three groove kinematic
couplings
% applies to standard symmetric (equal angle, equal groove) and asymmetric
couplings

% Adapted from kincoup.xls by John Hart, MIT PERG, March 2001

% Adds bolt integrity calculations
%   specify bolt diameter,

% All metric units (N-m-s)

% Symmetry Specification -----
-----

symmetric = 0; % 1 IF SYMMETRIC (EQUILATERAL, EQUAL RADIUS, EQUAL PRELOAD,
ALL BALLS SAME MAT, ALL GRVS SAME MAT)
               % 0 IF ASYMMETRIC - REQUIRES INDIVIDUAL DATA ENTRY

% Coupling materials library -----
-----

% Set 'Matgrv' and 'Matball' to 1 for Carbide
% 2 for Plastic
% 3 for RC 62 Steel
% 3 for RC 57 420 Stainless
% 4 for other values, and enter in Matball(4,:) and Matgroove(4,:)

Matball = [2.758e9, 3.103e11, 0.3]; % Carbide [Hertz limit, elastic modulus,
Poisson ratio]
Matball(2,:) = [1.034e8, 1.034e10, 0.2]; % Plastic
Matball(3,:) = [1.724e9, 2.041e11, 0.29]; % RC62 Steel
Matball(4,:) = [1.36e9*0.75, 2.0e11, 0.29]; % RC57 420 Stainless
Matball(5,:) = [2.758e9, 3.103e11, 0.3]; % Other - set to appropriate val-
ues, dummy = carbide

Matgroove = [2.758e9, 3.103e11, 0.3]; % Carbide [Hertz limit, elastic modu-
lus, Poisson ratio]
Matgroove(2,:) = [1.034e8, 1.034e10, 0.2]; % Plastic
Matgroove(3,:) = [1.724e9, 2.041e11, 0.29]; % RC62 Steel
Matgroove(4,:) = [1.36e9*0.75, 2.0e11, 0.29]; % RC57 420 Stainless
Matgroove(5,:) = [2.758e9, 3.103e11, 0.3]; % Other - set to appropriate val-
ues, dummy = carbide
```

```

% Bolt materials library -----
-----

% Assumes size > M16

% Set 'Qualbolt' to 1 for quality = 9.8
%               2 for          10.9
%               3 for          12.9

Matbolt(1,:) = [7.20e9, 9.00e9]; % [Tensile yield strength, UTS]
Matbolt(2,:) = [9.40e9, 1.040e10];
Matbolt(3,:) = [1.10e10, 1.220e10];

% Setup opening of design loop (s) here -----
-----

%Default no loop
i = 1;

for param1 = -100000:-100000;%-2000:-400000 % first varying parameter
for param2 = 1:1:1 % second varying parameter

    % set varied paramaters to 'param 1' and 'param 2' below
    % nest more loops if desired

% Disturbance parameters -----
-----

FLx = param1(i,1);% (X,Y,Z) applied force
FLy = param1(i,2);
FLz = param1(i,3);

MLx = param1(i,4); % (X,Y,Z) applied torque
MLy = param1(i,5);
MLz = param1(i,6);

XL = 0; % (X,Y,Z) location of force and torque application
YL = 0;
ZL = 0;

Xerr = 0.5; % (X,Y,Z) location of error reporting
Yerr = 2.5;
Zerr = 2.0;

% Disturbance force matrix (for bolt calculations) - include effect of non-
centroidal disturbance
Fdist = [FLx;
        FLy;
        FLz;
        MLx + FLz*YL - FLY*ZL;
        MLy + FLx*ZL - FLz*XL;

```

```

        MLz + FLy*XL - FLx*XL];

% Coupling Data Entry -----
-----

% Coupling 1 - applies to all couplings if symmetric = 1
r1 = 0.5;           % Radial coordinate of coupling position
th1 = pi/2;         % Angular coordinate of coupling position
thg1 = pi/4;        % Groove angle
Dball1 = 0.075;     % Equivalent ball diameter that would contact groove at same
points
Rbminor1 = 0.5;% Minor ball radius
Rbmajor1 = 0.5;% Major ball radius
Rgrv1 = 1000;      % Groove radius (negative for trough)
Matgrv1 = 1;       % Groove material
Matball1 = 1;      % Ball material
Fpxone = 0;        % X-component of preload force
Fpyone = 0;        % Y-component of preload force
Fpzone = param1;   % Z-component of preload force
rpone = 0.5;       % Radial coordinate of preload application
thpone = pi/2;     % Angular coordinate of preload application
zpone = 2*Dball1;  % Z-coordinate of preload application (default =
2*Dball1)
Dbolt1 = 28/1000;  % Bolt diameter (divided to mm)
Matbolt1 = 2;      % Bolt material
Leng1 = 50/1000;   % Length of bolt thread engagement

% Coupling 2 - enter values here if asymmetric design, else these are set
appropriately later
r2 = 0.5;           % Radial coordinate of coupling position
th2 = 7*pi/6;       % Angular coordinate of coupling position
thg2 = pi/4;        % Groove angle
Dball2 = 0.075;% Equivalent ball diameter that would contact groove at same
points
Rbminor2 = 0.5;% Minor ball radius
Rbmajor2 = 0.5;% Major ball radius
Rgrv2 = 1000;      % Groove radius (negative for trough)
Matgrv2 = 4;       % Groove material
Matbal2 = 4;      % Ball material
Fpxtwo = 0;        % X-component of preload force
Fpytwo = 0;        % Y-component of preload force
Fpztwo = -100000;  % Z-component of preload force
rptwo = 0.5;       % Radial coordinate of preload application
thptwo = 7*pi/6;   % Angular coordinate of preload application
zptwo = 2*Dball2;  % Z-coordinate of preload application (default =
2*Dball2)
Dbolt2 = 28/1000;  % Bolt diameter (divided to mm)
Matbolt2 = 2;      % Bolt material
Leng2 = 50/1000;   % Length of bolt thread engagement

% Coupling 3 - enter values here if asymmetric design, else these are set
appropriately later
r3 = 0.5;           % Radial coordinate of coupling position

```

```

th3 = 11*pi/6;           % Angular coordinate of coupling position
thg3 = pi/4;             % Groove angle
Dball3 = 0.075;% Equivalent ball diameter that would contact groove at same
points
Rbminor3 = 0.5;% Minor ball radius
Rbmajor3 = 0.5;% Major ball radius
Rgrv3 = 1000;           % Groove radius (negative for trough)
Matgrv3 = 4;            % Groove material
Matbal3 = 4;            % Ball material
Fpxthree = 0;           % X-component of preload force
Fpythree = 0;           % Y-component of preload force
Fpzthree = -100000;     % Z-component of preload force
rpthree = 0.5;          % Radial coordinate of preload application
thpthree = 11*pi/6;     % Angular coordinate of preload application
zpthree = 2*Dball3;     % Z-coordinate of preload application (default =
2*Dball)
Dbolt3 = 28/1000;       % Bolt diameter (divided to mm)
Matbolt3 = 2;           % Bolt material
Leng3 = 50/1000;        % Length of bolt thread engagement

% Skip this section - propagates uniform parameters if symmetric design
if symmetric == 1
    r2 = r1;
    r3 = r1;
    th2 = th1 + 2*pi/3;
    th3 = th1 + 4*pi/3;
    Dball2 = Dball1;
    Dball3 = Dball1;
    Rbminor2 = Rbminor1;
    Rbminor3 = Rbminor1;
    Rbmajor2 = Rbmajor1;
    Rbmajor3 = Rbmajor1;
    Rgrv2 = Rgrv1;
    Rgrv3 = Rgrv1;
    Fpxtwo = Fpxone;
    Fpytwo = Fpyone;
    Fpztwo = Fpzone;
    Fpxthree = Fpxone;
    Fpythree = Fpyone;
    Fpzthree = Fpzone;
    rptwo = rpone;
    rpthree = rpone;
    thptwo = thpone + 2*pi/3;
    thpthree = thpone + 4*pi/3;
    Matbal2 = Matbal1;
    Matgrv2 = Matgrv1;
    Matbal3 = Matbal1;
    Matgrv3 = Matgrv1;
    Dbolt2 = Dbolt1;
    Dbolt3 = Dbolt1;
    Matbolt2 = Matbolt1;
    Matbolt3 = Matbolt1;
    Leng2 = Leng1;
    Leng3 = Leng1;

```

end

% Computation of coupling locations and direction cosines -----

% Coupling 1

Xba = r1*cos(th1) + Dball1*sqrt(2)*sin(th1)/4;% (XYZ) of ball-groove1 contact points (a and b)

Xbb = r1*cos(th1) - Dball1*sqrt(2)*sin(th1)/4;

Yba = r1*sin(th1) - Dball1*sqrt(2)*cos(th1)/4;

Ybb = r1*sin(th1) + Dball1*sqrt(2)*cos(th1)/4;

Zba = -Dball1*sqrt(2)/4;

Zbb = -Dball1*sqrt(2)/4;

Aba = -sin(th1)/sqrt(1+tan(thg1)^2); % (ABG) direction cosines

ball1-groove1 contact points (a and b)

Abb = sin(th1)/sqrt(1+tan(thg1)^2);

Bba = cos(th1)/sqrt(1+tan(thg1)^2);

Bbb = -cos(th1)/sqrt(1+tan(thg1)^2);

Gba = tan(thg1)/sqrt(1+tan(thg1)^2);

Gbb = tan(thg1)/sqrt(1+tan(thg1)^2);

xpone = rpone*cos(thpone);

ypone = rpone*sin(thpone);

Sone = min(Matgroove(Matgrv1,1),Matball(Matball1,1));% Hertz stress limit, pair1

Egone = Matgroove(Matgrv1,2); % Elastic modulus,

groove1

vgone = Matgroove(Matgrv1,3); % Poisson ratio, groove1

Ebone = Matball(Matball1,2); % Elastic modulus, ball1

vbone = Matball(Matball1,3); % Poisson ratio, ball1

Eeone = 1/((1-vgone^2)/Egone+(1-vbone^2)/Ebone); % Equivalent modulus, pair1

Reone = 1/(1/Rgrv1 + 1/Rbminor1 + 1/Rbmajor1);

ctone = Reone*sqrt((1/Rgrv1)^2+(1/Rbmajor1-1/Rbminor1)^2+2*(-1/Rgrv1)*(1/Rbmajor1-1/Rbminor1));

theta_1 = acos(ctone);

alpha_1 = 1.939*2.71831^(-5.26*theta_1)+1.78*2.71831^(-1.09*theta_1)+0.723/theta_1+0.221;

beta_1 = 35.228*2.71831^(-0.98*theta_1)-32.424*2.71831^(-1.0475*theta_1)+1.486*theta_1-2.634;

lambda_1 = -0.214*2.71831^(-4.95*theta_1)-0.179*theta_1^2+0.555*theta_1+0.319;

% Coupling 2

Xbc = r2*cos(th2) + Dball2*sqrt(2)*sin(th2)/4;% (XYZ) of ball-groove1 contact points (c and d)

Xbd = r2*cos(th2) - Dball2*sqrt(2)*sin(th2)/4;

Ybc = r2*sin(th2) - Dball2*sqrt(2)*cos(th2)/4;

Ybd = r2*sin(th2) + Dball2*sqrt(2)*cos(th2)/4;

Zbc = -Dball2*sqrt(2)/4;

Zbd = -Dball2*sqrt(2)/4;

```

Abc = -sin(th2)/sqrt(1+tan(thg2)^2); % (ABG) direction cosines
ball1-groove1 contact points (c and d)
Abd = sin(th2)/sqrt(1+tan(thg2)^2);
Bbc = cos(th2)/sqrt(1+tan(thg2)^2);
Bbd = -cos(th2)/sqrt(1+tan(thg2)^2);
Gbc = tan(thg2)/sqrt(1+tan(thg2)^2);
Gbd = tan(thg2)/sqrt(1+tan(thg2)^2);

xptwo = rptwo*cos(thptwo);
yptwo = rptwo*sin(thptwo);

Stwo = min(Matgroove(Matgrv2,1),Matball(Matbal2,1));
Egtwo = Matgroove(Matgrv2,2);
vgtwo = Matgroove(Matgrv2,3);
Ebtwo = Matball(Matbal2,2);
vbtwo = Matball(Matbal2,3);
Eetwo = 1/((1-vgtwo^2)/Egtwo+(1-vbtwo^2)/Ebtwo);
Retwo = 1/(1/Rgrv2 + 1/Rbminor2 + 1/Rbmajor2);
cttwo = Retwo*sqrt((1/Rgrv2)^2+(1/Rbmajor2-1/Rbminor2)^2+2*(-1/Rgrv2)*(1/
Rbmajor2-1/Rbminor2));
theta_2 = acos(cttwo);
alpha_2 = 1.939*2.71831^(-5.26*theta_2)+1.78*2.71831^(-1.09*theta_2)+0.723/
theta_2+0.221;
beta_2 = 35.228*2.71831^(-0.98*theta_2)-32.424*2.71831^(-
1.0475*theta_2)+1.486*theta_2-2.634;
lambda_2 = -0.214*2.71831^(-4.95*theta_2)-
0.179*theta_2^2+0.555*theta_2+0.319;

% Coupling 3
Xbe = r3*cos(th3) + Dball3*sqrt(2)*sin(th3)/4;% (XYZ) of ball1-groove1 con-
tact points (c and d)
Xbf = r3*cos(th3) - Dball3*sqrt(2)*sin(th3)/4;
Ybe = r3*sin(th3) - Dball3*sqrt(2)*cos(th3)/4;
Ybf = r3*sin(th3) +g Dball3*sqrt(2)*cos(th3)/4;
Zbe = -Dball3*sqrt(2)/4;
Zbf = -Dball3*sqrt(2)/4;
Abe = -sin(th3)/sqrt(1+tan(thg3)^2); % (ABG) direction cosines
ball1-groove1 contact points (c and d)
Abf = sin(th3)/sqrt(1+tan(thg3)^2);
Bbe = cos(th3)/sqrt(1+tan(thg3)^2);
Bbf = -cos(th3)/sqrt(1+tan(thg3)^2);
Gbe = tan(thg3)/sqrt(1+tan(thg3)^2);
Gbfe = tan(thg3)/sqrt(1+tan(thg3)^2);

xpthree = rpthree*cos(thpthree);
ypthree = rpthree*sin(thpthree);

Sthree = min(Matgroove(Matgrv3,1),Matball(Matbal3,1));
Egthree = Matgroove(Matgrv3,2);
vgthree = Matgroove(Matgrv3,3);
Ebthree = Matball(Matbal3,2);
vbthree = Matball(Matbal3,3);
Eethree = 1/((1-vgthree^2)/Egthree+(1-vbthree^2)/Ebthree);
Rethree = 1/(1/Rgrv3 + 1/Rbminor3 + 1/Rbmajor3);

```

```

ctthree = Rethree*sqrt((1/Rgrv3)^2+(1/Rbmajor3-1/Rbminor3)^2+2*(-1/
Rgrv3)*(1/Rbmajor3-1/Rbminor3))
theta_3 = acos(ctthree);
alpha_3 = 1.939*2.71831^(-5.26*theta_3)+1.78*2.71831^(-1.09*theta_3)+0.723/
theta_3+0.221;
beta_3 = 35.228*2.71831^(-0.98*theta_3)-32.424*2.71831^(-
1.0475*theta_3)+1.486*theta_3-2.634;
lambda_3 = -0.214*2.71831^(-4.95*theta_3)-
0.179*theta_3^2+0.555*theta_3+0.319;

% Interface force-deflection calculations -----
-----

% Build force-moment equilibrium equation AF = B
A = [Aba, Abb, Abc, Abd, Abe, Abf;...
     Bba, Bbb, Bbc, Bbd, Bbe, Bbf;...
     Gba, Gbb, Gbc, Gbd, Gbe, Gbf;...
     -Bba*Zba+Gba*Yba, -Bbb*Zbb+Gbb*Ybb, -Bbc*Zbc+Gbc*Ybc, -
Bbd*Zbd+Gbd*Ybd, -Bbe*Zbe+Gbe*Ybe, -Bbf*Zbf+Gbf*Ybf;...
     Aba*Zba-Gba*Xba, Abb*Zbb-Gbb*Xbb, Abc*Zbc-Gbc*Xbc, Abd*Zbd-Gbd*Xbd,
Abe*Zbe-Gbe*Xbe, Abf*Zbf-Gbf*Xbf;...
     -Aba*Yba+Bba*Xba, -Abb*Ybb+Bbb*Xbb, -Abc*Ybc+Bbc*Xbc, -
Abd*Ybd+Bbd*Xbd, -Abe*Ybe+Bbe*Xbe, -Abf*Ybf+Bbf*Xbf];

Bwithloads = [ -(Fpxone+Fpxtwo+Fpxthree+FLx);
                -(Fpyone+Fpytwo+Fpythree+FLy);...
                -(Fpzone+Fpztwo+Fpzthree+FLz);...
                -(-Fpyone*zpone-Fpytwo*zptwo-Fpyth-
ree*zpthree+Fpzone*ypone+Fpztwo*yptwo+Fpzthree*ypthree-
FLy*ZL+FLz*YL+MLx);...
                -(Fpxone*zpone+Fpxtwo*zptwo+Fpxthree*zpthree-Fpzone*xpone-
Fpztwo*xptwo-Fpzthree*xpthree+FLx*ZL-FLz*XL+MLy);...
                -(-Fpxone*ypone-Fpxtwo*yptwo-Fpxthree*ypthree+Fpy-
one*xpone+Fpytwo*xptwo+Fpythree*xpthree-FLx*YL+FLy*XL+MLz) ];

Bnoloads = [ -(Fpxone+Fpxtwo+Fpxthree); -(Fpyone+Fpytwo+Fpythree); -
(Fpzone+Fpztwo+Fpzthree);...
              -(-Fpyone*zpone-Fpytwo*zptwo-Fpythree*zpthree+Fpzone*ypone+Fpz-
two*yptwo+Fpzthree*ypthree);...
              -(Fpxone*zpone+Fpxtwo*zptwo+Fpxthree*zpthree-Fpzone*xpone-Fpz-
two*xptwo-Fpzthree*xpthree);...
              -(-Fpxone*ypone-Fpxtwo*yptwo-Fpxthree*ypthree+Fpy-
one*xpone+Fpytwo*xptwo+Fpythree*xpthree) ];

Fbn = inv(A)*Bwithloads;
Fb = inv(A)*Bnoloads;

fbnone = Fbn(1);
fbntwo = Fbn(2);
fbnthree = Fbn(3);
fbnfour = Fbn(4);
fbnfive = Fbn(5);
fbnsix = Fbn(6);

```

```

fone = Fb(1);
ftwo = Fb(2);
fthree = Fb(3);
ffour = Fb(4);
ffive = Fb(5);
fsix = Fb(6);

% Deflections into balls
delone = lambda_1*(2*fbnone^2/(3*Reone*Eeone^2))^0.33333-
lambda_1*(2*fone^2/(3*Reone*Eeone^2))^0.33333;
deltwo = lambda_1*(2*fbntwo^2/(3*Reone*Eeone^2))^0.33333-
lambda_1*(2*ftwo^2/(3*Reone*Eeone^2))^0.33333;
delthree = lambda_2*(2*fbnthree^2/(3*Retwo*Eetwo^2))^0.33333-
lambda_2*(2*fthree^2/(3*Retwo*Eetwo^2))^0.33333;
delfour = lambda_2*(2*fbnfour^2/(3*Retwo*Eetwo^2))^0.33333-
lambda_2*(2*ffour^2/(3*Retwo*Eetwo^2))^0.33333;
delfive = lambda_3*(2*fbnfive^2/(3*Rethree*Eethree^2))^0.33333-
lambda_3*(2*ffive^2/(3*Rethree*Eethree^2))^0.33333;
delsix = lambda_3*(2*fbnsix^2/(3*Rethree*Eethree^2))^0.33333-
lambda_3*(2*fsix^2/(3*Rethree*Eethree^2))^0.33333;

% Contact ellipse radii
rmajone = alpha_1*(1.5*fbnone*Reone/Eeone)^0.333333;
rmajtwo = alpha_1*(1.5*fbntwo*Reone/Eeone)^0.333333;
rmajthree = alpha_2*(1.5*fbnthree*Retwo/Eetwo)^0.333333;
rmajfour = alpha_2*(1.5*fbnfour*Retwo/Eetwo)^0.333333;
rmajfive = alpha_3*(1.5*fbnfive*Rethree/Eethree)^0.333333;
rmajsix = alpha_3*(1.5*fbnsix*Rethree/Eethree)^0.333333;
rminone = beta_1*(1.5*fbnone*Reone/Eeone)^0.333333;
rmintwo = beta_1*(1.5*fbntwo*Reone/Eeone)^0.333333;
rminthree = beta_2*(1.5*fbnthree*Retwo/Eetwo)^0.333333;
rminfour = beta_2*(1.5*fbnfour*Retwo/Eetwo)^0.333333;
rminfive = beta_3*(1.5*fbnfive*Rethree/Eethree)^0.333333;
rminsix = beta_3*(1.5*fbnsix*Rethree/Eethree)^0.333333;

% Contact stress values
sigone = 3*fbnone/(2*pi*rmajone*rminone)
sigtwo = 3*fbntwo/(2*pi*rmajtwo*rmintwo)
sigthree = 3*fbnthree/(2*pi*rmajthree*rminthree)
sigfour = 3*fbnfour/(2*pi*rmajfour*rminfour)
sigfive = 3*fbnfive/(2*pi*rmajfive*rminfive)
sigsix = 3*fbnsix/(2*pi*rmajsix*rminsix)

% Original ball coordinates
xbone0 = (Xba+Xbb+Dball1*Aba+Dball1*Abb)/2;
ybone0 = (Yba+Ybb+Dball1*Bba+Dball1*Bbb)/2;
zbone0 = (Zba+Zbb+0.5*Dball1*Gba+0.5*Dball1*Gbb)/2;
xbtwo0 = (Xbc+Xbd+Dball2*Abc+Dball2*Abd)/2;
ybtwo0 = (Ybc+Ybd+Dball2*Bbc+Dball2*Bbd)/2;
zbtwo0 = (Zbc+Zbd+0.5*Dball2*Gbc+0.5*Dball2*Gbd)/2;
xbthree0 = (Xbe+Xbf+Dball3*Abe+Dball3*Abf)/2;
ybthree0 = (Ybe+Ybf+Dball3*Bbe+Dball3*Bbf)/2;
zbthree0 = (Zbe+Zbf+0.5*Dball3*Gbe+0.5*Dball3*Gbf)/2;

```



```

% New ball coordinates
xboneN = xbone0+(Aba*delone+Abb*deltwo)/2;
yboneN = ybone0+(Bba*delone+Bbb*deltwo)/2;
zboneN = zbone0+(Gba*delone+Gbb*deltwo)/2;
xbtwoN = xbtwo0+(Abc*delthree+Abd*delfour)/2;
ybtwoN = ybtwo0+(Bbc*delthree+Bbd*delfour)/2;
zbtwoN = zbtwo0+(Gbc*delthree+Gbd*delfour)/2;
xbthreeN = xbthree0+(Abe*delfive+Abf*delsix)/2;
ybthreeN = ybthree0+(Bbe*delfive+Bbf*delsix)/2;
zbthreeN = zbthree0+(Gbe*delfive+Gbf*delsix)/2;

% Original sides' angle with x axis
Aot = 180*atan2((ybone0-ybtwo0),(xbone0-xbtwo0))/pi;
Att = 180*atan2((ybthree0-ybtwo0),(xbthree0-xbtwo0))/pi;
Ato = 180*atan2((ybone0-ybthree0),(xbone0-xbthree0))/pi;

% Ball center displacements
dxone = xboneN - xbone0;
dyone = yboneN - ybone0;
dzone = zboneN - zbone0;
dxtwo = xbtwoN - xbtwo0;
dytwo = ybtwoN - ybtwo0;
dztwo = zbtwoN - zbtwo0;
dxthree = xbthreeN - xbthree0;
dythree = ybthreeN - ybthree0;
dzthree = zbthreeN - zbthree0;

% Theory applicability check
% Initial distance between balls
LotI = sqrt((xbone0-xbtwo0)^2+(ybone0-ybtwo0)^2+(zbone0-zbtwo0)^2);
LttI = sqrt((xbtwo0-xbthree0)^2+(ybtwo0-ybthree0)^2+(zbtwo0-zbthree0)^2);
LtoI = sqrt((xbthree0-xbone0)^2+(ybthree0-ybone0)^2+(zbthree0-zbone0)^2);

% Final distance between balls
LotN = sqrt((xboneN-xbtwoN)^2+(yboneN-ybtwoN)^2+(zboneN-zbtwoN)^2);
LttN = sqrt((xbtwoN-xbthreeN)^2+(ybtwoN-ybthreeN)^2+(zbtwoN-zbthreeN)^2);
LtoN = sqrt((xbthreeN-xboneN)^2+(ybthreeN-yboneN)^2+(zbthreeN-zboneN)^2);

% Original angle between balls
Angone = 180*acos((LttI^2-LotI^2-LtoI^2)/(-2*LotI*LtoI))/pi;
Angtwo = 180*acos((LtoI^2-LotI^2-LttI^2)/(-2*LotI*LttI))/pi;
Angthree = 180*acos((LotI^2-LtoI^2-LttI^2)/(-2*LtoI*LttI))/pi;

% Original altitude lengths
Aone = LotN*sin(pi*abs(Aot-Att)/180);
Atwo = LttN*sin(pi*abs(Aot-Att)/180);
Athree = LttN*sin(pi*abs(Ato-Att)/180);

% New angles between balls
AngoneN = 180*acos((LttN^2-LotN^2-LtoN^2)/(-2*LotN*LtoN))/pi;
AngtwoN = 180*acos((LtoN^2-LotN^2-LttN^2)/(-2*LotN*LttN))/pi;
AngthreeN = 180*acos((LotN^2-LtoN^2-LttN^2)/(-2*LtoN*LttN))/pi;

```

```

% Rotation about opposite side (radians)
Ttt = dzzone/Aone;% rotation about side 23 due to Z motion at ball 1
Tto = dztwo/Atwo;% rotation about side 13 due to Z motion at ball 2
Tot = dzthree/Athree; % rotation about side 12 due to Z motion at ball 3

AmtwoO = Att+Angtwo/2;
AmthreeO = Ato+Angthree/2;
AbtwoO = ybtwoO-tan(pi*AmtwoO/180)*xbtwoO;
AbthreeO = ybthreeO-tan(pi*AmthreeO/180)*xbthreeO;

% Initial coupling centroid
xci = (AbthreeO-AbtwoO)/(pi*(AmtwoO-AmthreeO)/180);
yci = (pi*AmtwoO/180)*xci+AbtwoO;
zci = (zboneO+zbtwoO+zbthreeO)/3;

% New ball-centroid distances
Dcone = sqrt((xboneN-xci)^2+(yboneN-yci)^2+(zboneN-zci)^2);
Dctwo = sqrt((xbtwoN-xci)^2+(ybtwoN-yci)^2+(zbtwoN-zci)^2);
Dctthree = sqrt((xbthreeN-xci)^2+(ybthreeN-yci)^2+(zbthreeN-zci)^2);

% Error motion at centroid from weighted ball motions
dxc = dxone*(LotI-Dcone)/LotI+dxtwo*(LttI-Dctwo)/LttI+dxthree*(LtoI-Dctthree)/LtoI;
dyc = dyone*(LotI-Dcone)/LotI+dytwo*(LttI-Dctwo)/LttI+dythree*(LtoI-Dctthree)/LtoI;
dzc = dzone*(LotI-Dcone)/LotI+dztwo*(LttI-Dctwo)/LttI+dzthree*(LtoI-Dctthree)/LtoI;

% Difference
DLotI = LotI - LotN;
DLttI = LttI - LttN;
DLtoI = LtoI - LtoN;

% Change in distance / distance between balls
DL_DD1 = abs(DLotI/LotI);
DL_DD2 = abs(DLttI/LttI);
DL_DD3 = abs(DLtoI/LtoI);

% Coupling theory applicability check - all fields should be >5
numer1 = max(abs(delone), abs(deltwo))/(Dball1/2);
numer2 = max(abs(delthree), abs(delfour))/(Dball2/2);
numer3 = max(abs(delfive), abs(delsix))/(Dball3/2);
denom1 = abs(DLotI/LotI);
denom2 = abs(DLttI/LttI);
denom3 = abs(DLtoI/LtoI);
ratio1 = numer1/denom1;
ratio2 = numer2/denom2;
ratio3 = numer3/denom3;

% Coupling error rotations
EpsZ1 = sqrt((0.5*(Aba*delone+Abb*deltwo))^2+(0.5*(Bba*delone+Bbb*deltwo))^2)*sign(-(Aba*delone+Abb*deltwo))/sqrt((xboneO-xci)^2+(yboneO-yci)^2);
EpsZ2 = sqrt((0.5*(Abc*delthree+Abd*delfour))^2+(0.5*(Bbc*delthree+Bbd*del-

```

```

four))^2)*sign(ABC*delthree+ABd*delfour)/sqrt((xbtwo0-xci)^2+(ybtwo0-
yci)^2);
EpsZ3 = sqrt((0.5*(Abe*delfive+Abf*delsix))^2+(0.5*(Bbe*delfive+Bbf*del-
six))^2)*sign(Abe*delfive+Abf*delsix)/sqrt((xbthree0-xci)^2+(ybthree0-
yci)^2);
EpsX = Ttt*cos(pi*Att/180)+Tto*cos(pi*Ato/180)-Tot*cos(pi*Aot/180)
EpsY = Ttt*sin(pi*Att/180)+Tto*sin(pi*Ato/180)-Tot*sin(pi*Aot/180)
EpsZ = (EpsZ1 + EpsZ2 + EpsZ3)/3

% Coupling homogenous transformation matrix
HTM = [1, -EpsZ, EpsY, dxc;...
        EpsZ, 1, -EpsX, dyc;...
        -EpsY, EpsX, 1, dzc;...
        0, 0, 0, 1];

% Point of interest
XYZInt = [Xerr; Yerr; Zerr; 1];

% Error motions at point of interest
ErrorInt = HTM*XYZInt - XYZInt;
DeltaX = ErrorInt(1);
DeltaY = ErrorInt(2);
DeltaZ = ErrorInt(3);
DeltaRMS = sqrt(DeltaX^2 + DeltaY^2 + DeltaZ^2);
DeltaRMS_mm = 1000*DeltaRMS;

% Output data to console -----
-----

if symmetric == 1

% This assumes spherical contact, z-preload only (ABB base case)
coupdata_symm(i,:) = [param1, param2, r1, th1, Dball1, Rbminor1, Fpzone,
sigone/Sone, sigtwo/Sone, sigthree/Stwo,...
    sigfour/Stwo, sigfive/Stthree, sigsix/Stthree, DeltaX, DeltaY, DeltaZ,
EpsX, EpsY, EpsZ, DeltaX, DeltaY, DeltaZ, DeltaRMS_mm ];
end

% This assumes z-preload only
if symmetric == 0
coupdata_asymm(i,:) = [param1, param2, r1, th1, Dball1, Rbminor1, Rbmajor1,
Fpzone, r2, th2, Dball2, Rbminor2, Rbmajor2, Fpztwo,...
    r3, th3, Dball3, Rbminor3, Rbmajor3, Fpzthree, sigone/Sone, sigtwo/
Sone, sigthree/Stwo,...
    sigfour/Stwo, sigfive/Stthree, sigsix/Stthree, DeltaX, DeltaY, DeltaZ,
EpsX, EpsY, EpsZ, DeltaX, DeltaY, DeltaZ, RMS_mm ];
end

% Coupling theory applicability check - all fields should be >5
theory_check(i,:) = [ratio1, ratio2, ratio3];

% Upper-bound bolt loads and stress checks
% Transformation matrix to from disturbance forces to bolt loads

```

```

% Fbolt = -Inv(Abolt)*Fdist
% Fbolt = [Fn1; Fn2; Fn3; Ft1; Ft2; Ft3];

Abolt = [
    0, 0, 0, sin(thpone),
    sin(thptwo), sin(thpthree);
    0, 0, 0, cos(thpone),
    cos(thptwo), cos(thpthree);
    1, 1, 1, 0, 0, 0;
    rpone*sin(thpone), rptwo*sin(thptwo), rpthree*sin(thpthree),
    0, 0, 0;
    -rpone*cos(thpone), -rptwo*cos(thptwo), -rpthree*cos(thpthree),
    0, 0, 0;
    0, 0, 0, -rpone, -rptwo,
    -rpthree];

Fbolt = -1*inv(Abolt)*Fdist;

% Add the preloads
Fbolt(1) = abs(Fbolt(1)) - Fpzone;
Fbolt(2) = abs(Fbolt(1)) - Fpzone;
Fbolt(3) = abs(Fbolt(1)) - Fpzone;

% Compute stress ratios in shank
nshank1 = ((Fbolt(1)/(pi*Dbolt1^2))*(1/Matbolt(Matbolt1,2)))^2 +
    ((16*Fbolt(4)/(3*pi*Dbolt1^2))*(1/(0.62*Matbolt(Matbolt1,2))))^2;
nshank2 = ((Fbolt(2)/(pi*Dbolt2^2))*(1/Matbolt(Matbolt2,2)))^2 +
    ((16*Fbolt(5)/(3*pi*Dbolt2^2))*(1/(0.62*Matbolt(Matbolt2,2))))^2;
nshank3 = ((Fbolt(3)/(pi*Dbolt3^2))*(1/Matbolt(Matbolt3,2)))^2 +
    ((16*Fbolt(6)/(3*pi*Dbolt3^2))*(1/(0.62*Matbolt(Matbolt3,2))))^2;

% Compute stress ratios in threads
nthreads1 = (Fbolt(1)/(pi*Dbolt1*Leng1))*(1/(0.62*Matbolt(Matbolt1,2)));
nthreads2 = (Fbolt(2)/(pi*Dbolt2*Leng2))*(1/(0.62*Matbolt(Matbolt2,2)));
nthreads3 = (Fbolt(3)/(pi*Dbolt3*Leng3))*(1/(0.62*Matbolt(Matbolt3,2)));

% This output assumes all bolts same diameter, same threaded engagement
length
boltdata(i,:) = [Dbolt1, Leng1, Fbolt', nshank1, nshank2, nshank3,
    nthreads1, nthreads2, nthreads3,...
    max(nshank1, nthreads1), max(nshank2, nthreads2),
    max(nshank3, nthreads3)];

i = i+1;

end
end

% -----
-----

```

B.2 Contact Force Calculation for Three-Pin Interface

```
% threepins.m - calculates pin reaction and bolt forces for three-pin
% kinematic coupling concept under robot base loading

% for simplicity, assume fastening bolt forces act at pin load points

% John Hart, MIT, November 2000

function [F] = threepins

angle = 1;
for angle = 1:1:180;

% define nominal geometric offsets
alpha = 56*pi/180; % quadrant 3 angle of pin 1, measured CW from -y axis
beta = 56*pi/180; % quadrant 4 angle of pin 2, measured CCW from -y axis
theta = 30*pi/180; % quadrant 1 angle of preload force application,
Rpins = 0.4; % radius offset of pins 1 and 2 from csys origin
yo = 0.35; % y-axis offset of bolt force and preload from csys origin

gamma = angle*pi/180; % z-axis rotation of foot coordinate frame (robot load-
ing frame)
R01 = [0, 0, 0.1]; % position vector offset from csys origin to point of
robot loading

Fpreload = 2; % specified external preload force [kN] (points toward coupling
circle)

% Robot loads in foot frame coordinates (frame 1)
% F1 = [Fx1; Fy1; Fz1; Mx1; My1; Mz1]
F1 = [38; -42; 38; 61; 61; -15]; % [kN, kN-M]

% Robot loads in base frame coordinates (frame 0)
F0 = [F1(1)*cos(gamma) - F1(2)*sin(gamma); F1(1)*sin(gamma) +
F1(2)*cos(gamma); F1(3);...
      F1(4)*cos(gamma) - F1(5)*sin(gamma); F1(4)*sin(gamma) +
F1(5)*cos(gamma) ; F1(6)];

% Add moments from Fx, Fy, Fz due to frame position offset;
F0(4) = F0(4) - F0(2)*R01(3) + F0(3)*R01(2);
F0(5) = F0(5) + F0(1)*R01(3) - F0(3)*R01(1);
F0(6) = F0(6) - F0(1)*R01(2) + F0(2)*R01(1);

% Add force and moment due to specified spring force;
F0(1) = F0(1) - Fpreload*cos(theta); % x-Force
F0(2) = F0(2) - Fpreload*sin(theta); % y-Force
F0(6) = F0(6) + Fpreload*cos(theta)*yo; % z-Moment

% Solve matrix equation A*F = F0
% where F = [Fanvil; Fpin1; Fpin2; Fbolt1 (at pin1); Fbolt2 (at pin2);
Fbolt3 (at coupbolt)]
```

```

A = [1, sin(alpha), -sin(beta), 0, 0, 0;...
     0, cos(alpha), cos(beta), 0, 0, 0;...
     0, 0, 0, 1, 1, 1;...
     0, 0, 0, -Rpins*cos(alpha), -Rpins*cos(beta), yo;...
     0, 0, 0, Rpins*sin(alpha), -Rpins*sin(beta), 0;...
     -yo, 0, 0, 0, 0, 0];

F = inv(A)*F0;

Fmatrix(angle,:) = F';
Anglematrix(angle,1) = angle;

angle = angle + 1;

end

Fmatrix
plot(Anglematrix(:,1),Fmatrix(:,1),'k-',Anglematrix,Fmatrix(:,2),'k--',
     ',Anglematrix,Fmatrix(:,3),'k-.',...
     Anglematrix,Fmatrix(:,4),'b-',Anglematrix,Fmatrix(:,5),'b--',Anglematrix,
     Fmatrix(:,6),'b-.')
legend('Fanvil', 'Fpin1', 'Fpin2','Fbolt1 - z', 'Fbolt2 - z', 'Fbolt3 - z');
xlabel('Load CSYS rotation (deg)');
ylabel('Force (kN)');
title('6400R base pin coupling: 150kg operation loads - forward');

```

B.3 In-Plane Preload Calculation (Friction Limit) for Three-Pin Interface

```

% threepins_friction.m - calculates necessary bolt preload force and torque
to
% deterministically seat three-pin interface under frictional resistance
between
% horizontal contact surfaces and one or two pins and their vertical contact
surfaces.

% For simplicity, assume fastening bolt forces act at pin load points

% John Hart, MIT, July 2001

% global coefficient of friction - dry and greased surfaces
mu = 0.15;
mu_g = 0.05;

% normal disturbance load [N]
fz = 2500*9.8;

% define nominal pin dimensions and placements - pin 1 is along y-axis
alpha = 52.5*pi/180;      % quadrant 3 angle of pin 1, measured CW from -y
axis
beta = 52.5*pi/180;      % quadrant 4 angle of pin 2, measured CCW from -y
axis
theta = 45*pi/180;      % quadrant 1 angle of preload force application,

```

```

Rpins = 0.5;      % radius offset of pins 1 and 2 from csys origin
yo = 0.5;        % y-axis offset of bolt force and preload from csys origin

% define resultant coordinates and directions of forces and preloads
cp1 = [0 yo 0];
cp2 = Rpins*[cos(3*pi/2 - alpha) sin(3*pi/2 - alpha) 0];
cp3 = Rpins*[cos(3*pi/2 + beta) sin(3*pi/2 - beta) 0];
v_prld = -1*[cos(theta) sin(theta) 0];           % normal direction,
into pin
v_cont1 = [1 0 0];                               % all contact direc-
tions toward center of circle
v_cont2 = [cos(pi/2 - alpha) sin(pi/2 - alpha) 0];
v_cont3 = [cos(pi/2 + beta) sin(pi/2 + beta) 0];
v_fr1_up = [0 1 0];
v_fr1_dn = [0 -1 0];
v_fr2_cw = [cos(-1*alpha) sin(-1*alpha) 0];
v_fr2_ccw = -1*v_fr2_cw;
v_fr3_cw = [cos(180 + beta) sin(180 + beta) 0];
v_fr3_ccw = -1*v_fr3_cw;

% define relative pin-to-pin position vectors
p_12 = cp2 - cp1;
p_21 = cp1 - cp2;
p_23 = cp2 - cp3;
p_32 = cp3 - cp2;
p_13 = cp3 - cp1;
p_31 = cp1 - cp3;

% find instant centers for cases of 2-pin contact
m1 = v_cont1(2)/v_cont1(1);
int1 = cp1(2) - m1*cp1(1);
m2 = v_cont2(2)/v_cont2(1);
int2 = cp2(2) - m2*cp2(1);
m3 = v_cont3(2)/v_cont3(1);
int3 = cp3(2) - m3*cp3(1);

a12 = [-1*m1 1; -1*m2 1];
b12 = [int1; int2];
a13 = [-1*m1 1; -1*m3 1];
b13 = [int1; int3];
a23 = [-1*m2 1; -1*m3 1];
b23 = [int2; int3];

xy_ic12 = inv(a12)*b12;
xy_ic13 = inv(a13)*b13;
xy_ic23 = inv(a23)*b23;

xyz_ic12 = [xy_ic12(1) xy_ic12(2) 0];
xyz_ic13 = [xy_ic13(1) xy_ic13(2) 0];
xyz_ic23 = [xy_ic23(1) xy_ic23(2) 0];

v1_ic12 = xyz_ic12 - cp1;
v2_ic12 = xyz_ic12 - cp2;
v3_ic12 = xyz_ic12 - cp3;

```

```

v1_ic13 = xyz_ic13 - cp1;
v2_ic13 = xyz_ic13 - cp2;
v3_ic13 = xyz_ic13 - cp3;
v1_ic23 = xyz_ic23 - cp1;
v2_ic23 = xyz_ic23 - cp2;
v3_ic23 = xyz_ic23 - cp3;

% preload bolt parameters [lengths in m]
diam = 0.012;
pitch = 0.00175;
eff = 0.6;
mubolt = 0.2;

% ANALYZE ALL CASES OF INTERFACE MOTION - Solve for required in-plane pre-
load to overcome friction
% independently, cases 2 and 3 will give a worst-case for combined sliding
along contact 2 and rotation about pin 2
% independently, cases 4 and 5 will give a worst-case for combined sliding
along contact 3 and rotation about pin 3

% case 0 - no pins in contact, sliding in preload direction
Fp(1) = mu*fz;
Fp_g(1) = mu_g*fz;

% case 1 - only pin 1 in contact, sliding along its vertical contact
Fp(2) = mu*fz/(sin(theta) - mu*cos(theta));
Fp_g(2) = mu_g*fz/(sin(theta) - mu_g*cos(theta));

% case 2 - only pin 2 in contact, sliding along its angled contact
pld_torquevector = cross(v_prld,cp1);
Fp(3) = mu*fz/(dot(v_prld,v_fr2_ccw) - pld_torquevector(3)/(mag(cp2)));
Fp_g(3) = mu_g*fz/(dot(v_prld,v_fr2_ccw) - pld_torquevector(3)/(mag(cp2)));

% case 3 - only pin 2 in contact, rotation about pin 2
pld_torquevector = cross(v_prld,p_12);
Fp(4) = (mag(p_12)*mu*fz + mag(p_23)*mu*fz)/pld_torquevector(3);
Fp_g(4) = (mag(p_12)*mu_g*fz + mag(p_23)*mu*fz)/pld_torquevector(3);

% case 4 - only pin 3 in contact, sliding along its angled contact
pld_torquevector = cross(v_prld,cp1);
Fp(5) = mu*fz/(dot(v_prld,v_fr3_ccw) - pld_torquevector(3)/(mag(cp3)));
Fp_g(5) = mu_g*fz/(dot(v_prld,v_fr3_ccw) - pld_torquevector(3)/(mag(cp3)));

% case 5 - only pin 3 in contact, rotation about pin 3
pld_torquevector = cross(v_prld,p_13);
Fp(6) = (mag(p_13)*mu*fz + mag(p_23)*mu*fz)/pld_torquevector(3);
Fp_g(6) = (mag(p_13)*mu_g*fz + mag(p_23)*mu*fz)/pld_torquevector(3);

% case 6 - pins 1 and 2 in contact, rotation of IC about z-axis
mut = mu;
pld_torquevector = cross(v_prld,v1_ic12);
n1_torquevector = cross(v_cont1,v1_ic12);
f1_torquevector = mut*cross(v_fr1_up,v1_ic12);
n2_torquevector = cross(v_cont2,v2_ic12);

```



```

f2_torquevector = mut*cross(v_fr2_ccw,v2_ic12);

A = [v_prld(1), v_cont1(1) + mut*v_fr1_up(1), v_cont2(1) +
mut*v_fr2_ccw(1);...
      v_prld(2), v_cont1(2) + mut*v_fr1_up(2), v_cont2(2) +
mut*v_fr2_ccw(2);...
      pld_torquevector(3), n1_torquevector(3) + f1_torquevector(3),
n2_torquevector(3) + f2_torquevector(3)];

B = [-1*mut*fz*(v1_ic12(2) + v2_ic12(2) + v3_ic12(2))/3;...
      mut*fz*(v1_ic12(1) + v2_ic12(1) + v3_ic12(1))/3;...
      -1*mut*(fz*mag(v1_ic12)/3 + fz*mag(v2_ic12)/3 + fz*mag(v3_ic12)/3)];

F_vect = inv(A)*B;
Fp(7) = F_vect(1);

mut = mu_g;
pld_torquevector = cross(v_prld,v1_ic12);
n1_torquevector = cross(v_cont1,v1_ic12);
f1_torquevector = mut*cross(v_fr1_up,v1_ic12);
n2_torquevector = cross(v_cont2,v2_ic12);
f2_torquevector = mut*cross(v_fr2_ccw,v2_ic12);

A = [v_prld(1), v_cont1(1) + mut*v_fr1_up(1), v_cont2(1) +
mut*v_fr2_ccw(1);...
      v_prld(2), v_cont1(2) + mut*v_fr1_up(2), v_cont2(2) +
mut*v_fr2_ccw(2);...
      pld_torquevector(3), n1_torquevector(3) + f1_torquevector(3),
n2_torquevector(3) + f2_torquevector(3)];

B = [-1*mut*fz*(v1_ic12(2) + v2_ic12(2) + v3_ic12(2))/3;...
      mut*fz*(v1_ic12(1) + v2_ic12(1) + v3_ic12(1))/3;...
      -1*mut*(fz*mag(v1_ic12)/3 + fz*mag(v2_ic12)/3 + fz*mag(v3_ic12)/3)];

F_vect = inv(A)*B;
Fp_g(7) = F_vect(1);

% case 7 - pins 1 and 3 in contact, rotation of IC about z-axis
mut = mu;
pld_torquevector = cross(v_prld,v1_ic13);
n1_torquevector = cross(v_cont1,v1_ic13);
f1_torquevector = mut*cross(v_fr1_dn,v1_ic13);
n3_torquevector = cross(v_cont3,v3_ic13);
f3_torquevector = mut*cross(v_fr3_ccw,v3_ic13);

A = [v_prld(1), v_cont1(1) + mut*v_fr1_dn(1), v_cont3(1) +
mut*v_fr3_ccw(1);...
      v_prld(2), v_cont1(2) + mut*v_fr1_dn(2), v_cont3(2) +
mut*v_fr3_ccw(2);...
      pld_torquevector(3), n1_torquevector(3) + f1_torquevector(3),
n3_torquevector(3) + f3_torquevector(3)];

B = [-1*mut*fz*(v1_ic13(2) + v2_ic13(2) + v3_ic13(2))/3;...

```

```

mut*fz*(v1_ic13(1) + v2_ic13(1) + v3_ic13(1))/3;...
-1*mut*(fz*mag(v1_ic13)/3 + fz*mag(v2_ic13)/3 + fz*mag(v3_ic13)/3)];

F_vect = inv(A)*B;
Fp(8) = F_vect(1);

mut = mu_g;
pld_torquevector = cross(v_prld,v1_ic13);
n1_torquevector = cross(v_cont1,v1_ic13);
f1_torquevector = mut*cross(v_fr1_dn,v1_ic13);
n3_torquevector = cross(v_cont3,v3_ic13);
f3_torquevector = mut*cross(v_fr3_ccw,v3_ic13);

A = [v_prld(1), v_cont1(1) + mut*v_fr1_dn(1), v_cont3(1) +
mut*v_fr3_ccw(1);...
      v_prld(2), v_cont1(2) + mut*v_fr1_dn(2), v_cont3(2) +
mut*v_fr3_ccw(2);...
      pld_torquevector(3), n1_torquevector(3) + f1_torquevector(3),
n3_torquevector(3) + f3_torquevector(3)];

B = [-1*mut*fz*(v1_ic13(2) + v2_ic13(2) + v3_ic13(2))/3;...
      mut*fz*(v1_ic13(1) + v2_ic13(1) + v3_ic13(1))/3;...
      -1*mut*(fz*mag(v1_ic13)/3 + fz*mag(v2_ic13)/3 + fz*mag(v3_ic13)/3)];

F_vect = inv(A)*B;
Fp_g(8) = F_vect(1);

% case 8 - pins 2 and 3 in contact, rotation of IC about z-axis
mut = mu;
pld_torquevector = cross(v_prld,v1_ic23);
n2_torquevector = cross(v_cont2,v2_ic23);
f2_torquevector = mut*cross(v_fr2_ccw,v2_ic23);
n3_torquevector = cross(v_cont3,v3_ic23);
f3_torquevector = mut*cross(v_fr3_ccw,v3_ic23);

A = [v_prld(1), v_cont2(1) + mut*v_fr2_ccw(1), v_cont3(1) +
mut*v_fr3_ccw(1);...
      v_prld(2), v_cont2(2) + mut*v_fr2_ccw(2), v_cont3(2) +
mut*v_fr3_ccw(2);...
      pld_torquevector(3), n2_torquevector(3) + f2_torquevector(3),
n3_torquevector(3) + f3_torquevector(3)];

B = [-1*mut*fz*(v1_ic23(2) + v2_ic23(2) + v3_ic23(2))/3;...
      mut*fz*(v1_ic23(1) + v2_ic23(1) + v3_ic23(1))/3;...
      -1*mut*(fz*mag(v1_ic23)/3 + fz*mag(v2_ic23)/3 + fz*mag(v3_ic23)/3)];

F_vect = inv(A)*B;
Fp(9) = F_vect(1);

mut = mu_g;
pld_torquevector = cross(v_prld,v1_ic23);
n2_torquevector = cross(v_cont2,v2_ic23);
f2_torquevector = mut*cross(v_fr2_ccw,v2_ic23);

```

```

n3_torquevector = cross(v_cont3,v3_ic23);
f3_torquevector = mut*cross(v_fr3_ccw,v3_ic23);

A = [v_prld(1), v_cont2(1) + mut*v_fr2_ccw(1), v_cont3(1) +
mut*v_fr3_ccw(1);...
      v_prld(2), v_cont2(2) + mut*v_fr2_ccw(2), v_cont3(2) +
mut*v_fr3_ccw(2);...
      pld_torquevector(3), n2_torquevector(3) + f2_torquevector(3),
n3_torquevector(3) + f3_torquevector(3)];

B = [-1*mut*fz*(v1_ic23(2) + v2_ic23(2) + v3_ic23(2))/3;...
      mut*fz*(v1_ic23(1) + v2_ic23(1) + v3_ic23(1))/3;...
      -1*mut*(fz*mag(v1_ic23)/3 + fz*mag(v2_ic23)/3 + fz*mag(v3_ic23)/3)];

F_vect = inv(A)*B;
Fp_g(9) = F_vect(1);

% Fp
% Fp_g

% Take absolute values - render sliding/rotation either direction for each
case
Fp = abs(Fp)
Fp_g = abs(Fp_g)

% Calculate necessary bolt torques
T = Fp*(2*pitch/eff + 3*pi*diam*mubolt)/(4*pi)
T_g = Fp_g*(2*pitch/eff + 3*pi*diam*mubolt)/(4*pi)

```

B.4 Bolt Tightening Torque Calculation

```

% bolttorque.m
p = 0.00305;
eff = 0.5;
Db = 0.03;
mu = 0.15;
F = 130000;
T = F*(2*p/eff + 3*pi*Db*mu)/(4*pi)
lbat1m = 2.2*T/9.8

```


Appendix C

Kinematic Exchangeability Analysis Code

C.1 Canoe Ball Interface Exchangeability

C.1.1 kincalibrate.m

```
% kincalibrate.m
% MATLAB code to calculate transformation of tool point under specified
% manufacturing variation in standard/canoe ball coupling positions and
% orientations
% via Monte Carlo random variate simulation

% Computes nominal error and calculates transformation benefit gained by
% calibration
% measurement of coupling positions and orientations.

% John Hart, MIT PERG, April 2001
% Revised to follow normal vector / surface constraint equations, October
% 2001

% Tolerance assumed to be uniformly 2-sided gaussian distributions, with 3-
% sigma limits
% All values in [N-mm-s]

%-----
%-----
%
% Command line usage: kincalibrate(numruns, caltype)
%
% Input parameter definitions:
% numruns = number of runs of the random simulation, recommended > 100
% caltype = calibration type
%           0 = no measurement (all locations and orientations nominal,
% perfect deterministic match)
%           11 = using offset measurement feature, measurement of groove
% positions only
%               (assume nominal groove orientations and nominal ball
% positions and orientations)
%           12 = using offset measurement feature, measurement of groove
% positions and orientations only
%               (assume nominal ball positions and orientations)
%           13 = using offset measurement feature, measurement of groove
% positions and orientations,
%               and ball positions (assume nominal groove positions)
%           14 = using offset measurement feature, measurement of groove
% positions and ball positions
%               (assume nominal groove orientations and nominal ball
% orientations)
%           15 = using offset measurement feature, measurement of groove
```

```

positions and orientations,
%               and ball positions and orientations (full calibration)
%               21 = by CMM to contact surfaces, measure ball curved surface
parameters (center, radius)
%               22 = by CMM to contact surfaces, measure groove parameters
(normal vectors w/base points)
%               23 = by CMM to contact surfaces, measure ball and groove
parameters (full calibration)
%
% Output parameter: rmsavg = ensemble rms average of TCP variation
%
%-----
-----

function [avgrms] = kincalibrate(numruns, caltype)

format long;

% Error distribution parameters - tolerances
%-----
-----

postol_holes = 0.24;      % machining holes, linear per meter of CNC travel
[mm]
tol_flat = 0.20;         % plate flatness, linear per meter of CNC travel
[mm]
tol_orient = 0.2*pi/180;  % angular placement balls and grooves, relative
to nominal centerline

tol_sphref = 0.02;       % positioning of first spherical surface (virtual
center) relative to
                        % protrusion hole center
tol_sphrel = 0.005;      % positioning of second spherical surface relative
to first spherical surface
                        % (error in spherical surface radius is insignificant
to model)

tol_grooveref = 0.02;    % positioning of first groove surface relative to
protrusion hole center
                        % ignore angular error (2nd order effect)
tol_grooverel = 0.005;   % positioning of second groove surface relative to
first groove surface
tol_grooveangle = 0.02*pi/180; % groove angle relative to reference
plane
tol_grooveanglerel = 0.002*pi/180;

tol_protheight = 0.02;   % height of coupling (ball or groove) bulk protru-
sion relative to reference plane
tol_mfhole = 0.02;       % position of measurement feature mounting hole in
coupling plane radial direction
tol_mfheight = 0.01;     % height of measurement feature relative to top of
coupling protrusion
tol_mfround = 0.000;     % radius of measurement feature (sphere)

```

```

tol_msys = 0.1;          % measurement system error, linear per meter of
travel relative to previous feature

% Measurement and cell parameters
%-----
-----

% Coordinates of TCP WRT coupling centroid, in BCS - this is location of
error reporting
Xtcp = 2000;
Ytcp = 2000;
Ztcp = 2000;
TCP = [Xtcp; Ytcp; Ztcp; 1];
TCPtrans = [1, 0, 0, Xtcp; ...
            0, 1, 0, Ytcp; ...
            0, 0, 1, Ztcp; ...
            0, 0, 0, 1];

% Default location of nominal coupling centroid is wrt MCS, with xy-MCS in
coupling plane
xc = 2000;
yc = 2000;
zc = 0;      % z = 0 is placed at the contact plane

% Kinematic interface parameters
%-----
-----

r1 = 500;
r2 = 500;
r3 = 500;
th1 = 100*pi/180;
th2 = 220*pi/180;
th3 = -20*pi/180;
ao = 15;      % alignment hole (measurement feature) offset from cou-
pling mounting hole
Rball = 500;   % Equivalent radius of coupling ball
Dbeq = 30;     % Equivalent sphere diameter that would contact groove at
same points as
               % true size coupling ball
thg = 45*pi/180; % coupling groove angle

%-----
-----

% Nominal interface geometry calculations for interchangeability model
%-----
-----

% Nominal ball and groove center locations, expressed in MCS (measurement
coord sys)
x1 = xc + (r1)*cos(th1);
y1 = yc + (r1)*sin(th1);
z1 = 0;

```

```

x2 = xc + (r2)*cos(th2);
y2 = yc + (r2)*sin(th2);
z2 = 0;
x3 = xc + (r3)*cos(th3);
y3 = yc + (r3)*sin(th3);
z3 = 0;
holecenters_nom = [x1; y1; z1; x2; y2; z2; x3; y3; z3];

% Nominal contact point locations (normal vector base points)
xc11 = x1 + Dbeq*sqrt(2)*sin(th1)/4;
xc12 = x1 - Dbeq*sqrt(2)*sin(th1)/4;
yc11 = y1 - Dbeq*sqrt(2)*cos(th1)/4;
yc12 = y1 + Dbeq*sqrt(2)*cos(th1)/4;
zc11 = 0;
zc12 = 0;
xc21 = x2 + Dbeq*sqrt(2)*sin(th2)/4;
xc22 = x2 - Dbeq*sqrt(2)*sin(th2)/4;
yc21 = y2 - Dbeq*sqrt(2)*cos(th2)/4;
yc22 = y2 + Dbeq*sqrt(2)*cos(th2)/4;
zc21 = 0;
zc22 = 0;
xc31 = x3 + Dbeq*sqrt(2)*sin(th3)/4;
xc32 = x3 - Dbeq*sqrt(2)*sin(th3)/4;
yc31 = y3 - Dbeq*sqrt(2)*cos(th3)/4;
yc32 = y3 + Dbeq*sqrt(2)*cos(th3)/4;
zc31 = 0;
zc32 = 0;
b11 = [xc11; yc11; zc11];
b12 = [xc12; yc12; zc12];
b21 = [xc21; yc21; zc21];
b22 = [xc22; yc22; zc22];
b31 = [xc31; yc31; zc31];
b32 = [xc32; yc32; zc32];
basepoints_nom = [b11; b12; b21; b22; b31; b32];

% Nominal groove direction cosines
a11 = -1*sin(th1)/sqrt(1+tan(thg)^2);
a12 = sin(th1)/sqrt(1+tan(thg)^2);
b11 = cos(th1)/sqrt(1+tan(thg)^2);
b12 = -cos(th1)/sqrt(1+tan(thg)^2);
g11 = tan(thg)/sqrt(1+tan(thg)^2);
g12 = tan(thg)/sqrt(1+tan(thg)^2);
a21 = -1*sin(th2)/sqrt(1+tan(thg)^2);
a22 = sin(th2)/sqrt(1+tan(thg)^2);
b21 = cos(th2)/sqrt(1+tan(thg)^2);
b22 = -cos(th2)/sqrt(1+tan(thg)^2);
g21 = tan(thg)/sqrt(1+tan(thg)^2);
g22 = tan(thg)/sqrt(1+tan(thg)^2);
a31 = -1*sin(th3)/sqrt(1+tan(thg)^2);
a32 = sin(th3)/sqrt(1+tan(thg)^2);
b31 = cos(th3)/sqrt(1+tan(thg)^2);
b32 = -cos(th3)/sqrt(1+tan(thg)^2);
g31 = tan(thg)/sqrt(1+tan(thg)^2);
g32 = tan(thg)/sqrt(1+tan(thg)^2);

```



```

% Nominal groove normal vectors
n11 = [a11; b11; g11];
n12 = [a12; b12; g12];
n21 = [a21; b21; g21];
n22 = [a22; b22; g22];
n31 = [a31; b31; g31];
n32 = [a32; b32; g32];
normals_nom = [n11; n12; n21; n22; n31; n32];

% Nominal sphere center positions
centers_nom = basepoints_nom + Rball*normals_nom;

%-----
%-----

% Calculate 1-sigma input tolerances from provided 3-sigma values and specified interface geometry
%-----
%-----

s = 3; % Sigma-level of input tolerances

% 1-sigma positional tolerances of holes in plates (absorb perturbations of alignment references into orientation error)
pt_p1 = postol_holes*r1/(s*1000);
pt_z1 = tol_flat*r1/(s*1000);
pt_p2 = postol_holes*r2/(s*1000);
pt_z2 = tol_flat*r2/(s*1000);
pt_p3 = postol_holes*r3/(s*1000);
pt_z3 = tol_flat*r3/(s*1000);

pt_ps = [pt_p1; pt_p2; pt_p3];
pt_zs = [pt_z1; pt_z2; pt_z3];

% 1-sigma positional tolerances of alignments
orient = tol_orient/s;

% 1-sigma positional tolerances of form error components
sphref = tol_sphref/s;
sphrel = tol_sphrel/s;
grooveref = tol_grooveref/s;
grooverel = tol_grooverel/s;
grooveangle = tol_grooveangle/s;
grooveanglerel = tol_grooveanglerel/s;
protheight = tol_protheight/s;
mfhole = tol_mfhole/s;
mfheight = tol_mfheight/s;
mfround = tol_mfround/s;
msys = tol_msys/s;

% For step 4, option 1: Measurement pattern representing direct measurement (use nominal geometry)
dist0_11 = sqrt((xc - basepoints_nom(1))^2 + (yc - basepoints_nom(2))^2 + (zc - basepoints_nom(3))^2);

```

```

dist11_12 = sqrt((basepoints_nom(4) - basepoints_nom(1))^2 +
(basepoints_nom(5) - basepoints_nom(2))^2 + ...
(basepoints_nom(6) - basepoints_nom(3))^2);
dist12_21 = sqrt((basepoints_nom(7) - basepoints_nom(4))^2 +
(basepoints_nom(8) - basepoints_nom(5))^2 + ...
(basepoints_nom(9) - basepoints_nom(6))^2);
dist21_22 = sqrt((basepoints_nom(10) - basepoints_nom(7))^2 +
(basepoints_nom(11) - basepoints_nom(8))^2 + ...
(basepoints_nom(12) - basepoints_nom(9))^2);
dist22_31 = sqrt((basepoints_nom(13) - basepoints_nom(10))^2 +
(basepoints_nom(14) - basepoints_nom(11))^2 + ...
(basepoints_nom(15) - basepoints_nom(12))^2);
dist31_32 = sqrt((basepoints_nom(16) - basepoints_nom(13))^2 +
(basepoints_nom(17) - basepoints_nom(14))^2 + ...
(basepoints_nom(18) - basepoints_nom(15))^2);

v0_11 = msys*1000/dist0_11;
v11_12 = msys*1000/dist11_12;
v12_21 = msys*1000/dist12_21;
v21_22 = msys*1000/dist21_22;
v22_31 = msys*1000/dist22_31;
v31_32 = msys*1000/dist31_32;

% For step 4, option 2: Measurement pattern representing offset measurement
(use nominal geometry)
    % Define a measurement sequence for the points, calculating measurement
system error relative
    % to the last measurement point
    % Chosen sequence is to measure ball or groove contacts CCW starting
with ball or groove 1 then
    % follow around the circle until complete.
dist01h = sqrt((xc - holecenters_nom(1))^2 + (yc - holecenters_nom(2))^2 +
(zc - holecenters_nom(3))^2);
dist1h2h = sqrt((holecenters_nom(4) - holecenters_nom(1))^2 +
(holecenters_nom(5) - holecenters_nom(2))^2 + ...
(holecenters_nom(6) - holecenters_nom(3))^2); % approximate
dist2h3h = sqrt((holecenters_nom(7) - holecenters_nom(4))^2 +
(holecenters_nom(8) - holecenters_nom(5))^2 + ...
(holecenters_nom(9) - holecenters_nom(6))^2); % approximate

v01h = msys*1000/dist01h;
v1h2h = msys*1000/dist1h2h;
v2h3h = msys*1000/dist2h3h;

% Simulation loop - specified number of Monte Carlo simulation runs
%-----
%-----
i = 1;
for i = 1:numruns

% Generate true dimensions by applying error perturbations in serial fashion

% Step 1: Perturb mounting hole positions;
pvr_balls = randn(3,1).*pt_ps;

```

```

pvr_grooves = randn(3,1).*pt_ps;
pvt_balls = rand(3,1).*(2*pi*ones(3,1));
pvt_grooves = rand(3,1).*(2*pi*ones(3,1));
pvz_balls = randn(3,1).*pt_zs;
pvz_grooves = randn(3,1).*pt_zs;

pvars_b1 = [pvr_balls(1)*cos(pvt_balls(1)); pvr_balls(1)*sin(pvt_balls(1));
pvz_balls(1)];
pvars_b2 = [pvr_balls(2)*cos(pvt_balls(2)); pvr_balls(2)*sin(pvt_balls(2));
pvz_balls(2)];
pvars_b3 = [pvr_balls(3)*cos(pvt_balls(3)); pvr_balls(3)*sin(pvt_balls(3));
pvz_balls(3)];
pvars_g1 = [pvr_grooves(1)*cos(pvt_grooves(1));
pvr_grooves(1)*sin(pvt_grooves(1)); pvz_grooves(1)];
pvars_g2 = [pvr_grooves(2)*cos(pvt_grooves(2));
pvr_grooves(2)*sin(pvt_grooves(2)); pvz_grooves(2)];
pvars_g3 = [pvr_grooves(3)*cos(pvt_grooves(3));
pvr_grooves(3)*sin(pvt_grooves(3)); pvz_grooves(3)];
pvars_b = [pvars_b1; pvars_b2; pvars_b3];
pvars_g = [pvars_g1; pvars_g2; pvars_g3];
pvars_b_db = [pvars_b1; pvars_b1; pvars_b2; pvars_b2; pvars_b3; pvars_b3];
pvars_g_db = [pvars_g1; pvars_g1; pvars_g2; pvars_g2; pvars_g3; pvars_g3];

% perturbed locations of points of interest on balls and grooves
b_holecenters_plpt = holecenters_nom + pvars_b;
g_holecenters_plpt = holecenters_nom + pvars_g;
centers_plpt = centers_nom + pvars_b_db;
basepoints_plpt = basepoints_nom + pvars_g_db;
normals_plpt = normals_nom;

% Step 2: Perturb ball and groove orientations;
tv = randn(6,1).*(orient*ones(6,1));
b_holecenters_plins = b_holecenters_plpt;
g_holecenters_plins = g_holecenters_plpt;

% calculate 'effective' angles WRT coupling centroid
th1b = th1 + tv(1);
th2b = th2 + tv(2);
th3b = th3 + tv(3);
th1g = th1 + tv(4);
th2g = th2 + tv(5);
th3g = th3 + tv(6);

% recalculate normal vector base points, using perturbed center loca-
tions as references
xc11pb = b_holecenters_plins(1) + Dbeq*sqrt(2)*sin(th1b)/4;
xc12pb = b_holecenters_plins(1) - Dbeq*sqrt(2)*sin(th1b)/4;
yc11pb = b_holecenters_plins(2) - Dbeq*sqrt(2)*cos(th1b)/4;
yc12pb = b_holecenters_plins(2) + Dbeq*sqrt(2)*cos(th1b)/4;
zc11pb = b_holecenters_plins(3);
zc12pb = b_holecenters_plins(3);
xc21pb = b_holecenters_plins(4) + Dbeq*sqrt(2)*sin(th2b)/4;
xc22pb = b_holecenters_plins(4) - Dbeq*sqrt(2)*sin(th2b)/4;

```

```

yc21pb = b_holecenters_plins(5) - Dbeq*sqrt(2)*cos(th2b)/4;
yc22pb = b_holecenters_plins(5) + Dbeq*sqrt(2)*cos(th2b)/4;
zc21pb = b_holecenters_plins(6);
zc22pb = b_holecenters_plins(6);
xc31pb = b_holecenters_plins(7) + Dbeq*sqrt(2)*sin(th3b)/4;
xc32pb = b_holecenters_plins(7) - Dbeq*sqrt(2)*sin(th3b)/4;
yc31pb = b_holecenters_plins(8) - Dbeq*sqrt(2)*cos(th3b)/4;
yc32pb = b_holecenters_plins(8) + Dbeq*sqrt(2)*cos(th3b)/4;
zc31pb = b_holecenters_plins(9);
zc32pb = b_holecenters_plins(9);
b11_plins = [xc11pb; yc11pb; zc11pb];
b12_plins = [xc12pb; yc12pb; zc12pb];
b21_plins = [xc21pb; yc21pb; zc21pb];
b22_plins = [xc22pb; yc22pb; zc22pb];
b31_plins = [xc31pb; yc31pb; zc31pb];
b32_plins = [xc32pb; yc32pb; zc32pb];
b_basepoints_plins = [b11_plins; b12_plins; b21_plins; b22_plins;
b31_plins; b32_plins];

xc11pg = g_holecenters_plins(1) + Dbeq*sqrt(2)*sin(th1g)/4;
xc12pg = g_holecenters_plins(1) - Dbeq*sqrt(2)*sin(th1g)/4;
yc11pg = g_holecenters_plins(2) - Dbeq*sqrt(2)*cos(th1g)/4;
yc12pg = g_holecenters_plins(2) + Dbeq*sqrt(2)*cos(th1g)/4;
zc11pg = g_holecenters_plins(3);
zc12pg = g_holecenters_plins(3);
xc21pg = g_holecenters_plins(4) + Dbeq*sqrt(2)*sin(th2g)/4;
xc22pg = g_holecenters_plins(4) - Dbeq*sqrt(2)*sin(th2g)/4;
yc21pg = g_holecenters_plins(5) - Dbeq*sqrt(2)*cos(th2g)/4;
yc22pg = g_holecenters_plins(5) + Dbeq*sqrt(2)*cos(th2g)/4;
zc21pg = g_holecenters_plins(6);
zc22pg = g_holecenters_plins(6);
xc31pg = g_holecenters_plins(7) + Dbeq*sqrt(2)*sin(th3g)/4;
xc32pg = g_holecenters_plins(7) - Dbeq*sqrt(2)*sin(th3g)/4;
yc31pg = g_holecenters_plins(8) - Dbeq*sqrt(2)*cos(th3g)/4;
yc32pg = g_holecenters_plins(8) + Dbeq*sqrt(2)*cos(th3g)/4;
zc31pg = g_holecenters_plins(9);
zc32pg = g_holecenters_plins(9);
g11_plins = [xc11pg; yc11pg; zc11pg];
g12_plins = [xc12pg; yc12pg; zc12pg];
g21_plins = [xc21pg; yc21pg; zc21pg];
g22_plins = [xc22pg; yc22pg; zc22pg];
g31_plins = [xc31pg; yc31pg; zc31pg];
g32_plins = [xc32pg; yc32pg; zc32pg];
basepoints_plins = [g11_plins; g12_plins; g21_plins; g22_plins; g31_plins;
g32_plins];

% recalculate direction cosines, including set for balls (to define true
offset of sphere centers)
a11b = -1*sin(th1b)/sqrt(1+tan(thg)^2);
a12b = sin(th1b)/sqrt(1+tan(thg)^2);
b11b = cos(th1b)/sqrt(1+tan(thg)^2);
b12b = -cos(th1b)/sqrt(1+tan(thg)^2);
g11b = tan(thg)/sqrt(1+tan(thg)^2);
g12b = tan(thg)/sqrt(1+tan(thg)^2);

```

```

a21b = -1*sin(th2b)/sqrt(1+tan(thg)^2);
a22b = sin(th2b)/sqrt(1+tan(thg)^2);
b21b = cos(th2b)/sqrt(1+tan(thg)^2);
b22b = -cos(th2b)/sqrt(1+tan(thg)^2);
g21b = tan(thg)/sqrt(1+tan(thg)^2);
g22b = tan(thg)/sqrt(1+tan(thg)^2);
a31b = -1*sin(th3b)/sqrt(1+tan(thg)^2);
a32b = sin(th3b)/sqrt(1+tan(thg)^2);
b31b = cos(th3b)/sqrt(1+tan(thg)^2);
b32b = -cos(th3b)/sqrt(1+tan(thg)^2);
g31b = tan(thg)/sqrt(1+tan(thg)^2);
g32b = tan(thg)/sqrt(1+tan(thg)^2);
n11b = [a11b; b11b; g11b];
n12b = [a12b; b12b; g12b];
n21b = [a21b; b21b; g21b];
n22b = [a22b; b22b; g22b];
n31b = [a31b; b31b; g31b];
n32b = [a32b; b32b; g32b];
b_normals_plins = [n11b; n12b; n21b; n22b; n31b; n32b];

a11g = -1*sin(th1g)/sqrt(1+tan(thg)^2);
a12g = sin(th1g)/sqrt(1+tan(thg)^2);
b11g = cos(th1g)/sqrt(1+tan(thg)^2);
b12g = -cos(th1g)/sqrt(1+tan(thg)^2);
g11g = tan(thg)/sqrt(1+tan(thg)^2);
g12g = tan(thg)/sqrt(1+tan(thg)^2);
a21g = -1*sin(th2g)/sqrt(1+tan(thg)^2);
a22g = sin(th2g)/sqrt(1+tan(thg)^2);
b21g = cos(th2g)/sqrt(1+tan(thg)^2);
b22g = -cos(th2g)/sqrt(1+tan(thg)^2);
g21g = tan(thg)/sqrt(1+tan(thg)^2);
g22g = tan(thg)/sqrt(1+tan(thg)^2);
a31g = -1*sin(th3g)/sqrt(1+tan(thg)^2);
a32g = sin(th3g)/sqrt(1+tan(thg)^2);
b31g = cos(th3g)/sqrt(1+tan(thg)^2);
b32g = -cos(th3g)/sqrt(1+tan(thg)^2);
g31g = tan(thg)/sqrt(1+tan(thg)^2);
g32g = tan(thg)/sqrt(1+tan(thg)^2);
n11g = [a11g; b11g; g11g];
n12g = [a12g; b12g; g12g];
n21g = [a21g; b21g; g21g];
n22g = [a22g; b22g; g22g];
n31g = [a31g; b31g; g31g];
n32g = [a32g; b32g; g32g];
normals_plins = [n11g; n12g; n21g; n22g; n31g; n32g];

% calculate perturbed sphere center locations
centers_plins = b_basepoints_plins + Rball*b_normals_plins;

% Step 3, option 1: Perturb ball and groove form - for direct measurement;

% Variations in sphere contact points
vcpl_1 = spherevar(sphref);
vcpl_2 = vcpl_1 + spherevar(sphrel);

```

```

vcp2_1 = spherevar(sphref);
vcp2_2 = vcp2_1 + spherevar(sphrel);
vcp3_1 = spherevar(sphref);
vcp3_2 = vcp3_1 + spherevar(sphrel);
vcps = [vcp1_1; vcp1_2; vcp2_1; vcp2_2; vcp3_1; vcp3_2];

% Variations in groove base points
vg1_1 = spherevar(grooveref);
vg1_2 = vg1_1 + spherevar(grooverel);
vg2_1 = spherevar(grooveref);
vg2_2 = vg2_1 + spherevar(grooverel);
vg3_1 = spherevar(grooveref);
vg3_2 = vg3_1 + spherevar(grooverel);
vgs = [vg1_1; vg1_2; vg2_1; vg2_2; vg3_1; vg3_2];

% Variations in groove angles (neglect covariance between groove angle
and base position)
gal_1 = grooveangle*randn;
gal_2 = gal_1 + grooveanglerel*randn;
ga2_1 = grooveangle*randn;
ga2_2 = ga2_1 + grooveanglerel*randn;
ga3_1 = grooveangle*randn;
ga3_2 = ga3_1 + grooveanglerel*randn;

thga1_1 = thg + gal_1;
thga1_2 = thg + gal_2;
thga2_1 = thg + ga2_1;
thga2_2 = thg + ga2_2;
thga3_1 = thg + ga3_1;
thga3_2 = thg + ga2_2;

% Propagate variations in contact points and vectors to give measured
dimensions
% Include calculation of new normal groove normal vectors,
% using in-plane angles from insertion perturbations as references
b_basepoints_true = b_basepoints_plins + vcps;
basepoints_true = basepoints_plins + vgs;
centers_true = b_basepoints_true + Rball*b_normals_plins;

a11gt = -1*sin(th1g)/sqrt(1+tan(thga1_1)^2);
a12gt = sin(th1g)/sqrt(1+tan(thga1_2)^2);
b11gt = cos(th1g)/sqrt(1+tan(thga1_1)^2);
b12gt = -cos(th1g)/sqrt(1+tan(thga1_2)^2);
g11gt = tan(thga1_1)/sqrt(1+tan(thga1_1)^2);
g12gt = tan(thga1_2)/sqrt(1+tan(thga1_2)^2);
a21gt = -1*sin(th2g)/sqrt(1+tan(thga2_1)^2);
a22gt = sin(th2g)/sqrt(1+tan(thga2_2)^2);
b21gt = cos(th2g)/sqrt(1+tan(thga2_1)^2);
b22gt = -cos(th2g)/sqrt(1+tan(thga2_2)^2);
g21gt = tan(thga2_1)/sqrt(1+tan(thga2_1)^2);
g22gt = tan(thga2_2)/sqrt(1+tan(thga2_2)^2);
a31gt = -1*sin(th3g)/sqrt(1+tan(thga3_1)^2);
a32gt = sin(th3g)/sqrt(1+tan(thga3_2)^2);
b31gt = cos(th3g)/sqrt(1+tan(thga3_1)^2);

```

```

b32gt = -cos(th3g)/sqrt(1+tan(thga3_2)^2);
g31gt = tan(thga3_1)/sqrt(1+tan(thga3_1)^2);
g32gt = tan(thga3_2)/sqrt(1+tan(thga3_2)^2);
n11gt = [a11gt; b11gt; g11gt];
n12gt = [a12gt; b12gt; g12gt];
n21gt = [a21gt; b21gt; g21gt];
n22gt = [a22gt; b22gt; g22gt];
n31gt = [a31gt; b31gt; g31gt];
n32gt = [a32gt; b32gt; g32gt];
normals_true = [n11gt; n12gt; n21gt; n22gt; n31gt; n32gt];

% Step 3, option 2: Perturb ball and groove form - for offset measurement -
additional error parameters;
b_heights = protheight*randn(1,3) + mfheight*randn(1,3);
b_planerad = mfhole*randn(1,3) + mfround*randn(1,3);
b_planetheta = 2*pi*rand(1,3);
b_mfx = b_planerad.*cos(b_planetheta);
b_mfy = b_planerad.*sin(b_planetheta);

b_holecenters_offp = [b_mfx(1); b_mfy(1); b_heights(1); b_mfx(2); b_mfy(2);
b_heights(2); ...
    b_mfx(3); b_mfy(3); b_heights(3)];
b_offsetperturb = [b_mfx(1); b_mfy(1); b_heights(1); b_mfx(1); b_mfy(1);
b_heights(1); ...
    b_mfx(2); b_mfy(2); b_heights(2); b_mfx(2); b_mfy(2); b_heights(2);
...
    b_mfx(3); b_mfy(3); b_heights(3); b_mfx(3); b_mfy(3); b_heights(3)];

g_heights = protheight*randn(1,3) + mfheight*randn(1,3);
g_planerad = mfhole*randn(1,3) + mfround*randn(1,3);
g_planetheta = 2*pi*rand(1,3);
g_mfx = g_planerad.*cos(g_planetheta);
g_mfy = g_planerad.*sin(g_planetheta);

g_holecenters_offp = [g_mfx(1); g_mfy(1); g_heights(1); g_mfx(2); g_mfy(2);
g_heights(2); ...
    g_mfx(3); g_mfy(3); g_heights(3)];
g_offsetperturb = [g_mfx(1); g_mfy(1); g_heights(1); g_mfx(1); g_mfy(1);
g_heights(1); ...
    g_mfx(2); g_mfy(2); g_heights(2); g_mfx(2); g_mfy(2); g_heights(2);
...
    g_mfx(3); g_mfy(3); g_heights(3); g_mfx(3); g_mfy(3); g_heights(3)];

basepoints_offsetmeas = basepoints_plins + g_offsetperturb;
basepoints_offsetmeas_po = basepoints_plpt + g_offsetperturb;
centers_offsetmeas = centers_plins + b_offsetperturb;
centers_offsetmeas_po = centers_plpt + b_offsetperturb;
b_holecenters_offsetmeas = b_holecenters_plpt + b_holecenters_offp;
g_holecenters_offsetmeas = g_holecenters_plpt + g_holecenters_offp;

% Step 4: Add measurement system error - effect on orientation assessment is
negligible (random errors cancel
% over measurement 'spot' on spherical surface or groove

```

```

    % direct measurement - balls
    b_mp_11 = spherevar(v01h);
    b_mp_12 = b_mp_11;
    b_mp_21 = b_mp_12 + spherevar(v1h2h);
    b_mp_22 = b_mp_21;
    b_mp_31 = b_mp_22 + spherevar(v2h3h);
    b_mp_32 = b_mp_31;
    b_mpvvars_direct = [b_mp_11; b_mp_12; b_mp_21; b_mp_22; b_mp_31; b_mp_32];
    centers_directmeas_ms = centers_true + b_mpvvars_direct;

    % direct measurement - grooves
    g_mp_11 = spherevar(v01h);
    g_mp_12 = g_mp_11;
    g_mp_21 = g_mp_12 + spherevar(v1h2h);
    g_mp_22 = g_mp_21;
    g_mp_31 = g_mp_22 + spherevar(v2h3h);
    g_mp_32 = g_mp_31;
    g_mpvvars_direct = [g_mp_11; g_mp_12; g_mp_21; g_mp_22; g_mp_31; g_mp_32];
    basepoints_directmeas_ms = basepoints_true + g_mpvvars_direct;

    % offset measurement - balls
    b_mp_1h = spherevar(v01h);
    b_mp_2h = b_mp_1h + spherevar(v1h2h);
    b_mp_3h = b_mp_2h + spherevar(v2h3h);
    b_mpvvars_offset = [b_mp_1h; b_mp_1h; b_mp_2h; b_mp_2h; b_mp_3h; b_mp_3h];
    centers_offsetmeas_ms = centers_offsetmeas + b_mpvvars_offset;
    centers_offsetmeas_ms_po = centers_offsetmeas_po + b_mpvvars_offset;

    % offset measurement - grooves
    g_mp_1h = spherevar(v01h);
    g_mp_2h = g_mp_1h + spherevar(v1h2h);
    g_mp_3h = g_mp_2h + spherevar(v2h3h);
    g_mpvvars_offset = [g_mp_1h; g_mp_1h; g_mp_2h; g_mp_2h; g_mp_3h; g_mp_3h];
    basepoints_offsetmeas_ms = basepoints_offsetmeas + g_mpvvars_offset;
    basepoints_offsetmeas_ms_po = basepoints_offsetmeas_po + g_mpvvars_offset;

    % Set radii for passage to errortransform.m
    radii = Rball*ones(6,1);

    % Set level of calibration from user input, and assign measured parameter
    sets appropriately

    %           0 = no measurement (all locations and orientations nominal,
    perfect deterministic match)
    %           11 = using offset measurement feature, measurement of groove
    positions only
    %               (assume nominal groove orientations and nominal ball
    positions and orientations)
    %           12 = using offset measurement feature, measurement of groove
    positions and orientations only
    %               (assume nominal ball positions and orientations)
    %           13 = using offset measurement feature, measurement of groove
    positions and orientations,
    %               and ball positions (assume nominal groove positions)

```



```

%           14 = using offset measurement feature, measurement of groove
positions and ball positions
%           (assume nominal groove orientations and nominal ball
orientations)
%           15 = using offset measurement feature, measurement of groove
positions and orientations,
%           and ball positions and orientations (full calibration)
%           21 = by CMM to contact surfaces, measure ball curved surface
parameters (center, radius)
%           22 = by CMM to contact surfaces, measure groove parameters
(normal vectors w/base points)
%           23 = by CMM to contact surfaces, measure ball and groove
parameters (full calibration)
%

if caltype == 0
    CENTERS = centers_nom;
    BASEPOINTS = basepoints_nom;
    NORMALS = normals_nom;
end

if caltype == 11
    CENTERS = centers_nom;
    BASEPOINTS = basepoints_offsetmeas_ms_po;
    NORMALS = normals_plpt;
end

if caltype == 12
    CENTERS = centers_nom;
    BASEPOINTS = basepoints_offsetmeas_ms;
    NORMALS = normals_plins;
end

if caltype == 13
    CENTERS = centers_offsetmeas_ms_po;
    BASEPOINTS = basepoints_offsetmeas_ms;
    NORMALS = normals_plins;
end

if caltype == 14
    CENTERS = centers_offsetmeas_ms_po;
    BASEPOINTS = basepoints_offsetmeas_ms_po;
    NORMALS = normals_plpt;
end

if caltype == 15
    CENTERS = centers_offsetmeas_ms;
    BASEPOINTS = basepoints_offsetmeas_ms;
    NORMALS = normals_plins;
end

if caltype == 21
    CENTERS = centers_directmeas_ms;
    BASEPOINTS = basepoints_nom;

```

```

        NORMALS = normals_nom;
    end

    if caltype == 22
        CENTERS = centers_nom;
        BASEPOINTS = basepoints_directmeas_ms;
        NORMALS = normals_true;
    end

    if caltype == 23
        CENTERS = centers_directmeas_ms;
        BASEPOINTS = basepoints_directmeas_ms;
        NORMALS = normals_true;
    end

    % Calculate measured and true error transformations
    errortrans = errortransform(centers_nom, CENTERS, radii, BASEPOINTS, NORMALS);
    errortrans_true = errortransform(centers_nom, centers_true, radii, basepoints_true, normals_true);

    % Determine error of the chosen calibration method
    Tglobal_meas = errortrans*TCPtrans;
    Tglobal_true = errortrans_true*TCPtrans;
    TCPloc_meas = Tglobal_meas*TCP;
    TCPloc_true = Tglobal_true*TCP;

    TCPerr = TCPloc_true - TCPloc_meas;

    TCPerror(i,1) = i;
    TCPerror(i,2) = TCPerr(1);
    TCPerror(i,3) = TCPerr(2);
    TCPerror(i,4) = TCPerr(3);
    TCPerror(i,5) = sqrt(TCPerror(i,2)^2 + TCPerror(i,3)^2 + TCPerror(i,4)^2);

    end

    % Simulation loop
    %-----
    -----

    avgrms = mean(TCPerror(:,5))

```

C.1.2 errortransform.m

```

% errortransform.m - calculates deterministic error transformation between
groove and ball sets
% of a standard/canoe ball kinematic coupling interface based upon measured
positions
% of mounting holes (centers) and alignment holes (alignment features)

% John Hart, MIT PERG, 2001

```

```

function [errorHTM] = errortransform(nomcenters, centers, radii, base-
points, normals);

% Assemble matrices for solution of 24-by-24 system giving of centroidal
frame error motions
% Original ball coordinates are nominal positions; distances from sphere
center to groove flat base points
% are perturbed as measured

nomcenters = centers;

% Matrix A = coefficients
A = [ 1, 0, 0, 0, nomcenters(3), -1*nomcenters(2), -1, 0, 0, 0, 0, 0, 0, 0,
0, 0, 0, 0, 0, 0, 0, 0, 0, 0, 0; ...
0, 1, 0, -1*nomcenters(3), 0, nomcenters(1), 0, -1, 0, 0, 0, 0, 0, 0,
0, 0, 0, 0, 0, 0, 0, 0, 0, 0, 0; ...
0, 0, 1, nomcenters(2), -1*nomcenters(1), 0, 0, 0, -1, 0, 0, 0, 0, 0,
0, 0, 0, 0, 0, 0, 0, 0, 0, 0, 0; ...
1, 0, 0, 0, nomcenters(6), -1*nomcenters(5), 0, 0, 0, -1, 0, 0, 0, 0,
0, 0, 0, 0, 0, 0, 0, 0, 0, 0, 0; ...
0, 1, 0, -1*nomcenters(6), 0, nomcenters(4), 0, 0, 0, 0, -1, 0, 0, 0,
0, 0, 0, 0, 0, 0, 0, 0, 0, 0, 0; ...
0, 0, 1, nomcenters(5), -1*nomcenters(4), 0, 0, 0, 0, 0, 0, -1, 0, 0,
0, 0, 0, 0, 0, 0, 0, 0, 0, 0, 0; ...
1, 0, 0, 0, nomcenters(9), -1*nomcenters(8), 0, 0, 0, 0, 0, 0, -1, 0,
0, 0, 0, 0, 0, 0, 0, 0, 0, 0, 0; ...
0, 1, 0, -1*nomcenters(9), 0, nomcenters(7), 0, 0, 0, 0, 0, 0, 0, -1,
0, 0, 0, 0, 0, 0, 0, 0, 0, 0, 0; ...
0, 0, 1, nomcenters(8), -1*nomcenters(7), 0, 0, 0, 0, 0, 0, 0, 0, 0, -
1, 0, 0, 0, 0, 0, 0, 0, 0, 0, 0; ...
1, 0, 0, 0, nomcenters(12), -1*nomcenters(11), 0, 0, 0, 0, 0, 0, 0, 0,
0, -1, 0, 0, 0, 0, 0, 0, 0, 0, 0; ...
0, 1, 0, -1*nomcenters(12), 0, nomcenters(10), 0, 0, 0, 0, 0, 0, 0, 0,
0, 0, -1, 0, 0, 0, 0, 0, 0, 0, 0; ...
0, 0, 1, nomcenters(11), -1*nomcenters(10), 0, 0, 0, 0, 0, 0, 0, 0, 0,
0, 0, 0, -1, 0, 0, 0, 0, 0, 0, 0; ...
1, 0, 0, 0, nomcenters(15), -1*nomcenters(14), 0, 0, 0, 0, 0, 0, 0, 0,
0, 0, 0, 0, -1, 0, 0, 0, 0, 0, 0; ...
0, 1, 0, -1*nomcenters(15), 0, nomcenters(13), 0, 0, 0, 0, 0, 0, 0, 0,
0, 0, 0, 0, 0, -1, 0, 0, 0, 0, 0; ...
0, 0, 1, nomcenters(14), -1*nomcenters(13), 0, 0, 0, 0, 0, 0, 0, 0, 0,
0, 0, 0, 0, 0, 0, -1, 0, 0, 0, 0; ...
1, 0, 0, 0, nomcenters(18), -1*nomcenters(17), 0, 0, 0, 0, 0, 0, 0, 0,
0, 0, 0, 0, 0, 0, 0, -1, 0, 0, 0; ...
0, 1, 0, -1*nomcenters(18), 0, nomcenters(16), 0, 0, 0, 0, 0, 0, 0, 0,
0, 0, 0, 0, 0, 0, 0, 0, -1, 0; ...
0, 0, 1, nomcenters(17), -1*nomcenters(16), 0, 0, 0, 0, 0, 0, 0, 0, 0,
0, 0, 0, 0, 0, 0, 0, 0, 0, -1; ...
0, 0, 0, 0, 0, 0, normals(1), normals(2), normals(3), 0, 0, 0, 0, 0,
0, 0, 0, 0, 0, 0, 0, 0, 0, 0; ...
0, 0, 0, 0, 0, 0, 0, 0, 0, 0, normals(4), normals(5), normals(6), 0, 0,
0, 0, 0, 0, 0, 0, 0, 0, 0; ...
0, 0, 0, 0, 0, 0, 0, 0, 0, 0, 0, 0, 0, 0, normals(7), normals(8), normals(9),
0, 0, 0, 0, 0, 0, 0, 0, 0, 0, 0, 0; ...

```

```

    0, 0, 0, 0, 0, 0, 0, 0, 0, 0, 0, 0, 0, 0, 0, normals(10), normals(11),
normals(12), 0, 0, 0, 0, 0, 0, 0; ...
    0, 0, 0, 0, 0, 0, 0, 0, 0, 0, 0, 0, 0, 0, 0, 0, 0, 0, normals(13), nor-
mals(14), normals(15), 0, 0, 0; ...
    0, 0, 0, 0, 0, 0, 0, 0, 0, 0, 0, 0, 0, 0, 0, 0, 0, 0, 0, 0, 0, 0, nor-
mals(16), normals(17), normals(18)];

% Matrix B = constants
B = [-1*nomcenters; ... % rows 1 through 18
    radii(1)*mag([normals(1), normals(2), normals(3)]) + base-
points(1)*normals(1) + basepoints(2)*normals(2) + basepoints(3)*normals(3);
...
    radii(2)*mag([normals(4), normals(5), normals(6)]) + base-
points(4)*normals(4) + basepoints(5)*normals(5) + basepoints(6)*normals(6);
...
    radii(3)*mag([normals(7), normals(8), normals(9)]) + base-
points(7)*normals(7) + basepoints(8)*normals(8) + basepoints(9)*normals(9);
...
    radii(4)*mag([normals(10), normals(11), normals(12)]) + base-
points(10)*normals(10) + basepoints(11)*normals(11) + basepoints(12)*nor-
mals(12); ...
    radii(5)*mag([normals(13), normals(14), normals(15)]) + base-
points(13)*normals(13) + basepoints(14)*normals(14) + basepoints(15)*nor-
mals(15); ...
    radii(6)*mag([normals(16), normals(17), normals(18)]) + base-
points(16)*normals(16) + basepoints(17)*normals(17) + basepoints(18)*nor-
mals(18)];

% Solve system
motions = inv(A)*B;

% Extract error motions (last six terms)
delX = motions(1);
delY = motions(2);
delZ = motions(3);
epsX = motions(4);
epsY = motions(5);
epsZ = motions(6);

% Determine HTM from solved error motions

errorHTM = [1, -1*epsZ, epsY, delX; ...
    epsZ, 1, -1*epsX, delY; ...
    -1*epsY, epsX, 1, delZ; ...
    0, 0, 0, 1];

```

C.2 Three-Pin Interface Exchangeability

C.2.1 pincalibrate.m

```

% pintransform.m - calculates deterministic error transformation between
pins and mating plate

```

```
% of a three-pin kinematic coupling interface based upon measured positions
% and sized of pins and positions and orientations of contact planes
```

```
% John Hart, MIT PERG, 2001
```

```
function [errorHTM] = pintransform(centers, radii, basepoints, normals);
```

```
% First, solve deterministic in-plane seating
% Assemble matrices for solution of 12-by-12 system giving centroidal frame
error motions (delX, delY, epsZ)
```

```
normal1 = [normals(1); normals(2); 0];
normal2 = [normals(4); normals(5); 0];
normal3 = [normals(7); normals(8); 0];
```

```
% Matrix A = coefficients
A = [ 1, 0, -1*centers(2), -1, 0, 0, 0, 0, 0; ...
      0, 1, centers(1), 0, -1, 0, 0, 0, 0; ...
      1, 0, -1*centers(5), 0, 0, -1, 0, 0, 0; ...
      0, 1, centers(4), 0, 0, 0, -1, 0, 0; ...
      1, 0, -1*centers(8), 0, 0, 0, 0, -1, 0; ...
      0, 1, centers(7), 0, 0, 0, 0, 0, -1; ...
      0, 0, 0, normal1(1), normal1(2), 0, 0, 0, 0; ...
      0, 0, 0, 0, 0, normal2(1), normal2(2), 0, 0; ...
      0, 0, 0, 0, 0, 0, 0, normal3(1), normal3(2)];
```

```
% Matrix B = constants
B = [ -1*centers(1); ...
      -1*centers(2); ...
      -1*centers(4); ...
      -1*centers(5); ...
      -1*centers(7); ...
      -1*centers(8); ...
      mag(normal1)*radii(1) + normal1(1)*basepoints(1) + normal1(2)*base-
points(2); ...
      mag(normal2)*radii(2) + normal2(1)*basepoints(4) + normal2(2)*base-
points(5); ...
      mag(normal3)*radii(3) + normal3(1)*basepoints(7) + normal3(2)*base-
points(8)];
```

```
% Solve system
motions = inv(A)*B;
```

```
% Extract error motions (last six terms)
delX = motions(1);
delY = motions(2);
epsZ = motions(3);
```

```
% Second, determine out-of-plane error motions (delZ, epsX, epsY) based on
normal offsets of pin shoulder
% thickness and plate contact height:
```

```
% - approximate delZ as the average of the normal motions at the contact
points
```

```
% - calculate the rotations from the placements of the contact points in
```

```

a centroidal frame

zs_final = [centers(3) + basepoints(3); centers(6) + basepoints(6); cen-
ters(9) + basepoints(9)];
delZ = mean(zs_final);

epsX = atan((centers(3) + basepoints(3) - delZ)/centers(2));
epsY = atan((centers(6) + basepoints(6) - delZ)/centers(4));

% Determine HTM from solved error motions

errorHTM = [1, -1*epsZ, epsY, delX; ...
            epsZ, 1, -1*epsX, delY; ...
            -1*epsY, epsX, 1, delZ; ...
            0, 0, 0, 1];

```

C.2.2 pintransform.m

```

% pintransform.m - calculates deterministic error transformation between
pins and mating plate
% of a three-pin kinematic coupling interface based upon measured positions
% and sized of pins and positions and orientations of contact planes

% John Hart, MIT PERG, 2001

function [errorHTM] = pintransform(centers, radii, basepoints, normals);

% First, solve deterministic in-plane seating
% Assemble matrices for solution of 12-by-12 system giving centroidal frame
error motions (delX, delY, epsZ)

normal1 = [normals(1); normals(2); 0];
normal2 = [normals(4); normals(5); 0];
normal3 = [normals(7); normals(8); 0];

% Matrix A = coefficients
A = [ 1, 0, -1*centers(2), -1, 0, 0, 0, 0, 0; ...
      0, 1, centers(1), 0, -1, 0, 0, 0, 0; ...
      1, 0, -1*centers(5), 0, 0, -1, 0, 0, 0; ...
      0, 1, centers(4), 0, 0, 0, -1, 0, 0; ...
      1, 0, -1*centers(8), 0, 0, 0, 0, -1, 0; ...
      0, 1, centers(7), 0, 0, 0, 0, 0, -1; ...
      0, 0, 0, normal1(1), normal1(2), 0, 0, 0, 0; ...
      0, 0, 0, 0, 0, normal2(1), normal2(2), 0, 0; ...
      0, 0, 0, 0, 0, 0, 0, normal3(1), normal3(2)];

% Matrix B = constants
B = [ -1*centers(1); ...
      -1*centers(2); ...
      -1*centers(4); ...
      -1*centers(5); ...
      -1*centers(7); ...
      -1*centers(8); ...

```

```

        mag(normal1)*radii(1) + normal1(1)*basepoints(1) + normal1(2)*base-
points(2); ...
        mag(normal2)*radii(2) + normal2(1)*basepoints(4) + normal2(2)*base-
points(5); ...
        mag(normal3)*radii(3) + normal3(1)*basepoints(7) + normal3(2)*base-
points(8)];

% Solve system
motions = inv(A)*B;

% Extract error motions (last six terms)
delX = motions(1);
delY = motions(2);
epsZ = motions(3);

% Second, determine out-of-plane error motions (delZ, epsX, epsY) based on
normal offsets of pin shoulder
% thickness and plate contact height:
% - approximate delZ as the average of the normal motions at the contact
points
% - calculate the rotations from the placements of the contact points in
a centroidal frame

zs_final = [centers(3) + basepoints(3); centers(6) + basepoints(6); cen-
ters(9) + basepoints(9)];
delZ = mean(zs_final);

epsX = atan((centers(3) + basepoints(3) - delZ)/centers(2));
epsY = atan((centers(6) + basepoints(6) - delZ)/centers(4));

% Determine HTM from solved error motions

errorHTM = [1, -1*epsZ, epsY, delX; ...
            epsZ, 1, -1*epsX, delY; ...
            -1*epsY, epsX, 1, delZ; ...
            0, 0, 0, 1];

```

C.3 Common Routines, Used By Both Simulation Models

C.3.1 mag.m

```

% mag.m - computes the magnitude of a three-component vector

function [magn] = mag(vec)

magn = sqrt(vec(1)^2 + vec(2)^2 + vec(3)^2);

```


Appendix D

Appended Thermal Stability Results

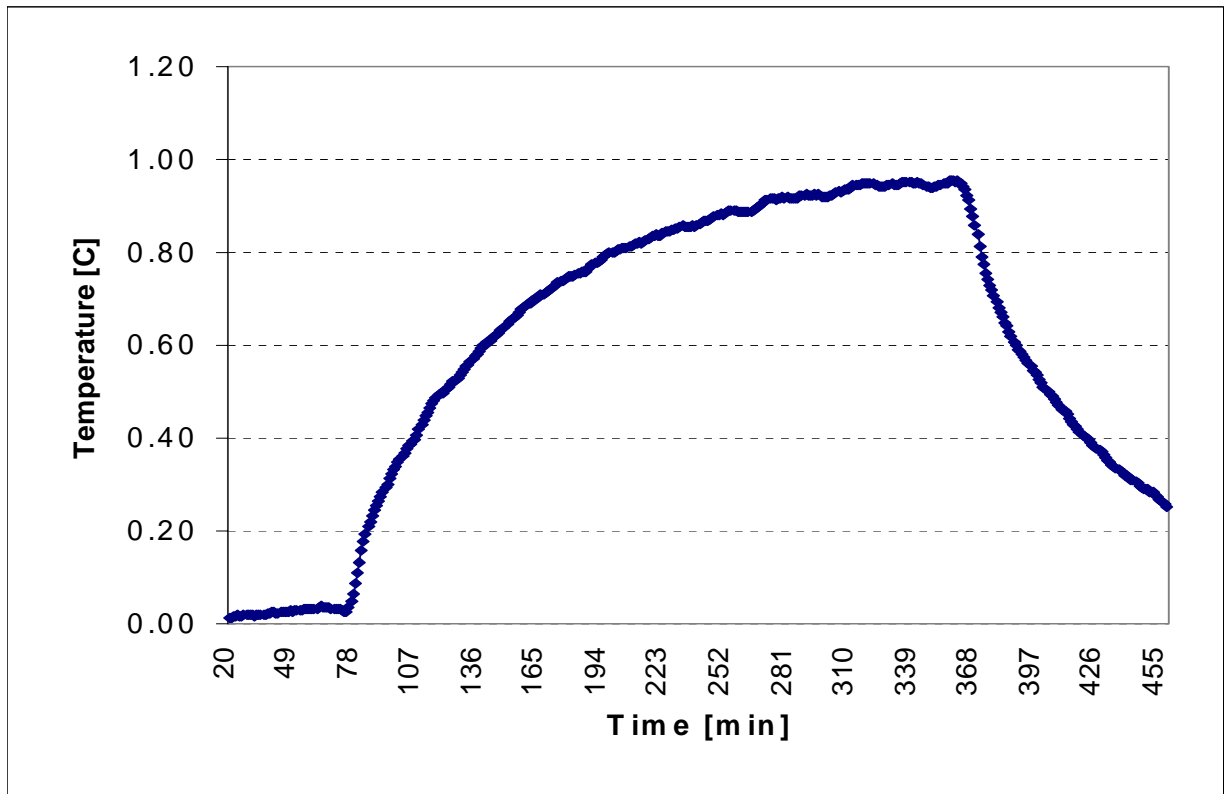


Figure D.1: Vertical temperature range on heated side of segmented structure.

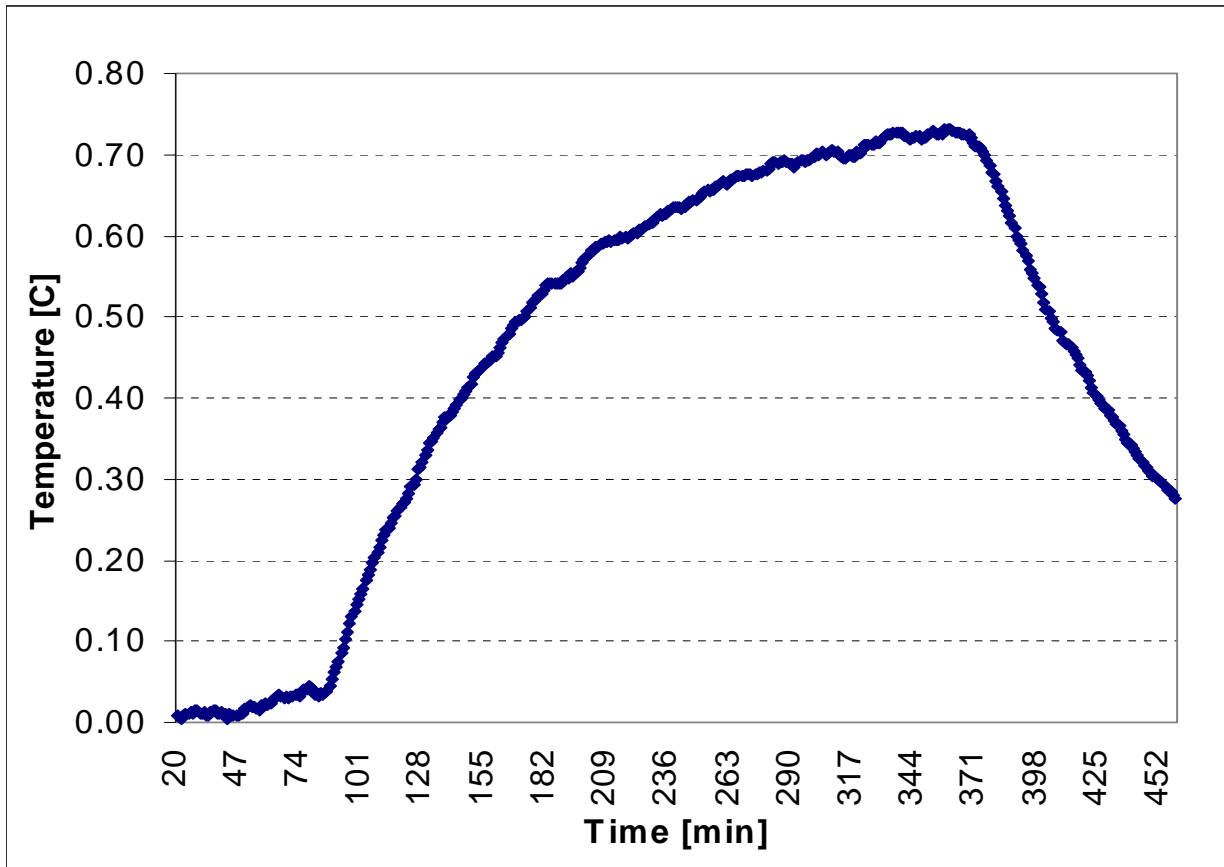


Figure D.2: Vertical temperature range on non-heated side of segmented structure.

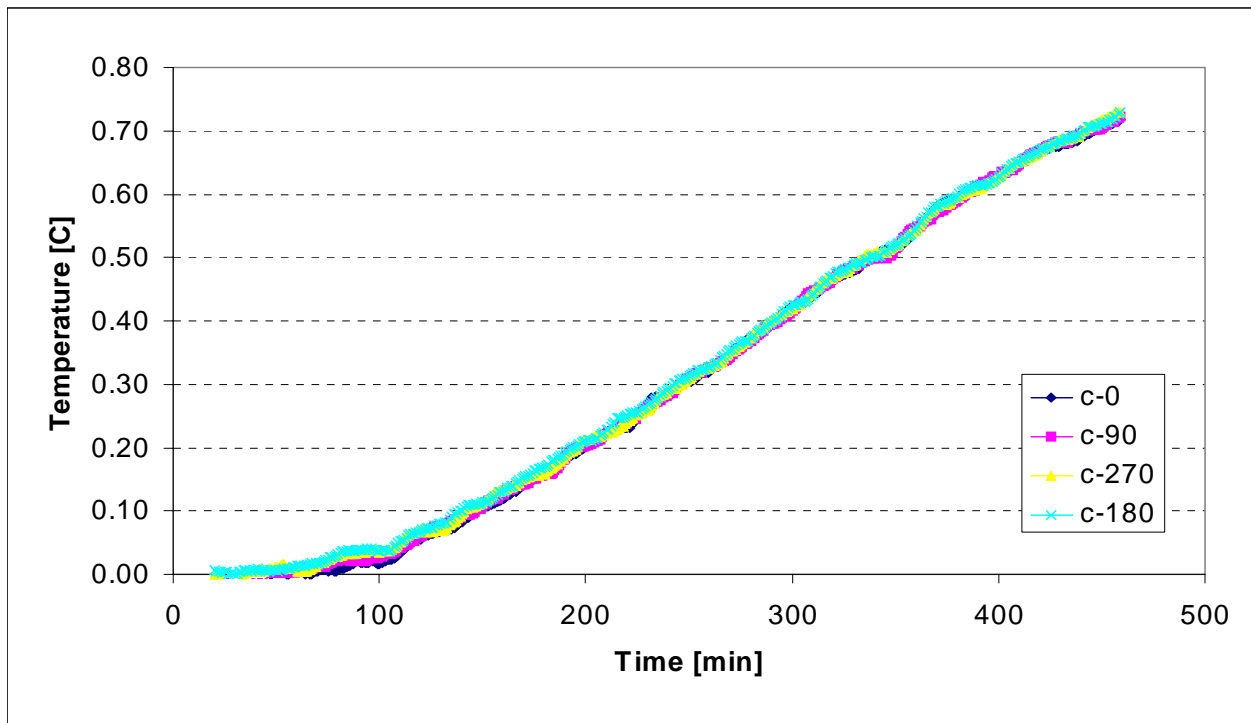


Figure D.3: Circumferential temperature distribution at interferometer mounting position on central column (segmented surrounding).

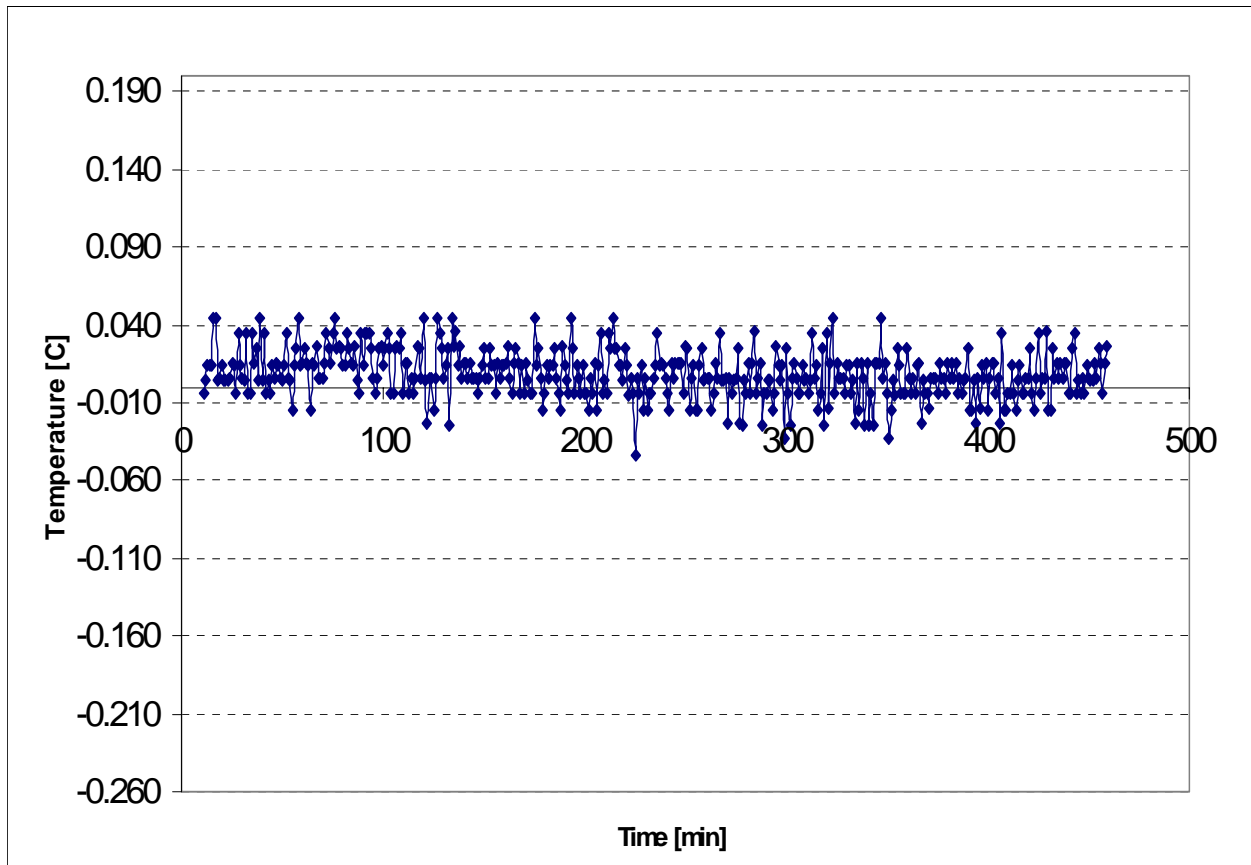


Figure D.4: End-to-end circumferential temperature range on central column (segmented surrounding).

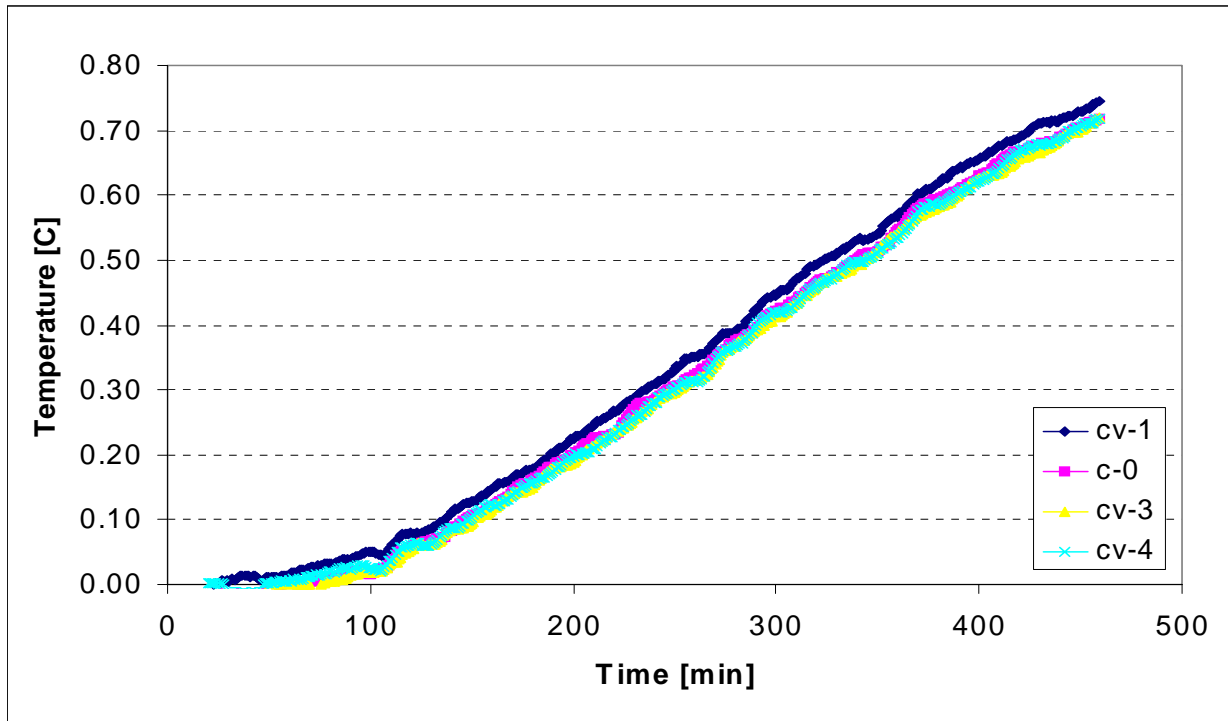


Figure D.5: Vertical temperature distribution on central column (segmented surrounding).

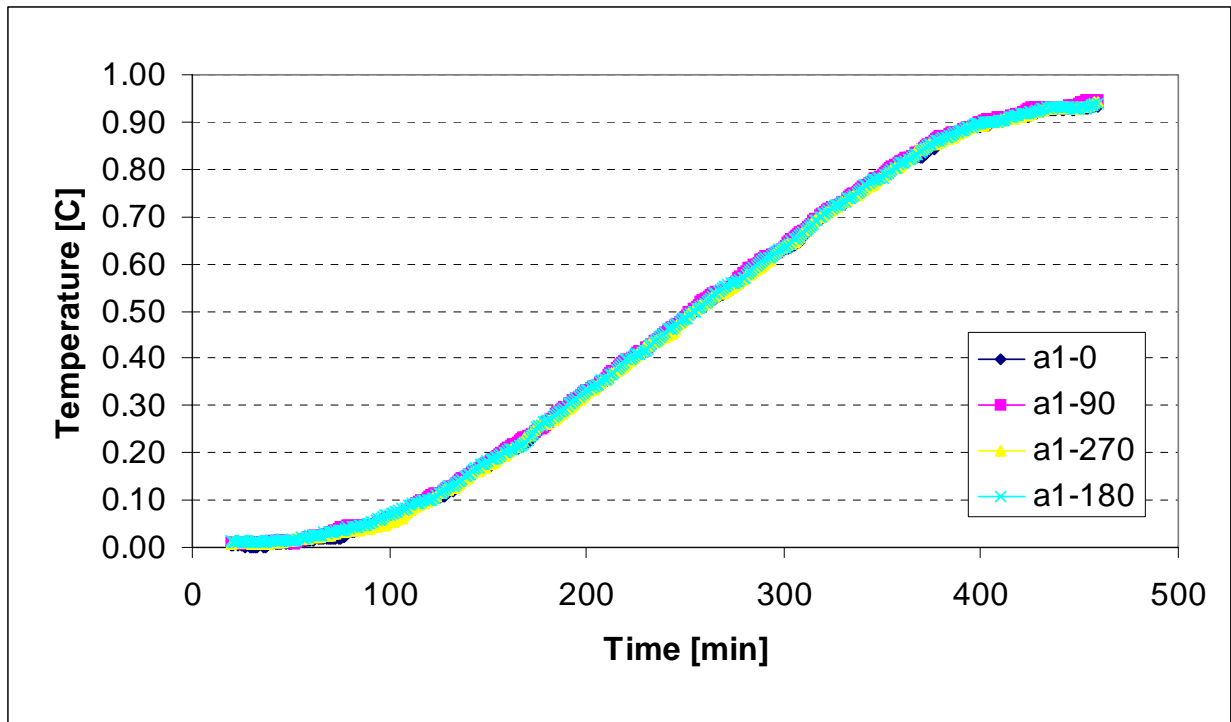


Figure D.6: Circumferential temperature variation in air inside thermal isolation chamber.s

Appendix E

Robot Calibration Pose Set Sequence Optimization

Insert: Kinematics Functions and Simple Solution Algorithms for Calibration Pose Sequence Optimization for a 6-Axis Industrial Robot Manipulator

